



## Rational design of the molecular Ru-based Water Oxidation Catalysts

Natalia Vereshchuk

**ADVERTIMENT.** L'accés als continguts d'aquesta tesi doctoral i la seva utilització ha de respectar els drets de la persona autora. Pot ser utilitzada per a consulta o estudi personal, així com en activitats o materials d'investigació i docència en els termes establerts a l'art. 32 del Text Refós de la Llei de Propietat Intel·lectual (RDL 1/1996). Per altres utilitzacions es requereix l'autorització prèvia i expressa de la persona autora. En qualsevol cas, en la utilització dels seus continguts caldrà indicar de forma clara el nom i cognoms de la persona autora i el títol de la tesi doctoral. No s'autoritza la seva reproducció o altres formes d'explotació efectuades amb finalitats de lucre ni la seva comunicació pública des d'un lloc aliè al servei TDX. Tampoc s'autoritza la presentació del seu contingut en una finestra o marc aliè a TDX (framing). Aquesta reserva de drets afecta tant als continguts de la tesi com als seus resums i índexs.

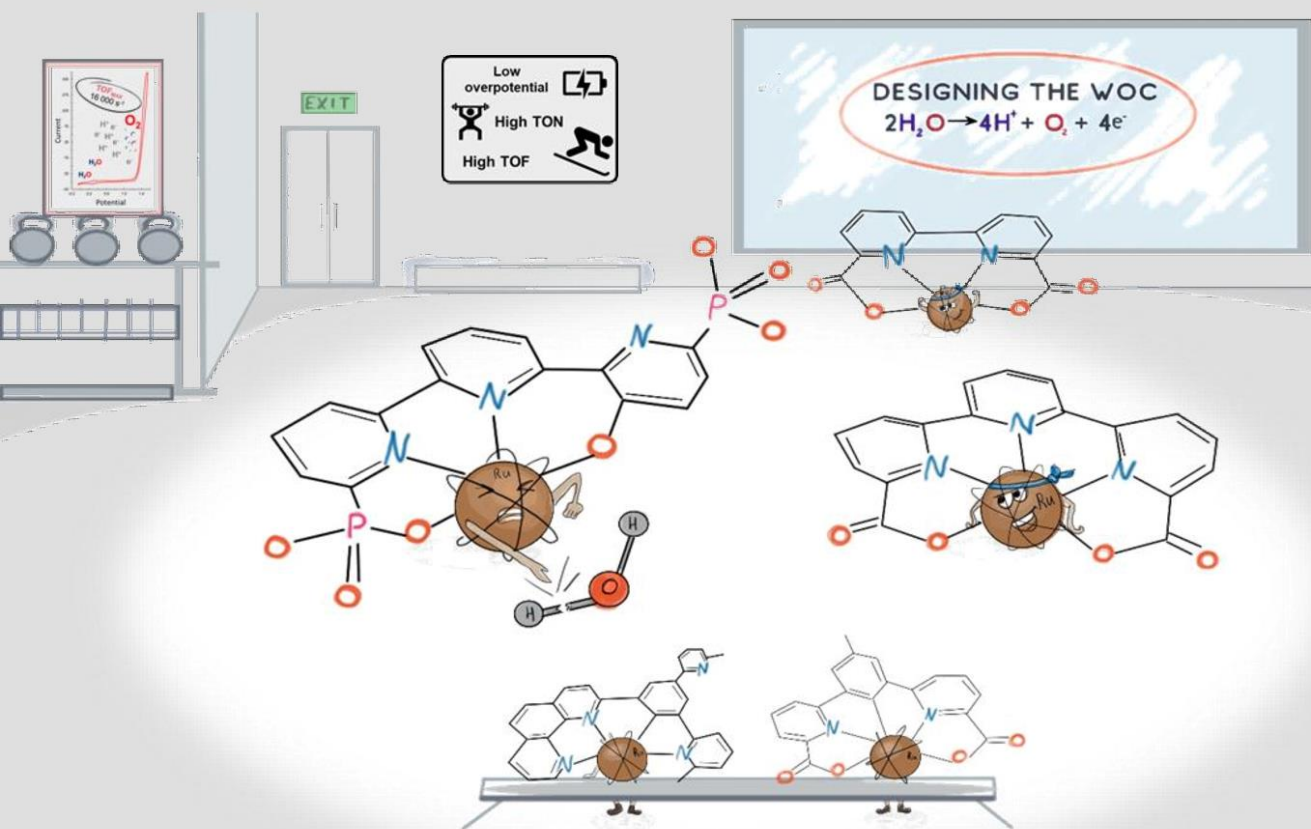
**ADVERTENCIA.** El acceso a los contenidos de esta tesis doctoral y su utilización debe respetar los derechos de la persona autora. Puede ser utilizada para consulta o estudio personal, así como en actividades o materiales de investigación y docencia en los términos establecidos en el art. 32 del Texto Refundido de la Ley de Propiedad Intelectual (RDL 1/1996). Para otros usos se requiere la autorización previa y expresa de la persona autora. En cualquier caso, en la utilización de sus contenidos se deberá indicar de forma clara el nombre y apellidos de la persona autora y el título de la tesis doctoral. No se autoriza su reproducción u otras formas de explotación efectuadas con fines lucrativos ni su comunicación pública desde un sitio ajeno al servicio TDR. Tampoco se autoriza la presentación de su contenido en una ventana o marco ajeno a TDR (framing). Esta reserva de derechos afecta tanto al contenido de la tesis como a sus resúmenes e índices.

**WARNING.** Access to the contents of this doctoral thesis and its use must respect the rights of the author. It can be used for reference or private study, as well as research and learning activities or materials in the terms established by the 32nd article of the Spanish Consolidated Copyright Act (RDL 1/1996). Express and previous authorization of the author is required for any other uses. In any case, when using its content, full name of the author and title of the thesis must be clearly indicated. Reproduction or other forms of for profit use or public communication from outside TDX service is not allowed. Presentation of its content in a window or frame external to TDX (framing) is not authorized either. These rights affect both the content of the thesis and its abstracts and indexes.



# Rational design of the molecular Ru-based Water Oxidation Catalysts

Natalia Vereshchuk



DOCTORAL THESIS

2021



Nataliia Vereshchuk

**Rational design of the molecular Ru-based  
Water Oxidation Catalysts**

DOCTORAL THESIS

Supervised by

**Prof. Antoni Llobet**

Institute of Chemical Research of Catalonia



Tarragona

2021





ICIQ - Institut Català d'Investigació Química

Avinguda Països Catalans 16,

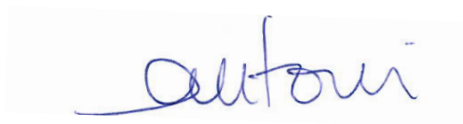
43007 Tarragona (Spain)

Prof. Antoni Llobet, Group Leader at the Institute of Chemical Research of Catalonia

*I STATE that the present study, entitled "Rational design of the molecular Ru-based Water Oxidation Catalysts", presented by Nataliia Vereshchuk for the award of the degree of Doctor, has been carried out under my supervision in my group at the Institut Català d'Investigació Química and that it fulfills all the requirements to be eligible for the International Doctor Distinction.*

Tarragona, November 17<sup>th</sup>, 2020

Doctoral Thesis Supervisors



Prof. Antoni Llobet



## ACKNOWLEDGMENTS

This thesis could not have been accomplished without the help and support of many people, to whom I am deeply grateful and would like to express my gratitude.

I wish to thank **Prof. Antoni Llobet**, foremost for giving me an opportunity to do my Ph.D. in his group, for believing in me from the first moment, and for introducing me into the world of coordination chemistry. I have been extremely lucky to have a supervisor who cared so much about my work, and who responded to my questions and queries so promptly. My enormous and endless gratitude for helping me to develop not only as a scientist but also as a person.

I would like to express my gratitude to **Maria José** for all the help from the first day I arrived at the institute. Personally, for me you are “*Saint*” **Maria José**, without your help, it would have been a nightmare for foreigners like me to do all the paperwork, so thank you a lot! I am thankful for all your hard and great work, for all your wise advice and huge empathy.

My enormous and endless gratitude goes to my mentor **Roc Matheu**, for sharing with me all the secrets of electrochemistry, for helping me in everything, and always being open to discussion. I have learned so much from you and with you and I will be always grateful for it.

I am very thankful to **Dr. Carolina Gimbert** for all the help and support during my Ph.D. journey, for always being very kind in answering questions.

I would like to acknowledge **Dr. Olaf Rudiger** and **Prof. Serena DeBeer** from the Max Planck Institute for Chemical Energy Conversion (Germany), for allowing me to work in their research group. I thank all the group people there for helping me in the lab whenever necessary as well as for the constant support and nice discussions inside and outside the lab and helping me to understand the chemistry occurring there.

A collective HUGE THANKS goes to the whole **Llobet group members** for a fantastic working atmosphere, for being always willing to help in everything, and for all the wonderful time enjoyed together during our work in the lab, our dinners and lunches, our group trips, and our unforgettable, always full of adventures parties. I wish to have co-workers like you always, but honestly, you are irreplaceable!



I thank all the group members during the journey from the beginning: **Pablo, Chuanjun, Abi, Laura, Navid, Andrew Howe, and Andrew Bagnall, Yuanyuan, Tingting, and Sayantan**. In addition, I would like to thank all the guests of our group for the time we shared: **Dooshaye, Irene, Florian, Doro, and Jana Oliveras**.

I would like to thank our international collaborators **Alice De Palo** and **Andrey Shatskiy** for such a nice collaboration that I have enjoyed and from which I learned a lot. Thanks a lot, to Andrey for our scientific discussions about electrochemistry, synthesis, and life; it helped me greatly!

I would like to thank all the technical staff and people who help me to perform the work done in this thesis: Isra and Kerman (NMR), Jordi Bennet and Marta (X-Ray), Marta and Cristina (CRT Unit), Marta, Simona, and Meritxell (Chromatography Unit), Fernando, Georgiana and Mariona (Spectroscopy Unit), Noemí (HR mass Unit), Xavier (for making the electrochemical cells and lots of other glass stuff), Maintenance and Purchase Units as well as IT and SHEQ Units, and Jesus and Alexandre from logistic for bringing to our lab not just all the chemicals but also cheerful vibes. Many thanks to all of you!

I'd like to give special thanks to my group/flatmate **Sergi**, for the nice time shared, for so many moments that we shared and so many things that I learned from you, this experience would not be the same without you. Your friendship is one of the best things this thesis has given me!

I am very thankful to **Marta** for being there, I have not enough words to thank you for all your support and help during this time, for '*chemical question of the day*' and for '*what did I learn today*', for '*tinder moment*' and '*que coincidencia*', for introducing me into Catalan culture and sharing your Catalan friends with me. However, the most important for being always enormously empathic and supportive in any situation that happened during this time.

Special big thanks to **Dr.Marcos** for being friendly and for creating such a nice and fun working atmosphere, which I doubt I could find in any other place, for always being there for me as a friend and supportive college.

I wish to express my deepest gratitude to **Jan Holub**, for believing in me, for teaching me to believe in myself, for our endless scientific discussions from which I have learned a lot, for being so patient listening to all my frustrations and endless complaining at work

and outside of it (especially during *Via Ferrata*!!, which I will never forget). All those things made me not just a better researcher, but also a better person. Thank you for encouraging me to grow as a scientist, but especially thank you for being such a good friend, who always take care of me!

Huge thanks go to my friends: **Ludovico and Martina, Asmaul and Leonie, Robin and Primavera, Jan Oldengott, and Jana Lucker, Vasilis and Marco**, who made my time in Spain memorable and I have lived unforgettable moments with you all! Thank you for all the sweetness and love during these four years and for being my family at the institute.

A special thanks to **Paulina, Anastasia, and Andrea** for being a friend inside and outside the work, helping, and encouraging me during a tough time, for constant positive support, and for helping me in all the aspects of my life.

Last, but foremost, I must thank my parents for their love and support throughout my life. Thank you both for giving me the strength to reach for the stars and chase my dreams.

І найголовніше, я хочу подякувати своїм батькам за їхню любов та підтримку протягом усього мого життя. Дякую вам обом за те, що ви дали мені сили тягнутися до зірок і переслідувати мої мрії .

The work performed in the present doctoral thesis has been possible thanks to the Institute of Chemical Research of Catalonia (ICIQ) and the funding of MINECO/MICINN, FEDER (CTQ2016-80058-R, CTQ2015-73028-EXP, SEV 2013-0319), AGAUR (2014 SGR-915 and 2017- SGR-1631) and Ph.D. founding of FI Grant: 2017 FI\_B 01160.



Barcelona Institute of  
Science and Technology



UNIÓN EUROPEA  
Fondo Europeo de  
Desarrollo Regional (FEDER)  
*Una manera de hacer Europa*



Agència  
de Gestió  
d'Ajuts  
Universitaris  
i de Recerca



GOBIERNO  
DE ESPAÑA

MINISTERIO  
DE CIENCIA, INNOVACIÓN  
Y UNIVERSIDADES



AGENCIA  
ESPAÑOLA  
DE INVESTIGACIÓN





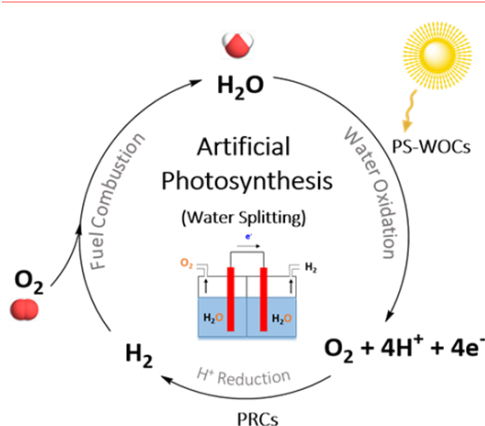
## LIST OF PUBLICATIONS

1. Vereshchuk, N.; Matheu, R.; Benet-Buchholz, J.; Pipelier, M.; Lebreton, J.; Dubreuil, D.; Tessier, A.; Gimbert-Suriñach, C.; Z. Ertem, M.; Llobet, A. **Second Coordination Sphere Effects in an Evolved Ru Complex Based on Highly Adaptable Ligand Results in Rapid Water Oxidation Catalysis.** *J. Am. Chem. Soc.* **2020**, *142* (11), 5068–5077.
2. Vereshchuk, N.; Holub, J.; Gil-Sepulcre M.; Benet-Buchholz, J.; Llobet, A. **The Fate of Molecular Ru-phosphonate Water Oxidation Catalyst under Turnover Conditions** (*submitted*).



## ABSTRACT

### Chapter 1. General introduction



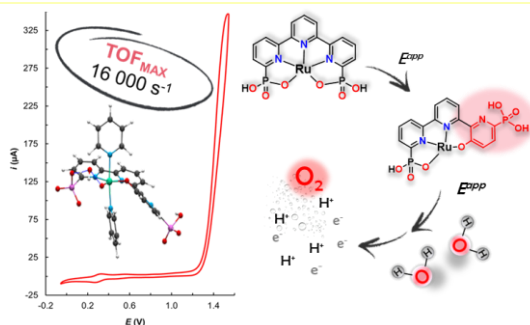
*This chapter includes a brief discussion regarding the energy challenges that society is facing nowadays as well as possible solutions. Then, we described the natural photosynthesis process as an inspiration for renewable energy schemes followed by a description of new technologies based on artificial photosynthesis. Afterward, we present a discussion on how scientists, inspired by*

*nature, developed alternatives to produce clean fuels together with the description of the historical development of the molecular catalysts for water oxidation. Finally, we are showing the analysis of the water oxidation reaction together with the main key factors that determine the progress in the field.*

### Chapter 2. Objectives

*Following the progress in the field of artificial photosynthesis discussed in the General Introduction, the main objectives are exposed in the current chapter. Objectives highlight many challenges that are remaining for achieving the required progress for practical applications.*

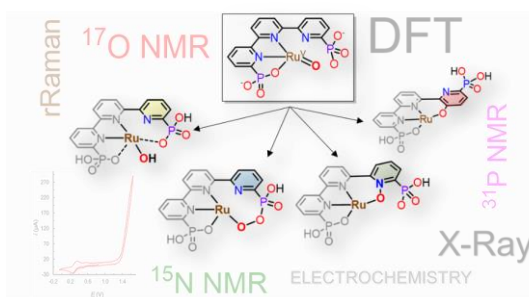
### Chapter 3. Second Coordination Sphere Effects in an Evolved Ru Complex Based on a Highly Adaptable Ligand Results in Rapid Water Oxidation Catalysis



*In the present work, we examined the synthetic and catalytic chemistry related to a Ru complex bonded to a new member of the family of FAME ligands (Flexible Adaptative Multidentate Equatorial). We determined that the initial complex*

*evolves via intramolecular aromatic O-atom insertion into a CH bond, leading to a completely new complex that has the highest TOF ever reported and remarkable long-term stability. Further, we illustrated how second coordination sphere effects are responsible not only for the generation of the active ion of the catalyst but also for the reduction of the energies of activation at the rate-determining step during the catalysis.*

### Chapter 4. Understanding Precatalyst Transformation: Advanced Spectroscopic Characterization



*We addressed the spectroscopic properties of the catalytic species generated over the catalytic conditions. Noteworthy, we compared their properties in both solution and solid-state. An investigation was performed through*

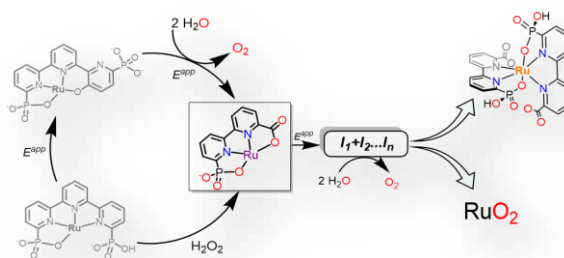
*UV-Vis, rR (resonance Raman), and NMR together with an isotopically labeling experiment with oxygen.*

## Chapter 5. The Fate of Molecular Ru-phosphonate Water Oxidation Catalyst under Turnover Conditions

The present work uncovers the oxidative transformations of a recently reported polypyridyl phosphonate-phenoxo Ru water oxidation catalyst  $[Ru^{III}(tPaO-\kappa-N^2OPc)(py)_2]^{2-}$ , where

$tPaO^{5-}$  is the 3-(hydroxo-[2,2':6',2''-terpyridine]-6,6''-diyl)bis(phosphonate)

ligand. Herein we describe how the catalyst  $[Ru^{III}(tPaO-\kappa-N^2OPc)(py)_2]^{2-}$  suffers

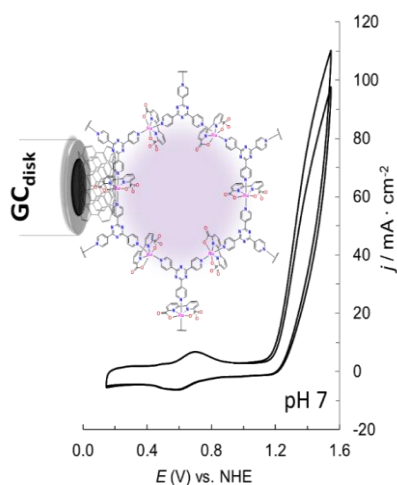


oxidative degradation during water oxidation catalysis and generate the phosphonate-carboxylate Ru complex  $[Ru^{II}(Hbpc)(py)_2]$ , where  $bpc^{3-}$  is 6'-phosphono-[2,2'-bipyridine]-6-carboxylic. Complex  $[Ru^{II}(Hbpc)(py)_2]$  has been prepared by three different methods and its oxidative transformations were studied in detail. Through the electrochemical analysis of  $[Ru^{II}(Hbpc)(py)_2]$ , we discovered several conversions, that  $[Ru^{II}(Hbpc)(py)_2]$  occur during catalysis and, consequently, forming the non-catalytic species  $[Ru^{II}(bpc-\kappa-N^2OP)_2]$  and  $RuO_2$ . Herein, the presented electrochemical data provide strong evidence of the  $[Ru^{III}(tPaO-\kappa-N^2OPc)(py)_2]^{2-}$  oxidative transformations and support the proposed mechanistic scenario. Furthermore, the data also suggest the co-occurrence of two WOC paths: a homogeneous pathway driven by the molecular complex/generated intermediates and a heterogeneous pathway, based on  $RuO_2$ .

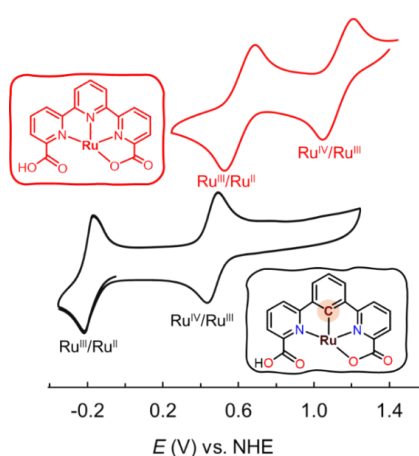


## Chapter 6. Efficient Ru-based Molecular 2D Catalyst on the Heterogeneous Phase

The present chapter uncovers the borderline between homogeneous and heterogeneous water oxidation catalysis using a Ru-based WOC containing  $bpc^{3-}$  as an equatorial ligand. Here we presented a functional two-dimensional (2D) coordination polymer based on  $[Ru(bpc)(DMSO)Cl]$  monomer, which has been prepared and evaluated as a water oxidation catalyst at neutral and acidic pHs. Different anchoring strategies were applied for anode preparation and their redox and spectroscopic features have been analyzed over various conditions.



## Chapter 7. Ruthenium-based cyclometalated complexes: Synthesis, structure and redox properties



The present chapter uncovers a series of novel cyclometalated **Ru** complexes in order to utilize the octahedral coordination mode around the **Ru** center and thus modulate its electrochemical and physical properties. The chelation mode was defined by steric effects and C-H activation selectivity of the ligand, which directed the development of a general synthetic protocol. Furthermore, the structural and electrochemical properties of the ruthenium complexes were

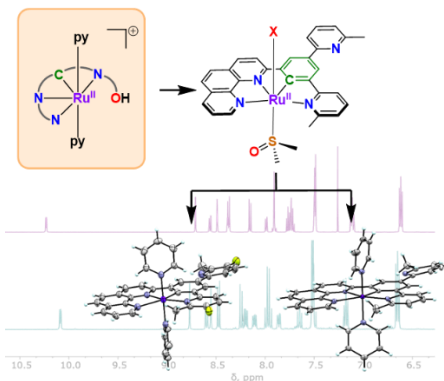
studied in-depth and the results are presented below.

## Chapter 8. Oxidation Properties of Asymmetric Cyclometalated Ru Complexes with Carbanionic Donor Sets

*New non-symmetric mononuclear ruthenium complexes containing an anionic tetradentate Phpp<sup>-</sup> type of ligand (Phpp is 2-(3-(pyridin-2-yl)phenyl)-1,10-*

*phenanthroline) have been synthesized to utilize the octahedral coordination mode around the Ru center to modulate the catalytic properties. These complexes and their synthetic intermediates have been*

*characterized using spectroscopic and electrochemical techniques. Their redox properties were investigated by electrochemical techniques under different conditions.*



## Chapter 9. Conclusions

*The specific and more detailed conclusions of each work are disclosed in Chapters 3-8. General conclusions are exposed in this Chapter in order to summarize the present doctoral thesis.*



## TABLE OF CONTENT

<b>1</b>	<b>CHAPTER 1. GENERAL INTRODUCTION .....</b>	<b>23</b>
1.1	GLOBAL CLIMATE PROBLEMS: CAUSES AND CONSEQUENCES .....	25
1.2	MOLECULAR WATER OXIDATION: FROM NATURAL TO ARTIFICIAL.....	31
1.3	MECHANISTIC ASPECTS OF WATER OXIDATION CATALYSIS .....	39
1.4	REMAINING CHALLENGES AND OUTLOOK .....	46
1.5	REFERENCES.....	48
<b>2</b>	<b>CHAPTER 2. OBJECTIVES .....</b>	<b>55</b>
<b>3</b>	<b>CHAPTER 3 .....</b>	<b>61</b>
3.1	INTRODUCTION.....	65
3.2	RESULTS.....	67
3.3	DISCUSSION .....	76
3.4	REFERENCES.....	80
3.5	SUPPORTING INFORMATION.....	84
<b>4</b>	<b>CHAPTER 4 .....</b>	<b>137</b>
4.1	INTRODUCTION.....	140
4.2	RESULTS AND DISCUSSION .....	141
4.3	CONCLUSIONS .....	149
4.4	REFERENCES.....	150
4.5	SUPPORTING INFORMATION.....	153
<b>5</b>	<b>CHAPTER 5 .....</b>	<b>167</b>
5.1	INTRODUCTION.....	170
5.2	RESULTS AND DISCUSSION.....	171
5.3	CONCLUSIONS .....	174
5.4	REFERENCES.....	183
5.5	SUPPORTING INFORMATION.....	186
<b>6</b>	<b>CHAPTER 6 .....</b>	<b>203</b>
6.1	INTRODUCTION.....	206

6.2	RESULTS AND DISCUSSION .....	209
6.3	CONCLUSION.....	219
6.4	EXPERIMENTAL SECTION .....	220
6.5	REFERENCES.....	222
6.6	SUPPORTING INFORMATION .....	224
<b>7</b>	<b>CHAPTER 7 .....</b>	<b>229</b>
7.1	INTRODUCTION.....	232
7.2	RESULTS AND DISCUSSION .....	234
7.3	CONCLUSION.....	240
7.4	EXPERIMENTAL SECTION .....	242
7.5	REFERENCES.....	246
7.6	SUPPORTING INFORMATION.....	247
<b>8</b>	<b>CHAPTER 8 .....</b>	<b>271</b>
8.1	INTRODUCTION.....	274
8.2	RESULTS AND DISCUSSION .....	277
8.3	CONCLUSION.....	286
8.4	EXPERIMENTAL SECTION .....	287
8.5	REFERENCES.....	292
8.6	SUPPORTING INFORMATION.....	293
<b>9</b>	<b>CHAPTER 9. CONCLUSIONS.....</b>	<b>319</b>

## Glossary of terms and abbreviations

APT	Atom proton transfer
bda	2,2'-bipyridine-6,6'-dicarboxylate
bpy	bipyridine
CAN	Ceric Ammonium Nitrate
CV	Cyclic Voltammetry
DCM	Dichloromethane
DFT	Density Functional Theory
DPV	Differential Pulse Voltammetry
$E$	Potential
$E^\circ$	Standard potential
$E_{1/2}$	Half-wave potential
EDG	Electron Donating Group
ESI-MS	Electrospray Ionization Mass Spectrometry
FOWA	Foot of the Wave Analysis
$i$	Current
I2M	Interaction between two M-O entities
$i_p$	Current intensity
Isoq	Isoquinoline
$j$	Current density
m/z	Mass-to-Charge ratio
NHE	Normal Hydrogen Electrode
NMR	Nuclear Magnetic Resonance
OEC	Oxygen Evolving Center
PCET	Proton Coupled Electron Transfer
phbf	Phosphate buffer
Pic	Picoline
PSI	Photosystem I
PSII	Photosystem II
py	pyridine

r.d.s	Rate limiting step
rR	Resonance Raman
HTfO	Triflic acid
tda	[2,2':6',2''-terpyridine]-6,6''-dicarboxylate
TOF	Turnover Frequency
TON	Turnover Numbers
tpy	2,2':6',2''-terpyridine
TS	Transition State
UV-Vis	Ultraviolet-visible Spectroscopy
WNA	Water Nucleophilic Attack
XAS	X-ray absorption spectroscopy
XRD	X-ray diffraction
$\epsilon$	Extinction coefficient

# 1 CHAPTER 1

## GENERAL INTRODUCTION

---

---

*This chapter includes a brief discussion regarding the energy challenges that society is facing nowadays as well as possible solutions. Then, we described the natural photosynthesis process as an inspiration for renewable energy schemes followed by a description of new technologies based on artificial photosynthesis. Afterward, we present a discussion on how scientists, inspired by nature, developed alternatives to produce clean fuels together with the description of the historical development of the molecular catalysts for water oxidation. Finally, we are showing the analysis of the water oxidation reaction together with the main key factors that determine the progress in the field.*

---

---



## CHAPTER 1. General Introduction

# I

## General Introduction

# I

### 1.1 Global climate problems: Causes and Consequences

The COVID-19 pandemic may well turn out to be the most catastrophic and disruptive event that society will have to deal with nowadays. As I write this – at the beginning of November – over 1.3 million people worldwide have lost their lives due to the infection.<sup>1</sup> As an outcome, the health crisis strongly affected the economic life and the employment market of millions more, which came at a huge economic and social cost.<sup>2–4</sup> Undoubtedly, the world is on the edge of an unprecedented turning point. Moreover, climate change is a real and inevitable threat to the well-being and secure lifestyle that many have already achieved today and for which millions of people strive and work. The overall crisis that we are facing now, combined with health and economic shock from it, can restructure the international economic, political, and social atmosphere in which we all live and operate. What is more, it might have the potential to accelerate emerging trends and generate prospects to shift the world into a more sustainable path.

Some aspects are encouraging, namely the ongoing rapid growth of renewable energy sources together with their continuous development leading to more efficient solar fuel production yields. The International Energy Agency's World Energy Outlook of 2020,<sup>5</sup> reflects these developments by illustrating that the world's best solar power schemes offer the "cheapest electricity in history"; cheaper than the technologies utilized for the combustion of coal and gas in most countries.<sup>6,7</sup> Led by wind and solar power, fuel production from renewable energies is constantly increased reaching the record amount of over 40% of the annual growth in primary energy in 2019.<sup>5</sup> Simultaneously, coal consumption decreased for the fourth time in the past six years, reaching the lowermost level for last 16 years of its utilization in the global energy balance.<sup>8,9</sup> Nonetheless, other aspects of the energy system continued to give cause for concern.<sup>10,11</sup> Despite last year's decline, coal was still the only largest source of energy, accounting for over 36% of global energy.

The global primary energy demand was projected to increase by about 37% during the period from 2012 to 2040,<sup>5,12–14</sup> due to the anticipated increase of the world's population

## CHAPTER 1. General Introduction

I

and the higher expected standards of cost livings (see Figure 1). The transition to societies that are based on environmental, renewable energy, and economic policies is one of the greatest challenges of the 21<sup>st</sup> century targeting to substantially decrease our ecological footprint.<sup>15,16</sup>

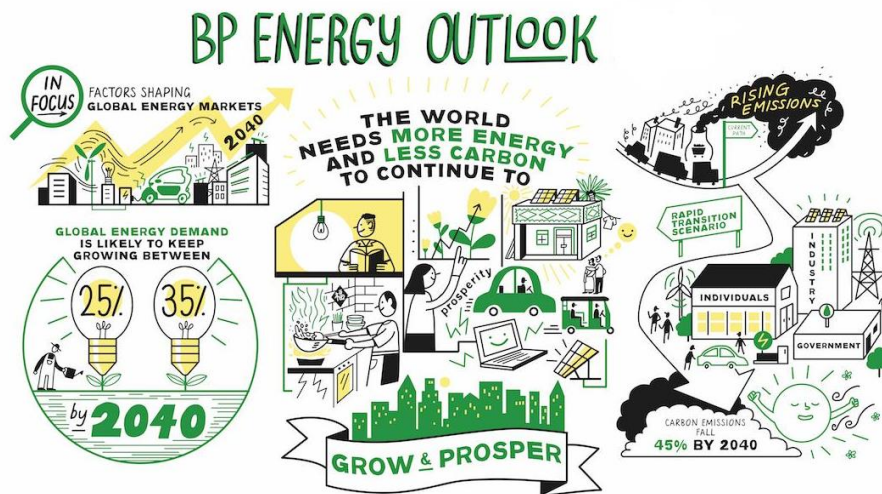


**Figure 1.** BP Energy Outlook for 2019, exploring key uncertainties that could influence global energy markets up until 2040.

Another disturbing trend over the last 40 years is the constant increase in carbon dioxide emissions due to the combustion of fossil fuels (see Figure 2 for the last 15 years dynamic). The reduction of CO<sub>2</sub> emissions in 2019 by 0.5% is a positive fact that offers a ground of optimism. However, this annual decrease is essential to be permanent and integrated with a big increase in CO<sub>2</sub> emissions in 2018 by 2.1%.<sup>17</sup> Noteworthy, the average annual growth in CO<sub>2</sub> emissions from 2018 to 2019 was greater than the last 10-year average. As the world emerges from the COVID-19 crisis, decisive changes towards more sustainable paths are needed. The disruption to our everyday lives caused by the lockdowns has provided a glimpse of a cleaner world with lower carbon emissions: air quality in many cities has improved and skies have become clearer.<sup>18</sup> Interestingly, the International Energy Agency<sup>5</sup> estimate that global CO<sub>2</sub> emissions may fall by as much as 2.6·10<sup>6</sup> tons this year.

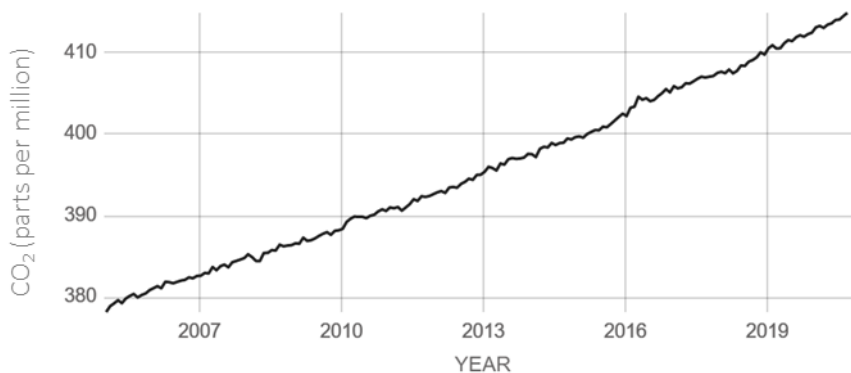


**Figure 2.** Atmospheric CO<sub>2</sub> concentrations in parts per million (ppm) for the past 15 years, from monthly measurements (average seasonal cycle removed).<sup>17</sup>

However, to get to net-zero by 2050,<sup>19</sup> similar-sized reductions in carbon emissions every other year are required for the next 25 years. This could only be achieved *via* a radical change in all our actions:

- Efficient consumption of natural resources and energy.
- Implementing the zero/low carbon energy sources together with the new technologies.

### 1.1.1 Fossil fuels

The use of fossil fuels has played a key role in shaping our society's lifestyle, allowing substantial economic and population growth over the last centuries. Over a hundred years, fossil fuels have been the primary energy source that guided human development. They are essential for several important sectors such as industry and transportation and almost 80% of the worldwide energy vectors derive from them. It is the most conventional energy resource, which is essential for the economic improvement of countries. Despite its bad effects on health and the environment, the world is still fully dependent on fossil fuels, due to its obvious benefits of fossil fuel production due to its huge energy density and ability to power anything together with its chemical stability, which makes it easy to store and to transport.

The limited sources of fossil fuels is one of the main problem in terms of looking for an alternative. Nevertheless, a more urgent problem is the lack of atmosphere in which to put

## CHAPTER 1. General Introduction

I

all the products that the world's energy metering now consumes. The amount that we are using now simply is not sustainable, and the problem is getting worse as the global population increases together with the CO<sub>2</sub> emission (see Figure 3).

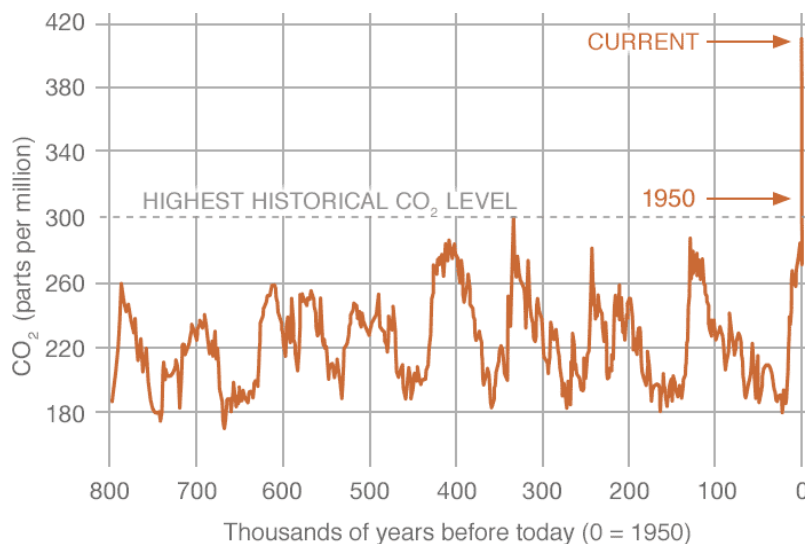


**Figure 3.** Atmospheric CO<sub>2</sub> concentrations in ppm for the past 800,000 years, based on EPICA (ice core) data, with the 2013 annual average concentration of 396.48 ppm (dashed line) appended. The peaks and valleys in CO<sub>2</sub> levels follow the coming and going of ice ages (low levels) and warmer interglacial (higher levels).<sup>17,20,21</sup>

Globally the burning of fossil fuels releases CO<sub>2</sub> and other greenhouse gases into the atmosphere, which is responsible for 90% of all greenhouse gas emissions from human activity (burning fossil fuels for electricity, heat, and transportation).<sup>22</sup> To keep the increase of average global temperature below 1.5°C, it is imperative to decrease the usage of fossil fuel by 80% – however globally, our reliance on fossil fuels is constantly increasing (see Figure 4).<sup>23</sup>

Multiple models predict<sup>24,25</sup> that further increase in the atmospheric CO<sub>2</sub> concentration and as the result, the rise of global average temperature, will strengthen these problems (Figure 3).<sup>21</sup>

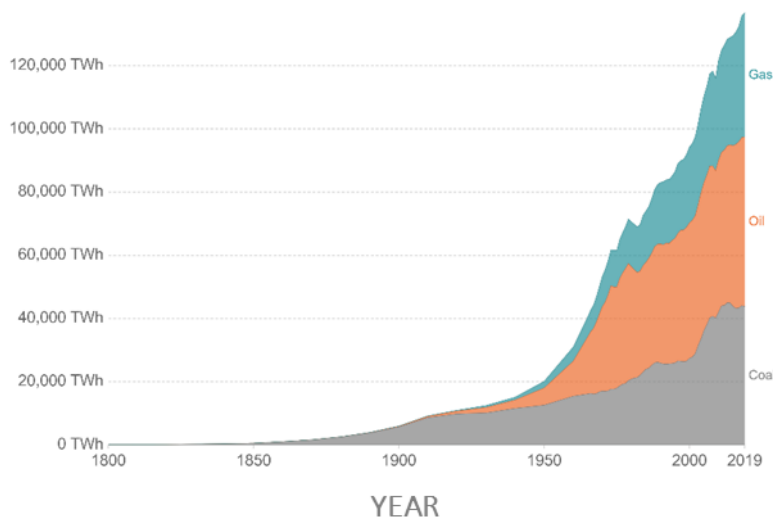


**Figure 4.** Graph displaying Global fossil fuel consumption, measured in terawatt-hours.<sup>26</sup>

Unlike fossil fuels, green energy made from wind and solar power is sustainable because its resources cannot run out. Besides, it provides a way to fight climate change by reducing and even offsetting carbon emissions. It is of top importance to develop technologies for the utilization of carbon-free or carbon-neutral renewable energy sources soon.

### 1.1.2 Artificial Photosynthesis as the Solution to the energy problem

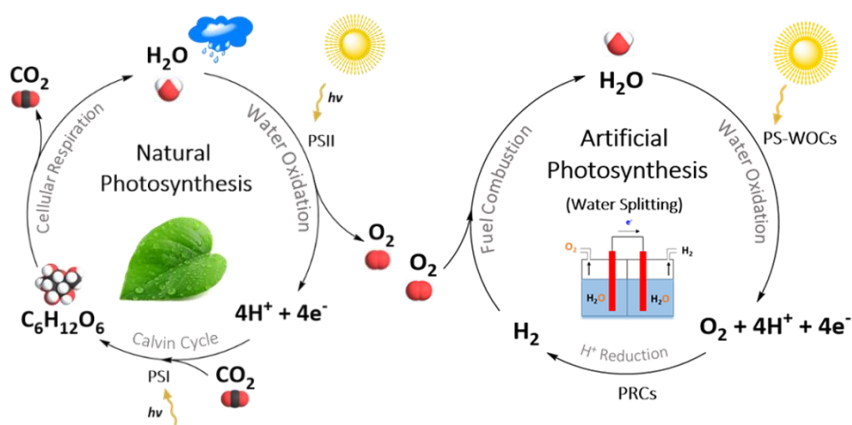
One of the prominent and biggest sources of renewable energy available to humanity by far is the energy of the Sun. According to the US Department of Energy,<sup>27</sup> in less than 80 minutes, the amount of power from the Sun to the Earth is 580 million terajoules, which is enough to cover total world energy usage for the whole year.<sup>5,26,28</sup> Recently, photovoltaic power has become commercially competitive<sup>29</sup> with a huge potential practical application.<sup>30</sup> Building photovoltaic cells are undoubtedly beneficial in the short term; however, they present an important problem, like unpredictable productivity of the generated electrical power as well as an incongruity between the maximum power output during the light time of the day and the grid demand during the dark time of the day. Besides, the generated electrical power illustrates an uneven power output throughout the year due to seasonal phenomena.<sup>31</sup> A conceivable solution would be to use solar energy for fuel production, which can be simply stored, transported, and utilized using the existing infrastructure.

## CHAPTER 1. General Introduction

# I

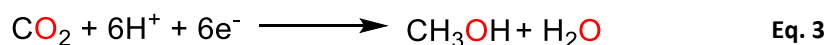
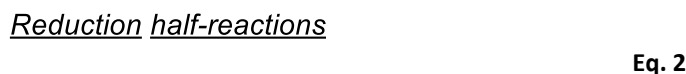
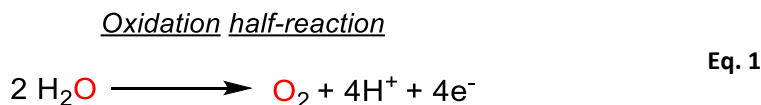
Unfortunately, cost-efficient technologies for storing electrical energy on large scale with possible practical applications are yet to be developed.<sup>32</sup>

Fortunately, nature figured this out and implemented it in the process known as photosynthesis, where green plants take the sunlight, water, and CO<sub>2</sub> and make fuel (carbohydrates). Those carbohydrates are later consumed as fuels to obtain energy for performing life's functions and releasing CO<sub>2</sub> to the environment. The reactions involved in the storage of solar energy are summarized in Scheme 1 and, from a redox point of view, they can be divided into two half-reactions: water oxidation and CO<sub>2</sub> reduction (Calvin Cycle).<sup>33</sup>



**Scheme 1.** Representation of natural photosynthesis (left part) and artificial photosynthesis processes (right part).

Following an analogous scheme, artificial photosynthesis has arisen as a promising technology to harvest solar energy into fuels.<sup>34,35</sup> This process generally involves the oxidation of water to molecular oxygen releasing protons and electrons (eq. 1) and the further reduction of those protons to molecular hydrogen (eq. 2), the reason why this process is also known as water splitting. In the same way, protons and electrons can be used for other reduction reactions coupled to water oxidation such as CO<sub>2</sub> to carbohydrates (eq. 3), nitrogen to ammonia (eq. 4), or any other reductions of organic compounds.



## 1.2 Molecular Water Oxidation: from Natural to Artificial

Water oxidation to molecular dioxygen is an essential reaction in biological systems, due to its implications in natural photosynthesis where plants carry out the reduction of  $\text{CO}_2$  to carbohydrate consuming protons and electrons from the oxidation of water.<sup>36</sup> Similarly, it is a key reaction in the development of sustainable energy schemes based on artificial photosynthesis.<sup>37,38</sup> Understanding the mechanism of water oxidation in Photosystem II (PSII) has long been considered one of the “Holy Grails” of chemistry.<sup>39,40</sup> Scientists emphasize the development of components, processes, and complete systems aiming at practical conversion and storage of solar energy in the form of fuel, using the photosynthetic principles of light-induced charge separation and redox catalysis. This includes direct photochemical water splitting into molecular hydrogen and oxygen, as well as reduction of  $\text{CO}_2$  into a gaseous or liquid fuel.

Oxygenic photosynthesis involves different steps,<sup>41,42</sup> which include light-harvesting, charge separation, electron transfer, production of energy carriers as well as catalytic water oxidation.

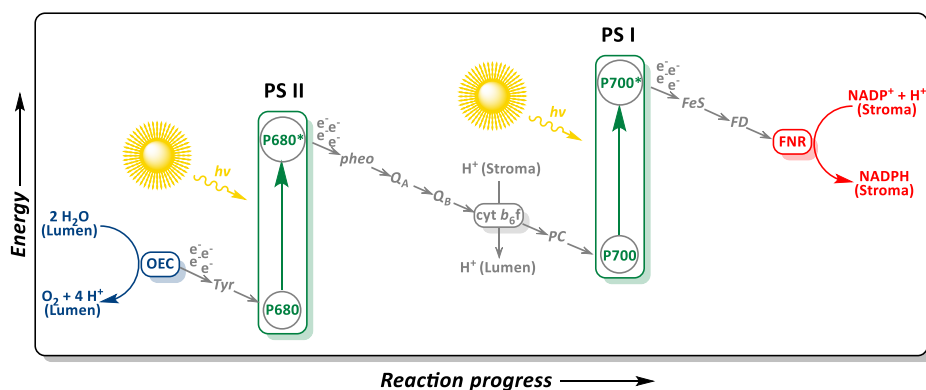
The energy from sunlight is converted into chemical bonds in the form of reducing equivalents such as nicotinamide adenine dinucleotide phosphate (NADPH) and the energy carrier adenosine triphosphate (ATP). They are used for the conversion of  $\text{CO}_2$  into carbohydrates as energy vectors. The electrons for this process are formed by water oxidation at the Oxygen Evolving Complex (OEC) in which dioxygen is formed as a by-



## CHAPTER 1. General Introduction

# I

product.<sup>43</sup> The large-scale oxidation of water and the consequent formation of an O<sub>2</sub> rich atmosphere have also forced life to adapt to survive in the presence of O<sub>2</sub>.<sup>44,45</sup>



**Scheme 2:** Simplified *Z-scheme* of the electron transfer pathway in natural photosynthesis (OEC: Oxygen Evolving Complex; PS: Photosystem; Tyr: Tyrosine; P680/P700: chlorophyll P680/P700; pheo: pheophytin; Q: Plastoquinone; cyt *b<sub>6</sub>f*: Cytochrome *b<sub>6</sub>f* protein complex; PC: Plastocyanin; FeS: Fe-S cluster; FD: Ferredoxin; FNR: Ferredoxin-NADP<sup>+</sup> oxidoreductase; NADPH: nicotinamide adenine dinucleotide phosphate).<sup>37,38</sup>

Photosynthesis can be considered as a membrane-spanning process involving a series of electron transfer steps that are described in the *Z-scheme* (Scheme 2). The OEC, composed of four manganese, one calcium, and five oxygen atoms acts as a charge accumulator and thereby connects the one-electron excitation and transfer processes in PS II and PS I with the four-electron oxidation of water. The structure of the OEC and mechanistic details of the water oxidation reaction have been a subject of intensive research and debate.<sup>46–48</sup>

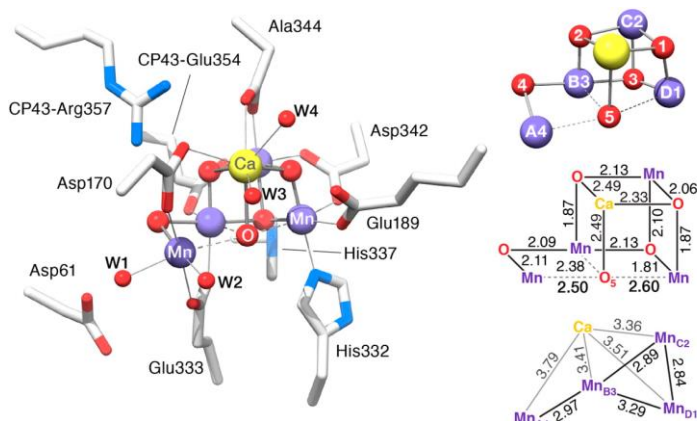


**Figure 5.** (a) X-ray crystallographic structure of the OEC in dark-adapted PSII at 1.9 Å resolution<sup>46</sup> and the Mn<sub>4</sub>O<sub>5</sub>Ca cluster from chain A of the PSII dimer.<sup>47,49</sup>

Thanks to the efforts made by researchers using X-ray Diffraction, X-Ray Absorption, electrochemical and computational studies, the mechanism of this catalyst has been partially revealed.<sup>46,47,49,50</sup> The Mn<sub>4</sub>O<sub>5</sub>Ca is known to be oxidized until four oxidative equivalents are accumulated while releasing four protons in the process. Then the O–O bond formation takes place following a mechanism that is still under investigation.

Investigation of the PSII functionality is essential in both fundamental and applied sciences, for providing data for solar fuel technologies where water oxidation is a bottleneck.<sup>51,52</sup> The Mn<sub>4</sub>O<sub>5</sub>Ca cluster has been a source of inspiration in the design of a catalytic system for water oxidation due to its efficiency and fast reaction rates (TOF: 100-400 s<sup>-1</sup>).<sup>49,53</sup> Specifically, in the case of molecular water oxidation catalysis (WOC) based on transition metal complexes, the design is based on the coordinative interaction of metal-aqua groups, similarly, as Mn and Ca atoms are bonded to aqua groups in the natural cluster. Control on the electronic and geometrical structure of the complexes by ligand design would determine their general features and particularly the catalytic performance toward water oxidation. Therefore, ligand design in catalysis has been an extensively studied field leading to rational discoveries of more efficient, fast, and stable catalysts.

### 1.2.1 Catalytic water oxidation by the Ru complexes

The molecular water oxidation catalysis started later than the other water oxidation fields due to the development of the coordination chemistry. The first molecular WOC, based on

## CHAPTER 1. General Introduction

I

the 2,2'-bipyridine ligand environments was the dinuclear *cis,cis*-[(bpy)<sub>2</sub>(H<sub>2</sub>O)Ru<sup>III</sup>(μ-O)Ru(H<sub>2</sub>O)(bpy)<sub>2</sub>]<sup>4+</sup> (**1** in Chart 1), which was studied and reported by Meyer and co-workers in 1982.<sup>54,55</sup> For the last 30 years the so-called “blue dimer” WOC was a subject of further detailed mechanistic studies. Despite the low activity (TOF = 10<sup>-3</sup> s<sup>-1</sup>) and stability,<sup>56-58</sup> complex **1** arranged the foundation for further investigation in the field of water oxidation.

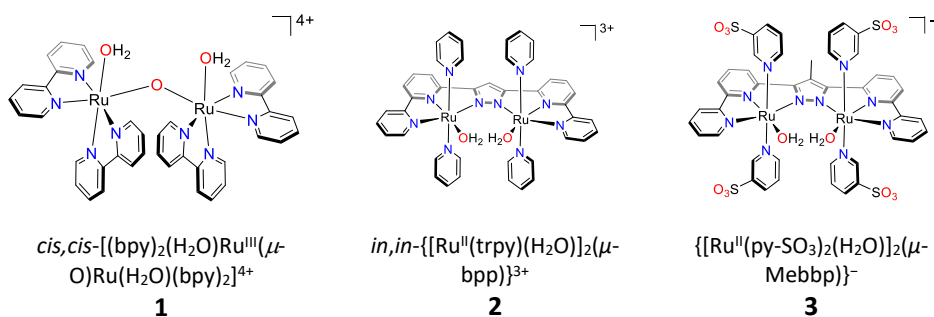


**Chart 1.** Structure for dinuclear Ru complexes **1**, **2**, and **3**.

The discovery of the first molecular catalyst activated the design of more efficient WOCs based on the use of different transition metals<sup>59-65</sup>, together with the variation of the diverse organic ligands. Nonetheless, most of the detailed kinetic, electrochemical, and mechanistic studies were performed for Ru-based coordination complexes. From this point on, we will only mention the most relevant Ruthenium complexes utilized for water oxidation catalysis. The most representative Ruthenium catalysts for water oxidation are provided in Charts 1, 2, and 3.

In 1982, the freshly established molecular water oxidation community assumed that the most suitable complex for water oxidation catalysis should be based on dinuclear complexes. The hypothesis was based on the ability of dinuclear complexes to accumulate four oxidative equivalents. Consequently, successive redesigns of the initial blue dimer complex were performed to enhance its catalytic performance. Later, the Ru–O–Ru bridge of the “blue dimer” was replaced by the more rugged bpp<sup>-</sup> platform with the complex *in,in*-{[Ru<sup>II</sup>(trpy)(H<sub>2</sub>O)]<sub>2</sub>(μ-bpp)}<sup>3+</sup>, **2** in Chart 1 (Hbbp is 2,2'-(1H-pyrazole-3,5-diyl)dipyridine). The bpp<sup>-</sup> bridge offered improved communication between the two Ru centers due to the rigid structure and, as a result, complex **2** oxidized water to O<sub>2</sub> with 70% efficiencies and higher turnover frequency (TOF = 0.01 s<sup>-1</sup>) than the parent complex **1**. However, complex **2** did not

## CHAPTER 1. General Introduction

# I

reach 100 % efficiency under water oxidation conditions due to oxidation of the CH group in the pyrazole and further degradation. Further, redesign dinuclear powerful and oxidatively rugged pyrazolate-based water oxidation catalyst  $\{[Ru^{II}(py-SO_3)_2(H_2O)]_2(\mu-Mebbp)\}^+$ , **3** has been developed.<sup>66</sup> Catalyst **3** has been designed to overcome the weakness of complex **2**, and its performance has been methodically improved (TOF = 0.068 s<sup>-1</sup>). It was demonstrated how small change in the ligand environment cause a significant improvement in the solubility, stability, but most importantly, in the O–O bond formation mechanism, resulting in the close activation energy barriers.

In 2005 Thummel presented an inspiring report featuring a first mononuclear Ru-based catalyst  $[Ru^{II}(npm)(pic)_2(OH_2)]^{2+}$  (npm = 4-t-butyl-2,6-di (1',8'-naphthyrid-2'-yl)pyridine, pic = 4-picoline), **4** in Chart 2, which was able to promote efficient water oxidation not just chemically, but also photochemically.<sup>67</sup> Shortly thereafter, Meyer presented another influential mononuclear catalyst  $[Ru^{II}(tpy)(bpm)(OH_2)]^{2+}$  (tpy = 2,2':6',2'-terpyridine, bpm = 2,2'-bipyrimidine), **5** in Chart 2, and its analog with bpz (2,2'-bipyrazine).<sup>68,69</sup> Despite the moderate catalytic activity, demonstrated by complexes, the knowledge extracted from them provided significant input for progressive mechanistic studies.

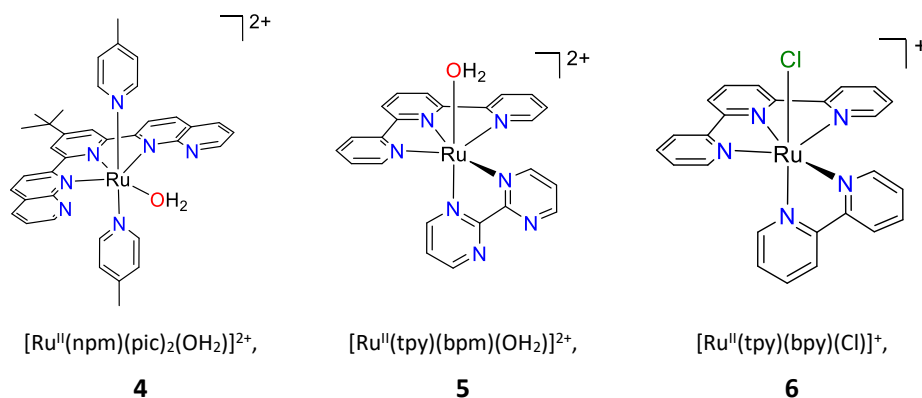


**Chart 2.** Structure for mononuclear Ru complexes **4**, **5**, and **6**.

A huge weakness of the Ru catalysts, described above, was a large potential that needs to be applied for the water oxidation performance, particularly to overcome the most difficult step - formation of the O–O bond. One of the reasons for such an energy demand might be neutral N-donor ligands, which can be overcome by introducing  $\sigma$ -donating negatively

## CHAPTER 1. General Introduction

# I

charged ligands (carboxylate, phosphonate, etc.) in the first coordination sphere of the metal center.

The real increase in activity and efficiency arose with the development of the Ru complexes based on the H<sub>2</sub>bda ligand (H<sub>2</sub>bda is [2,2'-bipyridine]-6,6'-dicarboxylic acid).<sup>70,71</sup> The tetradentate bda<sup>2-</sup> ligand coordinates Ru in the equatorial plane and two picolines (pic) ligands coordinate in the axial plane generating coordination complex [Ru<sup>II</sup>(bda)(pic)<sub>2</sub>], **7** in Chart 3. The bda<sup>2-</sup> ligand stabilizes the high oxidation states of the Ru center through the two anionic charges and the access to a seven-coordinate Ru center. In the contrast to all previously discussed mononuclear Ru-based WOCs, catalyst **7** favors the bimolecular mechanism for the O–O bond formation (explained in detail in the next section), which was demonstrated by several mechanistic and kinetic studies.<sup>70–74</sup> The characteristic bimolecular mechanism for this type of catalyst family significantly limits their practical applicability for anchoring and functionalized it into anodes and photoanodes.<sup>74</sup> The catalysts with the bimolecular mechanism, while being anchored, facing the challenges in restricting the translational mobility, which is needed for the bimolecular catalytic pathway. The efforts of immobilizing this catalyst on the electrode surface shown to operate *via* a higher energy monomolecular mechanism, leading to its decomposition to RuO<sub>2</sub>.<sup>75</sup>

In pursuit of improvements, Concepcion and co-workers presented two Ru(bda)-related WOCs, in which one or both carboxylate groups in the bda<sup>2-</sup> ligand were substituted by phosphonate groups, resulting in complexes [Ru<sup>II</sup>(Hbpc)(pic)<sub>2</sub>]<sup>76</sup>, **8** and [Ru<sup>II</sup>(H<sub>2</sub>bpa)(pic)<sub>2</sub>]<sup>77,78</sup> **9**, (see Chart 3) (Hbpc<sup>2-</sup> = 2,2'-bipyridine-6-hydrogen phosphonate-6'-carboxylate; H<sub>2</sub>bpa<sup>2-</sup> = 2,2'-bipyridine-6,6'-bis-(hydrogen phosphonate)). Despite the similarity to the coordination geometry of Ru(bda), both catalysts were shown to operate *via* a monomolecular mechanism for the O–O bond formation and the monocarboxylate complex **8** could carry out chemically driven water oxidation with a TOF as high as 100 s<sup>-1</sup> (triggered by Ceric ammonium nitrate (CAN) at pH 1.0).

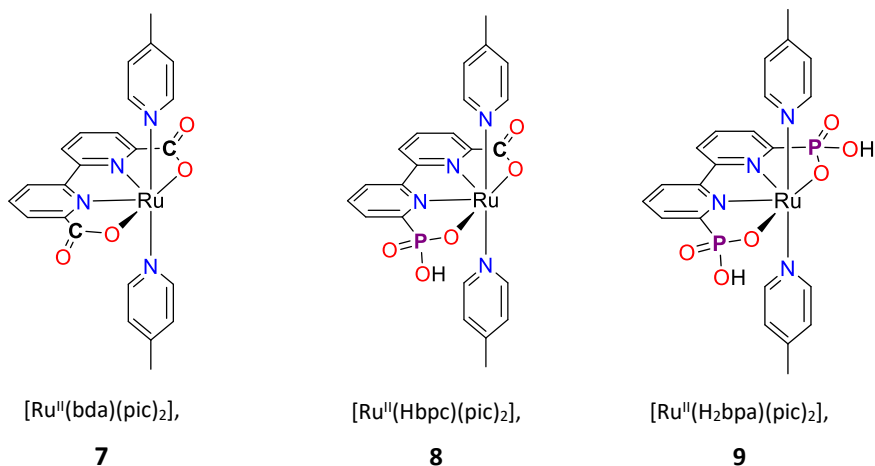


**Chart 3.** Structure for mononuclear Ru complexes **7**, **8**, and **9**.

Another recent Ru(bda)-inspired WOC operating *via* a monomolecular mechanism for the O–O bond formation was developed by Llobet and co-workers.<sup>79</sup> In this catalyst, the bipyridine ligand core was substituted with terpyridine, resulting in the coordination complex [Ru<sup>II</sup>(tda)(py)<sub>2</sub>] (tda<sup>2-</sup> = 2,2':6',2''-terpyridine-6,6''-dicarboxylate), **10** (see Chart 4).<sup>79–81</sup>

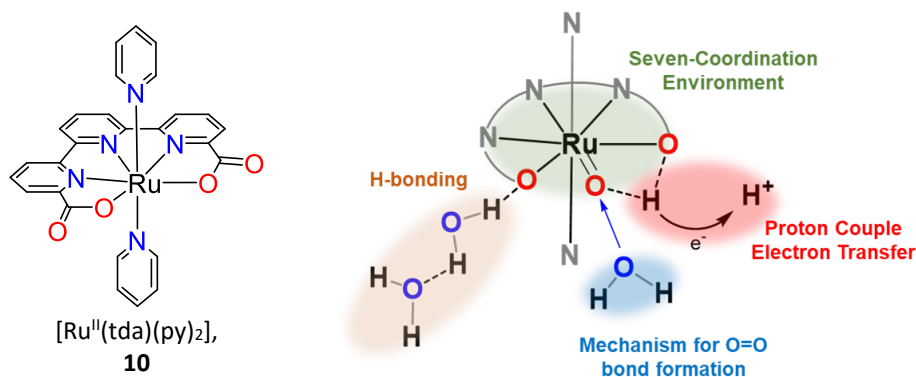


**Chart 4.** (left) Structure for mononuclear Ru complex **10**. (right) Important features for the design of a powerful water oxidation catalyst.

Originally, this coordination complex did not show any catalytic activity, however, electrochemical oxidation of complex **10** from Ru<sup>II</sup> to the Ru<sup>IV</sup> oxidation state triggered the

## CHAPTER 1. General Introduction

# I

formation of an extremely active catalyst  $[\text{Ru}^{\text{V}}(\text{O})(\text{tda})(\text{py})_2]$ , that could promote electrochemical water oxidation with  $\text{TOF}_{\text{max}} = 8000 \text{ s}^{-1}$  in pH 7.0 and  $\text{TOF}_{\text{max}} = 50\,000 \text{ s}^{-1}$  in pH 11.5.<sup>79</sup>

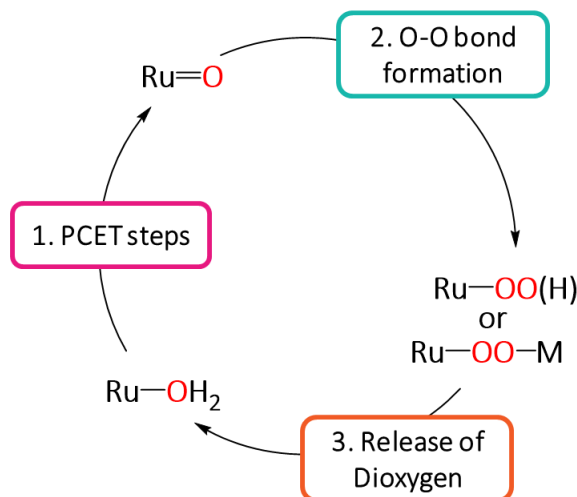
Up to this point, we described the progress of the performance of the water oxidation catalysts based on Ru complexes over the last 40 years. Through the sequential analysis, we have discussed the most prominent Ru-based complexes that have contributed to the significant improvement in the field of molecular water oxidation. This improvement can be reflected in the increase in the TOF values for seven orders of magnitude since the first well-characterized WOC was reported. However, it is essential to investigate which are the fundamental features of the catalysts that have permitted this exponential increase. To conclude, in Chart 4 (right) we highlighted the most relevant features for molecular water oxidation catalysts:

- Proton Coupled Electron Transfer (PCET) performance.
- Appropriate O–O bond formation mechanism.
- Ligand environment that provides 7-coordination.<sup>82</sup>

The following section analyses the influence of the most relevant features on the performance and properties of the WOCs.

### 1.3 Mechanistic Aspects of Water Oxidation Catalysis

The mechanism of water oxidation by the Ru-based catalysts can be divided into three main parts (see Scheme 3). The primary step is the formation of high-valent metal-oxo units *via* a series of PCET steps. The metal-oxo moieties are the key components in the second step - the O–O bond formation. The last part consists of the release of dioxygen accompanied by the regeneration of the catalyst.



**Scheme 3.** A general mechanism for water oxidation by transition metal complexes.

#### 1.3.1 Proton Coupled Electron Transfer (PCET)

The PCET process is a fundamental step in numerous biological and chemical processes, including photosynthesis and respiration in the plants and algae, solar energy conversion as well as small molecule activation. PCET plays an important role in reaching the high oxidation state of the metal during water oxidation. It restrains the oxidation potentials for reaching a highly oxidized metal-oxo species due to involving protons from the solvent environment or coordination sphere in the electron transfer process.<sup>83–87</sup> The initial phase in any water oxidation mechanism requires the first water molecule to be oxidatively activated, resulting in a metal-oxo or metal-oxyl,<sup>88</sup> which can be reached by consecutive oxidation and water binding.

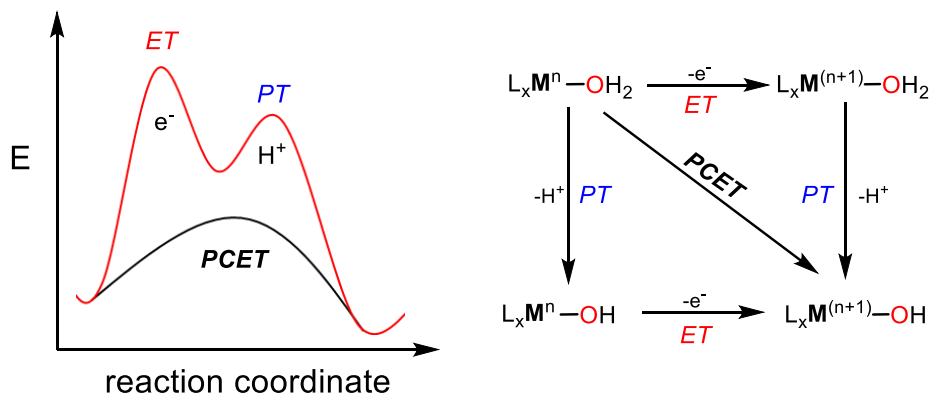
High-valent metal-oxo complexes are key intermediates in the water oxidation reaction and are involved in the O–O bond formation. Starting from the corresponding aqua complexes



## CHAPTER 1. General Introduction

# I

of metal in a low oxidation state, metal-oxo moieties are formed *via* a series of proton-coupled electron transfer steps. A general overview of the pathway for oxidative water activation is shown in Scheme 4.<sup>89</sup>



**Scheme 4.** Proton Coupled Electron Transfer process.

Due to the simultaneous transfer of protons and electrons, the overall charge of species involved in the oxidation remains unchanged. From a thermodynamic point of view, we can avoid charge accumulation as well as the formation of high-energy intermediates, facilitating the process. As a result, reaching a high oxidation state occurs at lower potentials, which is the key advantage of PCET step during water oxidation catalysis. At the same time, from a kinetic point of view, PCET process is more complex compared to independent proton and electron transfer.

The effect of PCET in Ru complexes can be observed by comparing the Pourbaix diagrams of a mononuclear complex  $[\text{Ru}(\text{bpy})_2(\text{H}_2\text{O})(\text{py})]^{2+}$ , **12** and its chloro relative complex  $[\text{Ru}(\text{bpy})_2(\text{Cl})_2]$ , **11** (see Figure 6).<sup>90–92</sup> In the  $\text{Ru}^{\text{II}}$  oxidation state, complex **11** is neutral while complex **12** is double-positive charged at pH 7.0. Consequently, the potential for  $\text{Ru}^{\text{III/II}}$  redox couple of **11** due to the strong  $\sigma$ -donating effect of  $\text{Cl}^-$  ligands is lower than that demonstrated by complex **12**. The remarkable part of the Pourbaix diagram is the decrease in the potential for accessing the  $\text{Ru}^{\text{IV}}$  oxidation state, for which complex **11** requires almost 900 mV more than complex **12** at pH 7.0. This clearly shows the noticeable advantage of the PCET mechanism that has prevented the charge accumulation for complex **12**, while complex **11** became positively charged. The  $\text{e}^-/\text{H}^+$  PCET nature of the  $[\text{Ru}^{\text{II}}-\text{OH}_2]^{2+}/[\text{Ru}^{\text{III}}-$

## CHAPTER 1. General Introduction

$\text{OH}_2^+$  couple at neutral pH for **12** is indicated by a slope of approximately 59 mV above its  $\text{pK}_a$  in the Pourbaix diagrams in Figure 6.

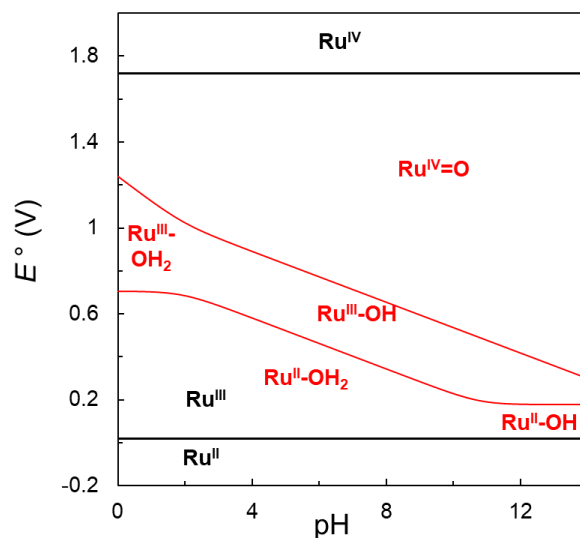
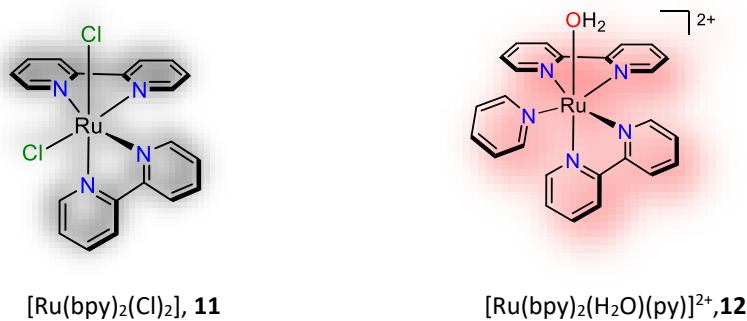


**Figure 6.** (up) Structure for  $[\text{Ru}(\text{bpy})_2(\text{Cl})_2]$  (**11**) and  $[\text{Ru}(\text{bpy})_2(\text{H}_2\text{O})(\text{py})]^{2+}$  (**12**). (down) Pourbaix diagram for **11** and **12**

The ultimate cause of PCET mechanism is the increase of acidity of the metal center upon its oxidation. Note how the  $\text{pK}_a$  of complex **12** decreases from the  $\text{Ru}^{\text{II}}$  oxidation state ( $\text{pK}_a$  10.6), to the  $\text{Ru}^{\text{III}}$  oxidation state ( $\text{pK}_a$  0.85) and  $\text{Ru}^{\text{IV}}$  oxidation state ( $\text{pK}_a < 0.0$ ). The increase of acidity upon oxidation eventually results in deprotonation that reduces the potential of the  $\text{Ru}=\text{O}$  accessing, which is crucial for the further O–O bond formation step.

## CHAPTER 1. General Introduction

# I

### 1.3.2 Oxygen-Oxygen Bond Formation

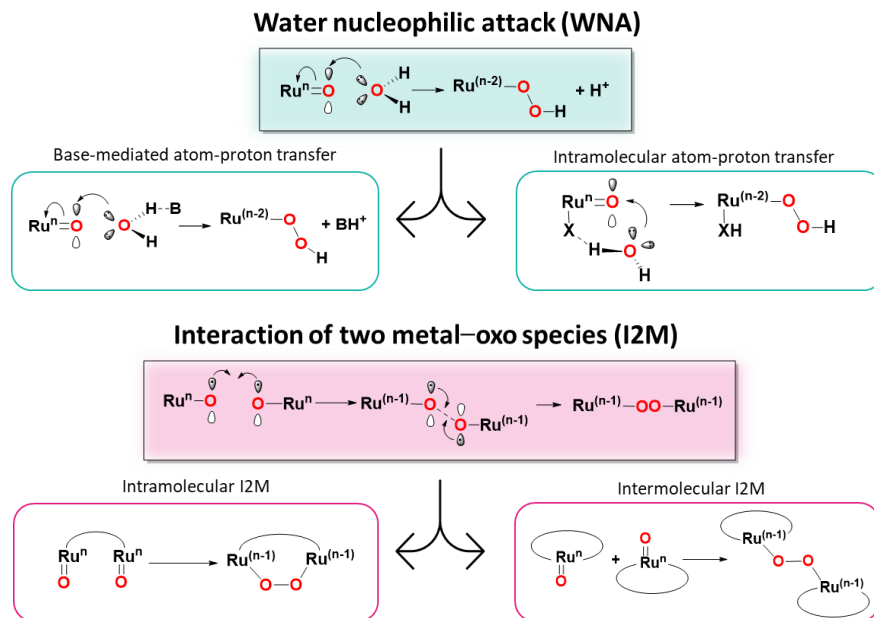
There are two different mechanistic pathways possible for the mechanism of O–O bond formation:<sup>93</sup>

- **I2M** - Interaction of Two Metal-oxo Species (Radical coupling of two Ru-oxo species).
- **WNA** - Water Nucleophilic Attack (Nucleophilic attack of water on a high-valent Ru=O species).

Both mechanisms involve high valent metal-oxo units (Scheme 5). In the case of a WNA, nucleophilic water or hydroxide from the solution attacks the electrophilic metal-oxo unit. In contrast, an I2M involves two metal-oxo units that form the O–O bond *via* an intra- or intermolecular radical coupling.

From the practical application aspects, most of the Ru-based WOCs are designed to follow the WNA mechanism.<sup>76,78,79,94,95</sup> In most cases, the nucleophilic attack of water is preferential for Ru<sup>V</sup>=O species, which facing water binding and resulting in the formation of a Ru<sup>III</sup>–OOH hydroperoxide. It is worth mentioning that oxo formation may take place already at Ru<sup>IV</sup> oxidation state generating Ru<sup>IV</sup>=O species, where Ru<sup>IV/III</sup> couple has sufficiently high potential for further participation in O–O bond formation. The O–O bond formation *via* WNA is the rate-determining step for most of the described WOCs, which consequently determines the rate of the reaction for mononuclear Ru complexes.

Proper mechanisms determination (WNA for complex **5** and I2M for complex **7**) can be a beneficial tool for tuning the catalytic performance. For instance, replacing initial axial picoline ligands by isoquinoline-type in complex **7** can favor  $\pi - \pi$  interactions during the catalytic cycles<sup>96–99</sup> and further stabilize the Ru–O–O–Ru formation together with the decrease of the activation barrier of the O–O bond formation step.



**Scheme 5** Representative O–O bond formation steps for water oxidation via water nucleophilic attack (WNA, upper part) and interaction of two metal–oxo (I2M, lower part) for mononuclear catalysts.

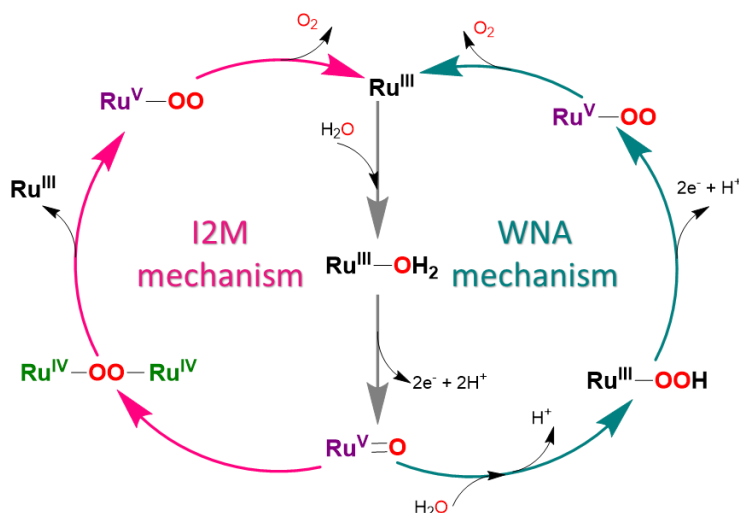
### 1.3.3 Release of Dioxygen

The ultimate step in the mechanism of water oxidation is the release of dioxygen and the reduction of the catalyst. The O–O bond formation step is followed by the formation of a peroxide- or hydroperoxido- ligand to the metal complex.

At that point, two additional electrons must be transferred from the metal to the hydroperoxo/peroxo and the release of the dioxygen can take place.

## CHAPTER 1. General Introduction

# I



**Scheme 6.** A general outline of the catalytic cycle of water oxidation through WNA and I2M mechanisms for the O–O bond formation (WNA for complex **5** and I2M for complex **7**).

The latter species is then responsible for  $\text{O}_2$  liberation and two-electron reduction of the metal center, which finishes the catalytic cycle. Scheme 6 shows a schematic illustration of the proposed pathways for the dioxygen releasing through WNA and I2M mechanisms.

### 1.3.4 Coordination Environments

Most of the molecular Ru water oxidation catalysts have octahedral geometry with coordination number 6 (CN6) (Charts 1-4). Crystal field splitting of octahedral ( $O_h$ ) type geometry predicts that the  $d$ -orbitals of Ruthenium split into two sets of orbitals: i) triply degenerate  $t_{2g}$  and doubly degenerate  $e_g$  orbitals (see in Figure 7). In some cases, Ru-based complexes with oxidation state  $\text{Ru}^{\text{IV}}$  or more can form seven coordination around the metal center with pentagonal bipyramidal geometry ( $D_{5h}$ ).<sup>82,100,101</sup>

## CHAPTER 1. General Introduction

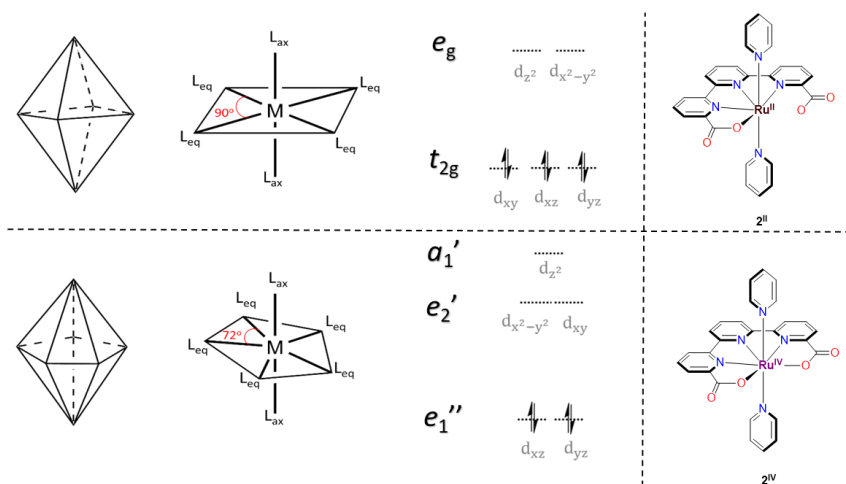


**Figure 7.** Representation of metal-ligand bonds in octahedral (CN6) and pentagonal bipyramidal geometry (CN7) together with the crystal field splitting of  $d$  orbitals for CN6 and CN7 complexes.

The additional coordination drops the energy of  $d_{xz}$  and  $d_{yz}$  orbitals compared to the six-coordinated Ru-based complex. In this case,  $d$ -orbitals split into three sets of orbitals:  $e_1''$ ,  $e_2'$  and  $a_1'$  (see Figure 7). The seven coordination stabilizes the Ru center due to an increase of the electron density to a deficient  $Ru^{IV}$  ion that is crucial O–O bond formation. This stabilization allows the reduction of the overall potential of the redox couples and resulting in the lower catalytic overpotential. Among all complexes discussed, the seven-coordinate complexes are the fastest water oxidation catalysts reaching TOF of  $10^4 s^{-1}$ .

Another important factor in catalyst design is the secondary coordination sphere effect.<sup>94,102</sup> As was discussed previously, the primary coordination sphere plays a crucial role in the properties of the transition metal complexes with the direct ligand connection to the metal center. At the same time, the secondary coordination sphere does not have a direct connection with the metal center but may also play an important role in the reactivity of the complexes. These secondary coordination sphere effects include hydrogen bonding, supramolecular  $\pi$ – $\pi$  interaction, accessible pendant base, steric effect, etc. All of them can influence the kinetics and the mechanism of the reaction.

## CHAPTER 1. General Introduction

# I

### 1.3.5 Catalyst deactivation

One of the most crucial considerations during the design of transition metal-based molecular WOCs is their stability under catalytic conditions. Although many pathways of deactivation, degradation, and inhibition have been reported for molecular catalysts, the high efficiency and selectivity of stable molecular WOCs are still deficient.<sup>103,104</sup> In many cases decomposition of molecular WOCs results in the formation of catalytically active metal oxide nanoparticles or clusters, casting doubts on the activity and mechanistic studies of the molecular complexes.<sup>105</sup> The decomposition of molecular WOCs is typically triggered by ligand oxidation and/or ligand substitution followed by leaching of the metal to the solution, or by the formation of polynuclear oxo-bridged species.<sup>106–108</sup> A robust WOC should therefore be based on a ligand that lacks oxidative labile functional groups and efficiently stabilizes the metal center at the relevant oxidation states, precluding the unwanted ligand-exchange reactions

## 1.4 Remaining Challenges and Outlook

Prominently, some of the presented molecular WOCs already exceeds the activity of the natural OEC ( $\text{TOF}_{\text{OEC}} 50\text{-}400 \text{ s}^{-1}$ ).<sup>50</sup> Furthermore, it is important to realize that although the photosynthesis in living organisms appears continuous, the components of the photosynthetic machinery in PSII must be repaired every 15-30 min due to irreversible photoinhibition, which limits the intrinsic stability of the OEC.<sup>44,45</sup> Nevertheless, the OEC remains the only catalyst, which can carry out water oxidation at a record low overpotential of 70 mV, setting the key goal for future research in the area. As was discussed previously, multiple problems regarding the evaluation of WOCs catalytic activity must be addressed to reliably compare the activity of different catalysts and gain a better understanding of the structure and reactivity relationships.

As a result, several considerations for the rational design of high-performance molecular WOCs have been identified.<sup>109</sup> These include:

- **Robust coordination** - The use of oxidative stable organic ligands, with nitrogen-containing aromatic heterocycles being the most common.
- **PCET** - The ability of the catalyst to undergo PCET, allowing the generation of the high oxidation states of the catalytically active species at low potentials.

## CHAPTER 1. General Introduction

# I

- **Ligand tuning** - The use of redox non-innocent ligands, which can increase the stability of the catalyst while facilitating access to high formal oxidation states of the metal center.
- **Seven Coordination** - The use of ligands that can promote the formation of seven-coordinated Ruthenium-aqua species, thereby lowering the potentials of the relevant redox couples.
- **Second Coordination** - Introduction of an internal base in the second coordination sphere of the metal center, which can assist the O-O bond formation through water nucleophilic attack (WNA) by a simultaneous abstraction of a proton from water (intramolecular atom–proton transfer).

Summarized considerations already showed how judicious tuning of the metal environment can increase TOF by seven orders of magnitude as well as the turnover number (TON) by three orders of magnitude, which has been achieved over the past decade. Nevertheless, there are remaining challenges in terms of lasting stability and operating potentials that have to be improved for further commercial application.



## CHAPTER 1. General Introduction

# I

### 1.5 References

- (1) World Health Organization (WHO). Novel Coronavirus (2019-nCoV) situation reports -.
- (2) Altig, D.; Barrero, J. M.; Bloom, N.; Davis, S. J.; Meyer, B. H.; Parker, N. Surveying Business Uncertainty. *Natl. Bur. Econ. Res. Work. Pap. Ser.* **2019**, No. 25956.
- (3) Anderson, R. M.; Heesterbeek, H.; Klinkenberg, D.; Hollingsworth, T. D. How Will Country-Based Mitigation Measures Influence the Course of the COVID-19 Epidemic? *Lancet (London, England)* **2020**, 395 (10228), 931–934.
- (4) Atkeson, A. What Will Be the Economic Impact of COVID-19 in the US? Rough Estimates of Disease Scenarios. *Natl. Bur. Econ. Res. Work. Pap. Ser.* **2020**, No. 26867.
- (5) *World Energy Outlook 2020*; IEA (2020), Paris, 2020.
- (6) Grossmann, W. D.; Grossmann, I.; Steininger, K. W. Solar Electricity Generation across Large Geographic Areas, Part II: A Pan-American Energy System Based on Solar. *Renew. Sustain. Energy Rev.* **2014**, 32, 983–993.
- (7) Lewis, N. S. Research Opportunities to Advance Solar Energy Utilization. *Science (80-. )*. **2016**, 351 (6271).
- (8) Coling, G. Energy, the Environment, and Human Health. *Am. J. Public Health* **1974**, 64 (12), 1166–1167.
- (9) McGlade, C.; Ekins, P. The Geographical Distribution of Fossil Fuels Unused When Limiting Global Warming to 2 °C. *Nature* **2015**, 517 (7533), 187–190.
- (10) Kandpal, T. C.; Broman, L. Renewable Energy Education: A Global Status Review. *Renew. Sustain. Energy Rev.* **2014**, 34, 300–324.
- (11) Bernstein, L.; Bosch, P.; Canziani, O.; Chen, Z.; Christ, R.; Davidson, O.; Hare, W.; Huq, S.; Karoly, D.; Kattsov, V.; Kundzewicz, Z. W.; Liu, J.; Lohmann, U.; Manning, M.; Matsuno, T.; Menne, B.; Metz, B.; Mirza, M.; Nicholls, N.; et al. Climate Change 2007 : Synthesis Report : An Assessment of the Intergovernmental Panel on Climate Change . IPCC : Geneva, Switzerland **2008**.
- (12) *Global Energy & CO2 Status Report 2019*, IEA, Paris; IEA (2019), **2019**.
- (13) Masson-Delmotte, V.; Zhai, P.; Pörtner, H.-O.; Roberts, D.; Skea, J.; Shukla, P. R.; Pirani, A.; Moufouma-Okia, W.; Péan, C.; Pidcock, R. . et al. *Global Warming of 1.5°C An IPCC Special Report*; **2018**.
- (14) *BP Statistical Review of World Energy. Statistical Review of World Energy*; London, 2018.
- (15) Su, J.; Vayssieres, L. A Place in the Sun for Artificial Photosynthesis? *ACS Energy Lett.* **2016**, 1 (1), 121–135.
- (16) Proposal by the President, P. C. C.; Conference. *Adoption of the Paris Agreement*; Paris, France.
- (17) NASA. *Global Climat Change*; 2020.
- (18) Kroll, J. H.; Heald, C. L.; Cappa, C. D.; Farmer, D. K.; Fry, J. L.; Murphy, J. G.; Steiner, A. L. The Complex Chemical Effects of COVID-19 Shutdowns on Air Quality. *Nat. Chem.* **2020**, 12 (9), 777–779.
- (19) Horowitz, C. A. Paris Agreement. *Int. Leg. Mater.* **2016**, 55 (4), 740–755.
- (20) Lüthi, D.; Le Floch, M.; Bereiter, B.; Blunier, T.; Barnola, J.-M.; Siegenthaler, U.; Raynaud, D.; Jouzel, J.; Fischer, H.; Kawamura, K.; Stocker, T. F. High-Resolution Carbon Dioxide Concentration Record 650,000–800,000 Years before Present. *Nature* **2008**, 453 (7193), 379–382.
- (21) Wuebbles, D.J., Fahey, D.W., Hibbard, K.A., Dokken, D. J.; Stewart, B.C., Maycock, T. K. *Climate Science Special Report: Fourth National Climate Assessment, Volume I*; Washington, DC, **2017**.
- (22) Environmental Protection Agency. *Inventory of U.S. Greenhouse Gas Emissions and Sinks: 1990–2018*; 2018.
- (23) Amir Bazaz, Paolo Bertoldi, Marcos Buckeridge, Anton Cartwright, Heleen de Coninck,

- Francois Engelbrecht, Daniela Jacob, Jean-Charles Hourcade, Ian Klaus, Kiane de Kleijne, Shauib Lwasa, Claire Markgraf, Peter Newman, Aromar Revi, Joeri Rogelj, Seth Schul, H. W. *Summary for Urban Policymakers*; 2018.
- (24) Edward G.W. Gasson | School of Geographical Sciences Bristol, UK and Benjamin A. Keisling | Lamont-Doherty Earth Observatory of Columbia University, Palisades, NY, USA, U. of B. The Antarctic Ice Sheet: A Paleoclimate Modeling Perspective. *Oceanography* **2020**, 33.
- (25) Zhu, J.; Poulsen, C. J.; Otto-Bliesner, B. L. High Climate Sensitivity in CMIP6 Model Not Supported by Paleoclimate. *Nat. Clim. Chang.* **2020**, 10 (5), 378–379.
- (26) *Statistical Review of World Energy 2020*; London, 2020.
- (27) US Department of Energy <https://www.energy.gov/>.
- (28) OECD. *OECD Environmental Outlook*; 2001.
- (29) ESMAP 2020. *Global Photovoltaic Power Potential by Country*; Washington, DC: World Bank.
- (30) Newman, J.; Hoertz, P. G.; Bonino, C. A.; Trainham, J. A. Review: An Economic Perspective on Liquid Solar Fuels. *J. Electrochem. Soc.* **2012**, 159 (10), A1722–A1729.
- (31) Obi, M.; Bass, R. Trends and Challenges of Grid-Connected Photovoltaic Systems – A Review. *Renew. Sustain. Energy Rev.* **2016**, 58, 1082–1094.
- (32) Luo, X.; Wang, J.; Dooner, M.; Clarke, J. Overview of Current Development in Electrical Energy Storage Technologies and the Application Potential in Power System Operation. *Appl. Energy* **2015**, 137, 511–536.
- (33) McEvoy, J. P.; Brudvig, G. W. Water-Splitting Chemistry of Photosystem II. *Chem. Rev.* **2006**, 106 (11), 4455–4483.
- (34) Berardi, S.; Drouet, S.; Francàs, L.; Gimbert-Suriñach, C.; Guttentag, M.; Richmond, C.; Stoll, T.; Llobet, A. Molecular Artificial Photosynthesis. *Chem. Soc. Rev.* **2014**, 43 (22), 7501–7519.
- (35) Concepcion, J. J.; House, R. L.; Papanikolas, J. M.; Meyer, T. J. Chemical Approaches to Artificial Photosynthesis. *Proc. Natl. Acad. Sci.* **2012**, 109 (39), 15560 LP – 15564.
- (36) Graetzel, M. Artificial Photosynthesis: Water Cleavage into Hydrogen and Oxygen by Visible Light. *Acc. Chem. Res.* **1981**, 14 (12), 376–384.
- (37) Mirkovic, T.; Ostroumov, E. E.; Anna, J. M.; van Grondelle, R.; Govindjee; Scholes, G. D. Light Absorption and Energy Transfer in the Antenna Complexes of Photosynthetic Organisms. *Chem. Rev.* **2017**, 117 (2), 249–293.
- (38) Eaton-Rye, J. J.; Tripathy, B. C.; Sharkey, T. D., E. *Photosynthesis: Plastid Biology, Energy Conversion and Carbon Assimilation; Advances in Photosynthesis and Respiration*, Vol.34.; Springer: Dordrecht, The Netherlands: The Netherlands, 2012.
- (39) Bard, A. J.; Fox, M. A. Artificial Photosynthesis: Solar Splitting of Water to Hydrogen and Oxygen. *Acc. Chem. Res.* **1995**, 28 (3), 141–145.
- (40) Nocera, D. G. Solar Fuels and Solar Chemicals Industry. *Acc. Chem. Res.* **2017**, 50 (3), 616–619.
- (41) *Energy Production and Storage: Inorganic Chemical Strategies for a Warming World*; Crabtree, R. H., Ed.; John Wiley & Sons: Chichester, UK, 2010.
- (42) Stillman, M. Biological Inorganic Chemistry. Structure and Reactivity. Edited by Ivano Bertini, Harry B. Gray, Edward I. Stiefel and Joan S. Valentine. *Angew. Chemie Int. Ed.* **2007**, 46 (46), 8741–8742.
- (43) Barber, J. Photosynthetic Energy Conversion: Natural and Artificial. *Chem. Soc. Rev.* **2009**, 38 (1), 185–196.
- (44) Kornienko, N.; Zhang, J. Z.; Sokol, K. P.; Lamaison, S.; Fantuzzi, A.; van Grondelle, R.; Rutherford, A. W.; Reisner, E. Oxygenic Photoreactivity in Photosystem II Studied by Rotating Ring Disk Electrochemistry. *J. Am. Chem. Soc.* **2018**, 140 (51), 17923–17931.
- (45) Zhang, J. Z.; Sokol, K. P.; Paul, N.; Romero, E.; van Grondelle, R.; Reisner, E. Competing Charge Transfer Pathways at the Photosystem II–Electrode Interface. *Nat. Chem. Biol.* **2016**, 12 (12), 1046–1052.
- (46) Umena, Y.; Kawakami, K.; Shen, J.-R.; Kamiya, N. Crystal Structure of Oxygen-Evolving

## CHAPTER 1. General Introduction

# I

- Photosystem II at a Resolution of 1.9 Å. *Nature* **2011**, 473 (7345), 55–60.
- (47) Cox, N.; Pantazis, D. A.; Neese, F.; Lubitz, W. Biological Water Oxidation. *Acc. Chem. Res.* **2013**, 46 (7), 1588–1596.
- (48) Yano, J.; Kern, J.; Irrgang, K.-D.; Latimer, M. J.; Bergmann, U.; Glatzel, P.; Pushkar, Y.; Biesiadka, J.; Loll, B.; Sauer, K.; Messinger, J.; Zouni, A.; Yachandra, V. K. X-Ray Damage to the Mn<sub>4</sub>Ca Complex in Single Crystals of Photosystem II: A Case Study for Metalloprotein Crystallography. *Proc. Natl. Acad. Sci. U. S. A.* **2005**, 102 (34), 12047 LP – 12052.
- (49) Suga, M.; Akita, F.; Hirata, K.; Ueno, G.; Murakami, H.; Nakajima, Y.; Shimizu, T.; Yamashita, K.; Yamamoto, M.; Ago, H.; Shen, J.-R. Native Structure of Photosystem II at 1.95 Å Resolution Viewed by Femtosecond X-Ray Pulses. *Nature* **2015**, 517 (7532), 99–103.
- (50) Glöckner, C.; Kern, J.; Broser, M.; Zouni, A.; Yachandra, V.; Yano, J. Structural Changes of the Oxygen-Evolving Complex in Photosystem II during the Catalytic Cycle. *J. Biol. Chem.* **2013**, 288 (31), 22607–22620.
- (51) Inoue, H.; Shimada, T.; Kou, Y.; Nabetani, Y.; Masui, D.; Takagi, S.; Tachibana, H. The Water Oxidation Bottleneck in Artificial Photosynthesis: How Can We Get Through It? An Alternative Route Involving a Two-Electron Process. *ChemSusChem* **2011**, 4 (2), 173–179.
- (52) Melis, A. Photosynthesis-to-Fuels: From Sunlight to Hydrogen, Isoprene, and Botryococcene Production. *Energy Environ. Sci.* **2012**, 5 (2), 5531–5539.
- (53) Suga, M.; Akita, F.; Yamashita, K.; Nakajima, Y.; Ueno, G.; Li, H.; Yamane, T.; Hirata, K.; Umena, Y.; Yonekura, S.; Yu, L.-J.; Murakami, H.; Nomura, T.; Kimura, T.; Kubo, M.; Baba, S.; Kumasaka, T.; Tono, K.; Yabashi, M.; et al. An Oxy/Oxo Mechanism for Oxygen-Oxygen Coupling in PSII Revealed by an x-Ray Free-Electron Laser. *Science (80-. )*. **2019**, 366 (6463), 334 LP – 338.
- (54) Gersten, S. W.; Samuels, G. J.; Meyer, T. J. Catalytic Oxidation of Water by an Oxo-Bridged Ruthenium Dimer. *J. Am. Chem. Soc.* **1982**, 104 (14), 4029–4030.
- (55) Gilbert, J. A.; Eggleston, D. S.; Murphy, W. R.; Geselowitz, D. A.; Gersten, S. W.; Hodgson, D. J.; Meyer, T. J. Structure and Redox Properties of the Water-Oxidation Catalyst [(bpy)<sub>2</sub>(OH<sub>2</sub>)RuORu(OH<sub>2</sub>)(bpy)<sub>2</sub>]<sup>4+</sup>. *J. Am. Chem. Soc.* **1985**, 107 (13), 3855–3864.
- (56) Collin, J. P.; Sauvage, J. P. Synthesis and Study of Mononuclear Ruthenium(II) Complexes of Sterically Hindering Diimine Chelates. Implications for the Catalytic Oxidation of Water to Molecular Oxygen. *Inorg. Chem.* **1986**, 25 (2), 135–141.
- (57) Nagoshi, K.; Yamashita, S.; Yagi, M.; Kaneko, M. Catalytic Activity of [(bpy)<sub>2</sub>(H<sub>2</sub>O)Ru–ORu(H<sub>2</sub>O)(bpy)<sub>2</sub>]<sup>4+</sup> for Four-Electron Water Oxidation. *J. Mol. Catal. A Chem.* **1999**, 144 (1), 71–76.
- (58) Liu, F.; Concepcion, J. J.; Jurss, J. W.; Cardolaccia, T.; Templeton, J. L.; Meyer, T. J. Mechanisms of Water Oxidation from the Blue Dimer to Photosystem II. *Inorg. Chem.* **2008**, 47 (6), 1727–1752.
- (59) Barnett, S. M.; Goldberg, K. I.; Mayer, J. M. A Soluble Copper–Bipyridine Water-Oxidation Electrocatalyst. *Nat. Chem.* **2012**, 4 (6), 498–502.
- (60) Zhang, T.; Wang, C.; Liu, S.; Wang, J.-L.; Lin, W. A Biomimetic Copper Water Oxidation Catalyst with Low Overpotential. *J. Am. Chem. Soc.* **2014**, 136 (1), 273–281.
- (61) Zhang, M.-T.; Chen, Z.; Kang, P.; Meyer, T. J. Electrocatalytic Water Oxidation with a Copper(II) Polypeptide Complex. *J. Am. Chem. Soc.* **2013**, 135 (6), 2048–2051.
- (62) Garrido-Barros, P.; Funes-Ardoiz, I.; Drouet, S.; Benet-Buchholz, J.; Maseras, F.; Llobet, A. Redox Non-Innocent Ligand Controls Water Oxidation Overpotential in a New Family of Mononuclear Cu-Based Efficient Catalysts. *J. Am. Chem. Soc.* **2015**, 137 (21), 6758–6761.
- (63) Ellis, W. C.; McDaniel, N. D.; Bernhard, S.; Collins, T. J. Fast Water Oxidation Using Iron. *J. Am. Chem. Soc.* **2010**, 132 (32), 10990–10991.
- (64) Rigsby, M. L.; Mandal, S.; Nam, W.; Spencer, L. C.; Llobet, A.; Stahl, S. S. Cobalt Analogs of Ru-Based Water Oxidation Catalysts: Overcoming Thermodynamic Instability and Kinetic Lability to Achieve Electrocatalytic O<sub>2</sub> Evolution. *Chem. Sci.* **2012**, 3 (10), 3058–3062.
- (65) Gimbert-Suriñach, C.; Moonshiram, D.; Francàs, L.; Planas, N.; Bernales, V.; Bozoglian, F.;

## CHAPTER 1. General Introduction

- Guda, A.; Mognon, L.; López, I.; Hoque, M. A.; Gagliardi, L.; Cramer, C. J.; Llobet, A. Structural and Spectroscopic Characterization of Reaction Intermediates Involved in a Dinuclear Co-Hbpp Water Oxidation Catalyst. *J. Am. Chem. Soc.* **2016**, *138* (47), 15291–15294.
- (66) Neudeck, S.; Maji, S.; Lo, I.; Meyer, F.; Llobet, A. New Powerful and Oxidatively Rugged Dinuclear Ru Water Oxidation Catalyst: Control of Mechanistic Pathways by Tailored Ligand Design. *J. Am. Chem. Soc.* **2013**, 2–5.
- (67) Zong, R.; Thummel, R. P. A New Family of Ru Complexes for Water Oxidation. *J. Am. Chem. Soc.* **2005**, *127* (37), 12802–12803.
- (68) Concepcion, J. J.; Jurss, J. W.; Templeton, J. L.; Meyer, T. J. One Site Is Enough. Catalytic Water Oxidation by  $[\text{Ru}(\text{tpy})(\text{bpm})(\text{OH}_2)]^{2+}$  and  $[\text{Ru}(\text{tpy})(\text{bpz})(\text{OH}_2)]^{2+}$ . *J. Am. Chem. Soc.* **2008**, *130* (49), 16462–16463.
- (69) Wasylenko, D. J.; Ganesamoorthy, C.; Henderson, M. A.; Koivisto, B. D.; Osthoff, H. D.; Berlinguette, C. P. Electronic Modification of the  $[\text{Ru}^{\text{II}}(\text{tpy})(\text{bpy})(\text{OH}_2)]^{2+}$  Scaffold: Effects on Catalytic Water Oxidation. *J. Am. Chem. Soc.* **2010**, *132* (45), 16094–16106.
- (70) Duan, L.; Bozoglian, F.; Mandal, S.; Stewart, B.; Privalov, T.; Llobet, A.; Sun, L. A Molecular Ruthenium Catalyst with Water-Oxidation Activity Comparable to That of Photosystem II. *Nat. Chem.* **2012**, *4* (5), 418–423.
- (71) Duan, L.; Fischer, A.; Xu, Y.; Sun, L. Isolated Seven-Coordinate Ru(IV) Dimer Complex with [HOHOH]- Bridging Ligand as an Intermediate for Catalytic Water Oxidation. *J. Am. Chem. Soc.* **2009**, *131* (30), 10397–10399.
- (72) Duan, L.; Wang, L.; Inge, A. K.; Fischer, A.; Zou, X.; Sun, L. Insights into Ru-Based Molecular Water Oxidation Catalysts: Electronic and Noncovalent-Interaction Effects on Their Catalytic Activities. *Inorg. Chem.* **2013**, *52* (14), 7844–7852.
- (73) Richmond, C. J.; Escayola, S.; Poater, A. Axial Ligand Effects of Ru-BDA Complexes in the O–O Bond Formation via the I2M Bimolecular Mechanism in Water Oxidation Catalysis. *Eur. J. Inorg. Chem.* **2019**, *2019* (15), 2101–2108.
- (74) Xie, Y.; Shaffer, D. W.; Concepcion, J. J. O–O Radical Coupling: From Detailed Mechanistic Understanding to Enhanced Water Oxidation Catalysis. *Inorg. Chem.* **2018**, *57* (17), 10533–10542.
- (75) Matheu, R.; Francàs, L.; Chernev, P.; Ertem, M. Z.; Batista, V.; Haumann, M.; Sala, X.; Llobet, A. Behavior of the Ru-Bda Water Oxidation Catalyst Covalently Anchored on Glassy Carbon Electrodes. *ACS Catal.* **2015**, *5* (6), 3422–3429.
- (76) Shaffer, D. W.; Xie, Y.; Szalda, D. J.; Concepcion, J. J. Lability and Basicity of Bipyridine-Carboxylate-Phosphonate Ligand Accelerate Single-Site Water Oxidation by Ruthenium-Based Molecular Catalysts. *J. Am. Chem. Soc.* **2017**, *139* (43), 15347–15355.
- (77) Kamdar, J. M.; Marelius, D. C.; Moore, C. E.; Rheingold, A. L.; Smith, D. K.; Grotjahn, D. B. Ruthenium Complexes of 2,2'-Bipyridine-6,6'-Diphosphonate Ligands for Water Oxidation. *ChemCatChem* **2016**, *8* (19), 3045–3049.
- (78) Xie, Y.; Shaffer, D. W.; Lewandowska-Andralojc, A.; Szalda, D. J.; Concepcion, J. J. Water Oxidation by Ruthenium Complexes Incorporating Multifunctional Bipyridyl Diphosphonate Ligands. *Angew. Chemie Int. Ed.* **2016**, *55* (28), 8067–8071.
- (79) Matheu, R.; Ertem, M. Z.; Benet-Buchholz, J.; Coronado, E.; Batista, V. S.; Sala, X.; Llobet, A. Intramolecular Proton Transfer Boosts Water Oxidation Catalyzed by a Ru Complex. *J. Am. Chem. Soc.* **2015**, *137* (33), 10786–10795.
- (80) Matheu, R.; Ertem, M. Z.; Gimbert-Suriñach, C.; Benet-Buchholz, J.; Sala, X.; Llobet, A. Hydrogen Bonding Rescues Overpotential in Seven-Coordinated Ru Water Oxidation Catalysts. *ACS Catal.* **2017**, *7* (10), 6525–6532.
- (81) Matheu, R.; Benet-Buchholz, J.; Sala, X.; Llobet, A. Synthesis, Structure, and Redox Properties of a Trans-Diaqua Ru Complex That Reaches Seven-Coordination at High Oxidation States. *Inorg. Chem.* **2018**, *57* (4), 1757–1765.
- (82) Matheu, R.; Ertem, M. Z.; Gimbert-Suriñach, C.; Sala, X.; Llobet, A. Seven Coordinated

## CHAPTER 1. General Introduction

# I

- Molecular Ruthenium-Water Oxidation Catalysts: A Coordination Chemistry Journey. *Chem. Rev.* **2019**, *119* (6), 3453–3471.
- (83) McCarthy, B. D.; Dempsey, J. L. Decoding Proton-Coupled Electron Transfer with Potential-PKaDiagrams. *Inorg. Chem.* **2017**, *56* (3), 1225–1231.
- (84) Warren, J. J.; Tronic, T. A.; Mayer, J. M. Thermochemistry of Proton-Coupled Electron Transfer Reagents and Its Implications. *Chem. Rev.* **2010**, *110* (12), 6961–7001.
- (85) Huynh, M. H. V.; Meyer, T. J. Proton-Coupled Electron Transfer. *Chem. Rev.* **2007**, *107* (11), 5004–5064.
- (86) Savéant, J.-M. Electrochemical Approach to Proton-Coupled Electron Transfers: Recent Advances. *Energy Environ. Sci.* **2012**, *5* (7), 7718–7731.
- (87) Weinberg, D. R.; Gagliardi, C. J.; Hull, J. F.; Murphy, C. F.; Kent, C. A.; Westlake, B. C.; Paul, A.; Ess, D. H.; McCafferty, D. G.; Meyer, T. J. Proton-Coupled Electron Transfer. *Chem. Rev.* **2012**, *112* (7), 4016–4093.
- (88) Betley, T. A.; Wu, Q.; Van Voorhis, T.; Nocera, D. G. Electronic Design Criteria for O–O Bond Formation via Metal–Oxo Complexes. *Inorg. Chem.* **2008**, *47* (6), 1849–1861.
- (89) Shi, S.; Szostak, R.; Szostak, M. Proton-Coupled Electron Transfer in the Reduction of Carbonyls Using Sml<sub>2</sub>–H<sub>2</sub>O: Implications for the Reductive Coupling of Acyl-Type Ketyl Radicals with Sml<sub>2</sub>–H<sub>2</sub>O. *Org. Biomol. Chem.* **2016**, *14* (38), 9151–9157.
- (90) Tong, L.; Thummel, R. P. Mononuclear Ruthenium Polypyridine Complexes That Catalyze Water Oxidation. *Chem. Sci.* **2016**, *7* (11), 6591–6603.
- (91) Dobson, J. C.; Sullivan, B. P.; Doppelt, P.; Meyer, T. J. Proton NMR Studies of Paramagnetic Polypyridyl,  $\mu$ -oxo Complexes of Ruthenium(III) and Their Diamagnetic Ruthenium(II) Precursors. *Inorg. Chem.* **1988**, *27* (21), 3863–3866.
- (92) Neyhart, G. A.; Meyer, T. J. PH-Induced Intramolecular Electron Transfer. *Inorg. Chem.* **1986**, *25* (27), 4807–4808.
- (93) Shaffer, D. W.; Xie, Y.; Concepcion, J. J. O–O Bond Formation in Ruthenium-Catalyzed Water Oxidation: Single-Site Nucleophilic Attack vs. O–O Radical Coupling. *Chem. Soc. Rev.* **2017**, *46* (20), 6170–6193.
- (94) Vereshchuk, N.; Matheu, R.; Benet-Buchholz, J.; Pipelier, M.; Lebreton, J.; Dubreuil, D.; Tessier, A.; Gimbert-Suriñach, C.; Z. Ertem, M.; Llobet, A. Second Coordination Sphere Effects in an Evolved Ru Complex Based on Highly Adaptable Ligand Results in Rapid Water Oxidation Catalysis. *J. Am. Chem. Soc.* **2020**, *142* (11), 5068–5077.
- (95) Matheu, R.; Ertem, M. Z.; Pipelier, M.; Lebreton, J.; Dubreuil, D.; Benet-Buchholz, J.; Sala, X.; Tessier, A.; Llobet, A. The Role of Seven-Coordination in Ru-Catalyzed Water Oxidation. *ACS Catal.* **2018**, *8* (3), 2039–2048.
- (96) Ohzu, S.; Ishizuka, T.; Hirai, Y.; Jiang, H.; Sakaguchi, M.; Ogura, T.; Fukuzumi, S.; Kojima, T. Mechanistic Insight into Catalytic Oxidations of Organic Compounds by Ruthenium(IV)-Oxo Complexes with Pyridylamine Ligands. *Chem. Sci.* **2012**, *3* (12), 3421–3431.
- (97) Jiang, Y.; Li, F.; Zhang, B.; Li, X.; Wang, X.; Huang, F.; Sun, L. Promoting the Activity of Catalysts for the Oxidation of Water with Bridged Dinuclear Ruthenium Complexes. *Angew. Chemie Int. Ed.* **2013**, *52* (12), 3398–3401.
- (98) Wang, L.; Duan, L.; Wang, Y.; Ahlquist, M. S. G.; Sun, L. Highly Efficient and Robust Molecular Water Oxidation Catalysts Based on Ruthenium Complexes. *Chem. Commun.* **2014**, *50* (85), 12947–12950.
- (99) Richmond, C. J.; Matheu, R.; Poater, A.; Falivene, L.; Benet-Buchholz, J.; Sala, X.; Cavallo, L.; Llobet, A. Supramolecular Water Oxidation with Ru–Bda-Based Catalysts. *Chem. – A Eur. J.* **2014**, *20* (52), 17282–17286.
- (100) Muckerman, J. T.; Kowalczyk, M.; Badieli, Y. M.; Polyansky, D. E.; Concepcion, J. J.; Zong, R.; Thummel, R. P.; Fujita, E. New Water Oxidation Chemistry of a Seven-Coordinate Ruthenium Complex with a Tetradentate Polypyridyl Ligand. *Inorg. Chem.* **2014**, *53* (13), 6904–6913.
- (101) Kojima, T.; Hirai, Y.; Ishizuka, T.; Shiota, Y.; Yoshizawa, K.; Ikemura, K.; Ogura, T.; Fukuzumi, S.

## CHAPTER 1. General Introduction

- A Low-Spin Ruthenium(IV)–Oxo Complex: Does the Spin State Have an Impact on the Reactivity? *Angew. Chemie Int. Ed.* **2010**, *49* (45), 8449–8453.
- (102) Matias, T. A.; Keppler, A. F.; Bartoloni, F. H. In Need of a Second-Hand? The Second Coordination Sphere of Ruthenium Complexes Enables Water Oxidation with Improved Catalytic Activity. *Dalt. Trans.* **2020**.
- (103) Lee, K. J.; McCarthy, B. D.; Dempsey, J. L. On Decomposition, Degradation, and Voltammetric Deviation: The Electrochemist's Field Guide to Identifying Precatalyst Transformation. *Chem. Soc. Rev.* **2019**, *48* (11), 2927–2945.
- (104) Pelosin, P.; Gil-Sepulcre, M.; Garrido-Barros, P.; Moonshiram, D.; Benet-Buchholz, J.; Gimbert-Suriñach, C.; Llobet, A. Analysis of the Active Species Responsible for Water Oxidation Using a Pentanuclear Fe Complex. *iScience* **2020**, *23* (8), 101378.
- (105) Li, J.; Güttinger, R.; Moré, R.; Song, F.; Wan, W.; Patzke, G. R. Frontiers of Water Oxidation: The Quest for True Catalysts. *Chem. Soc. Rev.* **2017**, *46* (20), 6124–6147.
- (106) Zhang, B.; Li, F.; Zhang, R.; Ma, C.; Chen, L.; Sun, L. Characterization of a Trinuclear Ruthenium Species in Catalytic Water Oxidation by Ru(Bda)(Pic)<sub>2</sub> in Neutral Media. *Chem. Commun.* **2016**, *52* (55), 8619–8622.
- (107) Yang, J.; Liu, B.; Duan, L. Structural Evolution of the Ru-Bms Complex to the Real Water Oxidation Catalyst of Ru-Bda: The Bite Angle Matters. *Dalt. Trans.* **2020**, *49* (14), 4369–4375.
- (108) Yang, Y.; Yang, J.; Li, F.; Liao, R.; Duan, L. Water Oxidation Catalyzed by Ruthenium Complexes with 4-Hydroxypyridine-2,6-Dicarboxylate as a Negatively Charged Tridentate Ligand. *Eur. J. Inorg. Chem.* **2020**, *2020* (23), 2238–2245.
- (109) Shatskiy, A.; Bardin, A. A.; Oschmann, M.; Matheu, R.; Benet-Buchholz, J.; Eriksson, L.; Kärkäs, M. D.; Johnston, E. V.; Gimbert-Suriñach, C.; Llobet, A.; Åkermark, B. Electrochemically Driven Water Oxidation by a Highly Active Ruthenium-Based Catalyst. *ChemSusChem* **2019**, *12* (10), 2251–2262.

## CHAPTER 1. General Introduction

# I

## 2 CHAPTER 2

### OBJECTIVES

---

*Following the progress in the field of artificial photosynthesis discussed in the General Introduction, the main objectives are exposed in the current chapter. Objectives highlight many challenges that are, nonetheless, remaining for achieving the required progress for practical applications.*

---



## CHAPTER 2. Objectives

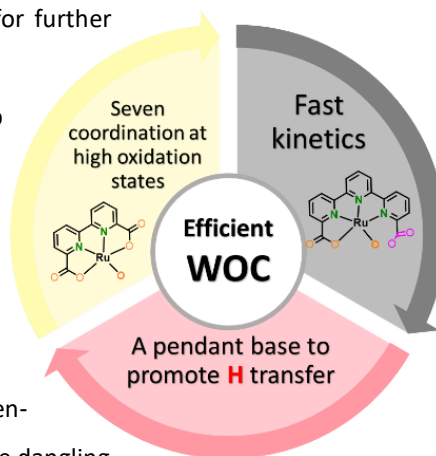
# II

As was described in the previous chapter, the development of the Ru-based water oxidation complexes had shown significant progress in terms of stability and reactivity. The recent progress in the field of coordination chemistry and rational design of catalysts has allowed the development of novel molecular systems with enhanced activity, greater stability during long-term catalysis. Nevertheless, there are remaining challenges in terms of stability and operating potentials that have to be improved for further anchoring and for building photoanodes.

The goal of this thesis was to design and develop novel water oxidation complexes based on Ru. As an inspiration for development, we took two of the best catalysts: **Ru(tda)** and **Ru(bda)** complexes. The remarkable performance of the **Ru(tda)** catalyst is attributed to the ability of the ligand to facilitate the formation of a seven-

coordinated high oxidation state. Furthermore, the dangling carboxylate group in complex acts as an internal base, promoting the PCET process and as the result opening a low-energy pathway for O–O bond formation step.

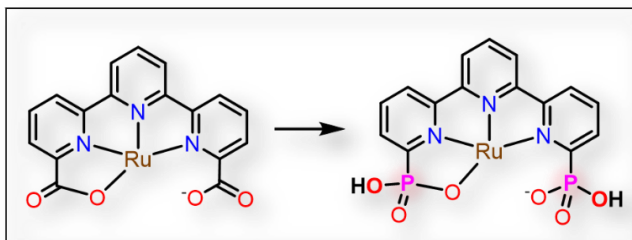
Based on the most important considerations for the rational design of high-performance molecular WOCs we designed a novel Ru-based complex, where we kept the terpyridine ligand core of **Ru(tda)**, but substitute two carboxylate groups with the phosphonate moieties. Implemented changes resulted in a coordination complex **Ru(tPa)**, with the general formula  $[\text{Ru}^{\text{II}}(\text{H}_2\text{tPa}-\kappa\text{-N}^3\text{O})(\text{py})_2]$  where tPa is [2,2':6',2''-terpyridine-6,6''-diphosphonic acid] and py is a pyridine. Together with two phosphonate groups, we introduce two extra protons into the system, which potentially might have a significant impact on catalyst performance. For these reasons, the general objective of the present Ph.D. thesis is the design and detailed analysis of molecular Ru-based catalysts to identify the factors that determine the activity and stability. The goal is to establish the factors that determine catalyst activity further redesign new catalysts with improved performance and as a final goal incorporating them into complete photoelectrochemical cells.



## CHAPTER 2. Objectives

### • OBJECTIVE 1.

Design, synthesis, and characterization of novel **Ru**-based catalyst, with the general formula  $[\text{Ru}^{\text{II}}(\text{H}_2\text{tPa}-\kappa\text{-N}^3\text{O})(\text{py})_2]$  where tPa is [2,2':6',2''-terpyridine-6,6''-diphosphonic acid]. By

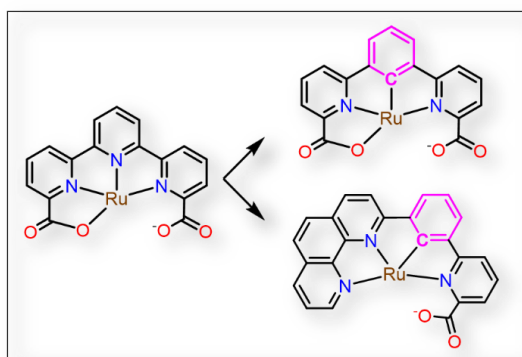


introducing four protons with the phosphonate groups into the system, we are expecting additional PCET processes throughout

reaching high oxidation states and, as the result, improving the kinetics during the catalysis.

### • OBJECTIVE 2

Synthesis and characterization of **Ru**-based complexes that can stabilize high oxidation states of the metal center and as the result lowering the overpotential towards water oxidation catalysis. This objective can be reached thanks to introducing a strong electron donation group from the ligand. This can be implemented by the introduction of carbon anion instead of nitrogen in the equatorial terpyridine core. The modification might show not just a significant cathodic shift in the potential of the high oxidation state reaching, but also affect robustness and reactivity of the obtained catalyst.



• **OBJECTIVE 3**

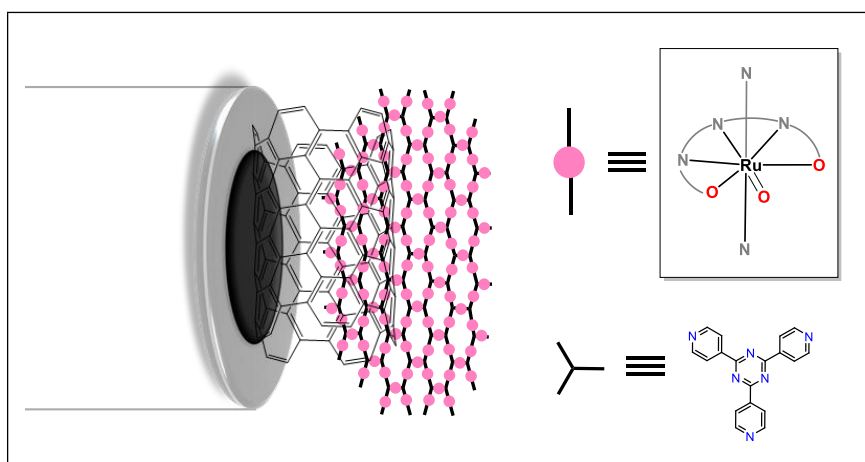
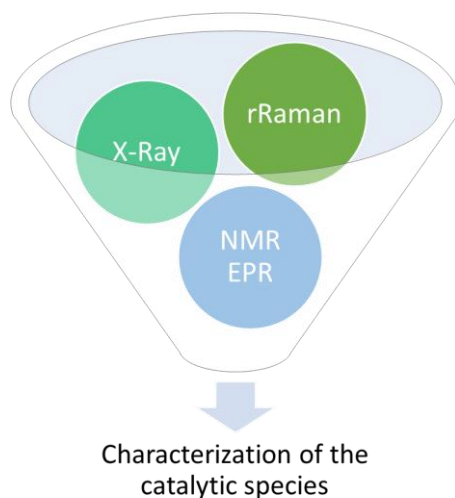
The development of the methodology for determining the catalyst active species generated during turnover conditions. The methodology is based on the combination of different spectroscopic techniques, including NMR, Resonance Raman, EPR, and UV-Vis.

• **OBJECTIVE 4**

To follow the oxidative decay of a **Ru**-based WOC depending on the pH and the applied potential. Electrochemical methods, together with surface characterization techniques, can show a complete mechanistic scenario of the molecular catalyst evolution during the water oxidation catalysis.

• **OBJECTIVE 5**

To prepare molecular anodes for water oxidation catalysis based on anchored Ru complexes. For that aim, **Ru-based** coordination polymer will be prepared and anchored to carbon-based surfaces by CH- $\pi$  interactions. The redox properties, catalytic performance, and stability will be investigated.



## CHAPTER 2. Objectives

# II

## 3 CHAPTER 3

### **Second Coordination Sphere Effects in an Evolved Ru Complex Based on a Highly Adaptable Ligand Results in Rapid Water Oxidation Catalysis**

---

*In the present work, we develop the synthetic and catalytic chemistry related to a Ru complex bonded to a new member of the family of FAME ligands (Flexible Adaptative Multidentate Equatorial). We find that the initial complex evolves via intramolecular aromatic O-atom insertion into a CH bond, leading to a completely new complex that has the highest TOF ever reported and remarkable long-term stability. Further, we show how second coordination sphere effects are responsible not only for the generate the active ion of the catalyst but also for the reduction of the energies of activation at the rate-determining step during the catalysis. In summary, the present work highlights the importance of designing catalysts with the right second coordination sphere environment and the need to evaluate the fate of the catalyst during turnover.*

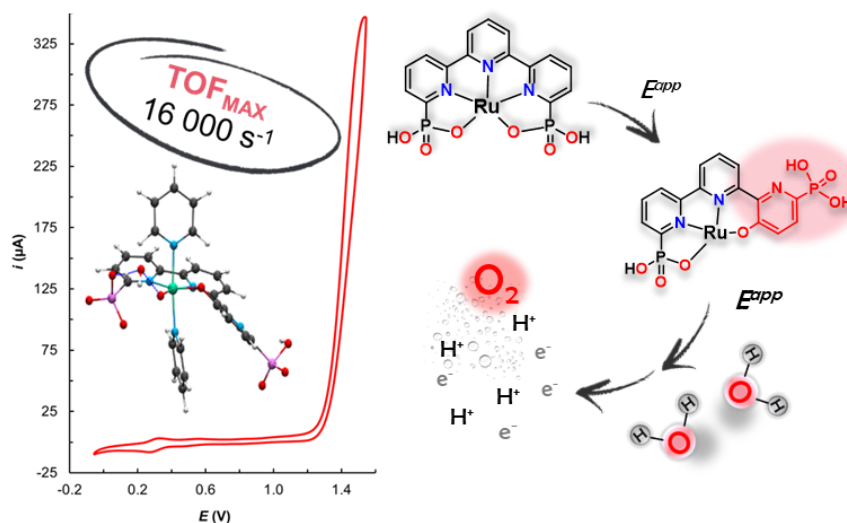
---

## CHAPTER 3.

**The research results presented in this chapter were included in the following scientific publication:**

Vereshchuk, N.; Matheu, R.; Benet-Buchholz, J.; Pipelier, M.; Lebreton, J.; Dubreuil, D.; Tessier, A.; Gimbert-Suriñach, C.; Z. Ertem, M.; Llobet, A. **Second Coordination Sphere Effects in an Evolved Ru Complex Based on Highly Adaptable Ligand Results in Rapid Water Oxidation Catalysis.** *J. Am. Chem. Soc.* **2020**, *142* (11), 5068–5077.

## Second Coordination Sphere Effects in an Evolved Ru Complex Based on a Highly Adaptable Ligand Results in Rapid Water Oxidation Catalysis



III

### Abstract

A new Ru complex containing the deprotonated 2,2':6',2''-terpyridine,6,6''-diphosphonic acid (H<sub>4</sub>tPa) and pyridine (py) of the general formula, [Ru<sup>II</sup>(H<sub>3</sub>tPa-κ-N<sup>3</sup>O)(py)<sub>2</sub>]<sup>2+</sup>, **2**<sup>+</sup>, has been prepared and thoroughly characterized through spectroscopic, electrochemical techniques, X-ray diffraction analysis and with DFT calculations. Complex **2**<sup>+</sup> presents a dynamic behavior in the solution that involves the synchronous coordination and the decoordination of the dangling phosphonic groups of the tPa<sup>4-</sup> ligand. However, at oxidation state IV complex **2**<sup>+</sup>, it becomes seven coordinated with the two phosphonic groups now bonded to the metal center. Further, at this oxidation state at neutral and basic pH, the Ru complex undergoes coordination of an exogenous OH<sup>-</sup> group from the solvent that leads to an intramolecular aromatic O-atom insertion into the CH bond of one of the pyridyl groups forming the corresponding phenoxo-phosphonate Ru complex [Ru<sup>III</sup>(tPaO-κ-N<sup>2</sup>O<sub>p</sub>Oc)(py)<sub>2</sub>]<sup>2-</sup>, **4**<sup>2-</sup>, where tPaO<sup>5-</sup> is 3-hydroxo-[2,2':6',2''-terpyridine]-6,6''-diyl)bis(phosphonate) ligand. This new in situ generated Ru complex, **4**<sup>2-</sup>, has been isolated and spectroscopically and electrochemically characterized. Besides, a crystal structure has



### CHAPTER 3.

been also obtained using single-crystal X-ray diffraction techniques. Complex **4**<sup>2-</sup> turns out to be an exceptional water oxidation catalyst achieving record high  $TOF_{max}$  in the order of 16,000 s<sup>-1</sup>. A mechanistic analysis complemented with DFT calculations has also been carried out showing the critical role of intramolecular second coordination sphere effects exerted by the phosphonate groups in lowering the activation energy at the rate-determining step.

#### *Contributions:*

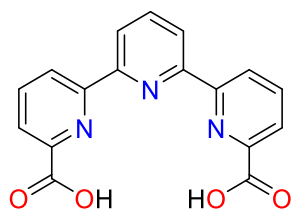
Nataliia Vereshchuk synthesized and characterized all the compounds, as well as carried out all the electrochemical and spectroscopic experiments

III

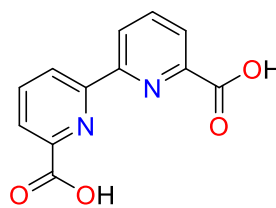
### 3.1 Introduction

Molecular water oxidation catalysis is a field that has been rapidly developing over the last decade mainly due to its potential application in new energy conversion schemes based on water splitting with sunlight.<sup>1-7</sup> In particular, Ru complexes have been leading the field and today the amount of information extracted from these complexes has generated a deep understanding of the different parameters involved in the catalytic cycle.<sup>8,9</sup> This has been possible thanks to the spectroscopic characterization of the reaction intermediates as well as due to the kinetic characterization of the different steps involved and complemented with a thorough computational analysis.<sup>10-13</sup> This wealth of information based on Ru complexes as water oxidation catalysts (WOCs) has also been extended to other transition metals as well as oxides reported as WOCs for their design and mechanistic proposals.<sup>14-17</sup> The best WOCs known today are based on the Flexible Adaptative Multidentate Equatorial (FAME) ligands<sup>18</sup> containing polypyridyl carboxylate groups such as H<sub>2</sub>tda<sup>19</sup> and H<sub>2</sub>bda<sup>20-22</sup> (see Chart I for the drawings of the ligands) and their related derivatives where the carboxylate groups have been partially or totally substituted by phosphonate groups.<sup>23-26</sup> In particular, the complex [Ru<sup>IV</sup>(OH)(tda-κ-N<sup>3</sup>O)(py)<sub>2</sub>]<sup>+</sup> (py for pyridine), **1**<sup>+</sup>, has been recently shown to achieve *TOF*<sub>max</sub> of 8,000 s<sup>-1</sup> at pH 7.0.<sup>19</sup> Further, the analysis of its performance shows a delicate balance among multiple equilibria at different oxidation states with diverse coordination number and degree of hydrogen bonding that is responsible for its performance as a catalyst.<sup>19,27</sup> Because of these delicate equilibria, the replacement of carboxylate groups in H<sub>2</sub>tda by phosphonate groups leading to the H<sub>4</sub>tPa ligand (Chart I), is expected to generate significant differences in its catalytic behavior. The electronic nature and geometry of the phosphonate with regard to those of the carboxylate group as well as an increase in steric will be responsible for the different catalytic behavior of the new Ru complexes based on H<sub>4</sub>tPa.<sup>28</sup>

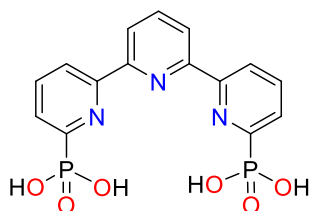
### CHAPTER 3.



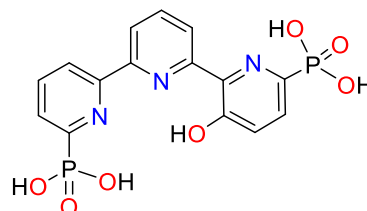
H<sub>2</sub>tda



H<sub>2</sub>bda



H<sub>4</sub>tPa



H<sub>5</sub>tPaO

**Chart 1.** Drawing and labeling of the ligands that were discussed in this work.

In addition, the increased number of acidic protons with substantially different  $pK_a$ 's are expected to not only facilitate remote proton-coupled electron transfer (PCET) events during redox leveling,<sup>29–35</sup> but also give rise to beneficial second sphere coordination effects such as hydrogen bonding interactions. Further, the phosphonate groups are expected to act as an intramolecular proton acceptor, at the O-O bond formation step, significantly reducing its activation energies.

Here on we present a new family of Ru complexes derived from the H<sub>4</sub>tPa ligand together with a thorough characterization of their redox and water oxidation catalytic properties.

## 3.2 Results

### 3.2.1 Synthesis and structure of the precursor complex $2^+$

The synthesis of the H<sub>4</sub>tPa ligand was carried out in three steps using 2,2':6',2''-terpyridine (trpy) as the starting material as described in the supporting information. Initially, the trpy ligand is oxidized to 2,2':6',2''-terpyridine-1,1''-dioxide using metachloroperbenzoic acid. The treatment of the latter with POEt<sub>3</sub> forms tetraethyl 2,2':6',2''-terpyridine-6,6''-diphosphonate that is hydrolyzed with trimethylbromosilane yielding the H<sub>4</sub>tPa ligand. The synthetic strategy for the preparation of the complexes described in this work is outlined in Figure 1. Complex [Ru<sup>II</sup>(H<sub>3</sub>tPa-κ-N<sup>3</sup>O)(py)<sub>2</sub>]<sup>+</sup>, **2**<sup>+</sup>, is prepared by refluxing stoichiometric amounts of H<sub>4</sub>tPa and [Ru(DMSO)<sub>4</sub>Cl<sub>2</sub>] in *n*-BuOH, followed by the addition of an excess of pyridine and further refluxing overnight. Proper column chromatography in silica generates pure **2**Cl in moderate yields where the equatorial H<sub>3</sub>tPa<sup>-</sup> ligand acts in a monoanionic fashion. Crystals of **2**PF<sub>6</sub>·3H<sub>2</sub>O sufficiently good for X-ray analysis were obtained by counteranion exchange crystallization from an acidic aqueous solution of **2**Cl and KPF<sub>6</sub>. The ORTEP view of its solvated cationic moiety is presented in Figure 1. The Ru(II) center features an octahedral type of geometry where the H<sub>3</sub>tPa<sup>-</sup> ligand coordinates in the equatorial plane in a κ-N<sup>3</sup>O fashion leaving a dangling non-coordinated phosphonic acid group. The octahedral geometry is completed with two pyridyl groups in the axial position. The bonding parameters are unremarkable<sup>36</sup> except for distortion due to the geometrical constraints of the HtPa<sup>3-</sup> ligand at the equatorial zone, which produces an N-Ru-O angle of 115°; 25° larger than the ideal *O<sub>h</sub>* geometry. The same angle for the [Ru<sup>II</sup>(tda)(py)<sub>2</sub>] is 125°,<sup>19</sup> that is 10° higher which is a consequence of the different bonding parameters associated with the phosphonate and carboxylate moieties.<sup>37,38</sup> Finally, there are three H<sub>2</sub>O molecules in the unit cell, interacting with the phosphonic groups by hydrogen bonding as can be observed in Figure 1. Density functional theory (DFT) calculations at the M06 level of theory<sup>39</sup> in conjunction with SMD aqueous continuum solvation model<sup>40</sup> (see computational methods for further details) have been carried out in order to complement the experimental work described here for **2**<sup>+</sup>. The computed structure for **2**<sup>+</sup> shows a very good agreement with the experimental structure in terms of bonding parameters (Figure S62) revealing its good degree of reliability.

## CHAPTER 3.

The addition of two equivalents of Ce(IV) generates the corresponding seven coordinated Ru(IV) complex  $[\text{Ru}^{\text{IV}}(\text{tPa-}\kappa\text{-N}^3\text{O}^2)(\text{py})_2]$ , **3**, where the  $\text{tPa}^{4-}$  ligand now acts in a pentadentate manner and the metal center possesses a pentagonal bipyramidal geometry as can be observed in the computed structure shown in Figure 1. This complex is diamagnetic at room temperature (RT) with a high field low spin  $d^4$  electronic configuration,  $(e_1'')^4(e_2')^0(a_1')^0$ , analogous to related Ru(IV) complexes.<sup>19,41,42</sup> Its  $^1\text{H}$ ,  $^{13}\text{C}$ , and  $^{31}\text{P}$  NMR are presented in the SI see Figures S27-29.

### 3.2.2 Spectroscopy and dynamic behavior of **2**

The spectroscopic properties were investigated through UV-Vis and NMR spectroscopy. The UV-Vis spectra of  $[\text{Ru}^{\text{II}}(\text{H}_2\text{tPa-}\kappa\text{-N}^3\text{O})(\text{py})_2]$ , **2**, and its one and two-electron oxidized species  $[\text{Ru}^{\text{III}}(\text{H}_2\text{tPa-}\kappa\text{-N}^3\text{O})(\text{py})_2]^+$  and  $[\text{Ru}^{\text{IV}}(\text{HtPa-}\kappa\text{-N}^3\text{O}^2)(\text{py})_2]^+$  were generated via redox titration using Ce(IV) as the oxidant at pH 1.0 in aqueous triflic acid (Figures S45-S46). Complex **2** is a diamagnetic low spin  $d^6$  ion with a typical  $(t_{2g})^6(e_g)^0$  electronic configuration and its NMR spectra and assignment are presented in Figure 2 and the supporting information (Figures S12-S26 and Figures S35-S36). At room temperature, the NMR spectrum displays eight resonances as if the complex had  $C_{2v}$  symmetry. However, at low temperatures, the resonances of the protons  $H_a$ ,  $H_b$ ,  $H_c$  and  $H_e$  split indicating the presence of dynamic behavior (Figure 2). The dynamic behavior is associated with the synchronic coordination and decoordination of the dangling phosphonate that has an activation energy of 13.3 kcal/mol based on Eyring plots generated from VT-NMR (Scheme S2). By computational methods, the estimated activation energy of 7.9 kcal/mol (see Figure S37) was obtained for this dynamic behavior in line with the experimental observations. The value of the activation energy is similar to that measured for Ru-bda complexes involving coordination and decoordination of the dangling carboxylates.<sup>43</sup>

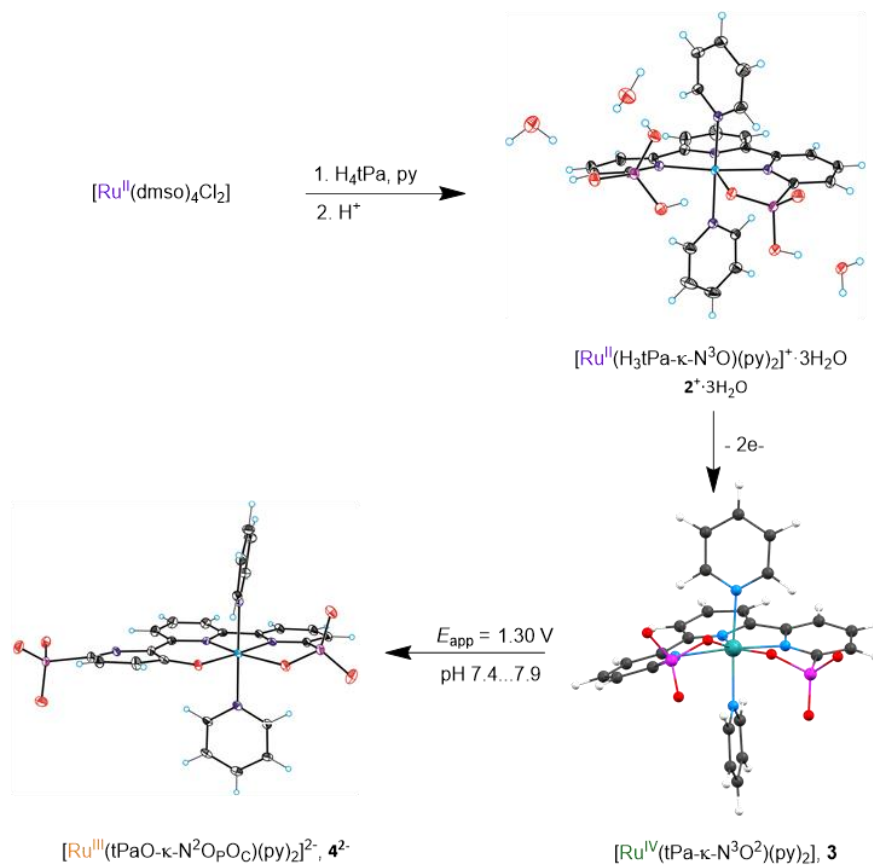


**Figure 1.** Synthetic scheme and structures of the complexes described in this work. X-ray structure ORTEP views for  $\{[\text{Ru}^{\text{II}}(\text{H}_3\text{tPa}-\kappa\text{-N}^3\text{O})(\text{py})_2](\text{H}_2\text{O})_3\}^+$ ,  $2^+ \cdot 3\text{H}_2\text{O}$ , showing the 3 hydrogen-bonded water molecules and for  $[\text{Ru}^{\text{III}}(\text{tPaO}-\kappa\text{-N}^2\text{O}_\text{P}\text{OC})(\text{py})_2]^{2-}$ , **4**<sup>2-</sup>. Calculated structure for  $[\text{Ru}^{\text{IV}}(\text{tPa}-\kappa\text{-N}^3\text{O}^2)(\text{py})_2]$ , **3**. Color code: Ru, cyan; P, pink; N, blue; O, red; C, black; H, white.

## CHAPTER 3.

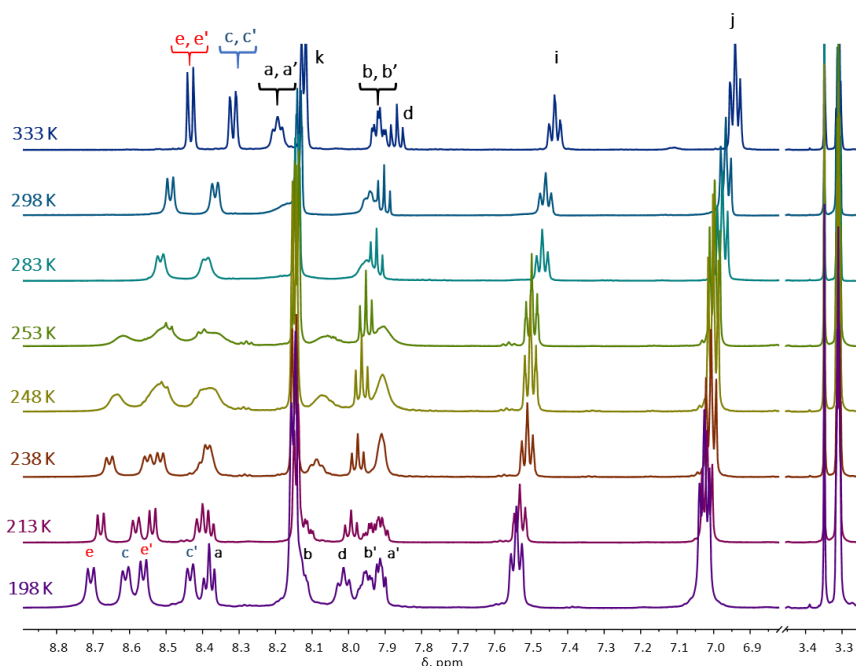
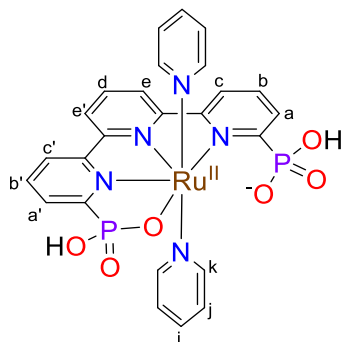


**Figure 2.** VT  $^1\text{H-NMR}$  of  $[\text{Ru}^{\text{II}}(\text{H}_2\text{tPa-}\kappa\text{-N}^3\text{O})(\text{py})_2]$ , **2** in  $\text{CD}_3\text{OD}$  together with labeling.

### 3.2.3 Redox properties of **2**

The redox properties of **2** were investigated by electrochemical techniques in a three-electrode cell using glassy carbon as a working electrode and all potentials were measured using a  $\text{Hg}/\text{Hg}_2\text{SO}_4$  as a reference electrode and converted to vs NHE by adding 0.65 V to the measured potential. Cyclic Voltammetry of **2** was performed in an aqueous solution as a function of pH that produces a different degree of protonation at the phosphonate groups. Cyclic voltammetry at pH 7.0 is shown in Figure 3 (red trace) where two chemically

reversible and electrochemically quasireversible redox processes can be observed. The first redox process at  $E_{1/2} = 0.83$  V is assigned to a PCET process to generate  $[\text{Ru}^{\text{III}}(\text{tPa}-\kappa\text{-N}^3\text{O}^2)(\text{py})_2]^-$  whereas the second wave at  $E_{1/2} = 0.92$  V is due to a one-electron oxidation process to form  $[\text{Ru}^{\text{IV}}(\text{tPa}-\kappa\text{-N}^3\text{O}^2)(\text{py})_2]$ .

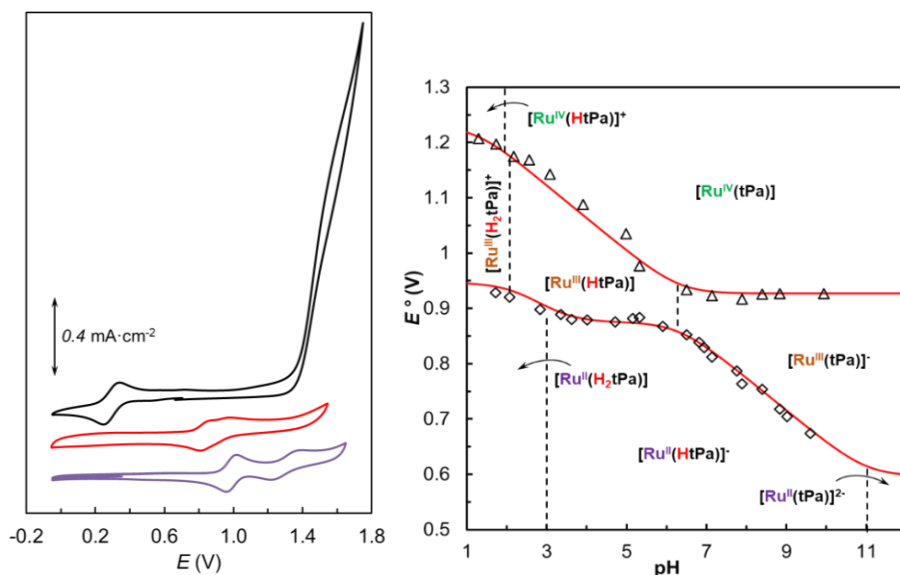


**Figure 3.** Left, cyclic voltammetry of 0.6 mM  $[\text{Ru}^{\text{II}}(\text{HtPa}-\kappa\text{-N}^3\text{O})(\text{py})_2]^-$ , **2**<sup>-</sup>, at pH 7.0 in a 0.1 M phosphate buffer aqueous solution (red trace) and at pH = 1.0 in 0.1 M triflic acid (purple trace). Solid line black trace, cyclic voltammetry of 0.6 mM  $[\text{Ru}^{\text{III}}(\text{tPaO}-\kappa\text{-N}^2\text{O}_F\text{OC})(\text{py})_2]^{2-}$ , **4**<sup>2-</sup>, at pH 7.0 in a 0.1 M phosphate buffer aqueous solution, generated from the precursor **2**<sup>-</sup>, by a 3h bulk electrolysis at 1.30 V. Right, Pourbaix diagram for **2**. The dominant species as a function of pH and potential are indicated with the labels such as  $[\text{Ru}^{\text{II}}(\text{H}_2\text{tPa})]$  where the oxidation state is indicated as well as the degree of protonation of the H<sub>4</sub>tPa ligand. The dashed vertical lines indicate the pK<sub>a</sub> of the species involved. The axial pyridyl ligands are omitted for clarity.

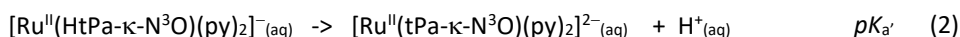
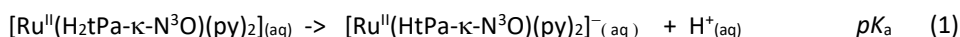
The one-electron nature of the two processes is corroborated by the spectrophotometric redox titration (Figure S45-S46), and the degree of protonation is deduced from the Pourbaix diagram shown in Figure 3 right. (see SI for the equations used for the simulation).

III



## CHAPTER 3.

The four protons potentially available from the two phosphonic groups in **2**, allow obtaining a rich family of complexes depending on the degree of oxidation and protonation as shown in the Pourbaix diagram. The  $pK_a$ 's coincide with the dashed vertical lines and are deduced from the change of slope in the  $E^0$  vs. pH plot. The first and second  $pK_a$ 's due to the monodeprotonation of each phosphonic group are expected to occur below pH 1.0.<sup>44–46</sup> Further, the  $pK_a$  for the third and fourth proton loss are labeled,  $pK_a$  and  $pK_{a'}$ , and are defined in equations 1 and 2 respectively,



The latter have been independently calculated via spectrophotometric acid-base titration as shown in Figure S47. It is interesting to see how due to the different proton content of the species involved at a given pH, the difference between the IV/III-III/II redox couples change considerably as a function of pH as can be graphically observed in Figure S49A. Indeed, at pH 7.0 this difference is only 100 mV, but it increases up to 330 mV at pH 13.0 (Figure S49B).

### 3.2.4 Generation of the active Ru species via O-atom insertion

The synthesis of the active catalyst  $[\text{Ru}^{\text{III}}(\text{tPaO-}\kappa\text{-N}^2\text{O}_p\text{O}_c)(\text{py})_2]^{2-}$ , **4**<sup>2-</sup>, (see a drawing of the HstPaO ligand in Chart 1;  $O_p$  refers to oxygen atom coordinated to the Ru center via the oxygen atom from the phosphonic group and  $O_c$  from the pyridyl group) was carried out electrochemically using  $[\text{Ru}^{\text{II}}(\text{H}_3\text{tPa-}\kappa\text{-N}^3\text{O})(\text{py})_2]^+$ , **2**<sup>+</sup>, (**2**<sup>+</sup> is predicted to convert to **2** at pH 7.7) as a precursor as outlined in Figure 1.

A sample of **2**<sup>+</sup> is dissolved in a pH 7.7 aqueous phosphate buffer solution and placed in a two-compartment electrochemical cell using a Pt mesh as a working electrode. Then a potential of 1.30 V is applied for 110 minutes. During this process, the initial **2**<sup>+</sup> precursor complex is quantitatively transformed into the final complex **4**<sup>2-</sup>, where an O atom insertion between the Ru center and one of the pyridyl groups takes place. This is reminiscent of the reactivity of dinuclear dicopper complexes at low oxidation states with dioxygen reported earlier.<sup>47</sup> One electron reduction of **4**<sup>2-</sup> yields the diamagnetic **4**<sup>3-</sup> complex that was

characterized by  $^1\text{H}$ ,  $^{13}\text{C}$ , and  $^{31}\text{P}$  NMR spectroscopy and whose spectra are shown in Figures S39-S44. Electrochemically only the initial and final species are detected (Figure S50).

Single crystals of  $\mathbf{4}^{3-}$  were obtained by adding excess  $\text{Cs}^+$  to a solution of  $\mathbf{4}^{2-}$  in MeOH. A crystal structure of  $\mathbf{4}^{3-}$  is displayed in Figure 1 showing the phenoxide bonding and the decoordination of the initial pyridyl-phosphonic group. The complex was further characterized by UV-Vis spectroscopy using an Optically Transparent Thin-Layer Electrochemical (OTTLE) cell (Figure S48).

In order to get further insight into the potential sequence of reactions that generate  $\mathbf{4}^{2-}$  from  $\mathbf{2}$  ( $\mathbf{2}$  converts to  $\mathbf{2}^{\cdot}$  at pH 7 according to the Pourbaix diagram) a computational analysis was carried out and the results obtained are summarized in Scheme 1. As the current flows at an applied potential of 1.30 V, the initial Ru(II) complex  $\mathbf{2}^+$  is initially converted to seven coordinate (CN7) Ru(IV) species,  $[\text{Ru}^{\text{IV}}(\text{tPa-}\kappa\text{-N}^3\text{O}^2)(\text{py})_2]$ ,  $\mathbf{3}$ , in agreement with its redox properties described in the previous section. This complex then reacts with a water molecule with concomitant proton release inducing the decoordination of one of the pyridyl phosphonate groups to generate  $[\text{Ru}^{\text{IV}}(\text{O})(\text{HtPa-}\kappa\text{-N}^2\text{O})(\text{py})_2]$ . The latter then undergoes a PCET step to form  $[\text{Ru}^{\text{V}}(\text{O})(\text{tPa-}\kappa\text{-N}^2\text{O})(\text{py})_2]$ . This species is responsible for the intramolecular hydroxylation of the dangling pyridyl group that is highly favored from a thermodynamic perspective ( $\Delta G = -9.0$  kcal/mol) and that finally leads to pure  $\mathbf{4}^{2-}$  following a deprotonation event ( $\Delta G = -54.6$  kcal/mol). A transition state for the electrophilic oxygen insertion into the CH bond has also been located with the low free energy of activation ( $\Delta G^\ddagger$ ) of 14.0 kcal/mol.

The redox and electrocatalytic properties of  $\mathbf{4}^{2-}$  were investigated by CV and Coulombimetric techniques. Figure 3 (black trace, left) shows the CV of  $\mathbf{4}^{2-}$  at pH 7.0 phosphate buffer solution where an electrochemically and chemically reversible wave appears at  $E_{1/2} = 0.35$  V that is assigned to the Ru(III)/Ru(II) couple. At higher anodic potentials a very large electrocatalytic current is observed at approximately 1.4 V that is due to the oxidation of water to dioxygen. This second wave is associated with a two-electron process and oxido coordination, reaching the Ru(V)=O species that is responsible for the reaction with solvent water and O-O bond formation. A two-electron process is proposed since no other waves are observed besides the III/II wave and the corresponding

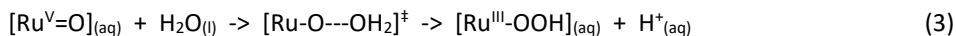
## CHAPTER 3.

Ru(IV)=O species are not sufficiently reactive for fast water oxidation and are further supported by DFT.

### 3.2.5 Water oxidation catalysis and mechanisms

Kinetic characterization of the electrocatalytic water oxidation reaction was carried out for **4**<sup>2-</sup>, based on Foot of the Wave Analysis (FOWA)<sup>48-50</sup> at pH 7.2 as shown in Figure S54A. A  $TOF_{max} = 1.6 \cdot 10^4 (\pm 0.2 \cdot 10^4) \text{ s}^{-1}$  is obtained that is found to be independent of catalyst concentration between 0.5 and 3.0 mM. This first-order kinetics behavior with regard to catalyst concentration points towards a water nucleophilic attack (WNA)<sup>51</sup> type of mechanism where the O-O bond formation between the Ru(V)=O species and the solvent is the rate-determining step (rds). This is further supported by theoretical calculations as will be shown in the next section. The performance of **4**<sup>2-</sup> as WOC was further tested by bulk electrolysis experiments described in detail in the supporting information (Figure S53). More than 42 million turnovers with Faradaic efficiencies above 93% were obtained using Saveant's methodology that takes into account the concentration of the catalyst close to the electrode surface and manifests the remarkable stability of this catalyst.<sup>21-23</sup> It is also interesting to point out here that catalyst **4**<sup>2-</sup> is also active at lower pH albeit with lower efficiency (Figure S51).

A thorough mechanistic analysis was also carried out based on theoretical calculations and is summarized in Figure 4 top, where the different reaction intermediates and the computed  $\Delta G$ s and redox potentials associated with each step are presented (see computational methods in the SI for further details). We propose that once the Ru(III) complex, **4**<sup>2-</sup>, is generated, water coordination together with a two-electron oxidation process proceeds to form Ru<sup>V</sup>=O species,  $[\text{Ru}^{\text{V}}(\text{O})(\text{HtPaO}-\kappa-\text{N}^3\text{O}_p)(\text{py})_2]^-$ , which will, in turn, react with a solvent H<sub>2</sub>O to generate the corresponding hydroxoperoxido derivative, as indicated in the equation below,



The optimized TS for WNA reaction is presented in Figure 4 bottom. It is interesting to realize here that the coordination number (CN) for the Ru(V) species is 6 with the tPaO<sup>5-</sup>

ligand acting in a  $\kappa\text{-N}^2\text{O}_c$  fashion and thus with a dangling phosphonate group. This dangling group is strategically situated so that it can act as an intramolecular proton acceptor to facilitate the WNA TS and to reduce the free energy activation ( $\Delta G^\ddagger = 22.1$  kcal/mol). Once Ru(III)-OOH is formed then it suffers a PCET that forms the Ru(IV)-OO that spontaneously evolves dioxygen and generates the initial Ru(II) species completing the catalytic cycle. The computed  $\Delta G^\ddagger$  of 22.1 kcal/mol for the proposed rate-limiting WNA step is relatively high compared to experimental TOF of 16,000  $\text{s}^{-1}$  so we further performed calculations at both M06 and M06-L<sup>52</sup> level of theories with additional explicit water molecules to account for hydrogen bonding effects from the solvent (Table S4).

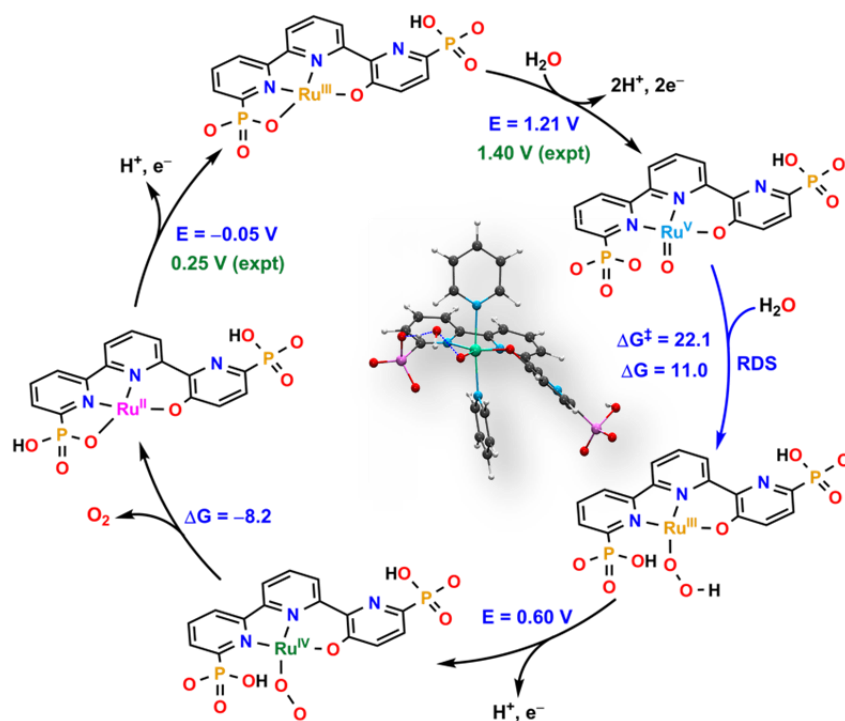


**Figure 4.** Calculated catalytic cycle for catalyst  $[\text{Ru}^{\text{V}}(\text{O})(\text{HtPaO}-\kappa\text{-N}^2\text{O}_c)(\text{py})_2]^-$  at pH 7.0 Redox potentials ( $E$ ) (experimental in green and calculated in blue) in units of volts (V) vs NHE,  $\Delta G$ s, and  $\Delta G^\ddagger$  in units of kcal/mol. Axial pyridyl ligands are omitted for clarity. Inset, optimized TS for the O-O bond formation step. Color code: Ru, cyan; P, orange; N, blue; O, red; C, black; H, white.

## CHAPTER 3.

The computed  $\Delta G^\ddagger$ s exhibit a notable decrease with additional water molecules and with four explicit water molecules the computed activation free energies are 18.7 and 16.3 kcal/mol at M06 and M06-L level of theories, respectively. We also considered O-O bond formation between Ru(V)=O species and an oxygen atom of the dangling phosphonate group similar to the oxide relay mechanism recently proposed for Ru-tda complex by Zhan et al<sup>53</sup> and located a TS structure featuring a  $\Delta G^\ddagger$  of 13.2 kcal/mol but the resulting Ru-O-O-P species is uphill by 6.3 kcal/mol indicating that reverse step has a much lower  $\Delta G^\ddagger$  of 6.9 kcal/mol. Moreover, at pH 7, nucleophilic addition of OH<sup>-</sup> to P atom of Ru-O-O-P moiety similar to that proposed in the oxide relay mechanism is very unlikely and H<sub>2</sub>O molecule should behave as the nucleophile for the hydrolysis of the Ru-O-O-P group, which is expected to result in higher activation energies. A future direction of our studies will be devoted to a closer inspection of WNA and alternative O-O bond formation pathways with full atomistic solvation models.”

### 3.3 Discussion

A detailed understanding of water oxidation catalysis is challenging due to the large number of reactions and intermediates involved in this complex process. The electronic demands imposed by the reaction intermediates accessed at each oxidation state at the different stages of the catalytic cycle involve a change in metal coordination number. Along this line, high oxidation states will prefer hard base ligands while lower oxidation states will prefer softer ones. Additional complexity arises because of the variety of reactions handled by the catalyst including outer-sphere electron transfers (OSET), PCET, and chemical reactions that might not necessarily involve ET such as proton transfer or O-O bond formation. Moreover, non-desired pathways that derail these reactions from the catalytic cycle towards non-productive or decomposition products also need to be understood,<sup>54</sup> to be able to avoid them and to obtain robust water oxidation catalysts. To control all the parameters indicated above, each step should occur with an activation barrier as low as possible so that efficient water oxidation catalysis can take place.

### 3.3.1 Geometrical and electronic consequences due to the presence of the phosphonate groups

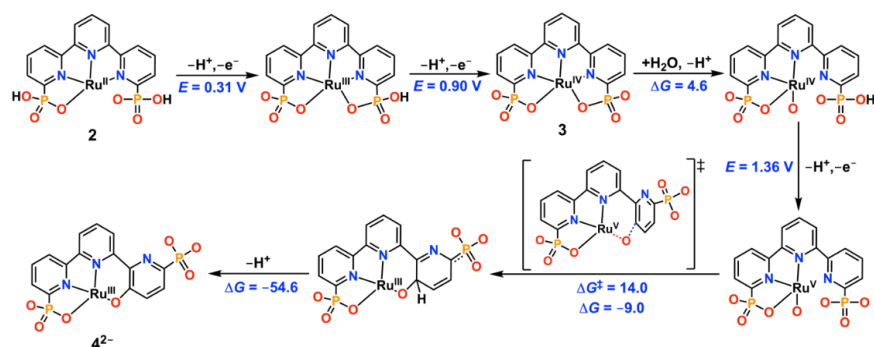
Complex  $[\text{Ru}^{\text{IV}}(\text{O})(\text{tda})(\text{py})_2]$ , **1**, is an example of a catalyst that complies with the above requirements and up to now appears as the fastest water oxidation catalyst ever reported.<sup>55</sup> The structural consequences of changing carboxylate by phosphonates can be graphically observed by comparing the structures of the diamagnetic seven coordinated catalyst precursors  $[\text{Ru}^{\text{IV}}(\text{tda}-\kappa\text{-N}^3\text{O}^2)(\text{py})_2]^{2+}$  and  $[\text{Ru}^{\text{IV}}(\text{tPa}-\kappa\text{-N}^3\text{O}^2)(\text{py})_2]$  (Figures S61 and S63). While the X-ray structure of  $[\text{Ru}^{\text{IV}}(\text{tda}-\kappa\text{-N}^3\text{O}^2)(\text{py})_2]^{2+}$  shows all the coordinating atoms of the  $\text{tda}^{2-}$  ligand nearly on the equatorial plane, the coordinating oxygen atoms of the phosphonate in  $[\text{Ru}^{\text{IV}}(\text{tPa}-\kappa\text{-N}^3\text{O}^2)(\text{py})_2]$  complex are significantly off the equatorial plane as observed in the computed structure shown in Figure 1. Furthermore, this distortion also breaks the planarity of the  $\text{trpy}$  moiety of the  $\text{tPa}^{4-}$  ligand diminishing the aromatic  $\pi$  delocalization. This distortion is due mainly to the different geometric parameters of the phosphonic acid group (pseudo  $T_d$ ) as compared to the carboxylate (pseudo  $C_{2v}$ ) and results in weaker Ru-O bonds for the phosphonic complex. From an electronic perspective, the phosphonate group acts as a stronger sigma donor than the carboxylate, leading in general to lower redox potentials and higher  $pK_a$  ( $pK_a$ 's are 3 and 11 for  $[\text{Ru}^{\text{II}}(\text{H}_2\text{tPa})(\text{py})_2]$  and 6.4 for  $[\text{Ru}^{\text{III}}(\text{HtPa})(\text{py})_2]$ ).<sup>27</sup> The existence of a range of  $pK_a$  values obtained at different oxidation states from the auxiliary ligands is interesting because it can promote remote PCET, that is a PCET where the proton is not associated with the Ru-OH<sub>2</sub> or Ru-OH group, but from auxiliary ligands such as the phosphonic ones. This is important because for typical polypyridyl Ru-aqua complexes such as  $[\text{Ru}(\text{trpy})(\text{bpy})(\text{H}_2\text{O})]^{2+}$ ,<sup>56</sup> the complex can access  $\text{Ru}^{\text{IV}}=\text{O}$  species by two consecutive PCET processes from its aqua derivatives but access to reactive Ru(V) occurs as an ET only process and therefore requires high energy input and overpotential (1.8 V for  $[\text{Ru}(\text{trpy})(\text{bpy})(\text{H}_2\text{O})]^{2+}$ ).<sup>57-59</sup> Thus, the possibility to reach Ru(V) via three PCET processes can open up access to a highly active  $\text{Ru}^{\text{V}}=\text{O}$  species at much lower overpotentials.

### 3.3.2 The importance of the second coordination sphere effects

The two electrons oxidation of the octahedral  $[\text{Ru}^{\text{II}}(\text{H}_2\text{tPa}-\kappa\text{-N}^3\text{O})(\text{py})_2]$ , **2**, complex generates the CN7 diamagnetic  $[\text{Ru}^{\text{IV}}(\text{tPa}-\kappa\text{-N}^3\text{O}^2)(\text{py})_2]$ . Here the importance of ligand

## CHAPTER 3.

flexibility and design is manifested by leaving a non-coordinated dangling phosphonic acid group at oxidation state II where the Ru complex needs to be CN6. The ligand flexibility also allows for a dynamic behavior where the phosphonic groups synchronically coordinate and decoordinate fast at room temperature. Upon reaching Ru(IV) the dangling group immediately coordinates thanks to the flexibility of the ligands achieving CN7. At oxidation state IV in basic solution,  $[\text{Ru}^{\text{IV}}(\text{tPa}-\kappa\text{-N}^3\text{O}^2)(\text{py})_2]$  undergoes  $\text{OH}^-$  substitution to form either  $[\text{Ru}^{\text{IV}}(\text{OH})(\text{tPa}-\kappa\text{-N}^2\text{O})(\text{py})_2]^-$  or  $[\text{Ru}^{\text{IV}}(\text{O})(\text{HtPa}-\kappa\text{-N}^2\text{O})(\text{py})_2]^-$ . Further oxidation leads to the formation of highly reactive  $[\text{Ru}^{\text{V}}(\text{O})(\text{tPa}-\kappa\text{-N}^2\text{O})(\text{py})_2]$  species. The generation of the  $\text{Ru}^{\text{IV}}\text{-OH}$  (or  $\text{Ru}^{\text{IV}}\text{=O}$ ) occurs simultaneously with the breaking of both the Ru-N and Ru-O bonds of one of the pyridyl-phosphonato arms of the  $\text{tPa}^{4-}$  ligand (Scheme 1).



**Scheme 1.** Computed reaction pathway at pH 7.0 for the generation of the catalytically active species  $[\text{Ru}^{\text{III}}(\text{tPaO}-\kappa\text{-N}^2\text{O}_\text{P}\text{OC})(\text{py})_2]^{2-}$ ,  $4^{2-}$ , from the precursor complex  $[\text{Ru}^{\text{II}}(\text{H}_2\text{tPa}-\kappa\text{-N}^3\text{O})(\text{py})_2]$ , **2**. Redox potentials ( $E$ ) in units of volts (V) vs NHE,  $\Delta G$ s, and  $\Delta G^\ddagger$  in units of kcal/mol. Axial pyridyl ligands are omitted for clarity.

This is due to the steric congestion generated by the phosphonate group that precludes the formation of the CN7 complexes  $[\text{Ru}^{\text{IV}}(\text{O})(\text{HtPa}-\kappa\text{-N}^3\text{O})(\text{py})_2]^-$  and  $[\text{Ru}^{\text{V}}(\text{O})(\text{tPa}-\kappa\text{-N}^3\text{O})(\text{py})_2]$ . Once the highly reactive  $\text{Ru}^{\text{V}}\text{=O}$  species is generated then the dangling pyridyl-phosphonato arm has the perfect geometry to undergo intramolecular oxygen atom transfer to the non-coordinated pyridyl ring. This intramolecular O-atom insertion into the CH bond generates the catalytically active complex precursor  $[\text{Ru}^{\text{III}}(\text{tPaO}-\kappa\text{-N}^2\text{O}_\text{P}\text{OC})(\text{py})_2]^{2-}$ ,  $4^{2-}$ .

Two electron oxidation of  $\mathbf{4}^{2-}$  forms the  $\text{Ru}^{\text{V}}=\text{O}$  species that perform O-O bond formation via WNA and generates the  $\text{Ru}^{\text{III}}\text{-OOH}$  intermediate. This step is the rate-determining step (rds) of the catalytic cycle and is favored by the intramolecular proton transfer from the incoming water molecule to the phosphonate group that again has the right geometry to promote this step reducing the activation free energy. This renders  $\mathbf{4}^{2-}$  as an extremely powerful catalyst giving a  $\text{TOF}_{\text{max}}$  of  $16,000 \text{ s}^{-1}$  with an overpotential of 530 mV at pH 7.0. It gives a higher  $\text{TOF}_{\text{max}}$  ( $8,000 \text{ s}^{-1}$ ) than  $\mathbf{1}$  at lower overpotential at (75 mV).

In summary, the dangling phosphonate group is responsible for the low energy pathway of the two key reactions: (i) The formation of active catalyst precursor  $[\text{Ru}^{\text{III}}(\text{tPaO-}\kappa\text{-N}^2\text{O}_p\text{Oc})(\text{py})_2]^{2-}$ ,  $\mathbf{4}^{2-}$ , via oxygen insertion and (ii) the intramolecular proton transfer from the incoming water molecule for the O-O bond formation step that is the rds in the WNA mechanism. These two key reactions occur intramolecularly thanks to the right positioning of the  $\text{Ru}^{\text{V}}=\text{O}$  groups versus the dangling phosphonato group and thus are entropically highly favored.

The present work highlights the importance of designing catalysts with the right *second coordination sphere environment* in the field of redox catalysis and in particular in the catalytic oxidation of water to dioxygen and the fate of the catalysts during turnover.



## CHAPTER 3.

### 3.4 References

- (1) Berardi, S.; Drouet, S.; Francàs, L.; Gimbert-Suriñach, C.; Guttentag, M.; Richmond, C.; Stoll, T.; Llobet, A. Molecular Artificial Photosynthesis. *Chem. Soc. Rev.* **2014**, *43* (22), 7501–7519.
- (2) Lewis, N. S. Research Opportunities to Advance Solar Energy Utilization. *Science (80- )*. **2016**, *351* (6271), aad1920.
- (3) Alstrum-Acevedo, J. H.; Brennaman, M. K.; Meyer, T. J. Chemical Approaches to Artificial Photosynthesis. 2. *Inorg. Chem.* **2005**, *44* (20), 6802–6827.
- (4) Kärkäs, M. D.; Johnston, E. V.; Verho, O.; Åkermark, B. Artificial Photosynthesis: From Nanosecond Electron Transfer to Catalytic Water Oxidation. *Acc. Chem. Res.* **2014**, *47* (1), 100–111.
- (5) Cook, T. R.; Dogutan, D. K.; Reece, S. Y.; Surendranath, Y.; Teets, T. S.; Nocera, D. G. Solar Energy Supply and Storage for the Legacy and Nonlegacy Worlds. *Chem. Rev.* **2010**, *110* (11), 6474–6502.
- (6) Walter, M. G.; Warren, E. L.; McKone, J. R.; Boettcher, S. W.; Mi, Q.; Santori, E. A.; Lewis, N. S. Solar Water Splitting Cells. *Chem. Rev.* **2010**, *110* (11), 6446–6473.
- (7) De Luna, P.; Hahn, C.; Higgins, D.; Jaffer, S. A.; Jaramillo, T. F.; Sargent, E. H. What Would It Take for Renewably Powered Electrosynthesis to Displace Petrochemical Processes? *Science (80- )*. **2019**, *364* (6438), eaav3506.
- (8) Garrido-Barros, P.; Gimbert-Suriñach, C.; Matheu, R.; Sala, X.; Llobet, A. How to Make an Efficient and Robust Molecular Catalyst for Water Oxidation. *Chem. Soc. Rev.* **2017**, *46* (20), 6088–6098.
- (9) Matheu, R.; Garrido-Barros, P.; Gil-Sepulcre, M.; Ertem, M. Z.; Sala, X.; Gimbert-Suriñach, C.; Llobet, A. The Development of Molecular Water Oxidation Catalysts. *Nat. Rev. Chem.* **2019**, *3* (5), 331–341.
- (10) Sala, X.; Maji, S.; Bofill, R.; García-Antón, J.; Escriche, L.; Llobet, A. Molecular Water Oxidation Mechanisms Followed by Transition Metals: State of the Art. *Acc. Chem. Res.* **2014**, *47* (2), 504–516.
- (11) Gimbert-Suriñach, C.; Moonshiram, D.; Francàs, L.; Planas, N.; Bernales, V.; Bozoglian, F.; Guda, A.; Mognon, L.; López, I.; Hoque, M. A.; Gagliardi, L.; Cramer, C. J.; Llobet, A. Structural and Spectroscopic Characterization of Reaction Intermediates Involved in a Dinuclear Co–Hbpp Water Oxidation Catalyst. *J. Am. Chem. Soc.* **2016**, *138* (47), 15291–15294.
- (12) Romain, S.; Bozoglian, F.; Sala, X.; Llobet, A. Oxygen–Oxygen Bond Formation by the Ru–Hbpp Water Oxidation Catalyst Occurssolely via an Intramolecular Reaction Pathway. *J. Am. Chem. Soc.* **2009**, *131* (8), 2768–2769.
- (13) Shaffer, D. W.; Xie, Y.; Concepcion, J. J. O–O Bond Formation in Ruthenium-Catalyzed Water Oxidation: Single-Site Nucleophilic Attack vs. O–O Radical Coupling. *Chem. Soc. Rev.* **2017**, *46* (20), 6170–6193.
- (14) Wang, L. P.; Van Voorhis, T. Direct-Coupling O<sub>2</sub> Bond Forming a Pathway in Cobalt Oxide Water Oxidation Catalysts. *J. Phys. Chem. Lett.* **2011**, *2* (17), 2200–2204.
- (15) McCrory, C. C. L.; Jung, S.; Ferrer, I. M.; Chatman, S. M.; Peters, J. C.; Jaramillo, T. F. Benchmarking Hydrogen Evolving Reaction and Oxygen Evolving Reaction Electrocatalysts for Solar Water Splitting Devices. *J. Am. Chem. Soc.* **2015**, *137* (13), 4347–4357.
- (16) Hong, W. T.; Stoerzinger, K. A.; Lee, Y. L.; Giordano, L.; Grimaud, A.; Johnson, A. M.; Hwang, J.; Crumlin, E. J.; Yang, W.; Shao-Horn, Y. Charge-Transfer-Energy-Dependent Oxygen Evolution Reaction Mechanisms for Perovskite Oxides. *Energy Environ. Sci.* **2017**, *10* (10), 2190–2200.
- (17) Surendranath, Y.; Kanan, M. W.; Nocera, D. G. Mechanistic Studies of the Oxygen Evolution Reaction by a Cobalt-Phosphate Catalyst at Neutral PH. *J. Am. Chem. Soc.* **2010**, *132* (46), 16501–16509.
- (18) Matheu, R.; Ertem, M. Z.; Gimbert-Suriñach, C.; Sala, X.; Llobet, A. Seven Coordinated

- Molecular Ruthenium–Water Oxidation Catalysts: A Coordination Chemistry Journey. *Chem. Rev.* **2019**, *119* (6), 3453–3471.
- (19) Matheu, R.; Ertem, M. Z.; Benet-Buchholz, J.; Coronado, E.; Batista, V. S.; Sala, X.; Llobet, A. Intramolecular Proton Transfer Boosts Water Oxidation Catalyzed by a Ru Complex. *J. Am. Chem. Soc.* **2015**, *137* (33), 10786–10795.
- (20) Richmond, C. J.; Matheu, R.; Poater, A.; Falivene, L.; Benet-Buchholz, J.; Sala, X.; Cavallo, L.; Llobet, A. Supramolecular Water Oxidation with Rubda-Based Catalysts. *Chem. - A Eur. J.* **2014**, *20* (52), 17282–17286.
- (21) Duan, L.; Bozoglian, F.; Mandal, S.; Stewart, B.; Privalov, T.; Llobet, A.; Sun, L. A Molecular Ruthenium Catalyst with Water-Oxidation Activity Comparable to That of Photosystem II. *Nat. Chem.* **2012**, *4* (5), 418–423.
- (22) Song, N.; Concepcion, J. J.; Binstead, R. A.; Rudd, J. A.; Vannucci, A. K.; Dares, C. J.; Coggins, M. K.; Meyer, T. J. Base-Enhanced Catalytic Water Oxidation by a Carboxylate–Bipyridine Ru(II) Complex. *Proc. Natl. Acad. Sci.* **2015**, *112* (16), 4935–4940.
- (23) Xie, Y.; Shaffer, D. W.; Lewandowska-Andralojc, A.; Szalda, D. J.; Concepcion, J. J. Water Oxidation by Ruthenium Complexes Incorporating Multifunctional Bipyridyl Diphosphonate Ligands. *Angew. Chemie - Int. Ed.* **2016**, *55* (28), 8067–8071.
- (24) Kamdar, J. M.; Marelius, D. C.; Moore, C. E.; Rheingold, A. L.; Smith, D. K.; Grotjahn, D. B. Ruthenium Complexes of 2,2'-Bipyridine-6,6'-Diphosphonate Ligands for Water Oxidation. *ChemCatChem* **2016**, *8* (19), 3045–3049.
- (25) Shaffer, D. W.; Xie, Y.; Szalda, D. J.; Concepcion, J. J. Lability and Basicity of Bipyridine-Carboxylate-Phosphonate Ligand Accelerate Single-Site Water Oxidation by Ruthenium-Based Molecular Catalysts. *J. Am. Chem. Soc.* **2017**, *139* (43), 15347–15355.
- (26) Surendranath, Y.; Dincă, M.; Nocera, D. G. Electrolyte-Dependent Electrosynthesis and Activity of Cobalt-Based Water Oxidation Catalysts. *J. Am. Chem. Soc.* **2009**, *131* (7), 2615–2620.
- (27) Matheu, R.; Ertem, M. Z.; Gimbert-Suriñach, C.; Benet-Buchholz, J.; Sala, X.; Llobet, A. Hydrogen Bonding Rescues Overpotential in Seven-Coordinated Ru Water Oxidation Catalysts. *ACS Catal.* **2017**, *7* (10), 6525–6532.
- (28) Zoń, J.; Garczarek, P.; Białek, M. Chapter 6 Synthesis of Phosphonic Acids and Their Esters as Possible Substrates for Reticular Chemistry. In *Metal Phosphonate Chemistry: From Synthesis to Applications*; Clearfield, A., Demadis, K., Eds.; The Royal Society of Chemistry, 2012; pp 170–191.
- (29) Hammes-Schiffer, S. Catalysts by Design: The Power of Theory. *Acc. Chem. Res.* **2017**, *50* (3), 561–566.
- (30) Meyer, T. J.; Sheridan, M. V.; Sherman, B. D. Mechanisms of Molecular Water Oxidation in Solution and on Oxide Surfaces. *Chem. Soc. Rev.* **2017**, *46* (20), 6148–6169.
- (31) Huynh, M. H. V.; Meyer, T. J. Proton-Coupled Electron Transfer. *Chem. Rev.* **2007**, *107* (11), 5004–5064.
- (32) Weinberg, D. R.; Gagliardi, C. J.; Hull, J. F.; Murphy, C. F.; Kent, C. A.; Westlake, B. C.; Paul, A.; Ess, D. H.; McCafferty, D. G.; Meyer, T. J. Proton-Coupled Electron Transfer. *Chem. Rev.* **2012**, *112* (7), 4016–4093.
- (33) Warren, J. J.; Tronic, T. A.; Mayer, J. M. Thermochemistry of Proton-Coupled Electron Transfer Reagents and Its Implications. *Chem. Rev.* **2010**, *110* (12), 6961–7001.
- (34) Shaffer, D. W.; Xie, Y.; Concepcion, J. J. O–O Bond Formation in Ruthenium-Catalyzed Water Oxidation: Single-Site Nucleophilic Attack: Vs. O–O Radical Coupling. *Chem. Soc. Rev.* **2017**, *46* (20), 6170–6193.
- (35) Hammes-Schiffer, S.; Soudackov, A. V. Proton-Coupled Electron Transfer in Solution, Proteins, and Electrochemistry. *J. Phys. Chem. B* **2008**, *112* (45), 14108–14123.
- (36) Laurent, F.; Plantalech, E.; Donnadiou, B.; Jiménez, A.; Hernández, F.; Martínez-Ripoll, M.; Biner, M.; Llobet, A. Synthesis, Structure and Redox Properties of Ruthenium Complexes

## CHAPTER 3.

- Containing the Tpm Facial and the Trpy Meridional Tridentate Ligands: Crystal Structures of [RuCl<sub>3</sub>(Trpy)] and [Ru(Tpm)(Py)<sub>3</sub>](PF<sub>6</sub>)<sub>2</sub>. *Polyhedron* **1999**, *18* (25), 3321–3331.
- (37) Albrecht-Schmitt, T.; Bujoli, B.; Cahill, C.; Murugavel, R.; Rocha, J.; Hix, G.; Shimizu, G.; Zubieta, J.; Zon, J.; Brunet, E.; Winpenny, R.; Wright, P. A.; Stock, N.; Mao, J. G.; Zheng, L.-M.; Clearfield, A.; Demadis, K. Metal Phosphonate Chemistry; The Royal Society of Chemistry, 2011; pp P001-655.
- (38) Kuppuraj, G.; Dudev, M.; Lim, C. Factors Governing Metal–Ligand Distances and Coordination Geometries of Metal Complexes. *J. Phys. Chem. B* **2009**, *113* (9), 2952–2960.
- (39) Zhao, Y.; Truhlar, D. G. The M06 Suite of Density Functionals for Main Group Thermochemistry, Thermochemical Kinetics, Noncovalent Interactions, Excited States, and Transition Elements: Two New Functionals and Systematic Testing of Four M06-Class Functionals and 12 Other Function. *Theor. Chem. Acc.* **2008**, *120* (1), 215–241.
- (40) Marenich, A. V.; Cramer, C. J.; Truhlar, D. G. Supporting Information ( PART I ) Universal Solvation Model Based on Solute Electron Density and on a Continuum Model of the Solvent Defined by the Bulk Dielectric Constant and Atomic Surface Tensions Contents : *J. Phys. Chem. B* **2009**, *113*, 6378.
- (41) Hoque, M. A.; Benet-Buchholz, J.; Llobet, A.; Gimbert-Suriñach, C. Catalytic Oxidation of Water to Dioxygen by Mononuclear Ru Complexes Bearing a 2,6-Pyridinedicarboxylato Ligand. *ChemSusChem* **2019**, *12* (9), 1949–1957.
- (42) Matheu, R.; Ertem, M. Z.; Pipelier, M.; Lebreton, J.; Dubreuil, D.; Benet-Buchholz, J.; Sala, X.; Tessier, A.; Llobet, A. The Role of Seven-Coordination in Ru-Catalyzed Water Oxidation. *ACS Catal.* **2018**, *8* (3), 2039–2048.
- (43) Matheu, R.; Ghaderian, A.; Francàs, L.; Chernev, P.; Ertem, M. Z.; Benet-Buchholz, J.; Batista, V. S.; Haumann, M.; Gimbert-Suriñach, C.; Sala, X.; Llobet, A. Behavior of Ru–Bda Water-Oxidation Catalysts in Low Oxidation States. *Chem. – A Eur. J.* **2018**, *24* (49), 12838–12847.
- (44) Brauman, J. I.; Bryson, J. A.; Kahl, D. C.; Nelson, N. J. Equilibrium Acidities in Dimethyl Sulfoxide. *J. Am. Chem. Soc.* **1970**, *92* (22), 6679–6680.
- (45) Nazeeruddin, M. K.; Zakeeruddin, S. M.; Humphry-Baker, R.; Kaden, T. A.; Grätzel, M. Determination of pKa Values of 4-Phosphonato-2,2':6',2''-Terpyridine and Its Ruthenium(II)-Based Photosensitizer by NMR, Potentiometric, and Spectrophotometric Methods. *Inorg. Chem.* **2000**, *39* (20), 4542–4547.
- (46) Ordóñez, M.; Viveros-Ceballos, J. L.; Sayago, F. J.; Cativiela, C. Stereoselective Synthesis of  $\alpha$ -Amino- H -Phosphinic Acids and Derivatives. *Synth.* **2017**, *49* (5), 987–997.
- (47) Becker, M.; Schindler, S.; Karlin, K. D.; Kaden, T. A.; Kaderli, S.; Palanché, T.; Zuberbühler, A. D. Intramolecular Ligand Hydroxylation: Mechanistic High-Pressure Studies on the Reaction of a Dinuclear Copper(I) Complex with Dioxygen. *Inorg. Chem.* **1999**, *38* (9), 1989–1995.
- (48) Costentin, C.; Drouet, S.; Robert, M.; Savéant, J.-M. Turnover Numbers, Turnover Frequencies, and Overpotential in Molecular Catalysis of Electrochemical Reactions. Cyclic Voltammetry and Preparative-Scale Electrolysis. *J. Am. Chem. Soc.* **2012**, *134* (27), 11235–11242.
- (49) Rountree, E. S.; McCarthy, B. D.; Eisenhart, T. T.; Dempsey, J. L. Evaluation of Homogeneous Electrocatalysts by Cyclic Voltammetry. *Inorg. Chem.* **2014**, *53* (19), 9983–10002.
- (50) Matheu, R.; Neudeck, S.; Meyer, F.; Sala, X.; Llobet, A. Foot of the Wave Analysis for Mechanistic Elucidation and Benchmarking Applications in Molecular Water Oxidation Catalysis. *ChemSusChem* **2016**, *9* (23), 3361–3369.
- (51) Wasylenko, D. J.; Ganesamoorthy, C.; Henderson, M. A.; Koivisto, B. D.; Osthoff, H. D.; Berlinguette, C. P. Electronic Modification of the [RuII(Tpy)(Bpy)(OH<sub>2</sub>)]<sup>2+</sup> Scaffold: Effects on Catalytic Water Oxidation. *J. Am. Chem. Soc.* **2010**, *132* (45), 16094–16106.
- (52) Zhao, Y.; Truhlar, D. G. A New Local Density Functional for Main-Group Thermochemistry, Transition Metal Bonding, Thermochemical Kinetics, and Noncovalent Interactions. *J. Chem. Phys.* **2006**, *125* (19), 194101.

## CHAPTER 3.

- (53) Zhan, S.; De Gracia Triviño, J. A.; Ahlquist, M. S. G. The Carboxylate Ligand as an Oxide Relay in Catalytic Water Oxidation. *J. Am. Chem. Soc.* **2019**, *141* (26), 10247–10252.
- (54) Wang, J. W.; Sahoo, P.; Lu, T. B. Reinvestigation of Water Oxidation Catalyzed by a Dinuclear Cobalt Polypyridine Complex: Identification of CoOx as a Real Heterogeneous Catalyst. *ACS Catal.* **2016**, *6* (8), 5062–5068.
- (55) Matheu, R.; Ertem, M. Z.; Gimbert-Suriñach, C.; Sala, X.; Llobet, A. Seven Coordinated Molecular Ruthenium-Water Oxidation Catalysts: A Coordination Chemistry Journey. *Chem. Rev.* **2019**, *119* (6), 3453–3471.
- (56) Moyer, B. A.; Thompson, M. S.; Meyer, T. J. Chemically Catalyzed Net Electrochemical Oxidation of Alcohols, Aldehydes, and Unsaturated Hydrocarbons Using the System (Trpy)(Bpy)Ru(OH<sub>2</sub>)<sup>2+</sup>/(Trpy)(Bpy)RuO<sup>2+</sup>. *J. Am. Chem. Soc.* **1980**, *102* (7), 2310–2312.
- (57) Wasylenko, D. J.; Ganesamoorthy, C.; Henderson, M. A.; Koivisto, B. D.; Osthoff, H. D.; Berlinguette, C. P. Supporting Information: Electronic Modification of the [Ru<sup>II</sup>(Tpy)(Bpy)(OH<sub>2</sub>)]<sup>2+</sup> Scaffold: Effects on Catalytic Water Oxidation. *J. Am. Chem. Soc.* **2010**, *132* (45), 16094–16106.
- (58) López, I.; Maji, S.; Benet-Buchholz, J.; Llobet, A. Oxo-Bridge Scenario behind Single-Site Water-Oxidation Catalysts. *Inorg. Chem.* **2015**, *54* (2), 658–666.
- (59) Takeuchi, K. J.; Thompson, M. S.; Pipes, D. W.; Meyer, T. J. Redox and Spectral Properties of Monooxo Polypyridyl Complexes of Ruthenium and Osmium in Aqueous Media. *Inorg. Chem.* **1984**, *23* (13), 1845–1851.

## CHAPTER 3.

### 3.5 Supporting Information

#### 3.5.1 Materials and Methods

##### 3.5.1.1 General considerations

Unless explicitly indicated all materials were provided by Sigma-Aldrich.  $[\text{Ru}(\text{DMSO})_4\text{Cl}_2]$  was synthesized and purified according to the literature.<sup>1</sup> High-purity deionized water was obtained by passing distilled water through a nanopure Milli-Q water purification system. Reactions were carried out under rigorously anhydrous conditions and with an argon stream or a positive pressure of argon. Automated flash chromatography was performed on the Teledyne Isco CombiFlash Rf flash chromatography purification system using SiliCycle silica gel columns (24 or 40 g, 230–400 mesh 40–63  $\mu\text{m}$ ).

##### 3.5.1.2 General instrumentations

*Electrospray ionization (ESI) mass spectrometry (MS)* experiments were performed on a Waters Micromass LCT Premier equipment.

*Low-resolution mass spectrometry (MS)* was recorded on a Thermo Finnigan DSQII quadrupolar spectrometer (coupled with a TracUltra GC apparatus) for Chemical Ionization (CI), on a Thermo Finnigan LCQ Advantage spectrometer for ElectroSpray Ionisation (ESI).

*High-resolution mass spectrometry (HRMS)* was recorded on a Thermo Finnigan MAT95XL spectrometer (for CI) and a ThermoFisher Scientific LTQ-Orbitrap spectrometer (for ESI).

*UV-Vis spectroscopy* was performed on a Cary 50 Bio (Varian) UV-Vis spectrophotometer with 1 cm quartz cells unless indicated.

*NMR Spectroscopy for ligands.*  $^1\text{H}$  and  $^{13}\text{C}$  NMR spectra were recorded on a *Bruker Avance 300* spectrometer fitted with a 5 mm i.d. BBO probe carefully tuned to the recording frequency of 300.13 MHz (for  $^1\text{H}$ ) and 75.47 MHz (for  $^{13}\text{C}$ ), the temperature of the probe was set at room temperature (around 293–294 K), on a *Bruker Avance 400* spectrometer fitted with a 5 mm i.d. BBFO+ probe carefully tuned to the recording frequency of 400.13 MHz (for  $^1\text{H}$ ) and 100.61 MHz (for  $^{13}\text{C}$ ). The spectra are referenced to the solvent in which they were run (7.26 ppm for  $^1\text{H}$   $\text{CDCl}_3$  and 77.16 ppm for  $^{13}\text{C}$   $\text{CDCl}_3$ , 2.5 ppm for  $^1\text{H}$  DMSO, and 39.52 ppm for  $^{13}\text{C}$  DMSO). Chemical shifts ( $\delta$ ) are given in ppm, coupling constants ( $J$ ) are given in Hz with the following splitting abbreviations: s = singlet, d = doublet, t = triplet,

q = quartet, qt = quintet, sx = sextuplet, sp = septuplet, m = massif and br = broad. All assignments were confirmed with the aid of two-dimensional  $^1\text{H}$ ,  $^1\text{H}$  (COSY), or  $^1\text{H}$ ,  $^{13}\text{C}$  (HSQC, HMBC) experiments using standard pulse programs.

*NMR Spectroscopy for Ru complexes.*  $^1\text{H}$  NMR,  $^{13}\text{C}$  NMR,  $^{31}\text{P}$  NMR, and  $^{15}\text{N}$  NMR spectra were recorded on a Bruker 400 MHz or a Bruker 500 MHz. Chemical shifts ( $\delta$ ) are reported in ppm and peak multiplicity is designated as s (singlet), d (doublet), t (triplet), m (multiplet), dd (doublet of doublets), dt (doublet of triplets), tt (triplet of triplets) and br (broad). All the collected spectra were referenced on residual solvent signal according to Nudelman et al.<sup>2</sup> Aqueous samples were recorded on an NMR spectrometer Bruker Avance 500 MHz spectrometer equipped with a Cryoprobe™ and denoted with a “\*” at the synthetic description. The pH of the solutions was determined by a pH meter (Mettler Toledo, SevenCompact™ pH/Ion) calibrated before measurements through standard solutions of pH's 4.01, 7.00, and 9.21.

III

#### 3.5.1.3 Preparation of 0.1 M ionic strength phosphate buffer (phbf) solutions.

- pH = 2.0: a solution of 7.2 mL of 85 wt. % aqueous  $\text{H}_3\text{PO}_4$  and 12.05 g of  $\text{NaH}_2\text{PO}_4$  were dissolved in deionized water up to 1 L solution.
- pH = 7.0: a sample of 1.96 g  $\text{NaH}_2\text{PO}_4$  and 3.99 g  $\text{Na}_2\text{HPO}_4$  were dissolved in deionized water up to 1 L solution.
- pH = 11.6: a sample of 0.78 g  $\text{Na}_2\text{HPO}_4$  and 2.06 g  $\text{Na}_3\text{PO}_4$  were dissolved in deionized water up to 1 L solution.
- pD = 7.0: a sample of 59 mg of  $\text{Na}_2\text{HPO}_4$  and 23 mg of  $\text{NaH}_2\text{PO}_4$  were dissolved in 10 mL of  $\text{D}_2\text{O}$ . Then the pD was adjusted to 7.0 with the addition of a 0.1 M NaOD solution in  $\text{D}_2\text{O}$ .

For NMR experiments, solutions of pD's between 2.0 and 12.0 (0.1 ionic strength) were prepared and adjusted to desirable pD with either 0.1 M NaOD or 0.1 M TfOD solutions in  $\text{D}_2\text{O}$ . The pD of the solutions was obtained by adding a 0.41 correction factor to the values measured by the glass pH-electrode.<sup>3</sup>

#### 3.5.1.4 Single Crystal X-Ray Methods

**Crystal preparation:** Crystals of  $2\text{PF}_6 \cdot 3\text{H}_2\text{O}$  were grown by counterion exchange crystallization from an acidic aqueous solution of  $2\text{Cl}$  and slow addition of a saturated

## CHAPTER 3.

solution of KPF<sub>6</sub>. Crystals of 4Cs<sub>3</sub>·8.5H<sub>2</sub>O·CH<sub>3</sub>OH were grown by counterion exchange crystallization from a methanol solution of 4<sup>2-</sup> and slow addition of a saturated solution of CsOH. The crystals used for structure determination were selected using a Zeiss stereomicroscope using polarized light and prepared under inert conditions immersed in perfluoropolyether as protecting oil for manipulation.

**Data collection:** Crystal structure determination for samples 2PF<sub>6</sub>·3H<sub>2</sub>O and 4Cs<sub>3</sub>·8.5H<sub>2</sub>O·CH<sub>3</sub>OH was carried out using an Apex DUO Kappa 4-axis goniometer equipped with an APEX 2 4K CCD area detector, a Microfocus Source E025 IuS using MoK<sub>α</sub> radiation, Quazar MX multilayer Optics as monochromator and an Oxford Cryosystems low-temperature device Cryostream 700 plus (*T* = -173 °C). Crystal structure determination for samples. Full-sphere data collection was used with  $\omega$  and  $\varphi$  scans. *Programs used:* Data collection APEX-2,<sup>4</sup> data reduction Bruker Saint<sup>5</sup> V/.60A and absorption correction SADABS.<sup>6</sup>

**Structure Solution and Refinement:** Crystal structure solution was achieved using the computer program SHELXT<sup>7</sup> Visualization was performed with the program SHELXle.<sup>8</sup> Missing atoms were subsequently located from difference Fourier synthesis and added to the atom list. Least-squares refinement on *F*<sup>2</sup> using all measured intensities was carried out using the program SHELXL 2015.<sup>9</sup> All non-hydrogen atoms were refined including anisotropic displacement parameters.

**Comments to the structures:** 2PF<sub>6</sub>·3H<sub>2</sub>O: The asymmetric unit contains one molecule of the Ruthenium metal complex, three water molecules, and one PF<sub>6</sub><sup>-</sup> anion. The water molecules and the -PO<sub>3</sub>H<sup>-</sup> / -PO<sub>3</sub>H<sub>2</sub> groups are interconnected making a network of hydrogen bonds. Between the -PO<sub>3</sub>H<sup>-</sup> and the -PO<sub>3</sub>H<sub>2</sub> groups is also an intramolecular hydrogen bond. All the hydrogen atoms attached to the -PO<sub>3</sub> group seem to be dynamic in their positions moving between the Oxygen atoms of the formed Hydrogen bond. The charge of the Ruthenium is +2. 4Cs<sub>3</sub>·8.5H<sub>2</sub>O·CH<sub>3</sub>OH: The asymmetric unit contains two molecules of the Ruthenium metal complex forming a dimer connected through a Cs cation. In total, it contains two metal complexes, six Cesium cations, 17 water molecules, and two methanol molecules.

The Cesium cations are partially highly disordered, so: Cs1 connecting the two metal complexes is not disordered; Cs2 is disordered in two positions (ratio 97:03); Cs3 is disordered in two positions (ratio 94:06); Cs4 is disordered in four positions (ratio:

43:15:31:11); Cs5 is disordered in four positions (ratio 54:9:13:24); Cs6 is not disordered. One of the  $\text{PO}_3^{2-}$  groups is disordered in two orientations (ratio: 77:23). One of the methanol molecules is disordered in two orientations (ratio 74:26). All Cesium cations are connected to water molecules. The water and methanol molecules are making a network of hydrogen bonds connecting with the  $\text{PO}_3^{2-}$  groups. The structure has an A-alert related to negative residual densities close to Cesium atoms. Errors due to missing twinning and/or wrongly assigned atoms could not be detected, so that these negative residual densities were assigned to the disorder of the heavy Cs-atoms and absorption correction problems. Additionally, there were also some B-alerts related to missing correlations between donor-acceptor and about forming a complete connected data set. These warnings were related to the high number of water molecules (17) in which is extremely difficult to localize correctly the positions of the hydrogen atoms.

CIF files for complexes  $2\text{PF}_6 \cdot 3\text{H}_2\text{O}$  and  $4\text{Cs}_3 \cdot 8.5\text{H}_2\text{O} \cdot \text{CH}_3\text{OH}$  with CCDC numbers 1890782 and 1954776, respectively, are available at <https://www.ccdc.cam.ac.uk/>.

#### 3.5.1.5 UV-Vis spectrophotometric acid-base titration<sup>10</sup>

A 0.1 mM pH 7 phbf solution of  $[\text{Ru}^{\text{II}}(\text{HtPa}-\kappa\text{-N}^3\text{O})(\text{py})_2]^-$ , **2**<sup>-</sup>, (dissolving **2**<sup>+</sup> in pH 7) was used as a stock solution. Then, 3 mL of this solution was placed in a 1 cm UV-Vis quartz cuvette, and the final pH was adjusted with either a solution of 0.1 M  $\text{H}_3\text{PO}_4$  or 0.1 M NaOH as needed.

#### 3.5.1.6 Electrochemical methods

##### General considerations

All electrochemical experiments were performed in an IJ-Cambria HI-730 bipotentiostat and IJ-Cambria CHI-660 potentiostat, using a three-electrode cell.  $E_{1/2}$  values reported in this work were estimated from Cyclic Voltammograms (CV) experiments as the average of the oxidative and reductive peak potentials  $(E_{p,o} + E_{p,c})/2$  or from DPV. A glassy carbon disk (GC) ( $\phi = 0.3$  cm,  $S = 0.07$  cm<sup>2</sup>) was used as working electrodes (WE), a Mercury/Mercurous sulfate ( $\text{K}_2\text{SO}_4$  sat) (MSE) as reference electrode (RE) (unless explicitly mentioned) and a Pt disk as counter electrode (CE). Working electrode pretreatment before each measurement consisted of polishing with 0.05  $\mu\text{m}$  alumina paste, rinsing after with water and acetone, and blow-dried finally. CVs and DPVs were  $iR$  compensated by the potentiostat in all the



## CHAPTER 3.

measurements unless indicated. CVs were recorded at 100 mV·s<sup>-1</sup> scan rate unless explicitly expressed. The DPV parameters were ΔE = 4 mV, Amplitude = 0.05 mV, Pulse width = 5 s, Sampling width = 0.0167 s, Pulse period = 5 s unless explicated. All redox potentials in the present work are reported versus NHE by adding 0.65 V to the measured potential.<sup>11</sup>

### Cells

A 15 mL vial was used as an electrochemical cell for CV measurements containing a homemade Teflon cap with holes to fit the three electrodes used. A two compartments cell (25 mL per compartment or 7 mL per compartment) separated with a glass frit was used for Bulk Electrolysis Experiments.

### Bulk electrolysis

A glassy carbon rod (S = 13.35 cm<sup>2</sup> or 9.35 cm<sup>2</sup>) was used as a WE, Pt grid as a CE, and a Hg/Hg<sub>2</sub>SO<sub>4</sub> (K<sub>2</sub>SO<sub>4</sub> saturated) as a RE.

### 3.5.2 Spectroelectrochemistry

Spectroelectrochemical studies were carried out in an optically transparent thin-layer electrochemical (OTTLE) cell (OMNI-CELL SPECAC, made by Prof. Frantisek Hartl, University of Reading) with a volume of approx. 0.3 mL and an optical path of 0.2 mm. This cell contains a Pt grid electrode, a Pt wire as a counter electrode, and a silver wire as a pseudo reference electrode. The OTTLE cell was connected to the SP-150 BioLogic potentiostat and the UV-Vis spectra were recorded using Varian Cary 50 Bio UV-Vis spectrometer. The cyclic voltammetry was typically recorded at 2 mV·s<sup>-1</sup>.

#### 3.5.2.1 Simulation of the Pourbaix diagram

The Pourbaix diagram for **2** was simulated<sup>12</sup> using equations S1 and S2.

$$E(\text{III}/\text{II}) = [E(\text{III}/\text{II})_{\text{pH}=0}] + \left( 0.05916 * \log \left( \frac{[\text{H}^+]^3 + [\text{H}^+]^2 K_{a1}^{\text{II}} + [\text{H}^+] K_{a1}^{\text{II}} K_{a2}^{\text{II}} + K_{a1}^{\text{II}} K_{a2}^{\text{II}} K_{a3}^{\text{II}}}{[\text{H}^+]^3 + [\text{H}^+]^2 K_{a1}^{\text{III}} + [\text{H}^+] K_{a1}^{\text{III}} K_{a2}^{\text{III}} + K_{a1}^{\text{III}} K_{a2}^{\text{III}} K_{a3}^{\text{III}}} \right) \right) \quad \text{S1}$$

$$E(\text{IV}/\text{III}) = [E(\text{IV}/\text{III})_{\text{pH}=0}] + \left( 0.05916 * \log \left( \frac{[\text{H}^+]^3 + [\text{H}^+]^2 K_{a1}^{\text{III}} + [\text{H}^+] K_{a1}^{\text{III}} K_{a2}^{\text{III}} + K_{a1}^{\text{III}} K_{a2}^{\text{III}} K_{a3}^{\text{III}}}{[\text{H}^+]^3 + [\text{H}^+]^2 K_{a1}^{\text{IV}} + [\text{H}^+] K_{a1}^{\text{IV}} K_{a2}^{\text{IV}} + K_{a1}^{\text{IV}} K_{a2}^{\text{IV}} K_{a3}^{\text{IV}}} \right) \right) \quad \text{S2}$$

This allows us to obtain the following pKa values:

$$E^\circ(\text{Ru}^{\text{III}}/\text{Ru}^{\text{II}}) = 0.95 \text{ V}$$

pKa<sup>1</sup>

pKa<sup>2</sup>

pKa<sup>3</sup>

$E^\circ(\text{Ru}^{\text{IV}}/\text{Ru}^{\text{III}}) = 1.28 \text{ V}$	0.1	3	11
	pKa <sup>1</sup>	pKa <sup>2</sup>	pKa <sup>3</sup>
	-0.4	2.2	6.3

### 3.5.2.2 Electrochemical O<sub>2</sub> evolution experiments

Controlled Potential Electrolysis (CPE) was carried out in a two-compartment cell (25 mL per compartment) separated with a glass frit and closed with septa. A solution of the catalyst was placed together with Ag/AgCl reference electrode (the observed potentials were converted to NHE by addition of 0.197 V) with a glassy carbon rod as a working electrode ( $S = 13.35 \text{ cm}^2$ ). A solution of pure electrolyte and Pt mesh auxiliary electrode were placed in the other compartment. Both compartments were vigorously stirred with a magnet during the CPE operation. The oxygen evolution was monitored with an OXNP type Clark electrode in the gas phase (from Unisense Company).

### 3.5.2.3 Kinetic analysis by FOWA and TON calculation

Kinetic analysis of the electrocatalytic currents was performed via Foot Of the Wave Analysis (FOWA).<sup>13,14</sup>

### 3.5.2.4 Computational Methods

**Density functional theory:** Geometry optimizations were performed at the M06 level of density functional theory<sup>15</sup> coupled with SMD aqueous continuum solvation model<sup>16</sup> using the Stuttgart [8s7p6d2f | 6s5p3d2f] ECP28MWB contracted pseudopotential basis set<sup>17</sup> on Ru and the 6-31G(d) basis set<sup>18</sup> on all other atoms. Non-analytical integral evaluations made use of a pruned grid having 99 radial shells and 590 angular points per shell as implemented in Gaussian 09 software package.<sup>19</sup> The nature of all stationary points was verified by analytic computation of vibrational frequencies, which were also used for the computation of zero-point vibrational energies, molecular partition functions, and for determining the reactants and products associated with each transition-state structure (by following the normal modes associated with imaginary frequencies). Partition functions were used in the computation of 298 K thermal contributions to free energy employing the usual ideal-gas, rigid-rotator, harmonic oscillator approximation.<sup>20</sup> Free energy contributions were added to single-point M06 electronic energies computed with SMD aqueous continuum solvation

## CHAPTER 3.

model and the SDD basis set on ruthenium and the 6-311+G(2df,p) basis set on all other atoms to arrive at final composite free energies.

Solvation and standard reduction potentials: As stated above, solvation effects associated with water as a solvent were accounted for using the SMD continuum solvation model. A 1 M standard state was used for all species in an aqueous solution except for water itself, for which a 55.6 M standard state was employed. Thus, for all molecules but water, the free energy in aqueous solution is computed as the 1 atm gas-phase free energy, plus an adjustment for the 1 atm to 1 M standard-state concentration change of  $RT \ln(24.5)$ , or 1.9 kcal/mol, plus the 1 M to 1 M transfer (solvation) free energy computed from the SMD model.<sup>20</sup> In the case of water, the 1 atm gas-phase free energy is adjusted by the sum of a 1 atm to 55.6 M standard-state concentration change, or 4.3 kcal/mol, and the experimental 1 M to 1 M solvation free energy,  $-6.3$  kcal/mol. The 1 M to 1 M solvation free energy of the proton was taken from the experiment as  $-265.9$  kcal/mol.<sup>21-24</sup>

Standard reduction potentials were calculated for various possible redox couples. For a redox reaction of the form



where  $O$  and  $R$  denote the oxidized and reduced states of the redox couple, respectively, and  $n$  is the number of electrons involved in a redox reaction, the reduction potential  $E_{O/R}^0$  relative to NHE was computed as

$$E_{O/R}^0 = -\frac{\Delta G_{O/R}^0 - \Delta G_{NHE}^0}{nF} \quad T2$$

where  $\Delta G_{O/R}^0$  is the free energy change associated with equation S7 (using Boltzmann statistics for the electron),  $\Delta G_{NHE}^0$  is the free energy change associated with



which is  $-4.28$  eV with Boltzmann statistics for the electron,<sup>25,26</sup> and  $F$  is the Faraday constant.

### 3.5.3 Synthetic Procedures and Analytical Data

#### 3.5.3.1 General considerations for the synthesis of the ligand *HatPa*

Solvents were purified and dried by standard methods before use. Dry dichloromethane was obtained by refluxing solvent on calcium hydride for an hour and distilled under argon or alternatively using the MB SPS-800-dry solvent system. Commercially available reagents were purchased from Sigma Aldrich and were used without purification. Glassware used for the reaction was either flame dried under vacuum or argon stream for several minutes. Reactions were carried out under rigorously anhydrous conditions and argon stream/positive pressure of argon. All reactions were monitored by TLC on commercially available pre-coated plates (Kieselgel 60 F254), and the compounds were visualized with KMnO<sub>4</sub> solution [KMnO<sub>4</sub> (3 g), K<sub>2</sub>CO<sub>3</sub> (20 g), NaOH (5% aq.; 5 mL), H<sub>2</sub>O (300 mL)] and heating or by UV (254 nm) when possible. Flash column chromatography was carried out using high purity grade (Merck grade 9385) pore size 60Å, 230-400 mesh particle size silica gel (Sigma Aldrich). Solvents used for chromatography were prior distilled on a Buchi Rotavapor R-220-SE.

#### 3.5.3.2 Synthesis of ligands and complexes

**2,2':6',2''-Terpyridine,1,1''-dioxide**<sup>27</sup>. To an ice-cooled solution of 2,2':6',2''-Terpyridine (391 mg, 1.67 mmol; 1 equiv) in 10 mL of dry DCM, was added metachloroperbenzoic acid (77%, 940 mg; 2.5 equiv.). After 30min of stirring at rt, precipitation occurred. After 3h of stirring, the TLC monitoring (DCM/MeOH : 95/5) showed partial conversion of the starting material and another excess of mCPBA (188 mg; 0.5 equiv) was added and the reaction mixture was kept stirring for an additional time of 6 hours. The reaction mixture was diluted with DCM (30mL) and was quenched by a solution of saturated solution (30 mL). The resulting organic phase was subsequently washed with 30 mL of NaCl saturated solution and was dried over MgSO<sub>4</sub>. After concentration under *vacuo*, the resulting crude was purified over silica gel by column chromatography (DCM/MeOH: 95/5, then 90/10) affording the expected 2,2':6',2''-terpyridine,1,1''-dioxide as a white solid (271 mg; 61% yield). m.p. 234°C. <sup>1</sup>H NMR (400 MHz, CDCl<sub>3</sub>) δ 8.93 (d, *J*=8.0 Hz, 2H); 8.41 (dd, *J*=6.5 Hz, *J*=0.8 Hz, 2H); 8.22 (dd, *J*=8.0 Hz, *J*=2.0 Hz, 2H); 8.00 (t, *J*=8.0 Hz, 1H); 7.44 (td, *J*=8.0 Hz, *J*=0.8 Hz, 2H); 7.34 (td, *J*=6.5 Hz, *J*=2.0 Hz, 2H). <sup>13</sup>C NMR (75 MHz, CDCl<sub>3</sub>) δ 149.2; 147.2; 140.8;

### CHAPTER 3.

136.8; 128.1; 126.8;126.4; 125.6. **HRMS m/z: calc for [M + H]<sup>+</sup>**: 266.0924. found m/z: 266.0919.

**Tetraethyl 2,2':6',2''-Terpyridine,6,6''-diphosphonate.** To a solution of 2,2':6',2''-Terpyridine,1,1''-dioxide (1.22 g; 4.6 mmol, 1 equiv.) in DCM (50 mL), was added ethyl chloroformate (1.31 mL; 13.7 mmol; 3 equiv.) giving rise to an insoluble mixture. After 10 min of stirring at rt, the reaction mixture became soluble and triethylphosphite (2.35 mL; 13.7 mmol; 3 equiv.) was added dropwise. After 12h of stirring at rt, the reaction mixture was diluted in DCM (50 mL) and was quenched by NaHCO<sub>3</sub> saturated solution (50 mL). The resulting aqueous layer was extracted twice with DCM (2\*50 mL). The combined organic phases were washed with NaCl saturated solution, were dried over Na<sub>2</sub>SO<sub>4</sub> and were concentrated under *vacuo*. The resulting crude was purified over silica gel by column chromatography (DCM/MeOH: 98/ 2 then 95/5) affording the expected tetraethyl 2,2':6',2''-terpyridine,6,6''-diphosphonate as a colorless liquid. (2.17 g; 93% yield). **<sup>1</sup>H NMR (400 MHz, CDCl<sub>3</sub>)** δ 8.67 (dt, *J*=7.0 Hz, 2H); 8.49 (d, *J*=7.8 Hz, 2H) ; 7.90 (m, 5H); 4.25 (m, 8H); 1.33 (t, *J*=7.1 Hz, 3H). **<sup>13</sup>C NMR (100.6 MHz, CDCl<sub>3</sub>)** δ 156.7 (d, *J*=22.6 Hz); 154.6; 151.7 (d, *J*=227.3 Hz); 138.1; 137.1 (d, *J*=12.2 Hz); 128.1 (d, *J*=25.2 Hz); 123.3; 122.0; 63.3; 16.5. **<sup>31</sup>P NMR (121.5 MHz, CDCl<sub>3</sub>)** δ 10.43. **HRMS m/z: calc for [M + H]<sup>+</sup>**: 506.1604. found m/z: 506.1604.

**2,2':6',2''-Terpyridine,6,6''-diphosphonic acid.** To a solution of tetraethyl 2,2':6',2''-terpyridine,6,6''-diphosphonate (638 mg, 1.26 mmol, 1 equiv.) in DCM (9 mL) was added TMSBr (1.5 mL, 11.37 mmol, 9 equiv.). After stirring at rt this yellow solution over 20h, the reaction mixture became insoluble and was concentrated under *vacuo*. The resulting yellow solid was diluted in MeOH (5 mL) and was stirred overnight. After removal of the volatiles under *vacuo*, the resulting powder was taken in a mixture (MeOH/Diethyl Ether : 1/4). After filtration on sintered funnel, the expected compound was isolated as a white solid (468 mg; 95% yield). Mp Decomposition > 330°C. **<sup>1</sup>H NMR (300 MHz, CDCl<sub>3</sub>)** δ 8.71 (d, *J*=8.0 Hz, 2H); 8.56 (d, *J* = 7.9 Hz, 2H), 8.22 (t, *J* = 7.9 Hz, 1H); 8.10 (dt, *J*=7.9 Hz, *J* = 4.9 Hz, 2H); 7.88 (t, *J* = 5.9 Hz, 2H). **<sup>13</sup>C NMR (100.6 MHz, CDCl<sub>3</sub>)** δ 156.1 (d, *J*=192.2 Hz); 155.0; 154.5; 138.5; 137.4

(d,  $J=11.1$  Hz); 126.4 (d,  $J=24.4$  Hz); 121.9; 121.4.  $^{31}\text{P}$  NMR (121.5 MHz,  $\text{CDCl}_3$ )  $\delta$  6.42. HRMS  $m/z$ : Calc for  $[\text{M} - \text{H}]^-$ : 392.0201, found  $m/z$ : 392.0209.

**$[\text{Ru}^{\text{II}}(\text{H}_3\text{tPa}-\kappa\text{-N}^3\text{O})(\text{py})]\text{Cl}$ , **2Cl**.** A sample of  $[\text{Ru}(\text{DMSO})_4\text{Cl}_2]$  (246.43 mg, 0.509 mmol), 2',2'':6',6''-terpyridine-6',6''-diphosphonic acid ( $\text{H}_4\text{tPa}$ ) (200 mg, 0.509 mmol) and  $\text{Et}_3\text{N}$  (0.5 mL) were dissolved in dry and degassed *n*-butanol (15 mL) and refluxed overnight. Afterwards pyridine (15 mL) was added and refluxed for 48 hours. A brown solution resulted that was cooled down to room temperature and then solvent reduced to dryness at low pressure. The resulting solid was treated by automated flash chromatography using a mixture of methanol: dichloromethane, 80:20 (V). The first fraction was isolated giving 140 mg of **2Cl** (0.19 mmol, 37 %).  $^1\text{H-NMR}$  (500Hz,  $[\text{d}_4]$  Methanol)  $\delta$  8.49 (d,  $J = 8.1$  Hz, 2H), 8.37 (d,  $J = 8.0$  Hz, 2H),  $\delta$  8.17 (br, 2H),  $\delta$  8.14 (dt,  $J = 5.2$  and 1.5Hz, 4H), 7.95 (br, 2H), 7.91 (t,  $J = 8.1$  Hz, 1H), 7.46 (t,  $J = 7.5$  Hz, 2H), 6.97 (t,  $J = 7.13$  and 7.13 Hz, 4H).  $^{13}\text{C-NMR}$  (101 Hz,  $[\text{d}_4]$  Methanol) 167.70, 165.83, 162.85, 159.60, 153.46, 137.47, 136.9, 132.50, 131.4, 125.62, 124.38.  $^{31}\text{P-NMR}$  (203 MHz\*,  $\text{D}_2\text{O}$ )  $\delta$  15.74 (2P,  $\alpha$  and  $\beta$ ) \*. Anal. Calc. for  $[\text{Ru}^{\text{II}}(\text{H}_3\text{tPa}-\kappa\text{-N}^3\text{O})(\text{py})_2]\text{Cl} \cdot 3\text{H}_2\text{O}$ , ( $\text{C}_{25}\text{H}_{28}\text{ClN}_5\text{O}_9\text{P}_2\text{Ru}$ ), C, 40.43 %; H, 3.67 %; N, 9.28%. Found C, 40.52 %; H, 3.81 %; N, 9.45 %. ESI<sup>-</sup>-HRMS  $m/z$ : calc. for  $2^-$  ( $\text{C}_{25}\text{H}_{21}\text{N}_5\text{O}_6\text{P}_2\text{Ru}^-$ ):  $m/z$  649.9965, found:  $m/z$  649.9951

**$[\text{Ru}^{\text{IV}}(\text{tPa}-\kappa\text{-N}^3\text{O}^2)(\text{py})_2]$ , **3**.** A solution of cerium ammonium nitrate ( $\text{Ce}^{4+}$ ) in  $\text{D}_2\text{O}$  (49.52 mM, 2.0 eq, 51  $\mu\text{L}$ ) was added to a solution of  $2^-$  ( $2^+$  in pH 7.0) in  $\text{D}_2\text{O}$  (2.57 mM, 0.5 mL) and the NMR measurements were performed.  $^1\text{H-NMR}$  (500Hz\*,  $\text{D}_2\text{O}$ )  $\delta$  8.93 (d,  $J = 7.9$  Hz, 2H), 8.79 (m, 3H), 8.61 (td,  $J = 7.6, 2.4$  Hz, 2H), 8.12 (t,  $J = 6.6$  Hz, 2H), 7.77 – 7.67 (m, 6H), 7.18 (t,  $J = 6.9$  Hz, 4H).  $^{13}\text{C-NMR}$  (126Hz\*,  $\text{D}_2\text{O}$ ) 163.54, 158.70, 151.77, 145.45, 140.80, 128.29, 128.12, 126.03  $^{31}\text{P-NMR}$  (203 MHz\*,  $\text{D}_2\text{O}$ )  $\delta$  29.87 (2P,  $\alpha$  and  $\beta$ )

**$[\text{Ru}^{\text{III}}(\text{tPaO}-\kappa\text{-N}^2\text{O}_2\text{P}_2\text{O})_2]^{2-}$ , **4** $^{2-}$ .** A sample of 5 mg of **2Cl** (0.008 mmol) was dissolved in 5 mL of a pH 7.6 phbf and placed in a bull electrolysis cell. A potential of 1.30 V was applied for 1 h. Then the pH was adjusted again to 7 and the potential was applied for 30 minutes more (see Figure S50) giving a green solution. Evaporation of the solvent to dryness gives a solid that contains  $4^{2-}$  and the initial phosphate salts.

## CHAPTER 3.

**$[Ru^{II}(tPaO-\kappa-N^2O_pOc)(py)_2]^{3-}$ ,  $4^{3-}$ .** All manipulations were carried out under Ar.

*Chemical synthesis.* The solid obtained in the previous synthesis was dissolved in 0.5 mL of  $D_2O$  and then an excess of sodium ascorbate (5 mg) was added.  **$^1H-NMR$  (500Hz,  $D_2O$ )**  $\delta$  9.08 (dd,  $J = 8.3$  Hz, 1H), 8.40 – 8.34 (m, 3H), 8.00 (m, 1H), 7.82 (m, 4H), 7.78 – 7.72 (m, 2H), 7.66 (m, 2H), 7.51 (m, 2H), 6.97 (m, 4H).  **$^{31}P-NMR$  (203Hz,  $D_2O$ )**  $\delta$  26.68 (1P,  $\alpha$ ), 10.16 (1P,  $\beta$ ).

*Electrochemical synthesis.* The solid obtained in the previous synthesis was placed in a bulk electrolysis cell and dissolved in 1 mL of  $D_2O$ . A potential of -0.1 V was applied for 150 minutes.  **$^1H-NMR$  (500Hz\*,  $D_2O$ )**  $\delta$  9.21 (d,  $J = 8.2$  Hz, 1H), 8.39 – 8.33 (m, 3H), 8.00 (t,  $J = 8.1$  Hz, 1H), 7.83 (m, 4H), 7.77 – 7.70 (m, 2H), 7.64 (m, 1H), 7.57 (m, 1H), 7.50 (m, 2H), 6.96 (m, 4H).

## III

3.5.4 Spectroscopic characterization of the compounds described in this work

3.5.4.1 Characterizations of the synthetic intermediates and the ligand H<sub>4</sub>Pa

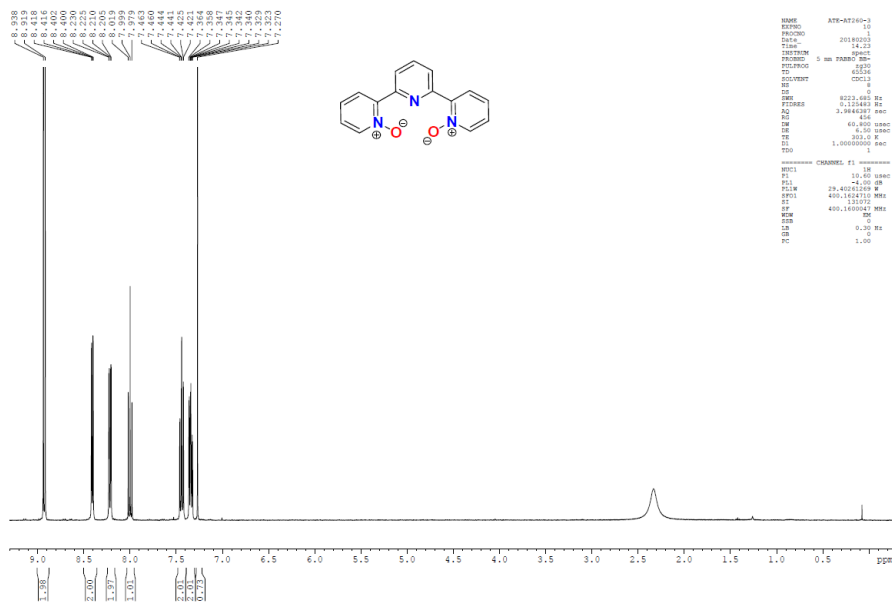


Figure S1. <sup>1</sup>H NMR of 2,2':6',2''-terpyridine,1,1''-dioxide in chloroform-d1 at RT.

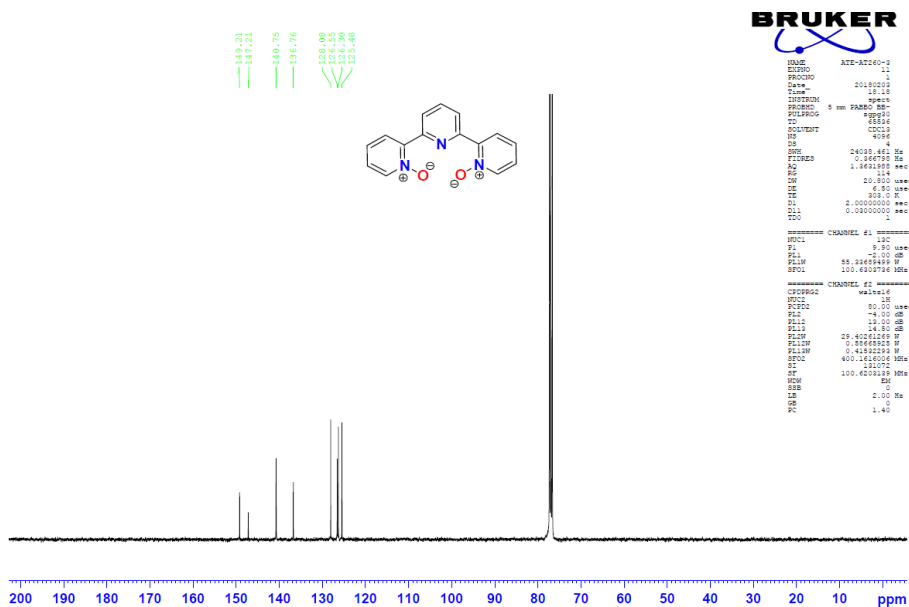


Figure S2. <sup>13</sup>C NMR of 2,2':6',2''-terpyridine,1,1''-dioxide in chloroform-d1 at RT.

III



CHAPTER 3.

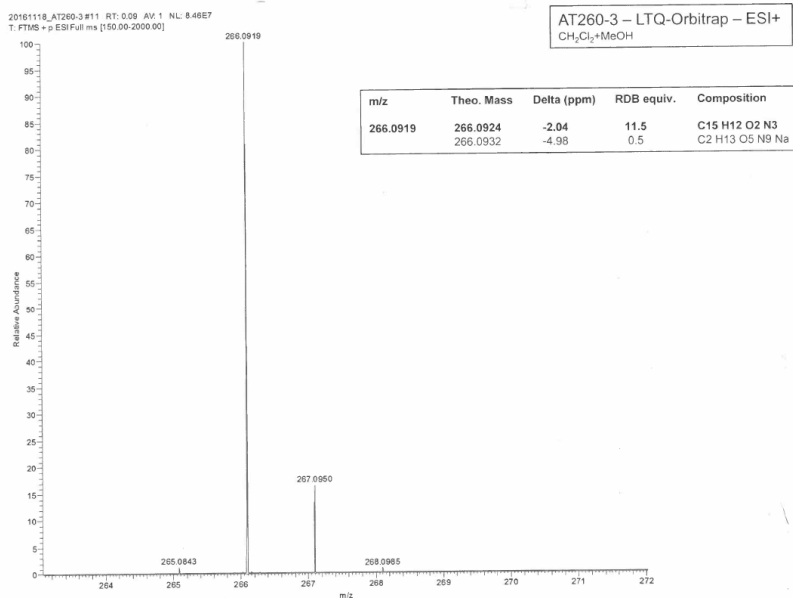


Figure S3: HR-MS for 2,2':6,2''-Terpyridine,1,1''-dioxide

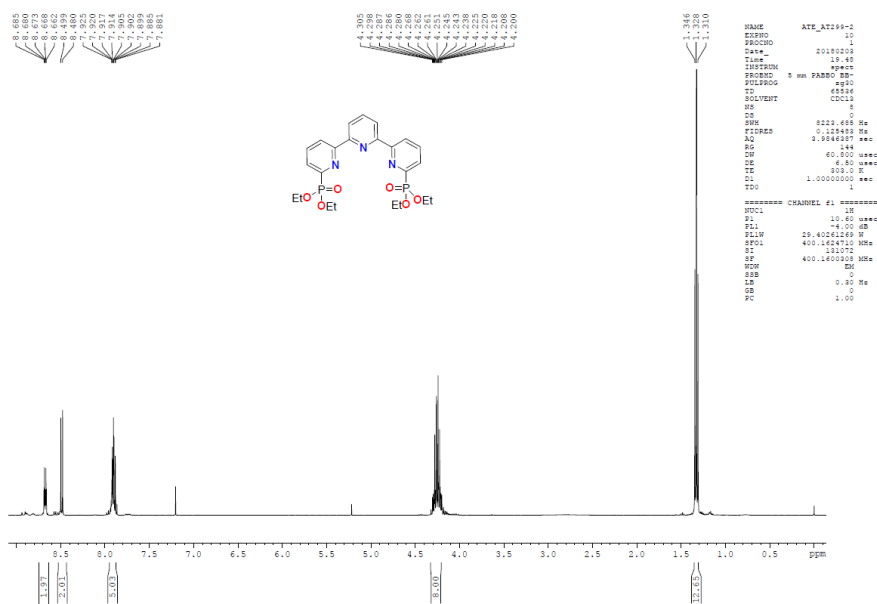
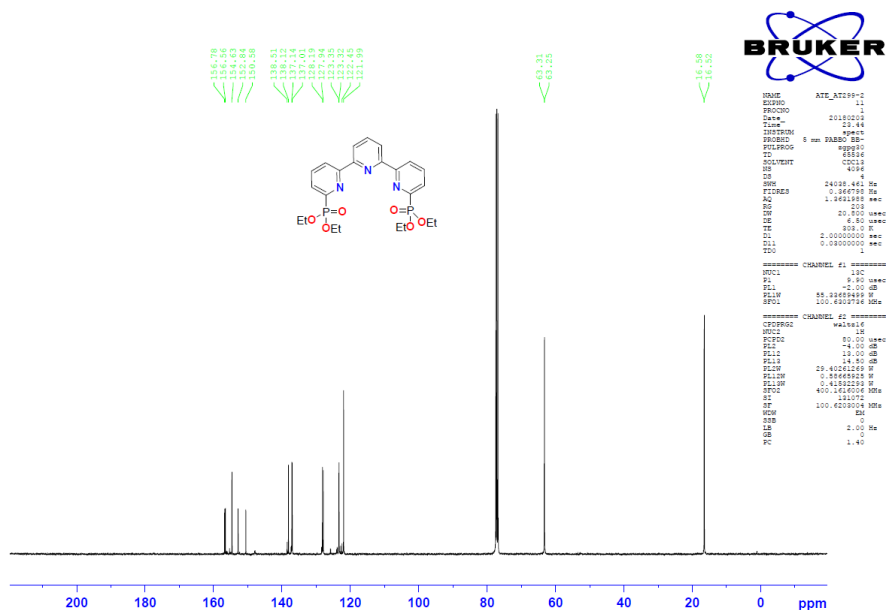
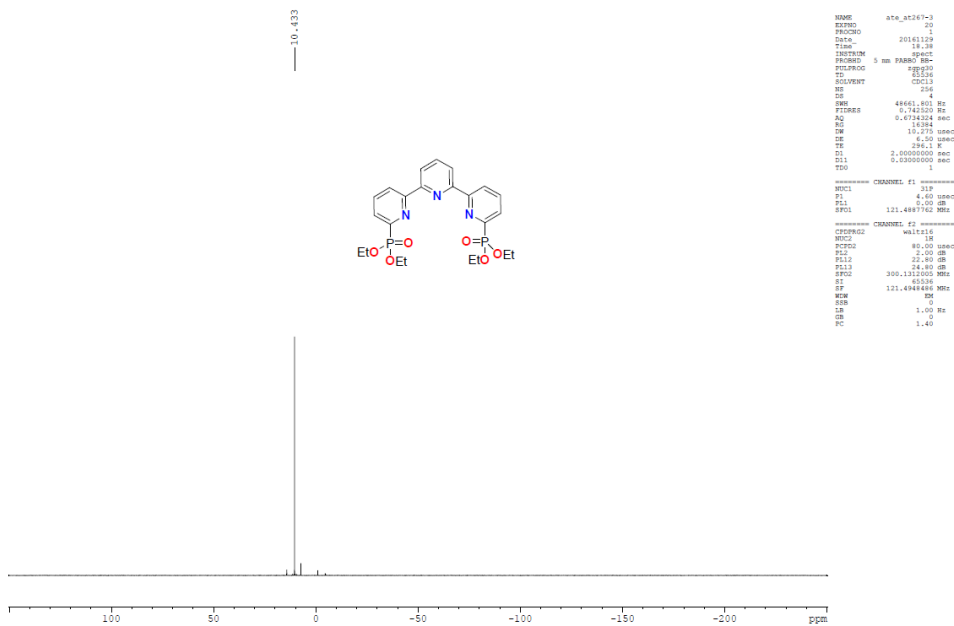


Figure S4. <sup>1</sup>H NMR of tetraethyl 2,2':6,2''-Terpyridine,6,6''-diphosphonate in chloroform-d1 at RT.

## CHAPTER 3.



**Figure S5.**  $^{13}\text{C}$  NMR of tetraethyl 2,2':6',2''-Terpyridine,6,6''-diphosphonate in chloroform-d<sub>1</sub> at RT.



**Figure S6.**  $^{31}\text{P}$  NMR of tetraethyl 2,2':6',2''-Terpyridine,6,6''-diphosphonate in chloroform-d<sub>1</sub> at RT.

III

### CHAPTER 3.

III

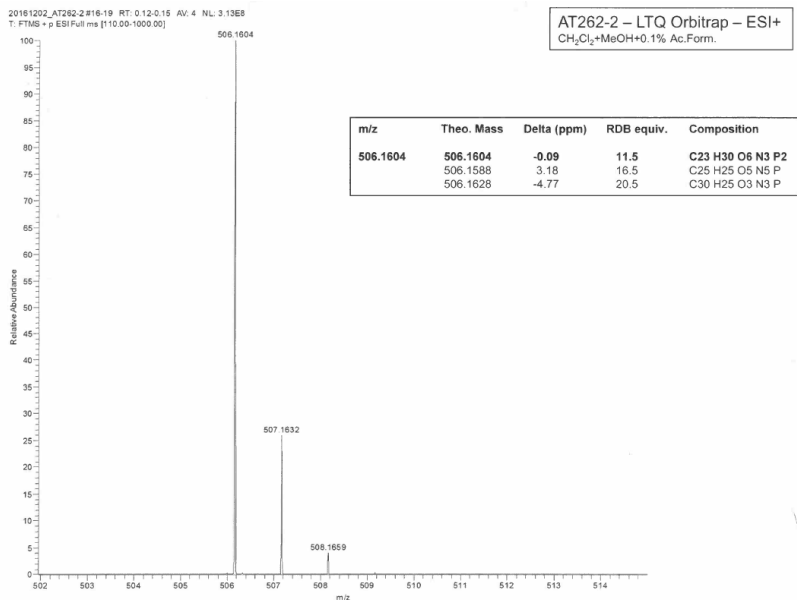


Figure S7: HR-MS for tetraethyl 2,2':6',2''-Terpyridine,6,6''-diphosphonate .

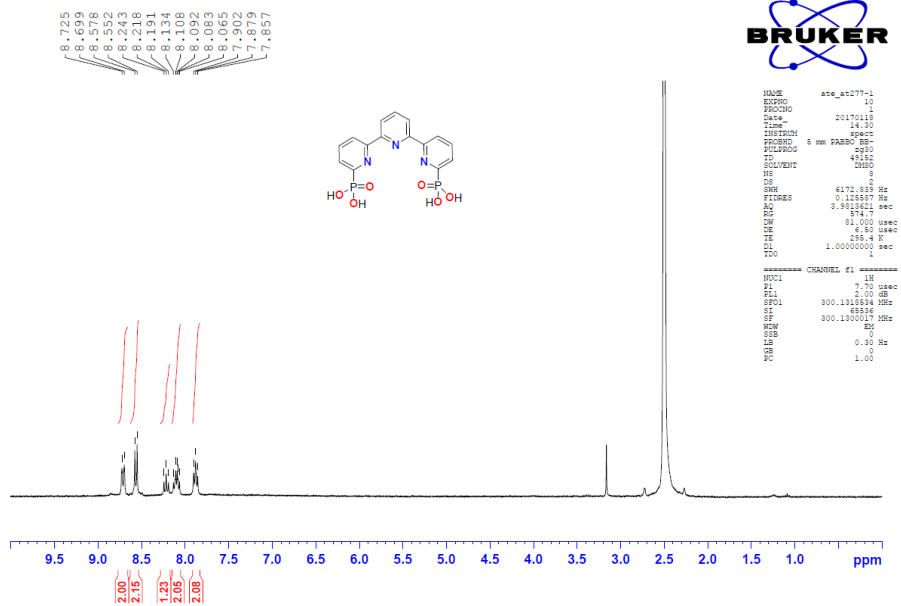


Figure S8. <sup>1</sup>H NMR of tetraethyl 2,2':6',2''-terpyridine,6,6''-diphosphonic acid in DMSO-d<sub>6</sub> at RT.

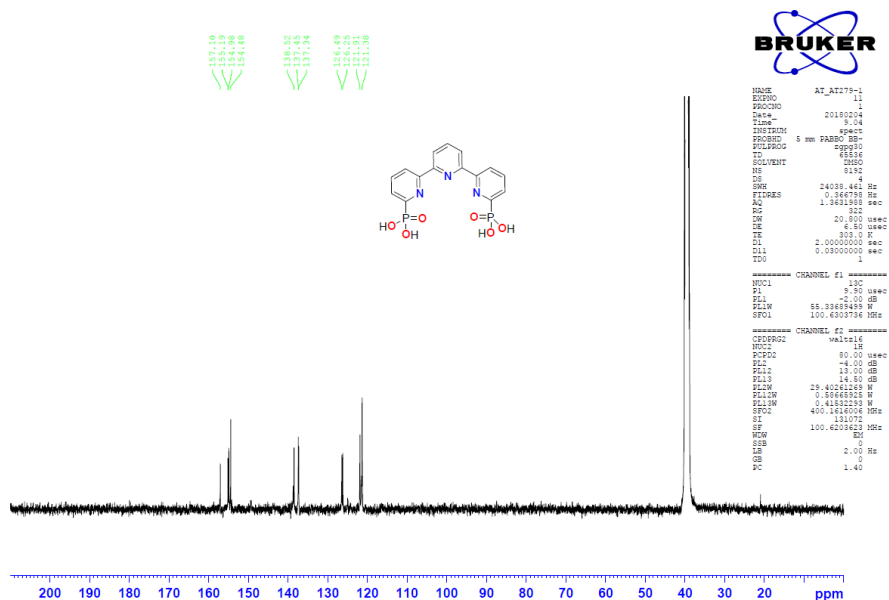


Figure S9. <sup>13</sup>C NMR of tetraethyl 2,2':6',2''-terpyridine,6,6''-diphosphonic acid in DMSO-d<sub>6</sub> at RT

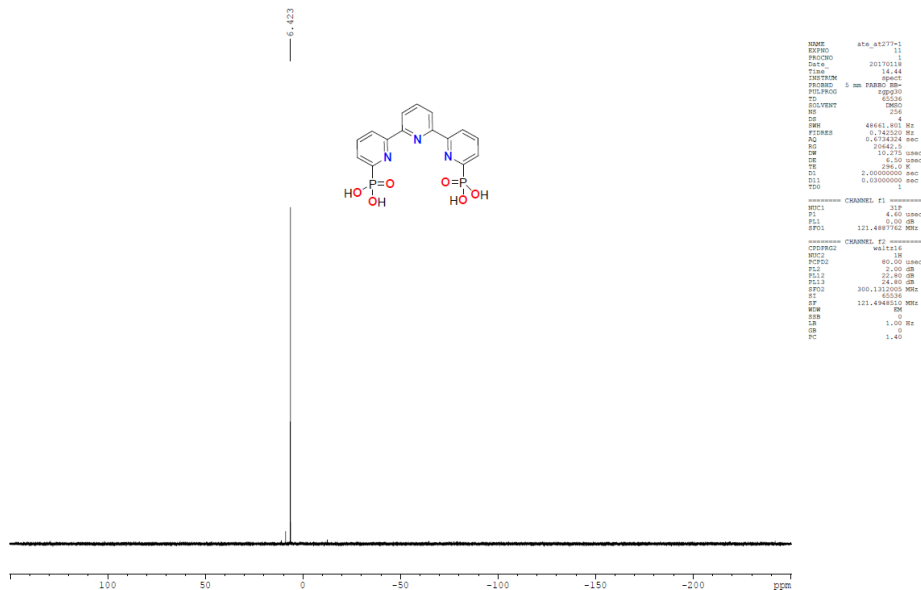


Figure S10. <sup>31</sup>P NMR of 2,2':6',2''-terpyridine,6,6''-diphosphonic acid in DMSO-d<sub>6</sub> at RT

## CHAPTER 3.

## Elemental Composition Report

Page 1

## Single Mass Analysis

Tolerance = 5.0 PPM / DBE: min = -1.5, max = 50.0

Element prediction: Off

Number of isotope peaks used for i-FIT = 4

## Monoisotopic Mass, Even Electron Ions

1178 formula(s) evaluated with 5 results within limits (up to 50 closest results for each mass)

## Elements Used:

C: 0-40 H: 0-100 N: 0-6 O: 0-10 Na: 0-1 P: 1-2

AT277-1 / DMSO/MeOH/H2O/NH4OH - H2O/MeOH/NH4OH (50/50/0.5) / ESI-

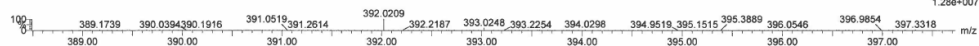
XEVO G2-XS QTOF

20170127\_AT277-1\_02 11 (0.242) AM2 (Ar,22000.0,0.00,0.00); Cm (11:14)

27-Jan-2017

1: TOF MS ES-

1.22e+007



Minimum: -1.5  
Maximum: 30.0 5.0 50.0

Mass	Calc. Mass	mDa	PPM	DBE	i-FIT	Norm	Conf(%)	Formula
392.0209	392.0201	0.8	2.0	18.5	1233.2	1.693	18.40	C20 H8 N3 O3 Na P
	392.0201	0.8	2.0	12.5	1233.2	1.643	19.35	C15 H12 N3 O6 P2
	392.0218	-0.9	-2.3	13.5	1232.3	0.738	47.83	C18 H13 N4 Na P2
	392.0219	-1.0	-2.6	9.5	1237.0	5.441	0.43	C8 H12 N5 O10 Na P
	392.0225	-1.6	-4.1	21.5	1233.5	1.967	13.99	C22 H7 N3 O3 P

Figure S11: HR-MS for 2,2':6,2''-terpyridine,6,6''-diphosphonic acid

3.5.4.2 Characterization of complex 2

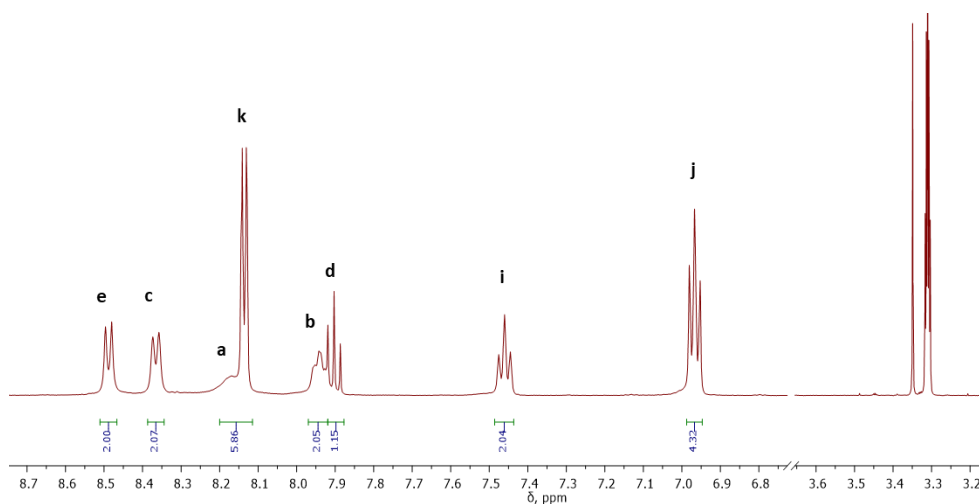


Figure S12.  $^1\text{H}$  NMR of 2 in methanol- $d_4$  at RT.

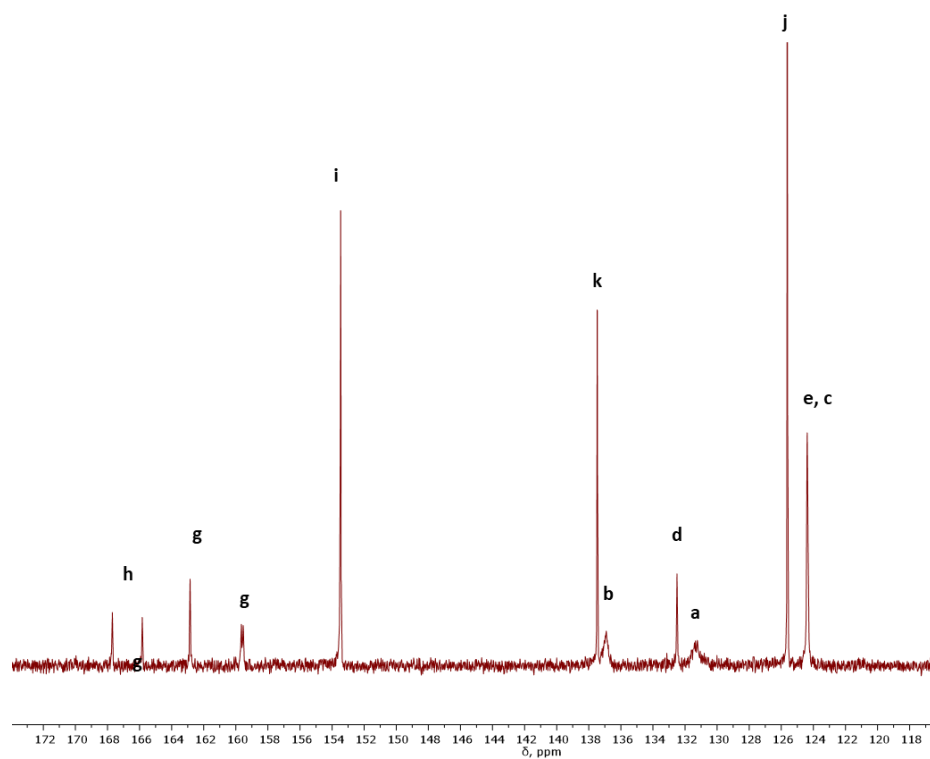


Figure S13:  $^{13}\text{C}$  NMR of 2 in methanol- $d_4$  at RT.

III

### CHAPTER 3.

III

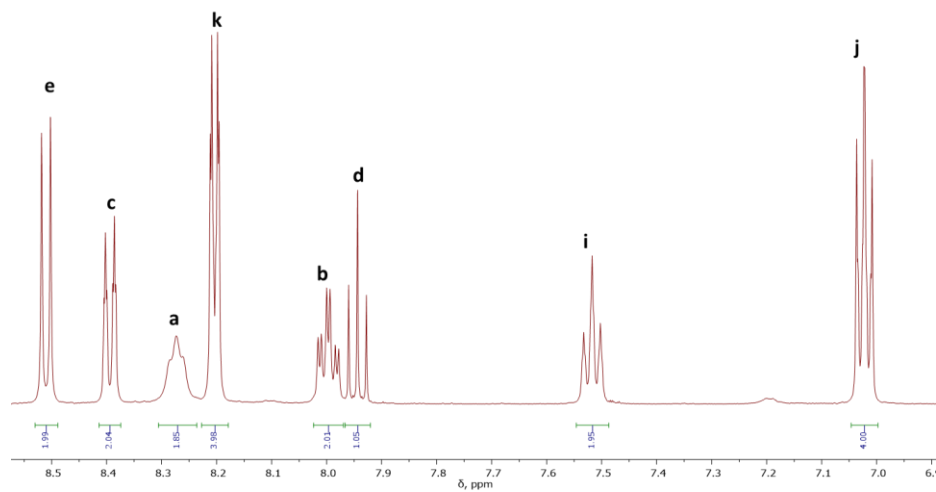


Figure S14.  $^1\text{H}$  NMR of **2** in methanol- $d_4$  at 333K.

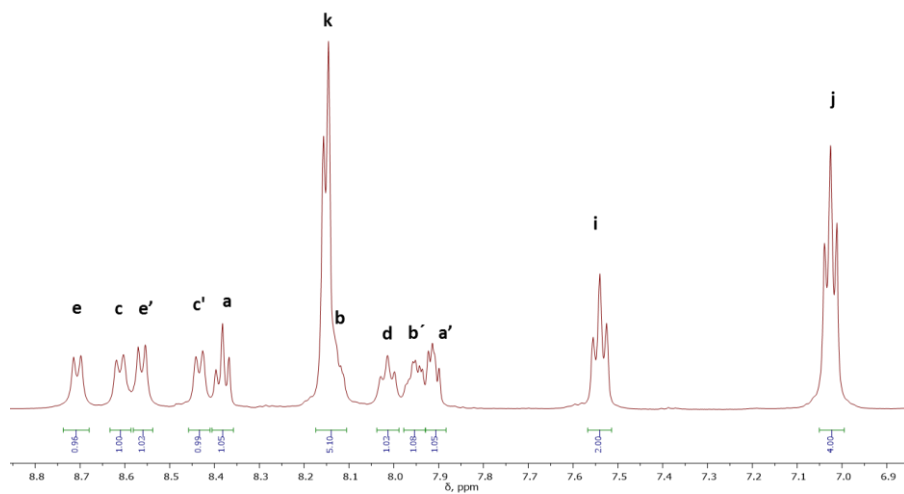


Figure S15.  $^1\text{H}$  NMR of **2** in methanol- $d_4$  at 193K

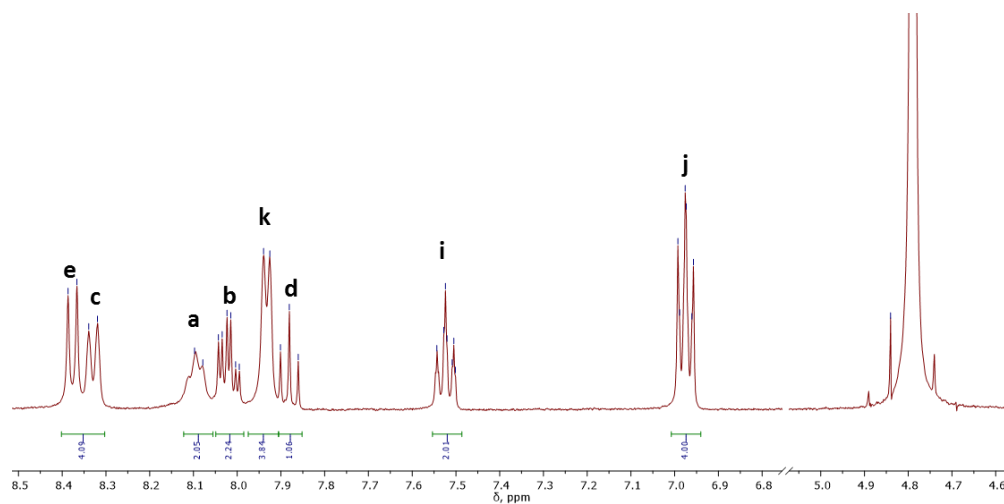


Figure S16.  $^1\text{H}$  NMR of **2** in  $\text{D}_2\text{O}$  at RT.

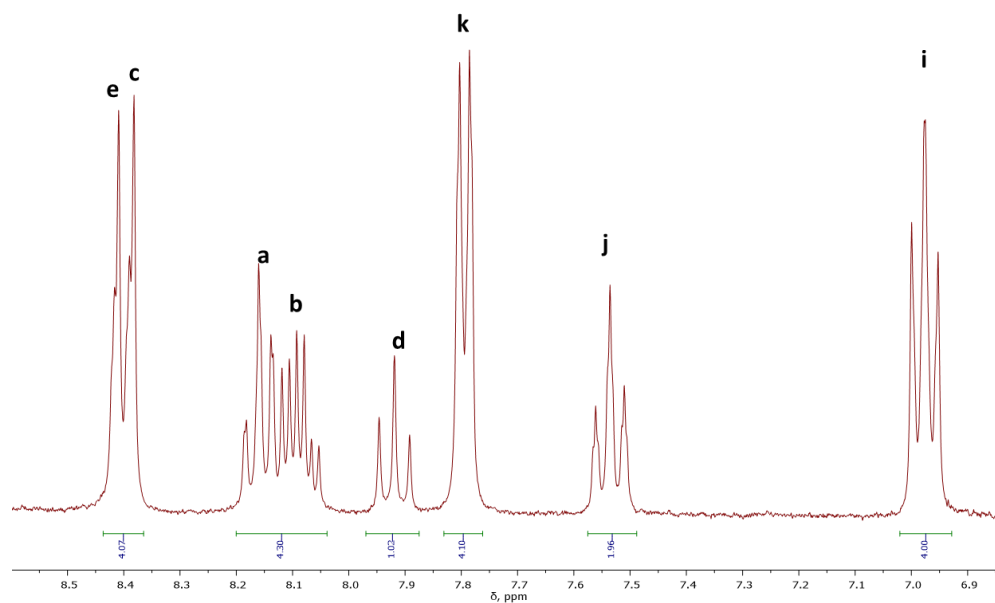


Figure S17.  $^1\text{H}$  NMR of **2** in pD 1 (0.1M  $[\text{d}_1]$ -triflic acid in  $\text{D}_2\text{O}$ ) at RT



### CHAPTER 3.

III

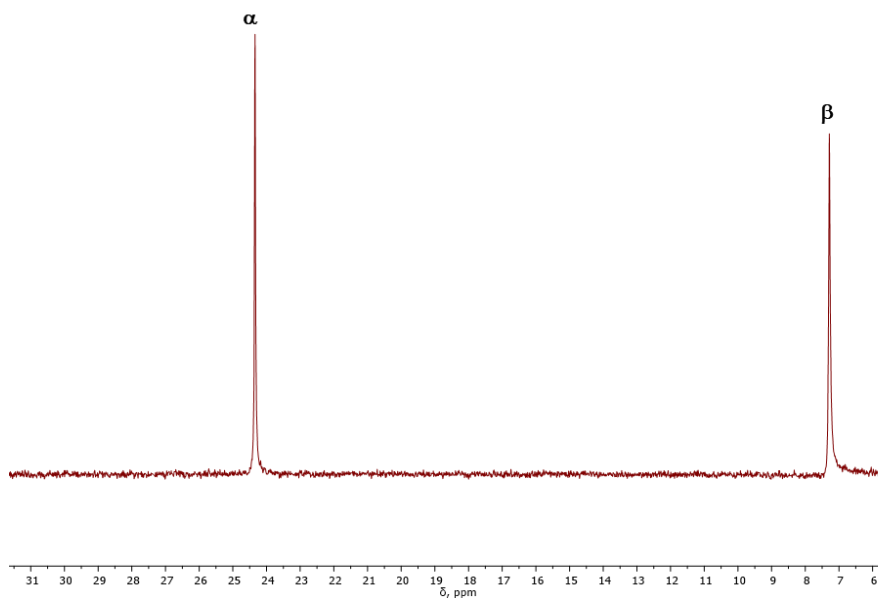


Figure S18.  $^{31}\text{P}$ -NMR of **2** in methanol- $d_4$  at 193K.

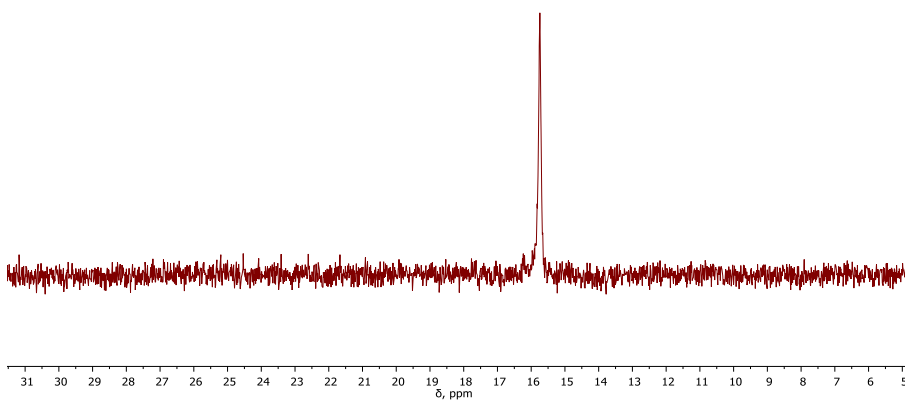


Figure S19.  $^{31}\text{P}$ -NMR of **2** in  $\text{D}_2\text{O}$  at RT

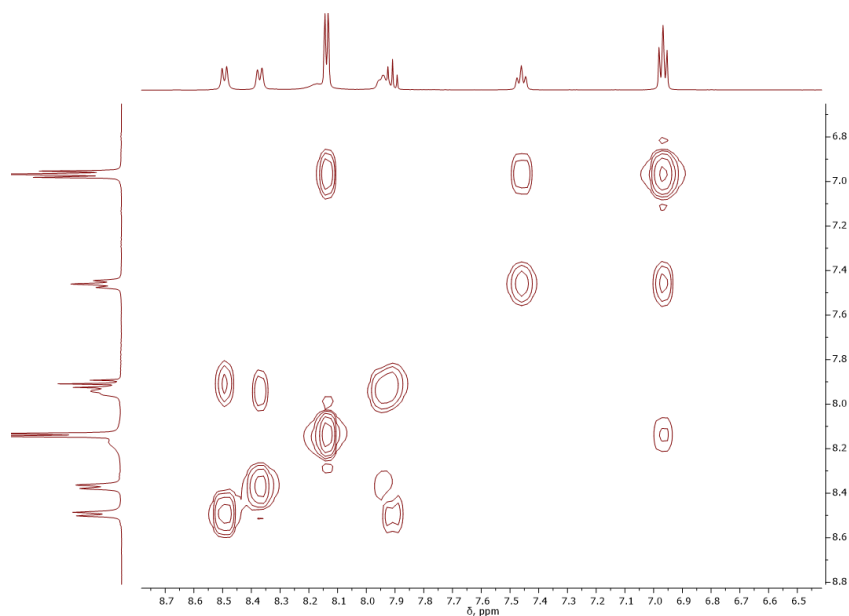


Figure S20.  $^1\text{H}$ - $^1\text{H}$  COSY NMR of **2** in methanol- $d_4$  at RT.

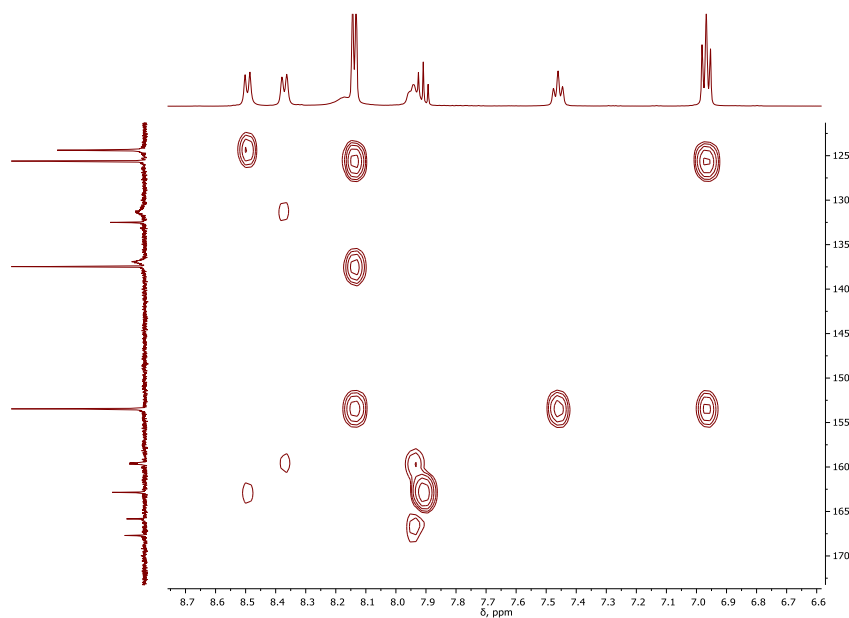


Figure S21.  $^1\text{H}$ - $^{13}\text{C}$  HMBC NMR of **2** in methanol- $d_4$  at RT.

### CHAPTER 3.

III

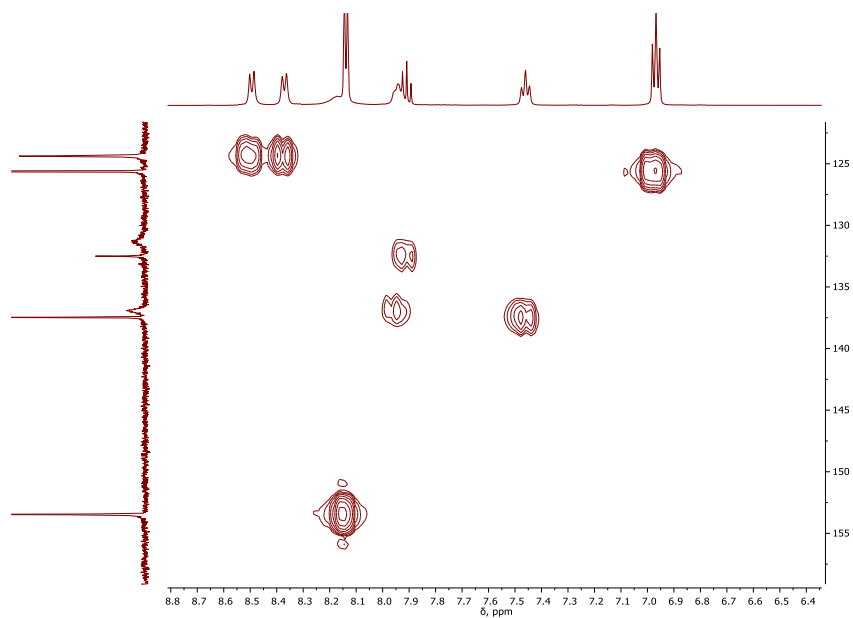


Figure S22.  $^1\text{H}$ - $^{13}\text{C}$  HSQC NMR of **2** in methanol- $\text{d}_4$  at RT.

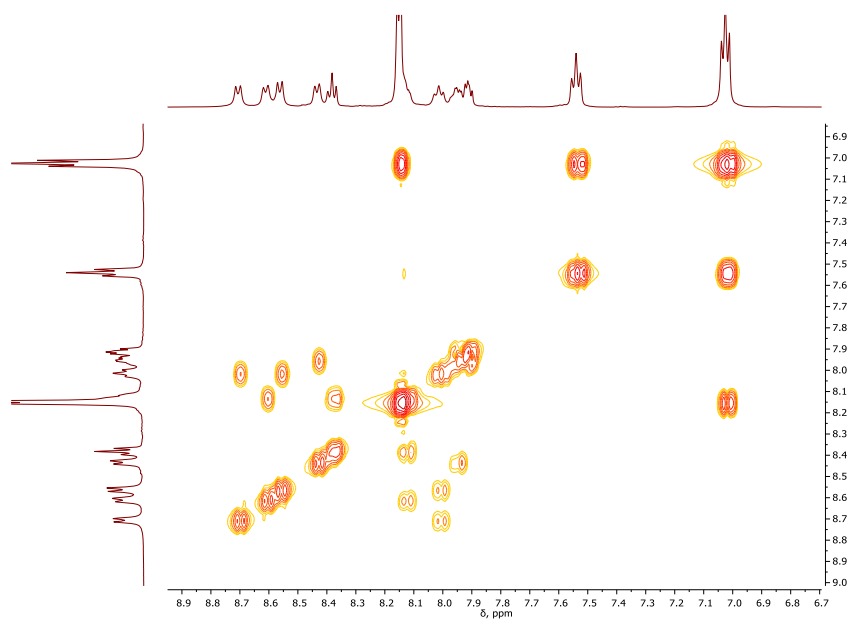


Figure S23.  $^1\text{H}$ - $^1\text{H}$  COSY NMR of **2** in methanol- $\text{d}_4$  at 193 K.

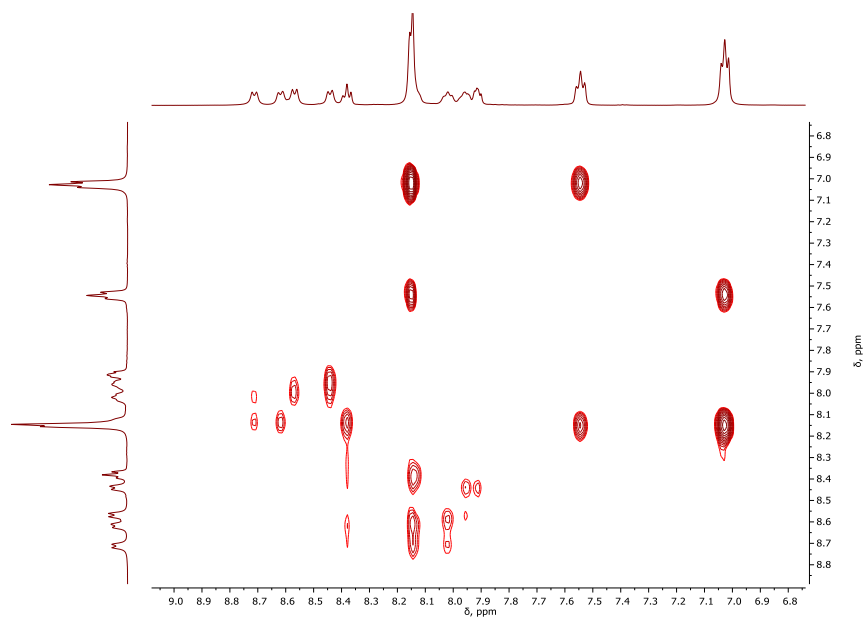


Figure S24.  $^1\text{H}$ - $^1\text{H}$  NOESY NMR of **2** in methanol- $d_4$  at 193 K.

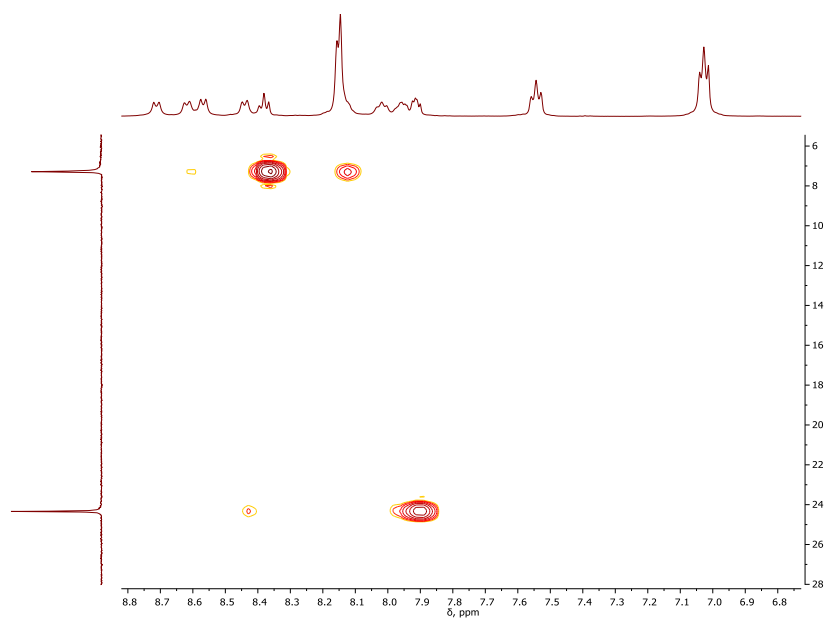


Figure S25.  $^1\text{H}$ - $^{31}\text{P}$  HMBC NMR of **2** in methanol- $d_4$  at 193 K.

### CHAPTER 3.

III

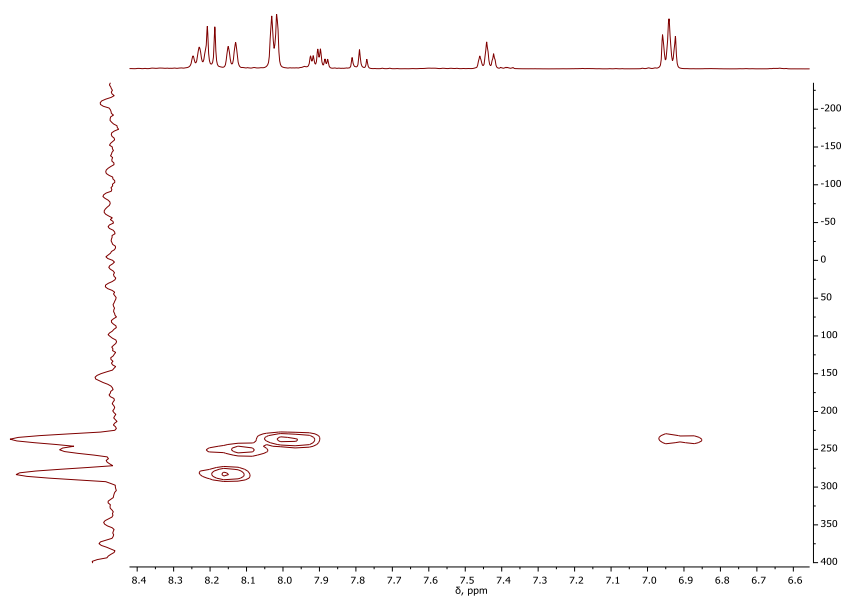


Figure S26.  $^1\text{H}$ - $^{15}\text{N}$  HMBC NMR of **2** in  $[\text{d}_4]$ -trifluoroethanol at RT

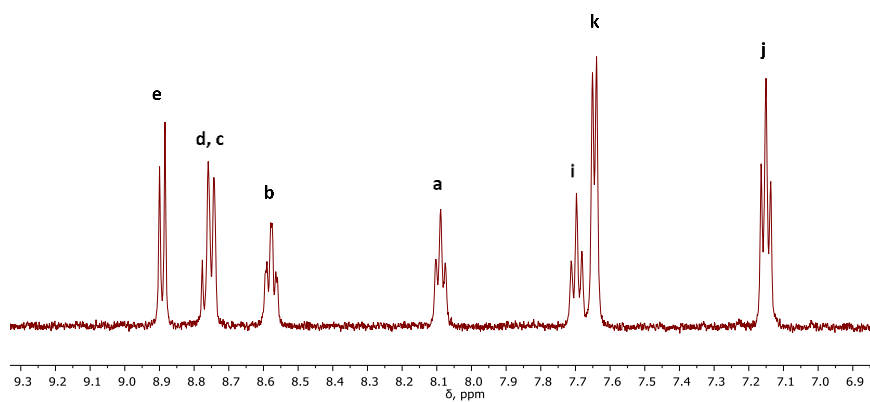


Figure S27.  $^1\text{H}$  NMR of **3** in  $\text{D}_2\text{O}$  at RT after addition of 2 eq. of  $\text{Ce}^{4+}$

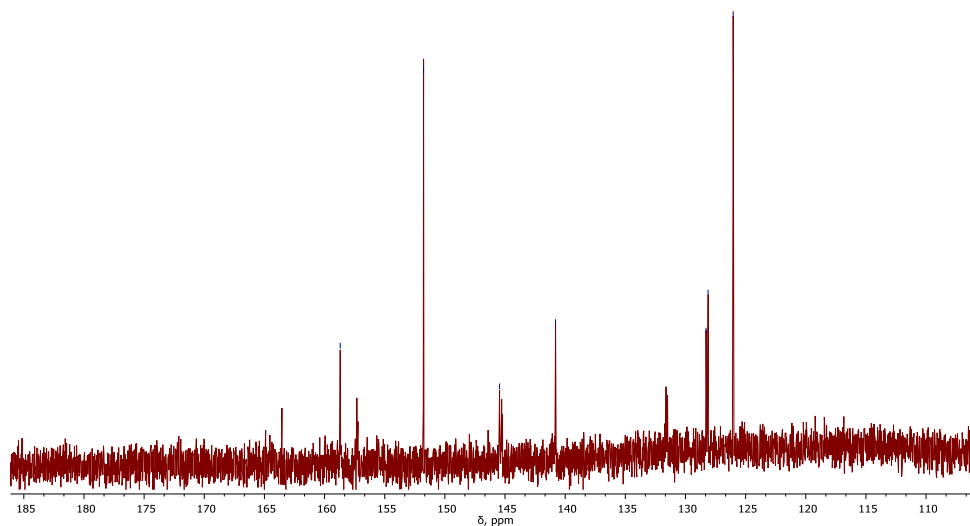


Figure S28.  $^{13}\text{C}$ -NMR of **3** in  $\text{D}_2\text{O}$  at RT after addition of 2 eq. of  $\text{Ce}^{4+}$

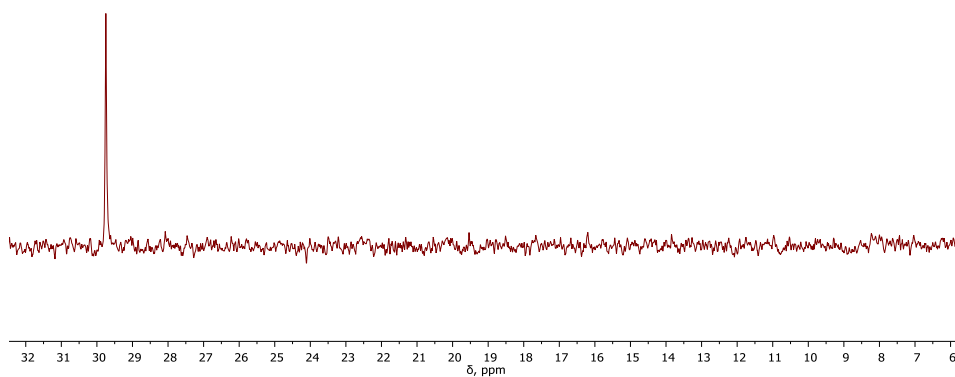


Figure S29.  $^{31}\text{P}$ -NMR of **3** in  $\text{D}_2\text{O}$  at RT after addition of 2 eq. of  $\text{Ce}^{4+}$

### CHAPTER 3.

III

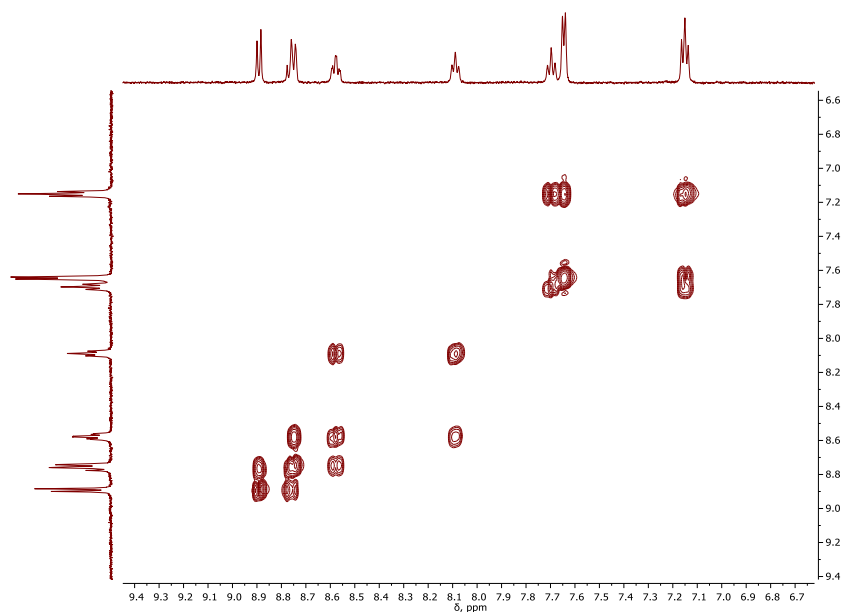


Figure S30.  $^1\text{H}$ - $^1\text{H}$  COSY NMR **3** in  $\text{D}_2\text{O}$  at RT after the addition of 2 eq. of  $\text{Ce}^{4+}$ .

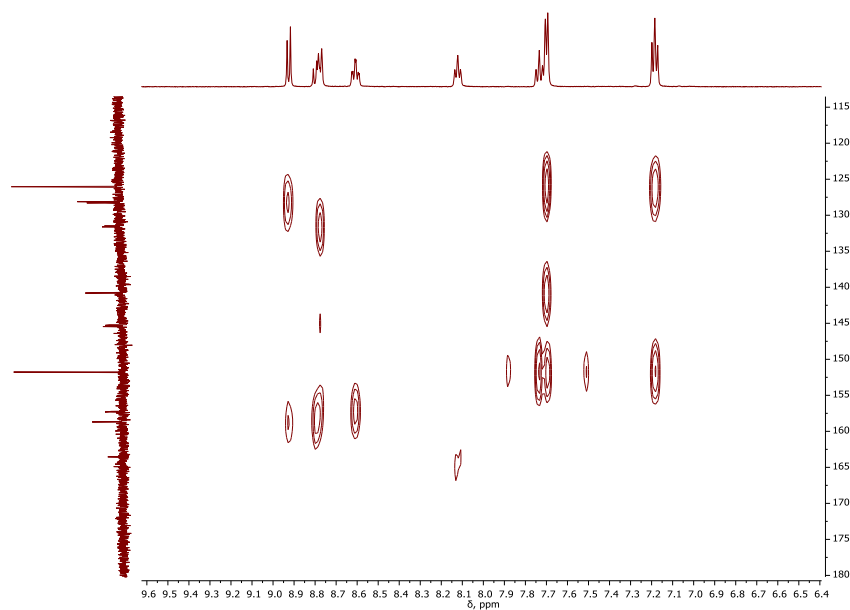


Figure S31.  $^1\text{H}$ - $^{13}\text{C}$  HMBC NMR of **3** in  $\text{D}_2\text{O}$  at RT after the addition of 2 eq. of  $\text{Ce}^{4+}$ .

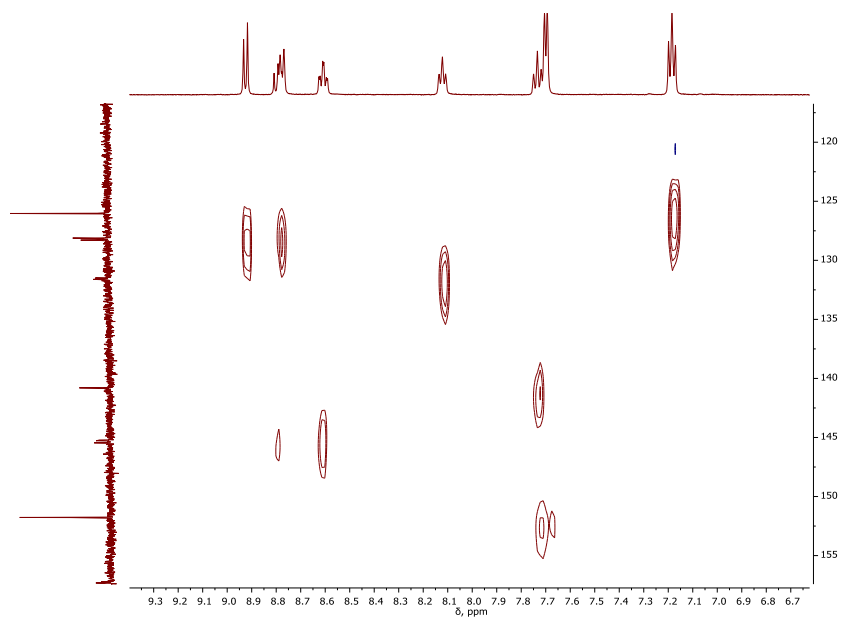


Figure S32.  $^1\text{H}$ - $^{13}\text{C}$  HSQC NMR of **3** in  $\text{D}_2\text{O}$  at RT after the addition of 2 eq. of  $\text{Ce}^{4+}$ .

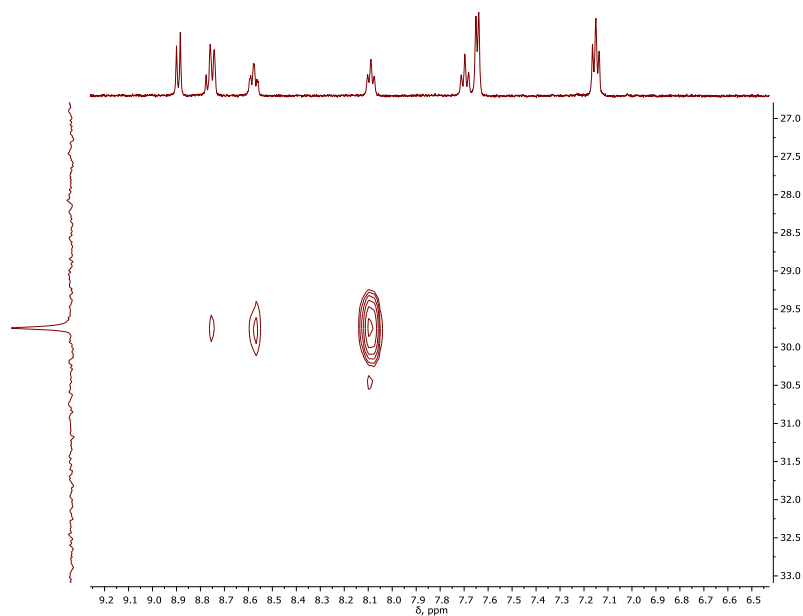


Figure S33.  $^1\text{H}$ - $^{31}\text{P}$  HMBC NMR of **3** in  $\text{D}_2\text{O}$  at RT after the addition of 2 eq. of  $\text{Ce}^{4+}$ .

III



## CHAPTER 3.

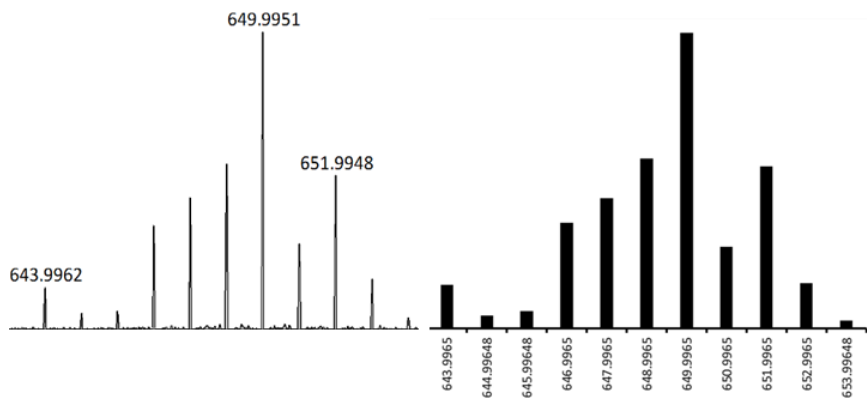
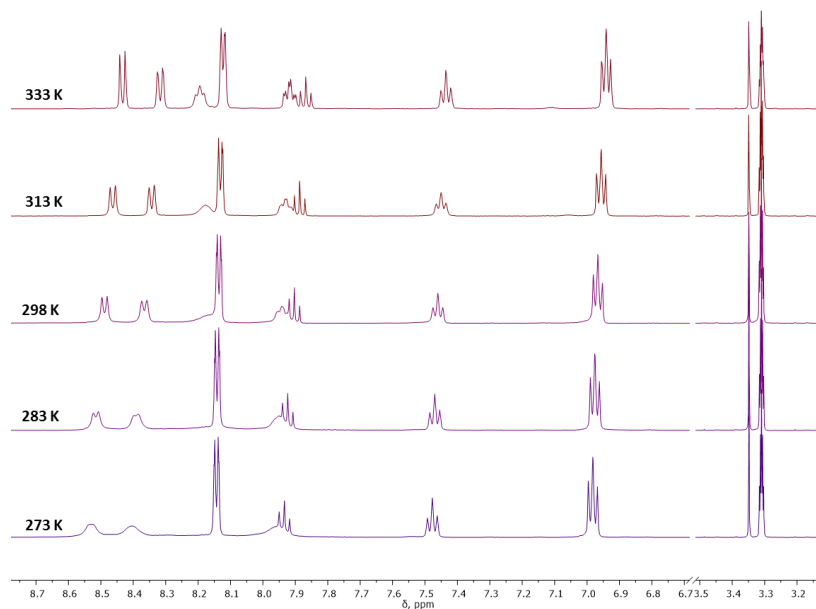


Figure S34. HR-MS for  $2^-$  (0.5 ppm error) (left) and simulated (right).

3.5.4.3 Dynamic behavior of **2**.



III

Figure S35.  $^1\text{H}$ -NMR of **2** in methanol- $\text{d}_4$  at different temperatures (high temperatures)

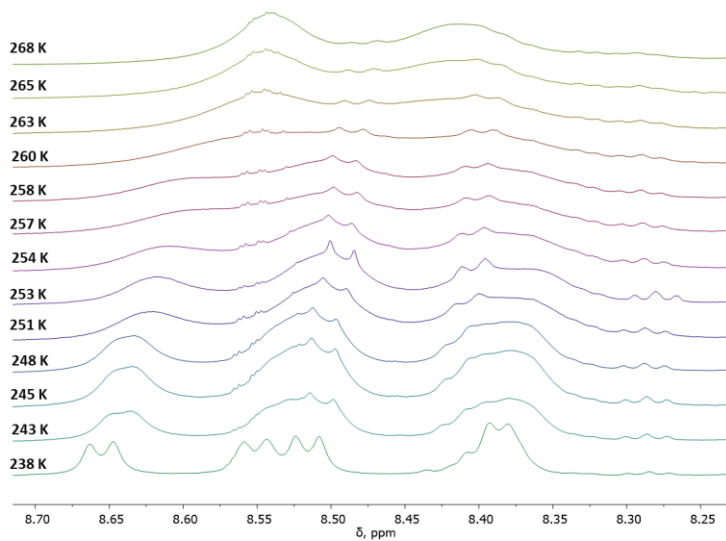
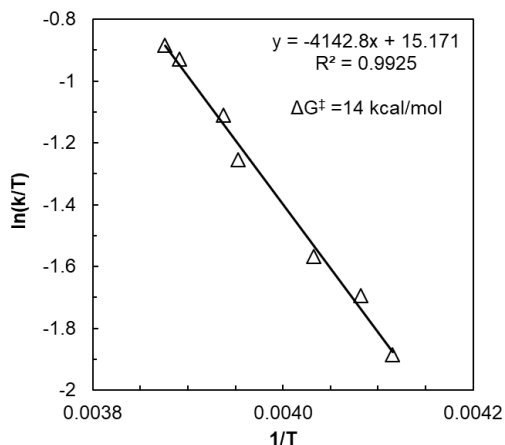
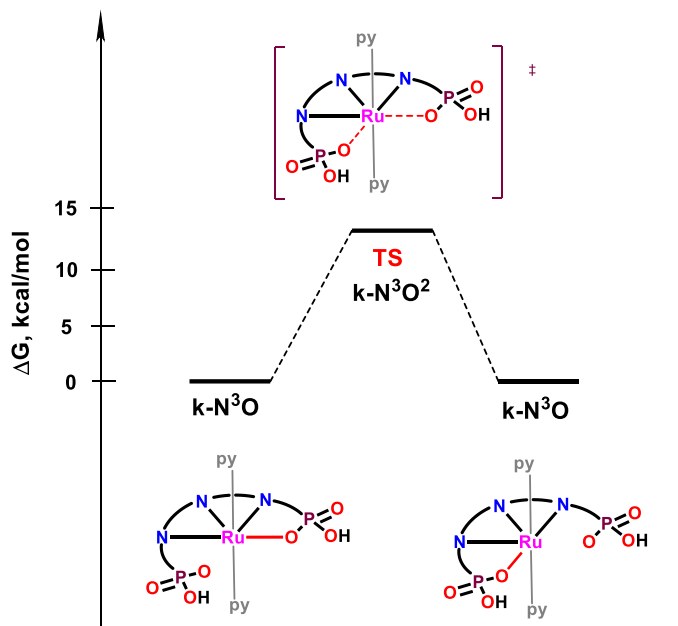


Figure S36.  $^1\text{H}$  NMR of **2** in methanol- $\text{d}_4$  in the region of the Hc and He resonances at different temperatures.

CHAPTER 3.



**Figure S37:** Experimental estimation of the  $\Delta G^\ddagger$  of **2** from VT-NMR. Eyring plot of the kinetic constant at different temperatures. The kinetic constant ( $k$ ) at each temperature was estimated by applying the formula  $k = \frac{\pi}{\sqrt{2}} \sqrt{(\delta v_o)^2 - \delta v_d^2}$  at temperatures 268 K to 238 K



**Scheme S1:** Linkage Isomerization equilibria at RT for  $[\text{Ru}^{\text{II}}(\text{H}_2\text{tPa-}\kappa\text{-N}^3\text{O})(\text{py})_2]$ , **2** involving the formation and breaking of Ru-O bonds. The  $\text{H}_2\text{tPa}^{2-}$  ligand is represented with arcs connecting the N of the pyridyl moieties and the phosphonate groups.

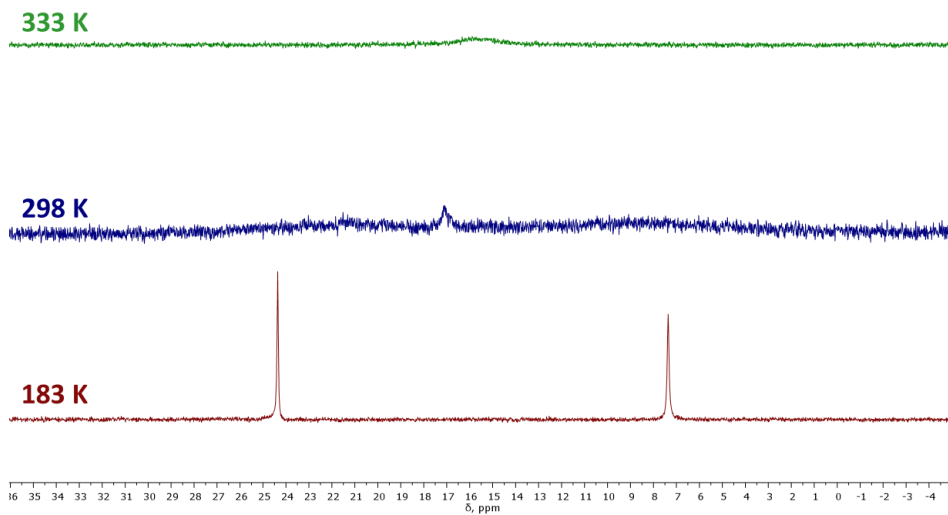


Figure S38.  $^{31}\text{P}$ -NMR of **2** in methanol- $\text{d}_4$  at different temperatures

## CHAPTER 3.

### 3.5.4.4 NMR characterization of complex $4^{3-}$

III

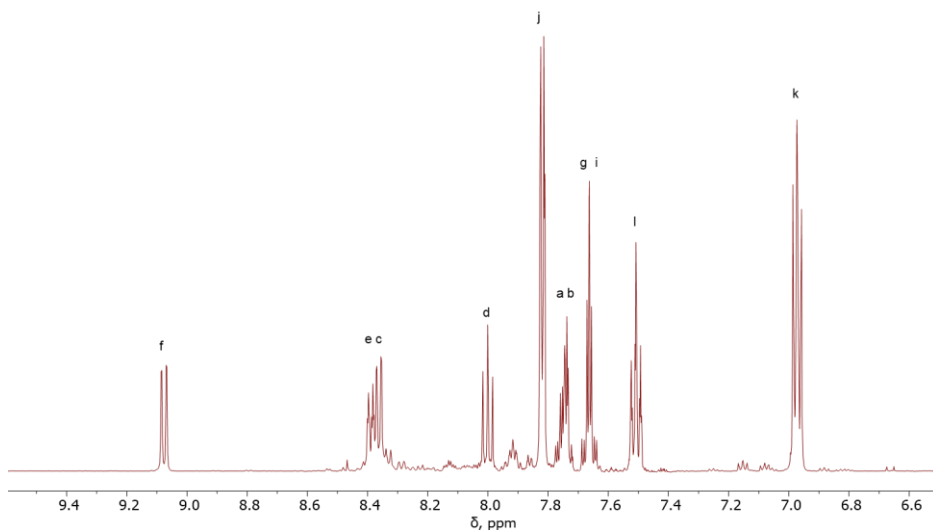


Figure S39.  $^1\text{H}$  NMR of  $4^{3-}$  in  $\text{D}_2\text{O}$  in the presence of sodium ascorbate at RT

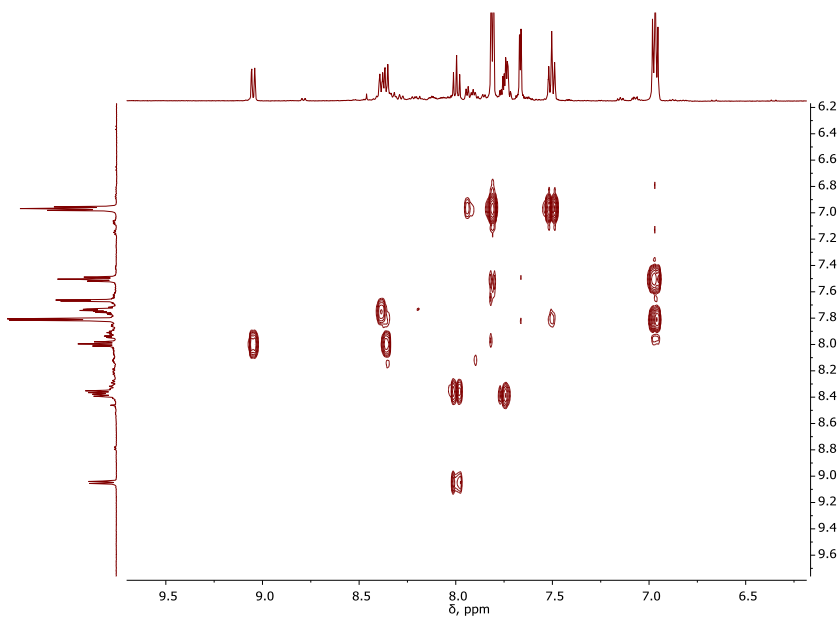


Figure S40.  $^1\text{H}$ - $^1\text{H}$  COSY NMR of  $4^{3-}$  in  $\text{D}_2\text{O}$  in the presence of sodium ascorbate at RT

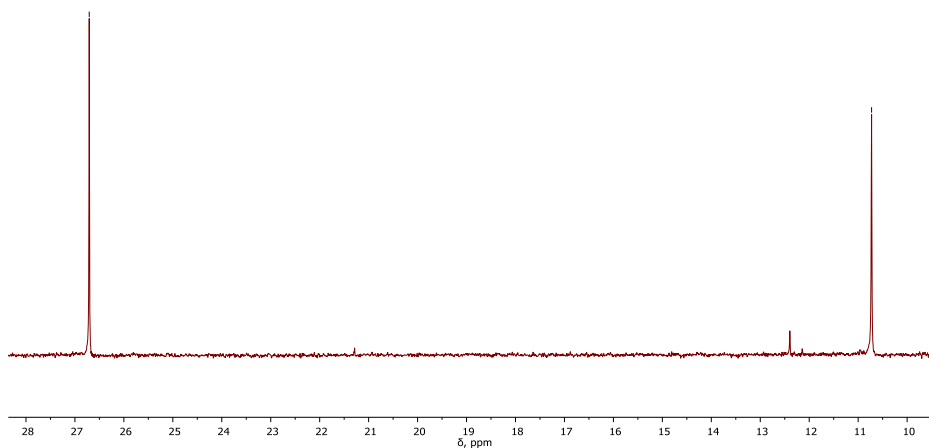


Figure S41.  $^{31}\text{P}$ -NMR of  $4^{3-}$  in  $\text{D}_2\text{O}$  in the presence of sodium ascorbate at RT.

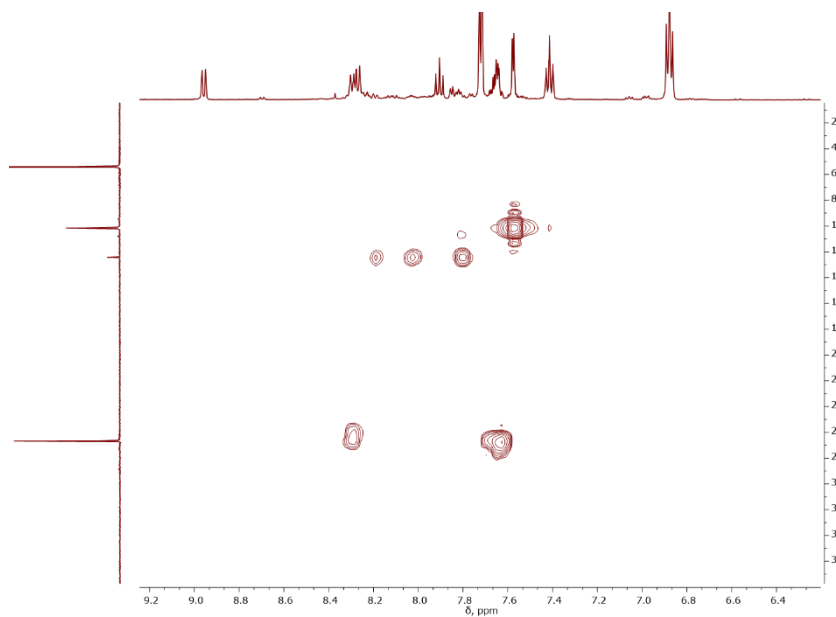
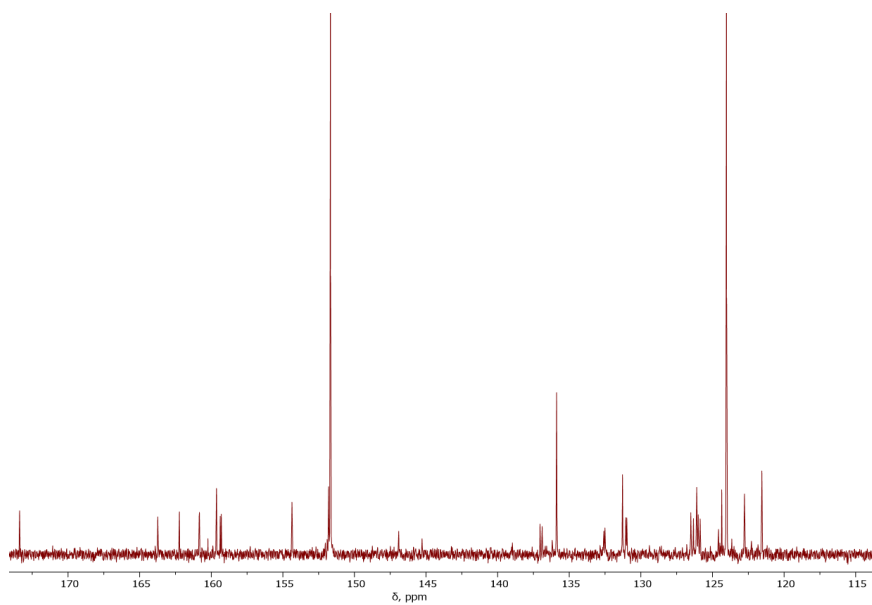


Figure S42.  $^1\text{H}$ - $^{31}\text{P}$  HMBC NMR of  $4^{3-}$  in  $\text{D}_2\text{O}$  in the presence of sodium ascorbate at RT.

### CHAPTER 3.

# III



**Figure S43.**  $^{13}\text{C}$  NMR of  $4^{3-}$  in  $\text{D}_2\text{O}$  in the presence of sodium ascorbate at RT.

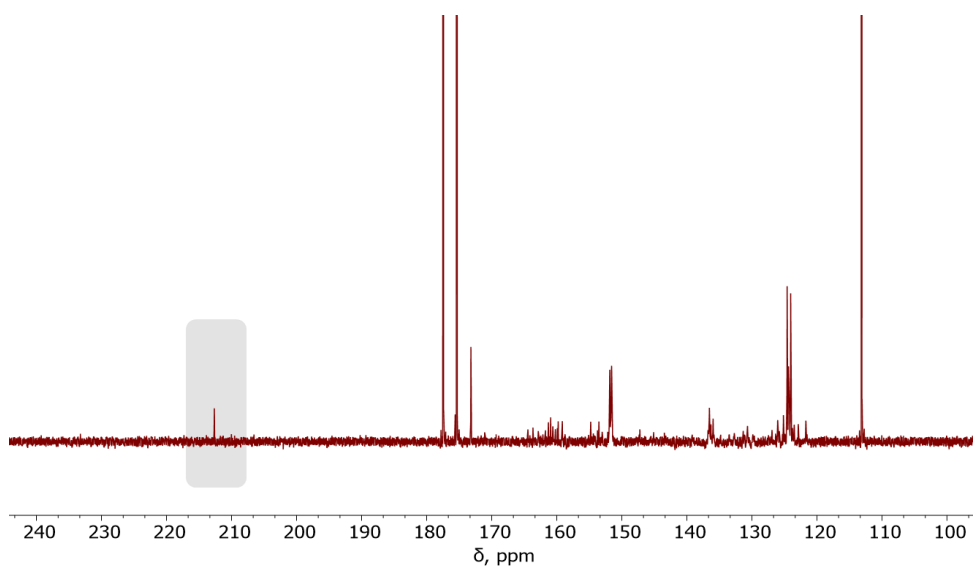


**Figure S44.**  $^{13}\text{C}$  NMR (downfield) of  $4^{3-}$  in  $\text{D}_2\text{O}$  in the presence of sodium ascorbate at RT

3.5.5 Spectral and Redox properties of **2**.

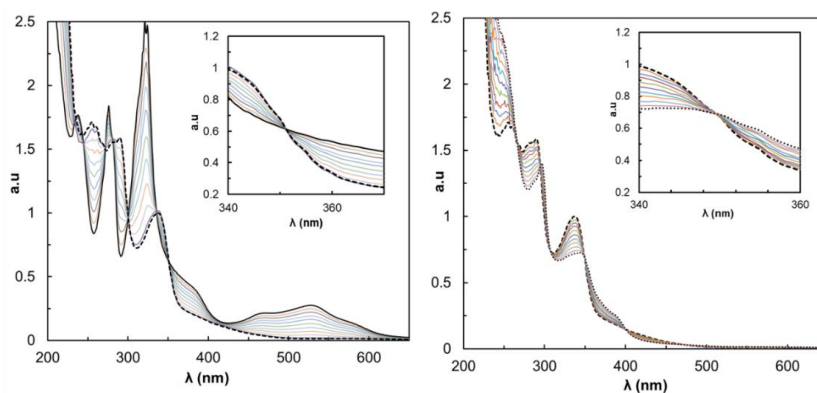


**Figure S45.** Spectrophotometric redox titration of of  $[\text{Ru}^{\text{II}}(\text{H}_2\text{tPa}-\kappa\text{-N}^3\text{O})(\text{py})_2]$ , **2** at pH = 1.0 by  $\text{Ce}^{4+}$  (10  $\mu\text{L}$ , 3.01 mM). **Left**, UV-Vis spectra of **2** (solid black line) and successive additions of 0.1 eq of  $\text{Ce}^{4+}$  (grey solid lines) up to 1 equivalent of  $\text{Ce}^{4+}$  (dashed black line). **Right**, UV-Vis spectra of  $[\text{Ru}^{\text{III}}(\text{HtPa}-\kappa\text{-N}^3\text{O}^2)\text{py}_2]$  (dashed black line), and successive additions of 0.1 eq. of  $\text{Ce}^{4+}$  (dashed grey lines) up to 1.5 equivalent of  $\text{Ce}^{4+}$  (pointed black line).

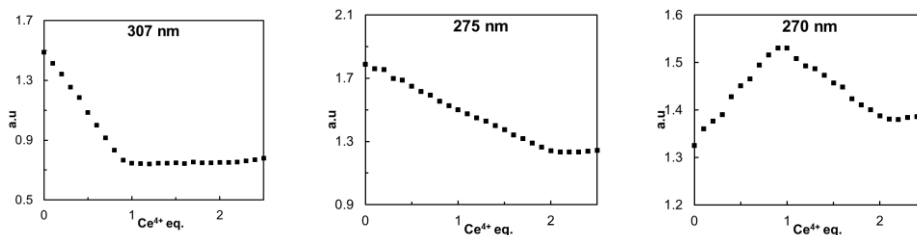


**Figure S46.** The plot of absorbance against added  $\text{Ce}^{4+}$  equivalents at 307 nm, 270 nm, and 275 nm.

III



CHAPTER 3.

III

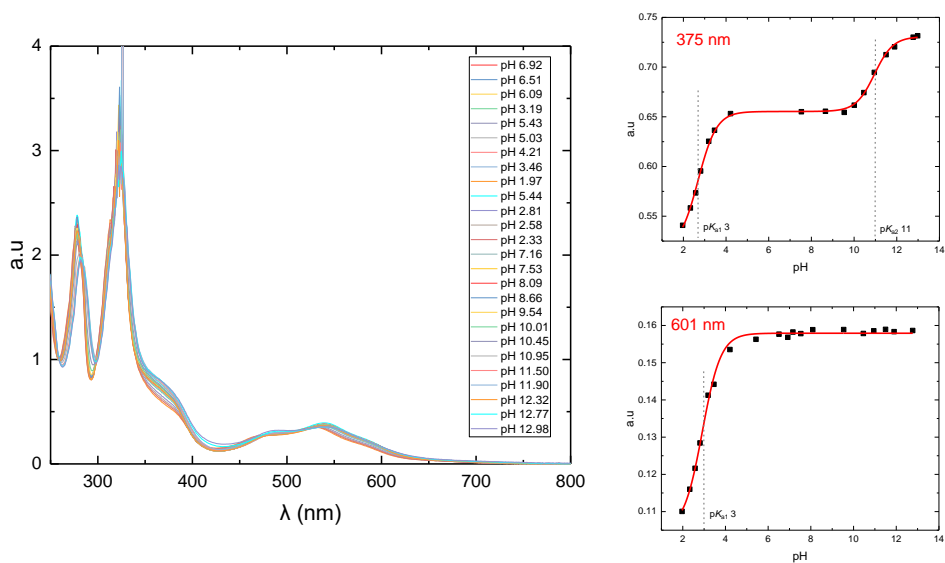


**Figure S47. Left**, UV-Vis acid-base titration. Spectra at different pH values for [Ru<sup>II</sup>(H<sub>2</sub>tPa-κ-N<sup>3</sup>O)(py)<sub>2</sub>] **2**, 0.1 mM. **Right**, absorbance vs. pH at 375 nm and 601 nm.

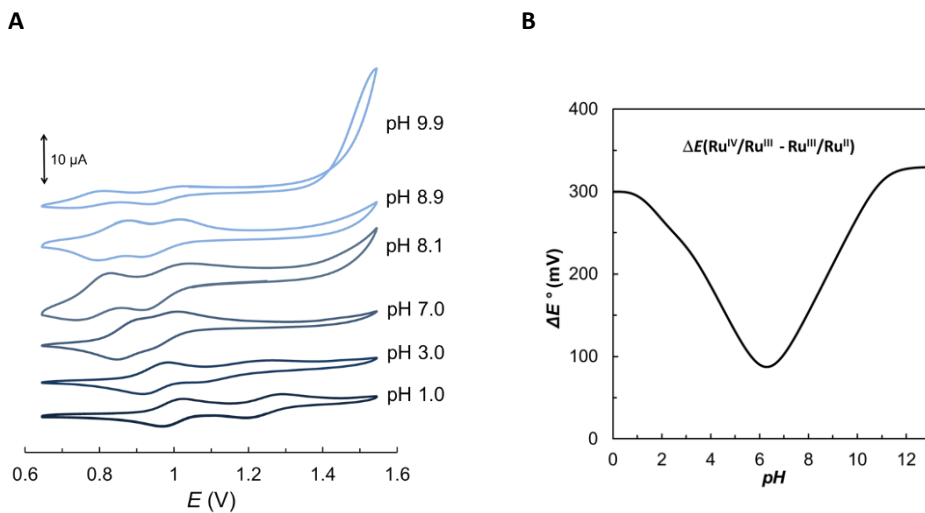
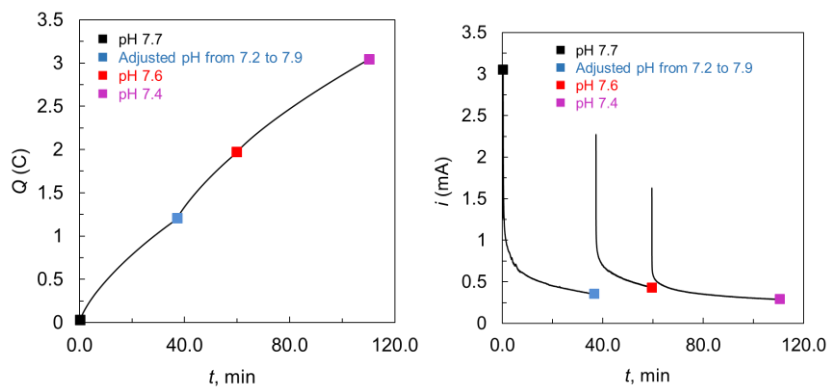


**Figure S48. A**, CV of **2** at pH 1.0-9.9. **B**, ΔE°, (Ru<sup>IV</sup>/Ru<sup>III</sup>-Ru<sup>III</sup>/Ru<sup>II</sup>) as a function of pH.

3.5.6 Spectral and redox properties of  $4^{2-}$

A



B

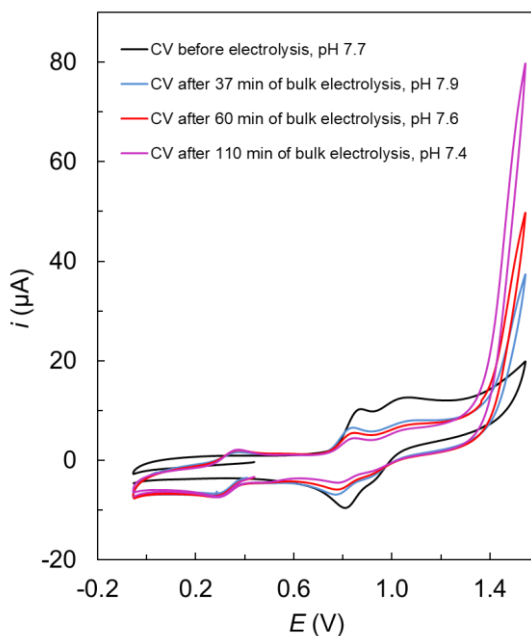


**Figure S49.** A, CPE monitoring profile obtained for the formation of  $[\text{Ru}^{\text{III}}(\text{tPaO}-\kappa\text{-N}^2\text{O}_p\text{OC})(\text{py})_2]^{2-}$ ,  $4^{2-}$ , from  $[\text{Ru}^{\text{II}}(\text{H}_3\text{tPa}-\kappa\text{-N}^3\text{O})(\text{py})_2]^+$ ,  $2^+$  (1.25 mM, in 5 mL pH 7 phbf) at  $E_{\text{app}} = 1.30$  V. B, CVs at different operating times during the CPE.

### CHAPTER 3.

III

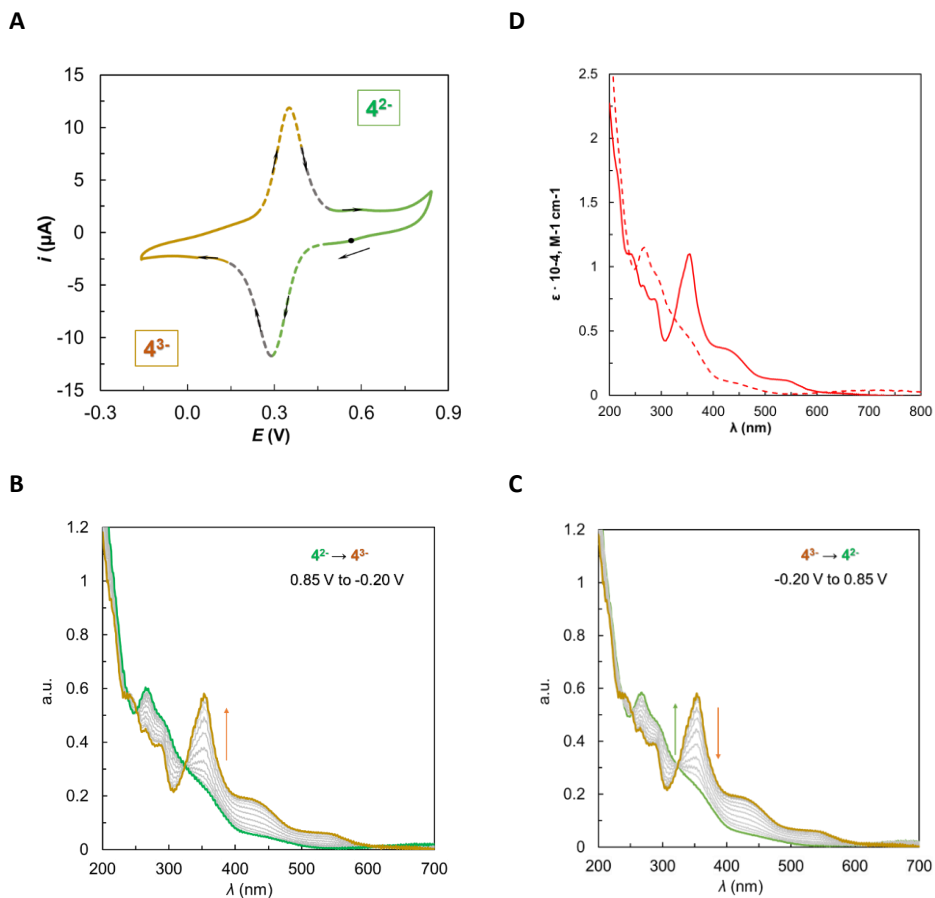
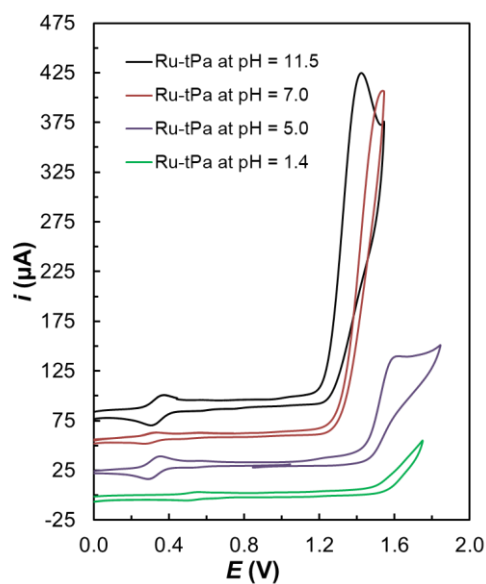


**Figure S50.** Spectroelectrochemical experiment using of 2.6 mM solution for complex  $4^{2-}$  at pH 7.0 phbf using an OTTLE cell. **A**, CV of complex  $4^{2-}$  recorded at  $0.002 \text{ V s}^{-1}$  scan rate between  $-0.15 \text{ V}$  and  $0.8 \text{ V}$ . **B**, Change in UV-Vis absorbance during the cathodic sweep from  $0.6$  to  $-0.15 \text{ V}$ . **C**, Change in UV-Vis absorbance during the anodic sweep from  $-0.15$  to  $0.8 \text{ V}$ . Vertical arrows indicate the direction of change in UV-Vis absorbance during CV scan. **D**, UV-vis spectra of  $[\text{Ru}^{\text{II}}(\text{tPaO-}\kappa\text{-N}^2\text{O}_\text{P}\text{OC})(\text{py})_2]^{3-}$  (red solid) and  $[\text{Ru}^{\text{III}}(\text{tPaO-}\kappa\text{-N}^2\text{O}_\text{P}\text{OC})(\text{py})_2]^{2-}$  (red dashed) in a pH 7.0 phbf solution.



III

Figure S51. CV of  $4^{2-}$  at different pH.

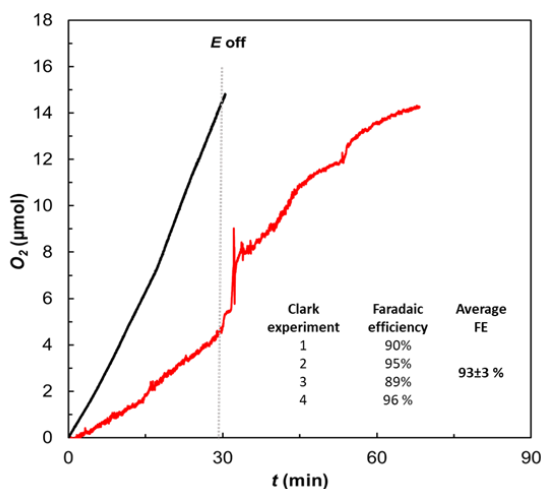
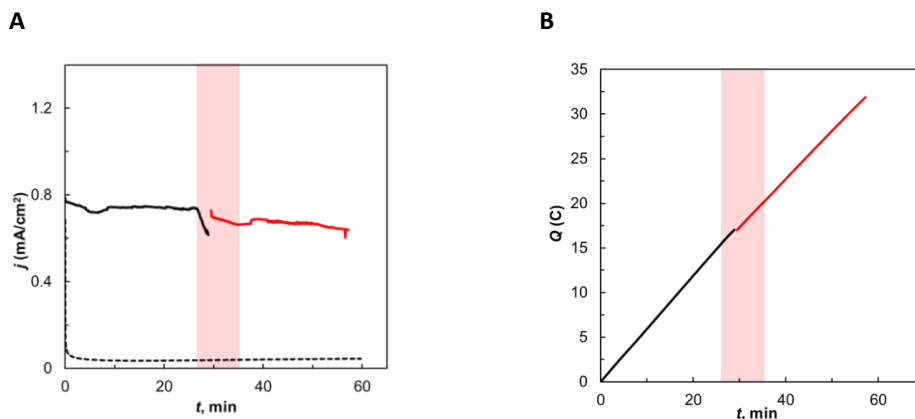
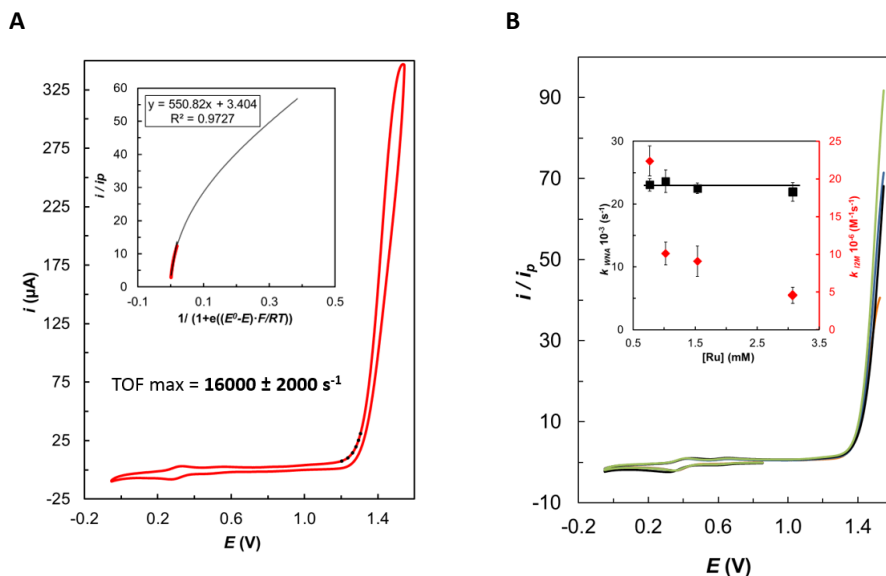


Figure S52. CPE at  $E_{app} = 1.45$  V vs. NHE of a solution of  $4^{2-}$  (1.04 mM, 20 mL pH 7 phbf; 20.8  $\mu$ mol) using a glassy carbon rod as a working electrode ( $S = 13.35$  cm<sup>2</sup>), Ag/AgCl as a reference electrode, and a Pt mesh as the auxiliary electrode. Red trace, oxygen evolution in the working electrode compartment monitored with an OXNP Clark electrode in the gas phase. The black corresponds to the amount of oxygen obtained from the charge passed assuming 100% Faradaic Efficiency. An average FE of 93% is obtained.

### CHAPTER 3.



**Figure S53.** CPE at  $E_{app} = 1.45$  V vs. NHE of a solution of  $4^{2-}$  (1.5 mM, 5 mL pH 7 phbf; 7.5  $\mu$ mol) using a glassy carbon rod as a working electrode ( $S = 13.35$  cm<sup>2</sup>), Ag/AgCl as a reference electrode, and a Pt mesh as the auxiliary electrode. The charge was integrated to be 32 C, giving a TON = 10.5 considering 93% FE. A TON of 42 million resulted in applying the equation,<sup>14</sup>  $TON = \frac{k_{WNA}t}{1 + \exp\left[\frac{F}{R.T}(E^{0,app} - E)\right]}$ , that takes into account only the catalyst that is close to the electrode surface. The sharp current drop after 30 minutes corresponds to a pH decrease to 5.5. Adjusting the pH back to 7.0 recovers the initial current density.



III

**Figure S54.** **A**, Red solid line CV of  $4^{2-}$  at pH = 7.2 phbf. The black dotted line indicates the data points used for the FOWA. Inset,  $i/i_p$  vs.  $1/(1+e((E^0-E)·F/RT))$  plot assuming a WNA mechanism. The fitting points for the extraction of rate constants at the foot of the wave are represented as a red solid line.  $TOF_{max} = 1.6 \cdot 10^4 (\pm 0.2 \cdot 10^4) s^{-1}$ . **B**,  $i_p$  normalized CVs of  $4^{2-}$  at pH 8.1 at different catalyst concentrations, 0.77 mM (black solid line), 1.02 mM (green solid line), 1.54 mM (blue solid line) and 3.07 mM (orange solid line). Inset, a plot of calculated  $k_D$  and  $k_{WNA}$  vs. the concentrations of  $4^{2-}$ . The standard deviation of each data point is represented with vertical lines. The black squares indicate the trend for the rate constants assuming WNA mechanism or red rhombs for the I2M.  $TOF_{max} = 2.3 \cdot 10^4 (\pm 0.2 \cdot 10^4) s^{-1}$

## CHAPTER 3.

### 3.5.7 Single Crystal X-Ray Structure Determination

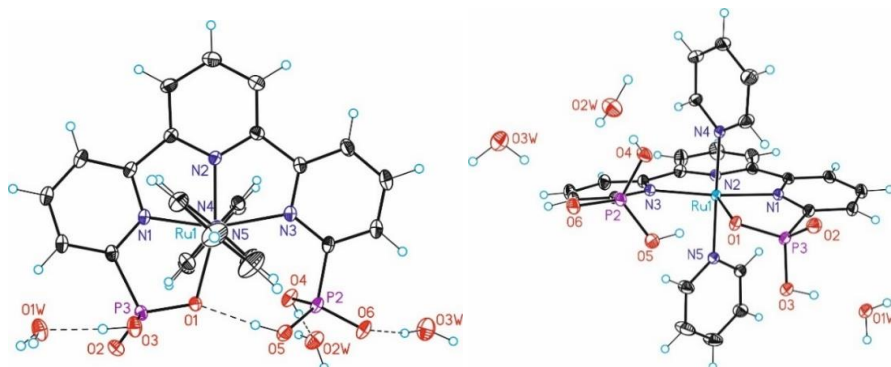


**Figure S55.** ORTEP views of the cationic structure of  $\{[Ru^{II}(H_3tPa-\kappa-N^3O)(py)_2](H_2O)_3\}^+$  showing the 3 hydrogen-bonded water molecules. Color code: Ru, cyan; P, pink; N, blue; O, red; C, black; H, white.

Metric parameters for H-bonded water molecules in 2·3H <sub>2</sub> O					
$d_{O_3 \cdots H}$	0.830 Å	$d_{O_4 \cdots H}$	0.840 Å	$d_{O_6 \cdots H}$	2.000
$d_{H \cdots O_{1W}}$	1.652 Å	$d_{H \cdots O_{2W}}$	1.575 Å	$d_{O_1 \cdots H}$	1.748
$d_{O_3 \cdots O_{1W}}$	2.477 Å	$d_{O_4 \cdots O_{2W}}$	2.414 Å	$d_{O_5 \cdots H}$	0.840
$\alpha_{O_3 \cdots O_{1W}}$	172.12	$\alpha_{O_4 \cdots O_{2W}}$	176.99	$d_{O_5 \cdots O_1}$	2.580

\*O.....H distance estimated from X-ray assignment.

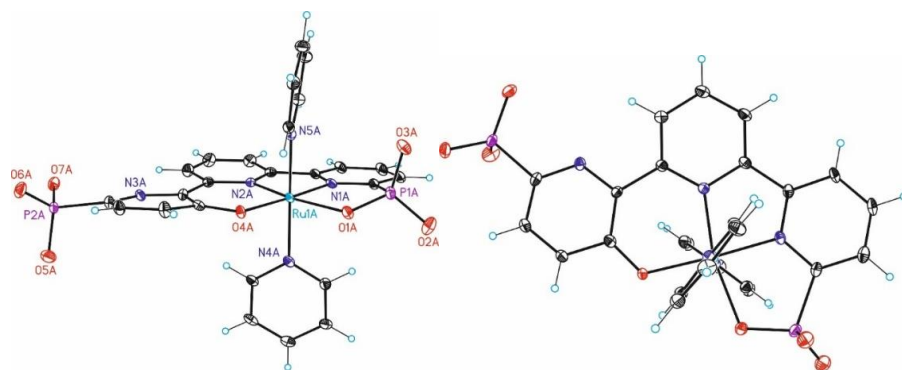
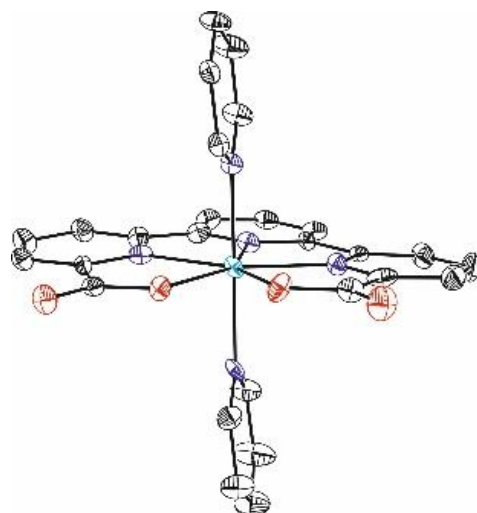


**Figure S56.** ORTEP plots (50 %) showing two views of the X-ray structure of the anionic complex  $[Ru^{II}(tPaO-\kappa-N^2OPc)(py)_2]^{3-}$ , **4**<sup>3-</sup>. Color code: Ru, cyan; P, pink; N, blue; O, red; C, black; H, white.



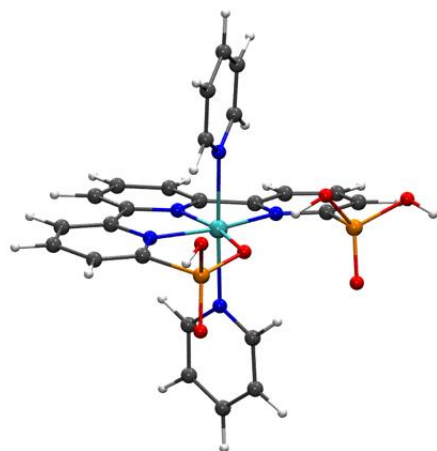
III

**Figure S57.** ORTEP plot of  $[\text{Ru}^{\text{IV}}(\text{tda-k-N}^3\text{O}^2)(\text{py})_2]^{2+}$ . Ellipsoids are plotted at 50 % probability. Broken lines indicate contacts. Color codes: Ru, cyan; N, blue; O, red; C, black. H-atoms are not shown.<sup>28</sup>



## CHAPTER 3.

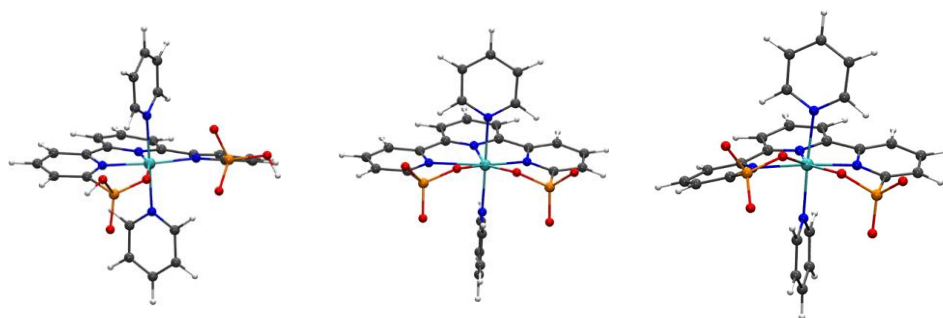
### 3.5.8 Computational data



$[\text{Ru}^{\text{II}}(\text{H}_3\text{tPa-}\kappa\text{-N}^3\text{O})(\text{py})_2]^+$

	Computed	X-ray
Ru-N <sub>1</sub>	2.00	1.9776(14)
Ru-N <sub>2</sub>	1.93	1.9160(15)
Ru-N <sub>3</sub>	2.17	2.1067(15)
Ru-N <sub>4</sub> (axial)	2.12	2.1003(14)
Ru-N <sub>5</sub> (axial)	2.10	2.0976(14)
Ru-O <sub>1</sub>	2.27	2.1898(13)
Ru-O <sub>2</sub>	3.67	3.49

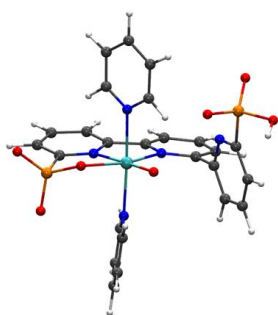
**Figure S58.** Optimized structure of  $[\text{Ru}^{\text{II}}(\text{H}_3\text{tPa-}\kappa\text{-N}^3\text{O})(\text{py})_2]^+$  at M06 level of theory (left) and its selected geometric features compared to X-ray crystallography data (right).



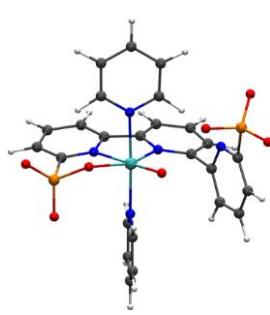
$[\text{Ru}^{\text{II}}(\text{H}_2\text{tPa-}\kappa\text{-N}^3\text{O})(\text{py})_2]$

$[\text{Ru}^{\text{III}}(\text{tPa-}\kappa\text{-N}^3\text{O}^2)(\text{py})_2]^-$

$[\text{Ru}^{\text{IV}}(\text{tPa-}\kappa\text{-N}^3\text{O}^2)(\text{py})_2]$



$[\text{Ru}^{\text{IV}}(\text{O})(\text{HtPa-}\kappa\text{-N}^2\text{O})(\text{py})_2]^-$



$[\text{Ru}^{\text{V}}(\text{O})(\text{tPa-}\kappa\text{-N}^2\text{O})(\text{py})_2]^-$

**Figure S60.** Optimized structures at M06 level of theory on the oxidation pathway from  $[\text{Ru}^{\text{II}}(\text{H}_2\text{tPa-}\kappa\text{-N}^3\text{O})(\text{py})_2]$  to  $[\text{Ru}^{\text{V}}(\text{O})(\text{tPa-}\kappa\text{-N}^2\text{O})(\text{py})_2]^-$  (Scheme 1 in the main text).

III

### CHAPTER 3.

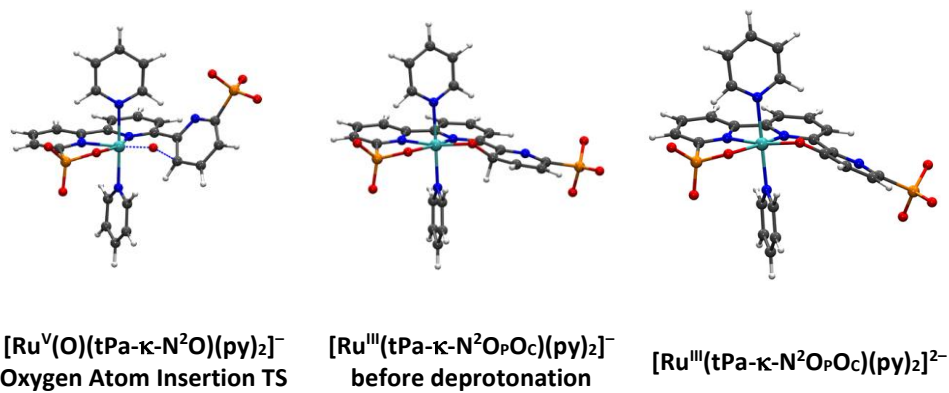
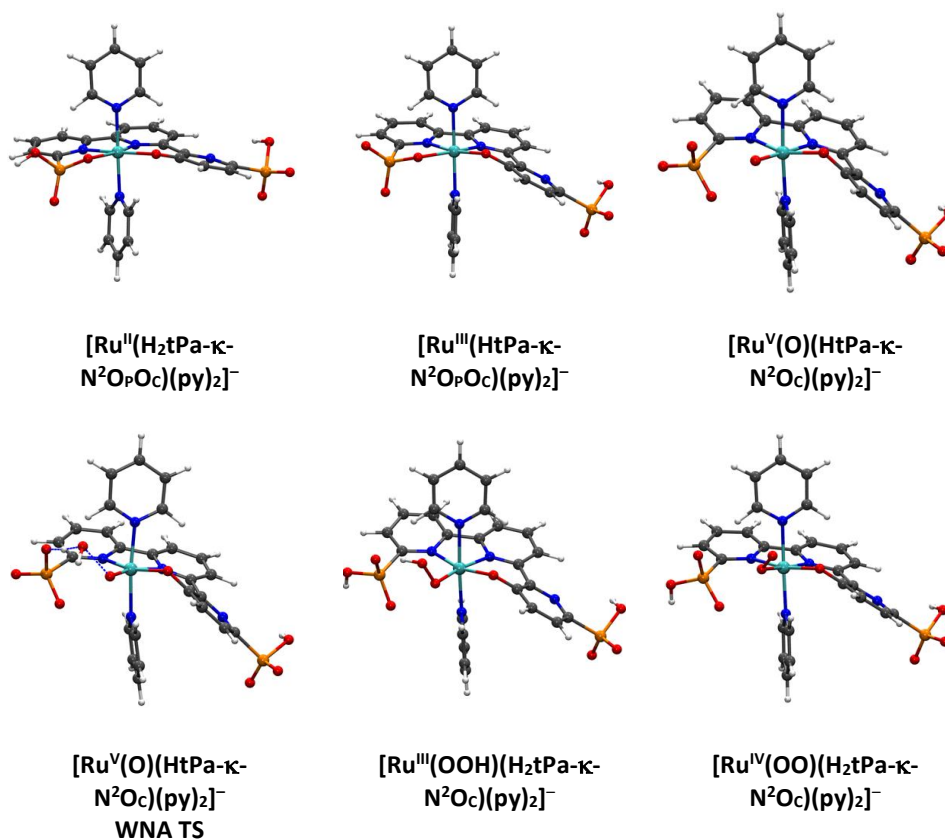


**Figure S61.** Optimized structures at M06 level of theory on the oxygen atom insertion pathway from  $[\text{Ru}^{\text{V}}(\text{O})(\text{tPa-}\kappa\text{-N}^2\text{O})(\text{py})_2]^-$  to  $[\text{Ru}^{\text{III}}(\text{tPaO-}\kappa\text{-N}^2\text{OPc})(\text{py})_2]^{2-}$  (Scheme 1 in the main text).



III

**Figure S62.** Optimized structures at M06 level of theory for catalytic water oxidation starting from **[Ru<sup>II</sup>(HtPaO-κ-N<sup>2</sup>O<sub>P</sub>Oc)(py)<sub>2</sub>]<sup>2-</sup>** (Figure 4 in the main text).

### CHAPTER 3.

**Table S1.** Relative free energies in units of kcal/mol for formally [Ru<sup>V</sup>=O] species at pH 0.0 and pH 7.0. Most stable species are highlighted in yellow.

Relative Free Energies ( $\Delta G$ ) in units of kcal/mol		
Molecular Complex	pH 0.0	pH 7.0
[Ru <sup>V</sup> (O)(H <sub>3</sub> tPa- $\kappa$ -N <sup>2</sup> O <sub>c</sub> )(py) <sub>2</sub> ] <sup>+</sup>	0.0	0.0
[Ru <sup>V</sup> (O)(H <sub>3</sub> tPa- $\kappa$ -N <sup>2</sup> O <sub>p</sub> )(py) <sub>2</sub> ] <sup>+</sup>	2.3	2.3
[Ru <sup>V</sup> (O)(H <sub>2</sub> tPa-HO <sub>c</sub> - $\kappa$ -N <sup>2</sup> O <sub>p</sub> )(py) <sub>2</sub> ] <sup>+</sup> Iso1	6.8	6.8
[Ru <sup>V</sup> (O)(H <sub>2</sub> tPa-HO <sub>c</sub> - $\kappa$ -N <sup>2</sup> O <sub>p</sub> )(py) <sub>2</sub> ] <sup>+</sup> Iso2	3.3	3.3
[Ru <sup>V</sup> (O)(H <sub>2</sub> tPa- $\kappa$ -N <sup>2</sup> O <sub>p</sub> )(py) <sub>2</sub> ]	0.2	-9.3
[Ru <sup>V</sup> (O)(HtPa-HO <sub>c</sub> - $\kappa$ -N <sup>2</sup> O <sub>p</sub> )(py) <sub>2</sub> ]	5.0	-4.5
[Ru <sup>V</sup> (O)(HtPa- $\kappa$ -N <sup>2</sup> O <sub>c</sub> )(py) <sub>2</sub> ] <sup>-</sup>	12.5	-6.5
[Ru <sup>V</sup> (O)(HtPa- $\kappa$ -N <sup>2</sup> O <sub>p</sub> )(py) <sub>2</sub> ] <sup>-</sup>	5.5	-13.5
[Ru <sup>V</sup> (O)tPa- $\kappa$ -N <sup>2</sup> O <sub>c</sub> )(py) <sub>2</sub> ] <sup>2-</sup>	30.6	2.0
[Ru <sup>V</sup> (O)tPa- $\kappa$ -N <sup>2</sup> O <sub>p</sub> )(py) <sub>2</sub> ] <sup>2-</sup>	21.1	-7.5

**Table S2.** Relative free energies in units of kcal/mol for formally [Ru<sup>III</sup>-OOH] and [Ru<sup>III</sup>-OO] species at pH 0.0 and pH 7.0. Most stable species are highlighted in yellow.

Relative Free Energies ( $\Delta G$ ) in units of kcal/mol		
Molecular Complex	pH 0.0	pH 7.0
[Ru <sup>III</sup> (OOH)(H <sub>2</sub> tPa-HO <sub>c</sub> - $\kappa$ -N <sup>2</sup> O <sub>p</sub> )(py) <sub>2</sub> ] Iso1	0.0	0.0
[Ru <sup>III</sup> (OOH)(H <sub>2</sub> tPa-HO <sub>c</sub> - $\kappa$ -N <sup>2</sup> O <sub>p</sub> )(py) <sub>2</sub> ] Iso2	-2.8	-2.8
[Ru <sup>III</sup> (OOH)(H <sub>2</sub> tPa- $\kappa$ -N <sup>2</sup> O <sub>c</sub> )(py) <sub>2</sub> ] <sup>-</sup>	-2.7	-12.2
[Ru <sup>III</sup> (OOH)(HtPa-HO <sub>c</sub> - $\kappa$ -N <sup>2</sup> O <sub>p</sub> )(py) <sub>2</sub> ] <sup>-</sup>	3.1	-6.4
[Ru <sup>III</sup> (OOH)(HtPa- $\kappa$ -N <sup>2</sup> O <sub>c</sub> )(py) <sub>2</sub> ] <sup>2-</sup> Iso1	15.4	-3.6
[Ru <sup>III</sup> (OOH)(HtPa- $\kappa$ -N <sup>2</sup> O <sub>c</sub> )(py) <sub>2</sub> ] <sup>2-</sup> Iso2	10.7	-8.4
[Ru <sup>III</sup> (OOH)(HtPa- $\kappa$ -N <sup>2</sup> O <sub>p</sub> )(py) <sub>2</sub> ] <sup>2-</sup> Conf1	15.6	-3.4
[Ru <sup>III</sup> (OOH)(HtPa- $\kappa$ -N <sup>2</sup> O <sub>p</sub> )(py) <sub>2</sub> ] <sup>2-</sup> Conf2	13.8	-5.2

$[\text{Ru}^{\text{III}}(\text{OOH})(\text{tPa-}\kappa\text{-N}^2\text{Oc})(\text{py})_2]^{3-}$	29.1	0.5
$[\text{Ru}^{\text{III}}(\text{OO})(\text{H}_2\text{tPa-}\kappa\text{-N}^2\text{Oc})(\text{py})_2]^{2-}$	19.3	0.3
$[\text{Ru}^{\text{III}}(\text{OO})(\text{HtPa-}\kappa\text{-N}^2\text{Oc})(\text{py})_2]^{3-}$	39.3	10.7

**Table S3.** Relative free energies in units of kcal/mol for formally  $[\text{Ru}^{\text{IV}}\text{-OOH}]$  and  $[\text{Ru}^{\text{IV}}\text{-OO}]$  species at pH 0.0 and pH 7.0. Most stable species are highlighted in yellow.

Relative Free Energies ( $\Delta G$ ) in units of kcal/mol		
Molecular Complex	pH 0.0	pH 7.0
$[\text{Ru}^{\text{IV}}(\text{OOH})(\text{H}_2\text{tPa-HO}_C\text{-}\kappa\text{-N}^2\text{O}_P)(\text{py})_2]^+$ Iso1	0.0	0.0
$[\text{Ru}^{\text{IV}}(\text{OOH})(\text{H}_2\text{tPa-HO}_C\text{-}\kappa\text{-N}^2\text{O}_P)(\text{py})_2]^+$ Iso2	-6.1	-6.1
$[\text{Ru}^{\text{IV}}(\text{OOH})(\text{H}_2\text{tPa-}\kappa\text{-N}^2\text{Oc})(\text{py})_2]$	-7.4	-16.9
$[\text{Ru}^{\text{IV}}(\text{OOH})(\text{HtPa-}\kappa\text{-N}^2\text{Oc})(\text{py})_2]^-$	8.2	-10.8
$[\text{Ru}^{\text{IV}}(\text{OOH})(\text{HtPa-}\kappa\text{-N}^2\text{O}_P)(\text{py})_2]^-$	18.9	-0.1
$[\text{Ru}^{\text{IV}}(\text{OO})(\text{H}_2\text{tPa-}\kappa\text{-N}^2\text{Oc})(\text{py})_2]^-$ Conf1	-7.6	-26.7
$[\text{Ru}^{\text{IV}}(\text{OO})(\text{H}_2\text{tPa-}\kappa\text{-N}^2\text{Oc})(\text{py})_2]^-$ Conf2	-7.9	-26.9
$[\text{Ru}^{\text{IV}}(\text{OO})(\text{HtPa-}\kappa\text{-N}^2\text{Oc})(\text{py})_2]^{2-}$	10.1	-18.5
$[\text{Ru}^{\text{IV}}(\text{OO})(\text{HtPa-}\kappa\text{-N}^2\text{O}_P)(\text{py})_2]^{2-}$	7.1	-21.5

III

**CHAPTER 3.**

**Table S4.** Computed activation free energies ( $\Delta G^\ddagger$ ) in units of kcal/mol for WNA TS at M06-L and M06 level of theories with the different number of explicit water molecules using separated reactants approach.

# of Explicit H <sub>2</sub> O Molecules	M06-L	M06
1	20.1	22.1
2	19.2	20.8
3	16.4	18.9
4	16.3	18.7

**III**

## References

- (1) Evans, I. P.; Spencer, A.; Wilkinson, G. Dichlorotetrakis(Dimethyl Sulphoxide)Ruthenium(II) and Its Use as a Source Material for Some New Ruthenium(II) Complexes. *J. Chem. Soc. Dalton Trans.* **1973**, No. 2, 204–209.
- (2) Gottlieb, H. E.; Kotlyar, V.; Nudelman, A. NMR Chemical Shifts of Common Laboratory Solvents as Trace Impurities. *J. Org. Chem.* **1997**, *62* (21), 7512–7515.
- (3) Covington, A. K.; Robinson, R. A.; Bates, R. G. The Ionization Constant of Deuterium Oxide from 5 to 50°. *J. Phys. Chem.* **1966**, *70* (12), 3820–3824.
- (4) Data Collection with APEX II Version V2013.4-1. Bruker (2007). Bruker AXS Inc., Madison, Wisconsin, USA.
- (5) Data Reduction with Bruker SAINT Version V8.30c. Bruker (2007). Bruker AXS Inc., Madison, Wisconsin, USA.
- (6) SADABS: V2012/1 Bruker (2001). Bruker AXS Inc., Madison, Wisconsin, USA. Blessing, *Acta Cryst.* **1995**, *A51*, 33–38.
- (7) SHELXT; V2014/4 (Sheldrick 2014). Sheldrick, G.M. *Acta Cryst.* **2015**, *A71*, 3–8.
- (8) SHELXL; C.B. Huebschle, G.M. Sheldrick & B. Dittrich; *J. Appl. Cryst.* **2011**, *44*, 1281–1284.
- (9) SHELXL; SHELXL-2014/7 (Sheldrick 2014). Sheldrick, G.M. *Acta Cryst.* **2015**, *C71*, 3–8.
- (10) Reijenga, J.; van Hoof, A.; van Loon, A.; Teunissen, B. Development of Methods for the Determination of PKvalues. *Anal. Chem. Insights* **2013**, *8* (1), 53–71.
- (11) Elgrishi, N.; Rountree, K. J.; McCarthy, B. D.; Rountree, E. S.; Eisenhart, T. T.; Dempsey, J. L. A Practical Beginner's Guide to Cyclic Voltammetry. *J. Chem. Educ.* **2018**, *95* (2), 197–206.
- (12) Mognon, L.; Benet-Buchholz, J.; Llobet, A. Single Site Isomeric Ru WOCs with an Electron-Withdrawing Group: Synthesis, Electrochemical Characterization, and Reactivity. *Inorg. Chem.* **2015**, *54* (24), 11948–11957.
- (13) Matheu, R.; Neudeck, S.; Meyer, F.; Sala, X.; Llobet, A. Foot of the Wave Analysis for Mechanistic Elucidation and Benchmarking Applications in Molecular Water Oxidation Catalysis. *ChemSusChem* **2016**, *9* (23), 3361–3369.
- (14) Costentin, C.; Drouet, S.; Robert, M.; Saveant, J. M. Turnover Numbers, Turnover Frequencies, and Overpotential in Molecular Catalysis of Electrochemical Reactions. Cyclic Voltammetry and Preparative-Scale Electrolysis. *J. Am. Chem. Soc.* **2012**, *134* (27), 11235–11242.
- (15) Zhao, Y.; Truhlar, D. G. The M06 Suite of Density Functionals for Main Group Thermochemistry, Thermochemical Kinetics, Noncovalent Interactions, Excited States, and Transition Elements: Two New Functionals and Systematic Testing of Four M06-Class Functionals and 12 Other Function. *Theor. Chem. Acc.* **2008**, *120* (1), 215–241.
- (16) Marenich, A. V.; Cramer, C. J.; Truhlar, D. G. Universal Solvation Model Based on Solute Electron Density and on a Continuum Model of the Solvent Defined by the Bulk Dielectric Constant and Atomic Surface Tensions. *J. Phys. Chem. B* **2009**, *113* (18), 6378–6396.
- (17) Andrae, D.; Häußermann, U.; Dolg, M.; Stoll, H.; Preuß, H. Energy-Adjustedab Initio Pseudopotentials for the Second and Third Row Transition Elements. *Theor. Chim. Acta* **1990**, *77* (2), 123–141.
- (18) Wiberg, K. B. Ab Initio Molecular Orbital Theory by W. J. Hehre, L. Radom, P. v. R. Schleyer, and J. A. Pople, John Wiley, New York, 548pp. (1986). *J. Comput. Chem.* **1986**, *7* (3), 379.
- (19) Frisch, M. J.; Trucks, G. W.; Schlegel, H. B.; Scuseria, G. E.; Robb, M. A.; Cheeseman, J. R.; Scalmani, G.; Barone, V.; Mennucci, B.; Petersson, G. A. et al. Gaussian, Inc.: Wallingford, CT, USA, 2009.
- (20) Cramer J. Christopher. *Essentials of Computational Chemistry: Theories and Models 2<sup>nd</sup> ed*; Wiley: John Wiley & Sons: Chichester, **2013**.
- (21) Tissandier, M. D.; Cowen, K. A.; Feng, W. Y.; Gundlach, E.; Cohen, M. H.; Earhart, A. D.; Coe, J. V.; Tuttle, T. R. The Proton's Absolute Aqueous Enthalpy and Gibbs Free Energy of Solvation



## CHAPTER 3.

- from Cluster-Ion Solvation Data. *J. Phys. Chem. A* **1998**, *102* (40), 7787–7794.
- (22) Camaioni, D. M.; Schwerdtfeger, C. A. Comment on “Accurate Experimental Values for the Free Energies of Hydration of H<sup>+</sup>, OH<sup>-</sup>, and H<sub>3</sub>O<sup>+</sup>.” *J. Phys. Chem. A* **2005**, *109* (47), 10795–10797.
- (23) Kelly, C. P.; Cramer, C. J.; Truhlar, D. G. Aqueous Solvation Free Energies of Ions and Ion–Water Clusters Based on an Accurate Value for the Absolute Aqueous Solvation Free Energy of the Proton. *J. Phys. Chem. B* **2006**, *110* (32), 16066–16081.
- (24) Bryantsev, V. S.; Diallo, M. S.; Goddard III, W. A. Calculation of Solvation Free Energies of Charged Solutes Using Mixed Cluster/Continuum Models. *J. Phys. Chem. B* **2008**, *112* (32), 9709–9719.
- (25) Lewis, A.; Bumpus, J. A.; Truhlar, D. G.; Cramer, C. Molecular Modeling of Environmentally Important Processes: Reduction Potentials. *J. Chem. Educ.* **2004**, *81* (4), 596–604.
- (26) Winget, P.; Cramer, C. J.; Truhlar, D. G. Computation of Equilibrium Oxidation and Reduction Potentials for Reversible and Dissociative Electron-Transfer Reactions in Solution. *Theor. Chem. Acc.* **2004**, *112* (4), 217–227.
- (27) Thummel, R. P.; Jahng, Y. N-Oxides of 2,2':6',2"-Terpyridine. *J. Org. Chem.* **1985**, *50* (19), 3635–3636.
- (28) Matheu, R.; Ertem, M. Z.; Benet-Buchholz, J.; Coronado, E.; Batista, V. S.; Sala, X.; Llobet, A. Intramolecular Proton Transfer Boosts Water Oxidation Catalyzed by a Ru Complex. *J. Am. Chem. Soc.* **2015**, *137* (33), 10786–10795.

## 4 CHAPTER 4

### **Understanding Precatalyst Transformation: Advanced Spectroscopic Characterization**

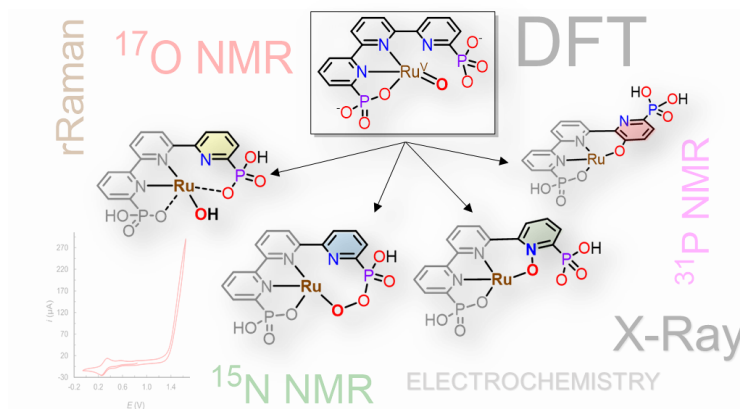
---

*We address the current study to the spectroscopic properties of the catalytic species generated over the catalytic conditions. The properties of the species were characterized and compared in the solution and solid-state. An investigation was performed through UV-Vis, rR (resonance Raman), and NMR together with an isotopically labeling experiment with oxygen.*

---



## Understanding Precatalyst Transformation: Advanced Spectroscopic Characterization



### **Abstract**

Herein, we performed the expanded spectroscopic characterization of the recently developed water oxidation catalyst based on  $[\text{Ru}(\text{H}_2\text{tPa})(\text{py})_2]$  coordination complex. We combined specific spectroscopic techniques with electrochemical methods and developed a powerful strategy for identifying the nature of the real catalyst. A combination of  $^{15}\text{N}$ ,  $^{17}\text{O}$ ,  $^{31}\text{P}$  NMR spectroscopy results together with resonance Raman experiments using isotopically labeled compounds provided essential information about the environment of Ru in the active catalytic form.

### **Contributions:**

Natalia Vereshchuk synthesized and characterized all the compounds, as well as carried out all the electrochemical and spectroscopic experiments.

## CHAPTER 4.

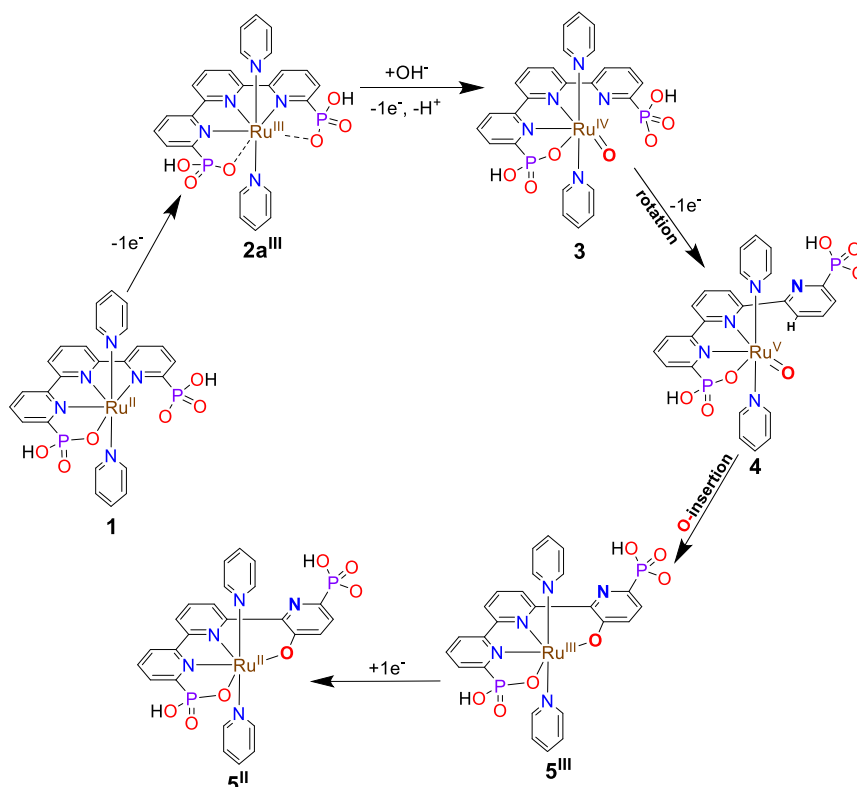
### 4.1 Introduction.

The present rate of consumption of fossil fuels from our society is mainly responsible for the increase in CO<sub>2</sub> concentration in the atmosphere that in turn is responsible for global warming and its catastrophic consequences.<sup>1-5</sup> In order to be able to fix this situation, the generation of clean and renewable fuels, is urgently needed. A potential option is the generation of solar fuels based on water oxidation coupled to either proton or CO<sub>2</sub> reduction using sunlight as the only external energy input.<sup>6-10</sup> To achieve this, one of the key challenges that need to be controlled and mastered is the oxidation of water to molecular dioxygen.<sup>11</sup> Therefore, robust and efficient WOCs are needed that will have to be coupled with light-absorbing molecules or materials.<sup>6</sup> From a molecular perspective, the best WOCs described up to now are based on Ru-aqua complexes that can access high oxidation states *via* PCET<sup>12-14</sup> coordinated with FAME type of ligands. This includes the family of Ru-tda and Ru-bda (tda<sup>2-</sup> being [2,2':6',2''-terpyridine]-6,6''-dicarboxylate and bda<sup>2-</sup> being 2,2'-bipyridine-6,6'-dicarboxylate) coordination complexes.<sup>15,16</sup> The high  $\Delta G$  values associated with the oxidation of water to dioxygen imply necessarily that the ligands used must be oxidatively robust since ligand oxidation will always be a competitive undesired pathway. For this reason, benzylpyridyl type of ligands even if they give access to a wide variety of potentially interesting ligands should be avoided.<sup>17,18</sup> Also, the need to carry out all reactions in water implies that transition metal complexes that undergo fast ligands substitution kinetics such as Mn or Fe iron should be avoided, or at least carefully checked.<sup>19,20</sup>

Therefore, the use of oxidatively rugged ligand in combination with Ru that is an inert ion with regard to ligand substitution reactions,<sup>19</sup> conforms an ideal platform for the design of new WOCS as well as the characterization of catalytic cycles and reaction intermediates. However, even under the best possible scenario, the initial water oxidation catalyst can also suffer ligand-based transformation under turnover conditions that can occur in parallel with productive oxygen generation pathways and whose detection and characterization can be indeed challenging.

Here on we show how for the particular case of the complex  $[\text{Ru}^{\text{II}}(\text{H}_2\text{tPa}-\kappa\text{-N}^3\text{O})(\text{py})_2]$  (tPa<sup>4-</sup> is the fame ligand 2,2':6',2''-terpyridine-6,6''-diphosphonate and py is pyridine), **1**, (See Scheme 1 for a drawing of its structure) the use of NMR and vibrational spectroscopy and

the support of DFT can be useful for the characterization of intermediates as well as for uncovering potential ligand-based transformations, that can occur during turnover. Besides, we also discuss the limitations of these techniques to discern among a variety of reasonable reaction intermediates.



IV

**Scheme 1.** The sequence of reactions followed by the transformation of 1 into 5<sup>II</sup>.

## 4.2 Results and Discussion

### 4.2.1 Preliminary statements

This work is based on the elucidation of the transformation undergone by a Ru water oxidation catalyst [Ru<sup>II</sup>(H<sub>2</sub>tPa-κ-N<sup>3</sup>O)(py)<sub>2</sub>], **1**, containing a phosphonate group. Electrochemical experiments after roughly four TONs showed that the initial complex had completely disappeared and that a new highly active water oxidation catalyst species was generated. We luckily managed to grow crystals of the new complex that showed the occurrence of an oxygen insertion into the CH group of the pyridyl ring forming the species,

## CHAPTER 4.

[Ru<sup>II</sup>(H<sub>2</sub>tPaO-κ-N<sup>2</sup>O<sub>P</sub>O<sub>C</sub>)(py)<sub>2</sub>], **5<sup>II</sup>** (tPaO<sup>5-</sup> is the 3-(hydroxo-[2,2':6',2''-terpyridine]-6,6''-diyl)bis(phosphonate)) (See Scheme 1, for a drawing of this structure). We have recently reported that complex **5<sup>II</sup>**, is a powerful water oxidation catalyst operating at very high turnover frequencies (TOF<sub>max</sub> = 16 000 s<sup>-1</sup>) at pH 7. The transformation of **1** to **5<sup>II</sup>** involves a high degree of rearrangement that is outlined in Scheme 1 and that includes several steps. First, one-electron oxidation and coordination of an OH-group to generate species **2a<sup>III</sup>** followed by the PCET step to generate the Ru(IV) species **3**. Then, an additional electron removal and rotation of the pyridyl-phosphonate arm fostered by the steric hindrance of the tetrahedral phosphonate group generates the water oxidation catalytically active species **4**. The latter can react either with exogenous water or OH<sup>-</sup> for O-O bond formation and final O<sub>2</sub> release closing the catalytic cycle (not shown in Scheme 1) or it can generate the pyridinolate group *via* intramolecular oxygen insertion into the CH group to generate **5<sup>III</sup>**, which can be further one-electron reduced to **5<sup>II</sup>** (a detailed synthetic description is provided in the SI).

The X-ray structure of **5<sup>II</sup>** was instrumental in realizing this large degree of rearrangement that occurred during turnover. However, single-crystal X-ray is not always available because in most cases it is difficult to obtain crystalline material even if we manage to isolate pure intermediate. In the vast majority of cases, this is further complicated by the presence of other compounds, either because the heavy TONs solution contains a mixture of compounds if chemically this will be the reduced oxidant (for instance Ce(III)) and in both chemically and electrochemically a typical concentration buffers (phosphate, borate or others)/supporting electrolyte will be involved. Further, if the catalytically spent solution might contain the starting WOC only partially converted together with other non-catalytically active compounds arising from deactivation pathways. Basically, in the vast majority of cases, an X-ray is not available and thus other techniques need to be used for structural elucidation.

### 4.2.2 Potential catalytically active species based on DFT

In the following section, we will discuss the utility of NMR and vibrational spectroscopy for the structural elucidation of intermediates that might have been formed in solution during

this transformation, based on related Ru complexes that had suffered ligand oxidations and back up with DFT calculations that are presented here.

Chart 1 shows four possible species. The first one **2a<sup>II</sup>** assumes that no ligand-based oxidations had occurred and only OH<sup>-</sup> has been coordinated to the metal center. In this case, we consider the equilibrium that occurs with this OH<sup>-</sup> coordination and that of the phosphonate groups that can coordinate and decoordinate very fast and compete for a position at the first coordination sphere, as has been previously shown.<sup>21</sup> The second involves an O–O bond formation at the phosphonate group that was proposed for a related Ru complex but at the carboxylate group.<sup>22</sup> This has been shown to be an energetically feasible reaction by DFT calculation. Complex **2c<sup>II</sup>**, assumes the formation of an N-oxide *via* intramolecular oxygen insertion into the Ru–N bond, as has been described for the [Ru(qpy)(py)<sub>2</sub>]<sup>2+</sup>, **6<sup>2+</sup>** (qpy is the 2,2':6',2'':6'',2'''-quaterpyridine) complex.<sup>23–26</sup>

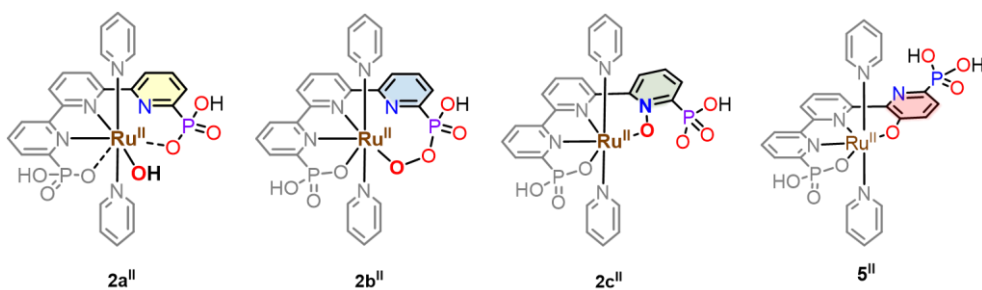


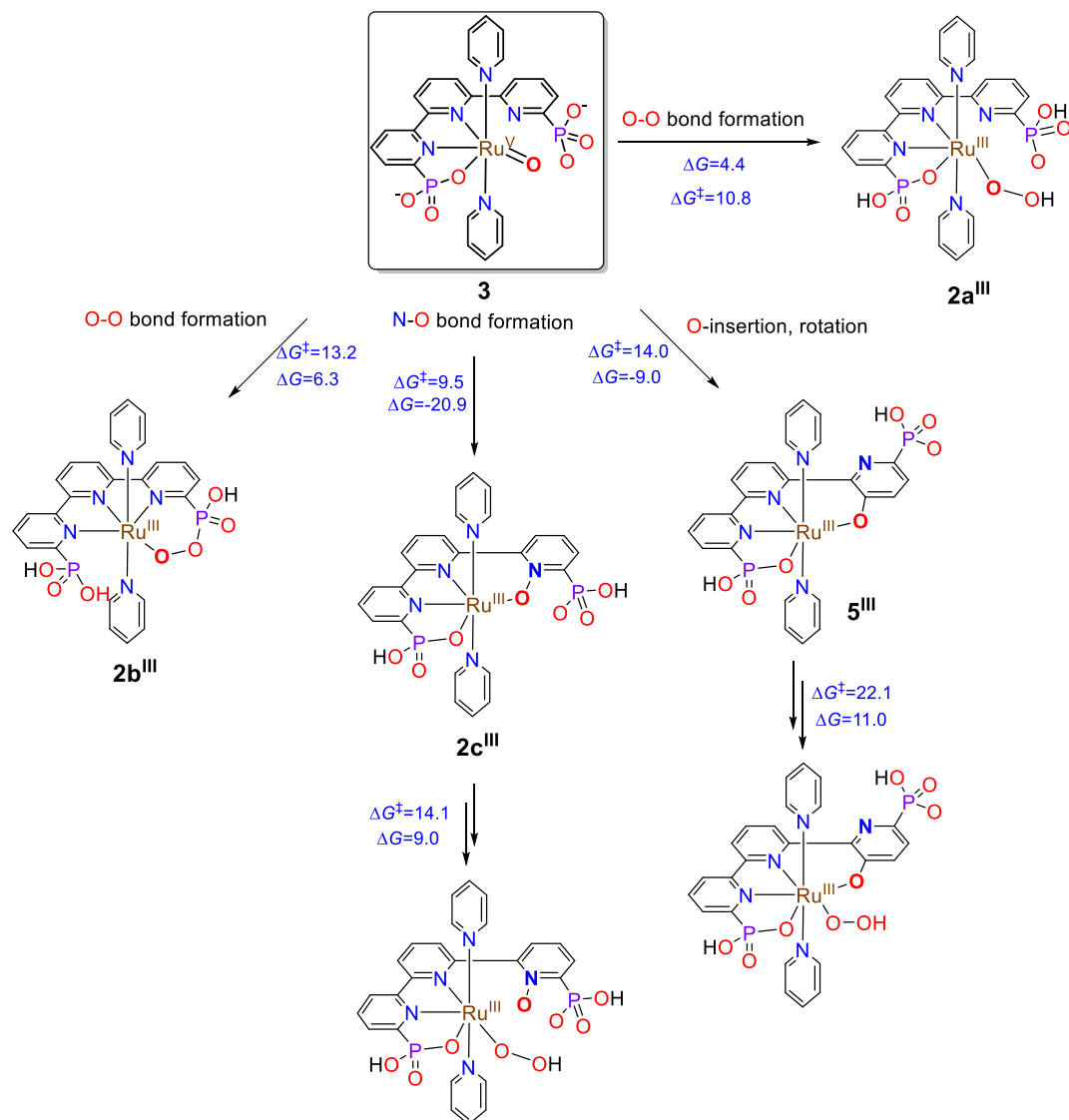
**Chart 1.** Reasonable species potentially involved in the evolution of WOC **1**, during turnover.

Finally, complex **5<sup>II</sup>** involves the largest degree of rearrangement from the initial complex as described in Scheme 1. All the transformations indicated here together with their complete DFT calculated catalytic cycles are being calculated at present and the main features of the available data are summarized in Scheme 2. The DFT show in all cases reasonable activation energies indicating that all pathways could be occurring at the same time. However, caution in this interpretation must be taken, since the data reported here is still preliminary and needs to be further refined.

The following is a set of NMR and vibrational spectroscopies used to elucidate the nature of the intermediates generated during water oxidation catalysis by **1**.



## CHAPTER 4.



**Scheme 2.** DFT calculated pathways for the ligand and non-ligand based water oxidation mechanisms from **3**.

### 4.2.3 $^1\text{H}$ - $^{15}\text{N}$ Heteronuclear Multiple Bond Correlation

Nitrogen 15 isotope has a very low natural abundance (0.4%) and thus it has not been used as a widespread technique for the characterization of organic compounds neither transition

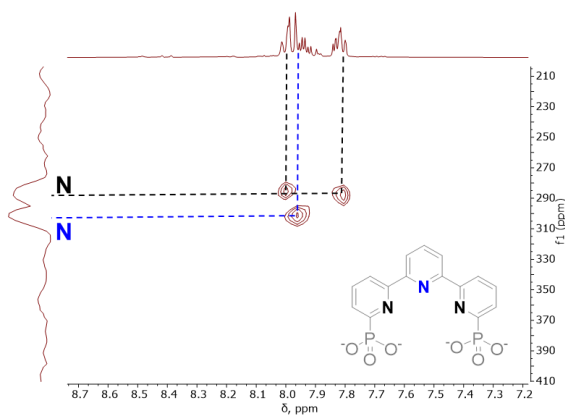
metal complexes. As a consequence of this, there is very scarce information in the literature.<sup>27-29</sup>

However recently with the new powerful machines together with the use of the appropriate pulses the  $^1\text{H}$ - $^{15}\text{N}$  correlation has become a readily available technique.<sup>30</sup> For Ru polypyridylic complexes this can be of help in the prediction/assignment of N-nuclei as is shown for the case of a polypyridyl Ru complex containing 4,4'-azobis(pyridine) ligand (abp),  $[\text{Ru}(\text{trpy})(\text{bpy})(\text{abp})]^{2+}$ , **7** (See Figure S9).<sup>30,31</sup> The spectra obtained for the  $^1\text{H}$ - $^{15}\text{N}$  correlations for **1** and **5**<sup>II</sup> in  $\text{D}_2\text{O}$  and TFE are shown in Figure 1 and their assignment is straightforward. Furthermore, we have carried out the NMR of pyridine compounds including the free  $\text{tPa}^{4-}$  ligand<sup>32,33</sup> for comparative purposes that are presented in Figure 1 and Figures S1 and S2.<sup>34</sup>

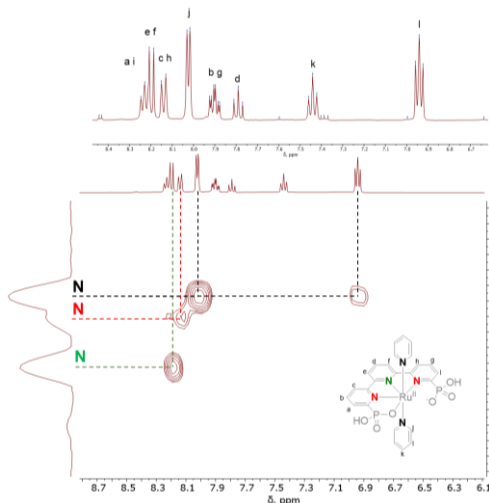
It is interesting to realize that the N-atoms of the pyridylic ligands coordinated to Ru appear in the region of 230-260 ppm. However, the non-coordinated N atoms are shifted downfield to approx. 290 ppm. Therefore, the absence of resonance at such a low field would be useful to discard the N-oxide structure **2c** as a potential candidate. Further, the expected fast dynamic behavior for **2a**<sup>II</sup>, would result in a pseudo  $C_{2v}$  symmetry and thus only N resonances would be expected in this case instead of the three observed. Finally, the  $^{15}\text{N}$  NMR alone would not be able to discriminate **2c**<sup>II</sup> from **5**<sup>II</sup>. However, based on independent  $^1\text{H}$  and  $^{13}\text{C}$  NMR (see Figure S3-5), the absence of the aromatic proton where the O-insertion has occurred would allow to easily discriminate **5**<sup>II</sup> from the rest of the proposed structures.

## CHAPTER 4.

A



B



C

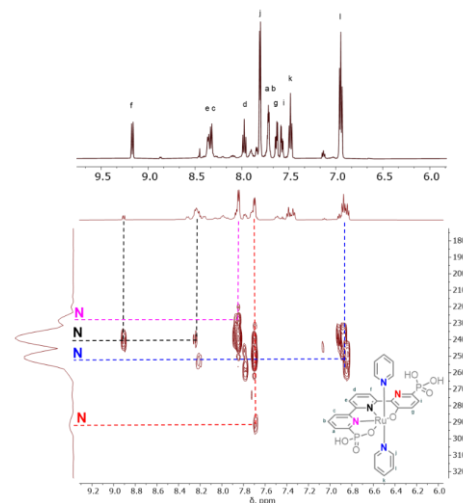


**Figure 1.**  $^1\text{H}$ - $^{15}\text{N}$  HMBC spectra of: **A**,  $\text{tPa}^{4-}$  (free ligand) in  $\text{D}_2\text{O}$  with the addition of the 10% 1.0 M NaOD at RT; **B**, the catalyst precursor **1** in  $[\text{d}_3]$ -trifluoroethanol at RT; **C**, the active catalyst  $[\text{Ru}^{\text{II}}(\text{tPaO}-\kappa\text{-N}^2\text{OPc})(\text{py})_2]^{3-}$ , **5<sup>II</sup>**, in  $\text{D}_2\text{O}$ .

### 4.2.4 $^{17}\text{O}$ NMR experiments

Enormously wide chemical shift range for  $^{17}\text{O}$  ( $I = 5/2$ ) makes oxygen NMR promising spectroscopic techniques for the characterization of oxygen-containing compounds.<sup>35–40</sup> However the natural abundance of  $^{17}\text{O}$  is only 0.037 %, and again this precludes widespread utilization.

Before we carried out the  $^{17}\text{O}$  NMR experiments, we did  $^{31}\text{P}$  NMR in water  $\text{H}_2\text{O}^{16}$  and  $\text{H}_2\text{O}^{18}$  for complex **1**, to check the potential oxygen exchange of the phosphonate groups. After 48 h stirring at room temperature there is no evidence of any change in the spectra (See SI Scheme S1) and thus confirms the absence of any oxygen exchange between the solvent and the phosphonate moiety of **1**.

The  $^{17}\text{O}$  NMR spectrum of **1** was recorded in a pH 8.5 phosphate buffer solution (phbf) of a mixture of  $\text{H}_2\text{O}^{17}:\text{D}_2\text{O}^{16}$  (1:1) and no resonances were observed except for the  $\text{H}_2\text{O}^{17}$  at 0 ppm (see Figure S8). In sharp contrast, the  $^{17}\text{O}$  NMR spectrum of **5<sup>III</sup>** run under the same conditions exhibits a singlet at 172 ppm as can be observed in Figure 2. The fact that only one resonance is observed also confirms the non-exchange of the O-phosphonates of **5<sup>III</sup>** with  $\text{H}_2\text{O}^{17}$ .

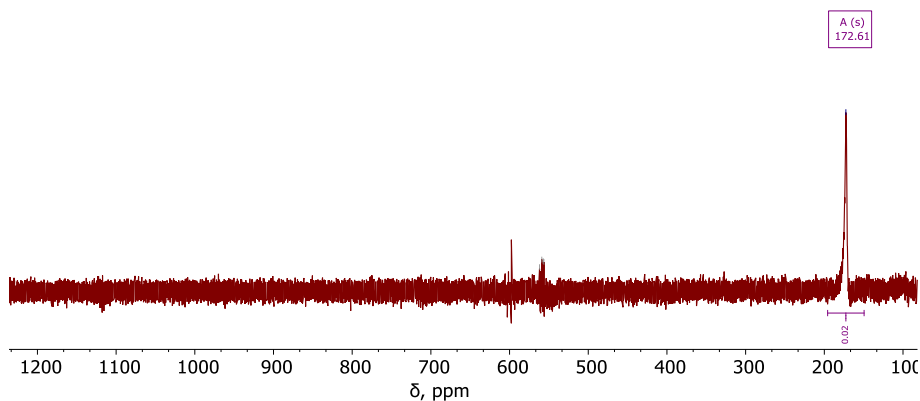


**Figure 2.**  $^{17}\text{O}$  NMR spectrum of **5<sup>III</sup>** in a pH = 8.5 phbf solution containing a mixture of  $\text{H}_2\text{O}^{17}:\text{D}_2\text{O}^{16}$  (1:1) at RT.

Regarding the potential diagnosis capacity of  $^{17}\text{O}$  NMR for our potentially evolved complexes, for the case of **2a<sup>II</sup>**, the chemical shift for the Ru-OH<sub>2</sub> complexes is not known, but methanol OH signal appears at -37 ppm and thus discards this option. For the formation of the phosphonate peroxide, a related compound would be tBuOOtBu with a chemical shift of 269 that is far from the obtained 172. However, the peroxides range appears in the zone of 180-220 ppm which is a bit closer. Nevertheless, given the non-symmetry of the phosphonate peroxide, two different resonances should be observed in the  $^{17}\text{O}$  spectrum

## CHAPTER 4.

which is not the case and thus fully discards this option. The potential formation of an N-oxide as indicated in the case of **2c<sup>II</sup>**, seems to be discarded by the chemical shift since the typical N-oxide range in the zone of 330-440 ppm.<sup>41,42</sup> However, there is no information regarding coordinated N-oxide and thus it could not be fully discarded. In the absence of an X-ray structure for **5<sup>III</sup>**, the literature shows that the PhO<sup>-</sup> group appears at 158 ppm which is in good agreement with the resonance at 172 ppm obtained for **5<sup>III</sup>**.<sup>43</sup>

### 4.2.5 Vibrational Spectroscopy

Vibrational spectroscopy combined with isotopic labeling is also a very valuable tool to characterize reaction intermediates. Here we used resonance Raman spectroscopy (rR) with the laser excitation operating at 532 nm under cryogenic conditions at 123K. Figure 3 shows the rR spectra obtained for complex **5<sup>III</sup>** prepared from bulk electrolysis of **1** in a pH 8.5 phbf solution using H<sub>2</sub>O<sup>16</sup> or H<sub>2</sub>O<sup>18</sup> (isotopically enriched up to 98%) and their difference spectra (see Figure 3).

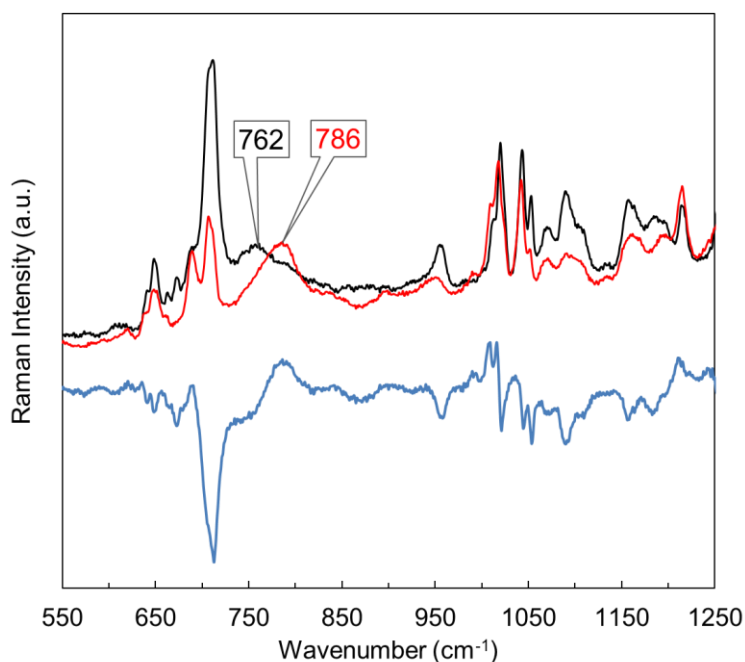


**Figure 3.** Normalized rR spectra of complex **5<sup>III</sup>** prepared using H<sub>2</sub>O<sup>16</sup> (red) or H<sub>2</sub>O<sup>18</sup> (black), using a  $\lambda_{\text{exc}} = 532$  nm. The blue trace is the difference spectra.

The most significant features of these spectra are the  $24\text{ cm}^{-1}$  isotopic shift observed for the vibration at  $786\text{ cm}^{-1}$  that changes to  $762\text{ cm}^{-1}$  ( $24\text{ cm}^{-1}$ ) in the  $\text{O}^{18}$  labeled spectrum. This vibrational shift can be assigned to the Ru–O–C bending mode. A DFT analysis is underway to confirm this.

When comparing with the other potential intermediates proposed earlier the phosphonato peroxide **2b**<sup>II</sup> is discarded since the typical O–O vibration for peroxides<sup>44</sup> appears at approximately  $800\text{ cm}^{-1}$  and our spectra are basically featureless from  $800$  to  $900\text{ cm}^{-1}$ . Similarly, the Ru–N–O vibration in **2c**<sup>II</sup> is expected in the range of  $820$ – $840\text{ cm}^{-1}$ , as observed for related Ru–N–oxide complexes.<sup>23,25</sup> Finally, the Ru–OH vibration for **2a**<sup>III</sup> would be expected in the low-frequency range of  $250$ – $400\text{ cm}^{-1}$ .

### 4.3 Conclusions

Understanding how transition metal-based complexes transform into the active water oxidation catalysts can provide important insight into advancing catalyst design. To characterize the active catalytic form, we combined specific spectroscopic techniques with electrochemical methods and had developed a powerful strategy for identifying the nature of the real catalyst. In the absence of an X-ray, the combination of spectroscopic techniques used here together with the electrochemistry can afford a reasonable guess on the potential structures of evolved WOCs that can suffer transformation on the auxiliary ligands

## CHAPTER 4.

### 4.4 References

- (1) McGlade, C.; Ekins, P. The Geographical Distribution of Fossil Fuels Unused When Limiting Global Warming to 2 °C. *Nature* **2015**, *517* (7533), 187–190.
- (2) Bernstein, L.; Bosch, P.; Canziani, O.; Chen, Z.; Christ, R.; Davidson, O.; Hare, W.; Huq, S.; Karoly, D.; Kattsov, V.; Kundzewicz, Z. W.; Liu, J.; Lohmann, U.; Manning, M.; Matsuno, T.; Menne, B.; Metz, B.; Mirza, M.; Nicholls, N.; et al. *Climate Change 2007 : Synthesis Report : An Assessment of the Intergovernmental Panel on Climate Change*. IPCC : Geneva, Switzerland 2008.
- (3) *Global Energy & CO<sub>2</sub> Status Report 2019*, IEA, Paris; IEA (2019), 2019.
- (4) Masson-Delmotte, V.; Zhai, P.; Pörtner, H.-O.; Roberts, D.; Skea, J.; Shukla, P. R.; Pirani, A.; Moufouma-Okia, W.; Péan, C.; Pidcock, R. et al. *Global Warming of 1.5°C An IPCC Special Report*; 2018.
- (5) Nathan S. Lewis. Research Opportunities to Advance Solar Energy Utilization. *Science* (80-. ). **2016**, *351* (6271), aad1920-1–9.
- (6) Berardi, S.; Drouet, S.; Francàs, L.; Gimbert-Suriñach, C.; Guttentag, M.; Richmond, C.; Stoll, T.; Llobet, A. Molecular Artificial Photosynthesis. *Chem. Soc. Rev.* **2014**, *43* (22), 7501–7519.
- (7) Bard, A. J.; Fox, M. A. Artificial Photosynthesis: Solar Splitting of Water to Hydrogen and Oxygen. *Acc. Chem. Res.* **1995**, *28* (3), 141–145.
- (8) Nocera, D. G. Solar Fuels and Solar Chemicals Industry. *Acc. Chem. Res.* **2017**, *50* (3), 616–619.
- (9) Barber, J. Photosynthetic Energy Conversion: Natural and Artificial. *Chem. Soc. Rev.* **2009**, *38* (1), 185–196.
- (10) Melis, A. Photosynthesis-to-Fuels: From Sunlight to Hydrogen, Isoprene, and Botryococcene Production. *Energy Environ. Sci.* **2012**, *5* (2), 5531–5539.
- (11) Inoue, H.; Shimada, T.; Kou, Y.; Nabetani, Y.; Masui, D.; Takagi, S.; Tachibana, H. The Water Oxidation Bottleneck in Artificial Photosynthesis: How Can We Get Through It? An Alternative Route Involving a Two-Electron Process. *ChemSusChem* **2011**, *4* (2), 173–179.
- (12) Weinberg, D. R.; Gagliardi, C. J.; Hull, J. F.; Murphy, C. F.; Kent, C. A.; Westlake, B. C.; Paul, A.; Ess, D. H.; McCafferty, D. G.; Meyer, T. J. Proton-Coupled Electron Transfer. *Chem. Rev.* **2012**, *112* (7), 4016–4093.
- (13) Huynh, M. H. V.; Meyer, T. J. Proton-Coupled Electron Transfer. *Chem. Rev.* **2007**, *107* (11), 5004–5064.
- (14) Gagliardi, C. J.; Vannucci, A. K.; Concepcion, J. J.; Chen, Z.; Meyer, T. J. The Role of Proton Coupled Electron Transfer in Water Oxidation. *Energy Environ. Sci.* **2012**, *5* (7), 7704–7717.
- (15) Matheu, R.; Ertem, M. Z.; Benet-Buchholz, J.; Coronado, E.; Batista, V. S.; Sala, X.; Llobet, A. Intramolecular Proton Transfer Boosts Water Oxidation Catalyzed by a Ru Complex. *J. Am. Chem. Soc.* **2015**, *137* (33), 10786–10795.
- (16) Duan, L.; Bozoglian, F.; Mandal, S.; Stewart, B.; Privalov, T.; Llobet, A.; Sun, L. A Molecular Ruthenium Catalyst with Water-Oxidation Activity Comparable to That of Photosystem II. *Nat. Chem.* **2012**, *4* (5), 418–423.
- (17) Sander, A. C.; Schober, A.; Dechert, S.; Meyer, F. A Pyrazolate-Bridged Bis(Pentadentate) Ligand and Its Dinuclear Ruthenium Complex. *Eur. J. Inorg. Chem.* **2015**, *2015* (26), 4348–4353.
- (18) Radaram, B.; Ivie, J. A.; Singh, W. M.; Grudzien, R. M.; Reibenspies, J. H.; Webster, C. E.; Zhao, X. Water Oxidation by Mononuclear Ruthenium Complexes with TPA-Based Ligands. *Inorg. Chem.* **2011**, *50* (21), 10564–10571.
- (19) Rapaport, I.; Helm, L.; Merbach, A. E.; Bernhard, P.; Ludi, A. High-Pressure NMR Kinetics. Part 34. Variable-Temperature and Variable-Pressure NMR Kinetic Study of Solvent Exchange on Hexaaquaruthenium(3+) and -(2+) and Hexakis(Acetonitrile)Ruthenium(2+). *Inorg. Chem.* **1988**, *27* (5), 873–879.

- (20) Pelosin, P.; Gil-Sepulcre, M.; Garrido-Barros, P.; Moonshiram, D.; Benet-Buchholz, J.; Gimbert-Suriñach, C.; Llobet, A. Analysis of the Active Species Responsible for Water Oxidation Using a Pentanuclear Fe Complex. *iScience* **2020**, *23* (8), 101378.
- (21) Vereshchuk, N.; Matheu, R.; Benet-Buchholz, J.; Pipelier, M.; Lebreton, J.; Dubreuil, D.; Tessier, A.; Gimbert-Suriñach, C.; Z. Ertem, M.; Llobet, A. Second Coordination Sphere Effects in an Evolved Ru Complex Based on Highly Adaptable Ligand Results in Rapid Water Oxidation Catalysis. *J. Am. Chem. Soc.* **2020**, *142* (11), 5068–5077.
- (22) Wang, L.; Duan, L.; Wang, Y.; Ahlquist, M. S. G.; Sun, L. Highly Efficient and Robust Molecular Water Oxidation Catalysts Based on Ruthenium Complexes. *Chem. Commun.* **2014**, *50* (85), 12947–12950.
- (23) Pineda-Galvan, Y.; Ravari, A. K.; Shmakov, S.; Lifshits, L.; Kaveevivitchai, N.; Thummel, R.; Pushkar, Y. Detection of the Site Protected 7-Coordinate RuV = O Species and Its Chemical Reactivity to Enable Catalytic Water Oxidation. *J. Catal.* **2019**, *375*, 1–7.
- (24) Wang, Y.; Rinkevicius, Z.; Ahlquist, M. S. G. Formation of N-Oxide in the Third Oxidation of [RuII(Tpy)(L)(OH<sub>2</sub>)]<sup>2+</sup>. *Chem. Commun.* **2017**, *53* (41), 5622–5624.
- (25) Liu, Y.; Ng, S. M.; Yiu, S. M.; Lam, W. W. Y.; Wei, X. G.; Lau, K. C.; Lau, T. C. Catalytic Water Oxidation by Ruthenium(II) Quaterpyridine (Qpy) Complexes: Evidence for Ruthenium(III) Qpy-N,N'-Dioxide as the Real Catalysts. *Angew. Chemie - Int. Ed.* **2014**, *53* (52), 14468–14471.
- (26) Ertem, M. Z.; Concepcion, J. J. Oxygen Atom Transfer as an Alternative Pathway for Oxygen–Oxygen Bond Formation. *Inorg. Chem.* **2020**, *59* (9), 5966–5974.
- (27) Fulmer, G. R.; Miller, A. J. M.; Sherden, N. H.; Gottlieb, H. E.; Nudelman, A.; Stoltz, B. M.; Bercaw, J. E.; Goldberg, K. I. NMR Chemical Shifts of Trace Impurities: Common Laboratory Solvents, Organics, and Gases in Deuterated Solvents Relevant to the Organometallic Chemist. *Organometallics* **2010**, *29* (9), 2176–2179.
- (28) Facelli, J. C.; Pugmire, R. J.; Grant, D. M. Effects of Hydrogen Bonding in the Calculation of 15N Chemical Shift Tensors: Benzamide. *J. Am. Chem. Soc.* **1996**, *118* (23), 5488–5489.
- (29) Martin, G. E.; Hadden, C. E. Long-Range 1H–15N Heteronuclear Shift Correlation at Natural Abundance. *J. Nat. Prod.* **2000**, *63* (4), 543–585.
- (30) Pérez-Trujillo, M.; Nolis, P.; Parella, T. CN-HMBC: A Powerful NMR Technique for the Simultaneous Detection of Long-Range 1H,13C and 1H,15N Connectivities. *Org. Lett.* **2007**, *9* (1), 29–32.
- (31) Pourrioux, G.; Fagalde, F.; Katz, N. E.; Parella, T.; Benet-Buchholz, J.; Llobet, A. Synthesis, Spectroscopic and Electrochemical Characterization and Molecular Structure of Polypyridyl Ruthenium Complexes Containing 4,4'-Azobis(Pyridine). *Polyhedron* **2008**, *27* (13), 2990–2996.
- (32) Belton, P. S. J. B. Lambert and F. G. Riddell (Editors). The Multinuclear Approach to NMR Spectroscopy. D. Reidel, Dordrecht, 1983, Xvi + 548 Pp. Cloth: Dfl. 165.00, US \$72.00. *Org. Magn. Reson.* **1984**, *22* (5), 354.
- (33) Laihia, K.; Puzsko, A.; Kolehmainen, E.; Lorenc, J. Synthesis and NMR Characterization of Seven New Substituted Pyridine N-Oxides. *J. Mol. Struct.* **2008**, *889* (1), 371–375.
- (34) Thummel, R. P.; Jahng, Y. N-Oxides of 2,2':6',2"-Terpyridine. *J. Org. Chem.* **1985**, *50* (19), 3635–3636.
- (35) Li, Y.; Wu, X.-P.; Jiang, N.; Lin, M.; Shen, L.; Sun, H.; Wang, Y.; Wang, M.; Ke, X.; Yu, Z.; Gao, F.; Dong, L.; Guo, X.; Hou, W.; Ding, W.; Gong, X.-Q.; Grey, C. P.; Peng, L. Distinguishing Faceted Oxide Nanocrystals with 17O Solid-State NMR Spectroscopy. *Nat. Commun.* **2017**, *8* (1), 581.
- (36) Shen, L.; Wu, X.-P.; Wang, Y.; Wang, M.; Chen, J.; Li, Y.; Huo, H.; Hou, W.; Ding, W.; Gong, X.-Q.; Peng, L. 17O Solid-State NMR Studies of ZrO<sub>2</sub> Nanoparticles. *J. Phys. Chem. C* **2019**, *123* (7), 4158–4167.
- (37) Ashbrook, S. E.; Smith, M. E. Solid State 17O NMR—an Introduction to the Background Principles and Applications to Inorganic Materials. *Chem. Soc. Rev.* **2006**, *35* (8), 718–735.
- (38) Bignami, G. P. M.; Davis, Z. H.; Dawson, D. M.; Morris, S. A.; Russell, S. E.; McKay, D.; Parke,



## CHAPTER 4.

- R. E.; Iuga, D.; Morris, R. E.; Ashbrook, S. E. Cost-Effective  $^{17}\text{O}$  Enrichment and NMR Spectroscopy of Mixed-Metal Terephthalate Metal-Organic Frameworks. *Chem. Sci.* **2018**, *9* (4), 850–859.
- (39) Huo, H.; Peng, L.; Gan, Z.; Grey, C. P. Solid-State MAS NMR Studies of Brønsted Acid Sites in Zeolite H-Mordenite. *J. Am. Chem. Soc.* **2012**, *134* (23), 9708–9720.
- (40) Gao, Y.; Toubaei, A.; Kong, X.; Wu, G. Acidity and Hydrogen Exchange Dynamics of Iron(II)-Bound Nitroxyl in Aqueous Solution. *Angew. Chemie Int. Ed.* **2014**, *53* (43), 11547–11551.
- (41) Boykin, D. W.; Balakrishnan, P.; Baumstark, A. L.  $^{17}\text{O}$  NMR Spectroscopy of Heterocycles. Steric Effects for N-Oxides. *Magn. Reson. Chem.* **1985**, *23* (9), 695–697.
- (42)  $^{17}\text{O}$  chemical shifts <https://wissen.science-and-fun.de/chemistry/spectroscopy/17o-chemical-shifts/>.
- (43) Christ, H. A.; Diehl, P.; Schneider, H.; Dahn, H. Chemische Verschiebungen in Der Kernmagnetischen Resonanz von  $^{17}\text{O}$  in Organischen Verbindungen. *Helv. Chim. Acta* **1961**, *44* (3), 865–880.
- (44) Gimbert-Suriñach, C.; Moonshiram, D.; Francàs, L.; Planas, N.; Bernales, V.; Bozoglian, F.; Guda, A.; Mognon, L.; López, I.; Hoque, M. A.; Gagliardi, L.; Cramer, C. J.; Llobet, A. Structural and Spectroscopic Characterization of Reaction Intermediates Involved in a Dinuclear Co–Hbpp Water Oxidation Catalyst. *J. Am. Chem. Soc.* **2016**, *138* (47), 15291–15294.

## 4.5 Supporting Information

### 4.5.1 Experimental Section

#### 4.5.1.1 Materials and methods

All materials were provided by Sigma-Aldrich unless indicated otherwise. High-purity deionized water was obtained by passing distilled water through a Nanopure Milli-Q water purification system. Unless specifically written, reactions were carried out under rigorously anhydrous conditions and with a positive pressure of argon. Automated flash chromatography was performed on the Teledyne Isco CombiFlash Rf flash chromatography purification system using SiliCycle silica gel columns (24 or 40 g, 230–400 mesh 40–63  $\mu\text{m}$ ).

#### 4.5.1.2 General instrumentation

UV–Vis spectroscopy was performed on a Cary 50 Bio (Varian) UV–Vis spectrophotometer with 1 cm quartz cells unless indicated otherwise. A 400 MHz Bruker Avance II spectrometer and a Bruker Avance 500 MHz were used to carry out NMR spectroscopy. The pH of the solutions was determined by a pH meter (CRISON, Basic 20<sup>+</sup>) calibrated before measurements through standard solutions at pH= 4.01, 7.00, and 9.21.

#### 4.5.1.3 Preparation of 0.1 M ionic strength phosphate solutions (pbhf).

**pH = 7.0** buffered solution: solids of  $\text{NaH}_2\text{PO}_4$  (2.31 g, 0.0193 M) and  $\text{Na}_2\text{HPO}_4$  (3.77g, 0.0266 M) were dissolved in 1 L of deionized water.

#### 4.5.1.4 Electrochemical methods

##### General considerations

All electrochemical experiments were performed in an IJ-Cambria HI-730 bipotentiostat and IJ-Cambria CHI-660 potentiostat, using a three-electrode cell.  $E_{1/2}$  values reported in this work were estimated from Cyclic Voltammetry (CV) experiments as the average of the oxidative and reductive peak potentials  $(E_{p,o}+E_{p,c})/2$ . Glassy carbon disk (GC) ( $\phi = 0.3$  cm,  $S = 0.07$  cm<sup>2</sup>) was used as working electrode (WE), Mercury/Mercurous sulfate ( $\text{K}_2\text{SO}_4$  sat.) (MSE) as reference electrode (RE) (unless explicitly mentioned) and Pt disk as counter electrode (CE). Working electrode pretreatment before each measurement consisted of polishing with 0.05  $\mu\text{m}$  alumina paste, rinsing after with water and acetone, and blow-dried finally. CVs and DPVs were  $iR$  compensated (85%) by the potentiostat in all the

## CHAPTER 4.

measurements unless indicated. CV was recorded at a  $100 \text{ mV}\cdot\text{s}^{-1}$  scan rate unless explicitly expressed. All redox potentials in the present work are reported versus NHE by adding 0.65 V to the measured potential.<sup>1</sup>

### *Electrochemical cells*

A 15 mL vial was used as an electrochemical cell for CV measurements. A Teflon-made holder equipped for the three electrodes was used as a lid to ensure a reproducible distance between the electrodes. A two compartments cell (25 mL per compartment or 7 mL per compartment) with a separation grid was used for (Controlled Potential Electrolysis) CPE experiments.

### *Controlled potential electrolysis (CPE)*

A Pt grid was used as a WE, Pt grid as a CE, and a Mercury/Mercurous sulfate ( $\text{K}_2\text{SO}_4$  saturated) as a RE.  $iR$  compensation by the potentiostat was not applied in this technique.

#### 4.5.2 Synthetic Procedures and Analytical Data

Solvents were purified and dried by standard methods prior to use. Commercially available reagents were purchased from Sigma Aldrich and were used without purification. Reactions were carried out under anhydrous conditions and stream/positive pressure of argon. All reactions were monitored by TLC on commercially available pre-coated plates (Kieselgel 60 F254). Flash column chromatography was carried out using high purity grade (Merck grade 9385) pore size 60Å, 230-400 mesh particle size silica gel (Sigma Aldrich). Solvents used for chromatography were prior distilled on a Buchi Rotavapor R-220-SE.

##### 4.5.2.1 Synthesis and characterization of **5<sup>II</sup>**

**[Ru<sup>II</sup>(tPaO-κ-N<sup>2</sup>O<sub>p</sub>O<sub>c</sub>)(py)<sub>2</sub>]<sup>2-</sup>, **5<sup>III</sup>**. A sample of 5 mg of **1Cl** (0.008 mmol) was dissolved in 5 mL of a pH 7.6 phbf and placed in a bull electrolysis cell. A potential of 1.30 V was applied for 1 h. Then the pH was adjusted again to 7 and the potential was applied for 30 minutes more (see Figure S50) giving a green solution. Evaporation of the solvent to dryness gives a solid that contains **5<sup>III</sup>** and the initial phosphate salts.**

**[Ru<sup>II</sup>(tPaO-κ-N<sup>2</sup>O<sub>p</sub>O<sub>c</sub>)(py)<sub>2</sub>]<sup>3-</sup>, **5<sup>II</sup>**. All manipulations were carried out under Ar.**

*Chemical synthesis.* The solid of **5<sup>III</sup>** obtained in the previous synthesis was dissolved in 0.5 mL of D<sub>2</sub>O and then an excess of sodium ascorbate (5 mg) was added. **<sup>1</sup>H-NMR (500Hz, D<sub>2</sub>O)** δ 9.08 (dd, *J* = 8.3 Hz, 1H), 8.40 – 8.34 (m, 3H), 8.00 (m, 1H), 7.82 (m, 4H), 7.78 – 7.72 (m, 2H), 7.66 (m, 2H), 7.51 (m, 2H), 6.97 (m, 4H). **<sup>31</sup>P-NMR (203Hz, D<sub>2</sub>O)** δ 26.68 (1P, α), 10.16 (1P, β).

*Electrochemical synthesis.* The solid obtained in the previous synthesis was placed in a bulk electrolysis cell and dissolved in 1 mL of D<sub>2</sub>O. A potential of -0.1 V was applied for 150 minutes. **<sup>1</sup>H-NMR (500Hz\*, D<sub>2</sub>O)** δ 9.21 (d, *J* = 8.2 Hz, 1H), 8.39 – 8.33 (m, 3H), 8.00 (t, *J* = 8.1 Hz, 1H), 7.83 (m, 4H), 7.77 – 7.70 (m, 2H), 7.64 (m, 1H), 7.57 (m, 1H), 7.50 (m, 2H), 6.96 (m, 4H).

##### 4.5.2.2 Synthesis and characterization of 2,2':6',2''-Terpyridine,1,1''-dioxide

**2,2':6',2''-Terpyridine,1,1''-dioxide<sup>2</sup>**. To an ice-cooled solution of 2,2':6',2''-Terpyridine (391 mg, 1.67 mmol; 1 equiv) in 10 mL of dry DCM, was added metachloroperbenzoic acid (77%, 940 mg; 2.5 equiv.). After 30 min of stirring at rt, precipitation occurred. After 3h of stirring,

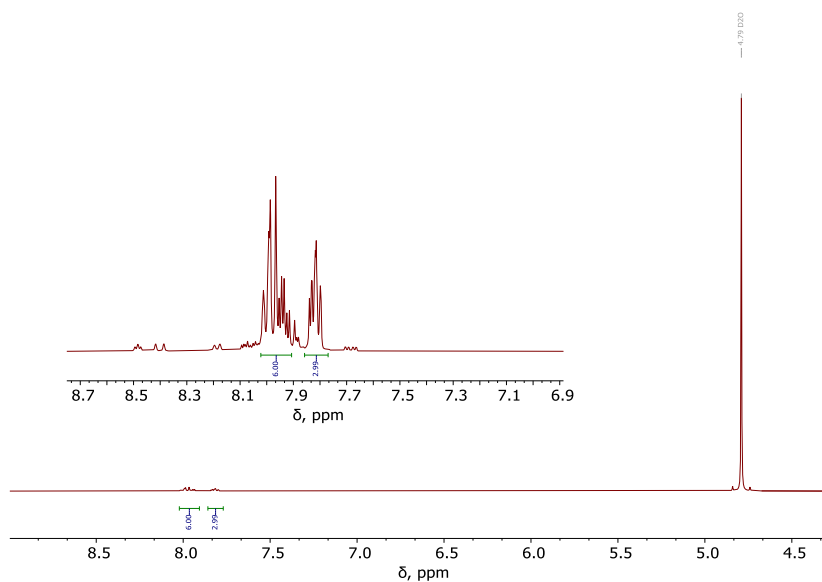
**CHAPTER 4.**

the TLC monitoring (DCM/MeOH : 95/5) showed partial conversion of the starting material, and another excess of mCPBA (188 mg; 0.5 equiv) was added and the reaction mixture was kept stirring for an additional time of 6 hours. The reaction mixture was diluted with DCM (30mL) and was quenched by a solution of saturated solution (30 mL). The resulting organic phase was subsequently washed with 30 mL of NaCl saturated solution and was dried over MgSO<sub>4</sub>. After concentration under *vacuo*, the resulting crude was purified over silica gel by column chromatography (DCM/MeOH: 95/5, then 90/10) affording the expected 2,2':6',2''-terpyridine,1,1''-dioxide as a white solid (271 mg; 61% yield).

**IV**

### 4.5.3 Spectral and Redox properties

#### 4.5.3.1 NMR characterization of the free ligand $tPa^{4-}$



IV

**Figure S1.**  $^1H$  NMR spectra of  $tPa^{4-}$  (free ligand) in  $D_2O$  with the addition of the 10% 1M NaOD at RT.

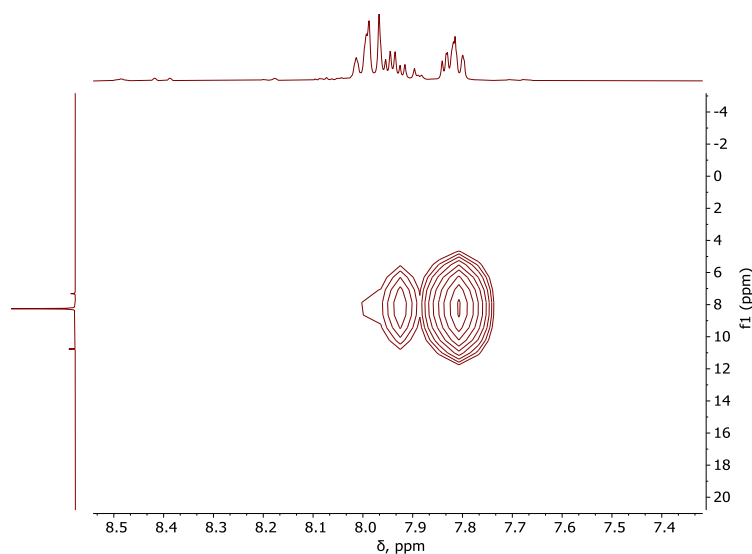


**Figure S2.**  $^1H$ - $^{31}P$  HMBC spectra of  $tPa^{4-}$  (free ligand) in  $D_2O$  with the addition of the 10% 1M NaOD at RT.

## CHAPTER 4.

### 4.5.3.2 NMR characterization of complex $5^{3-}$

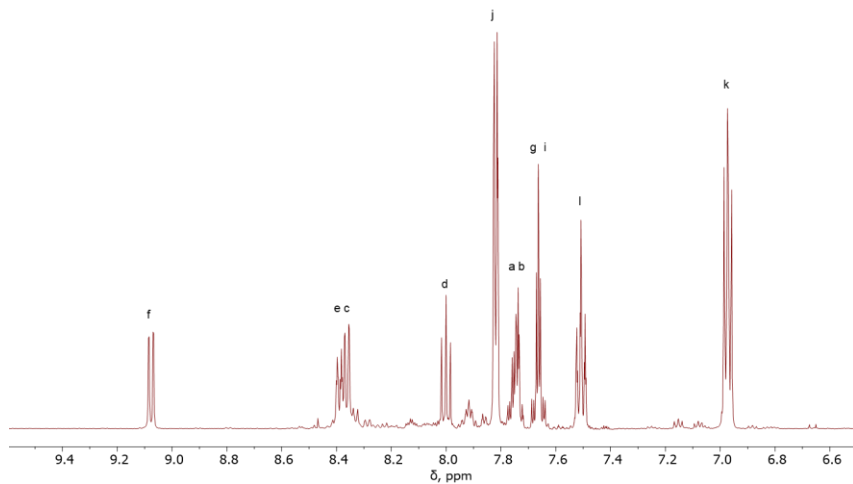


**Figure S3.**  $^1\text{H}$  NMR of  $4^{3-}$  in  $\text{D}_2\text{O}$  in the presence of sodium ascorbate at RT

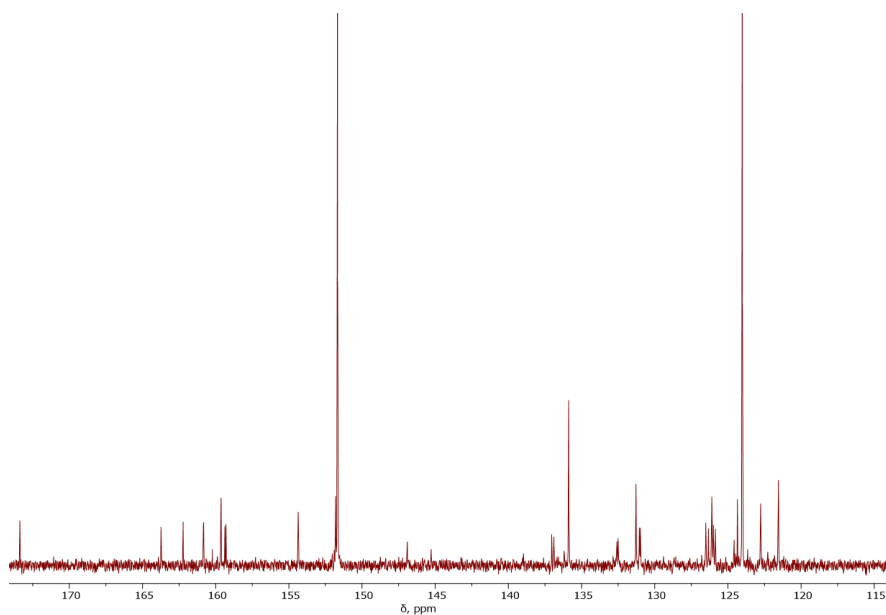
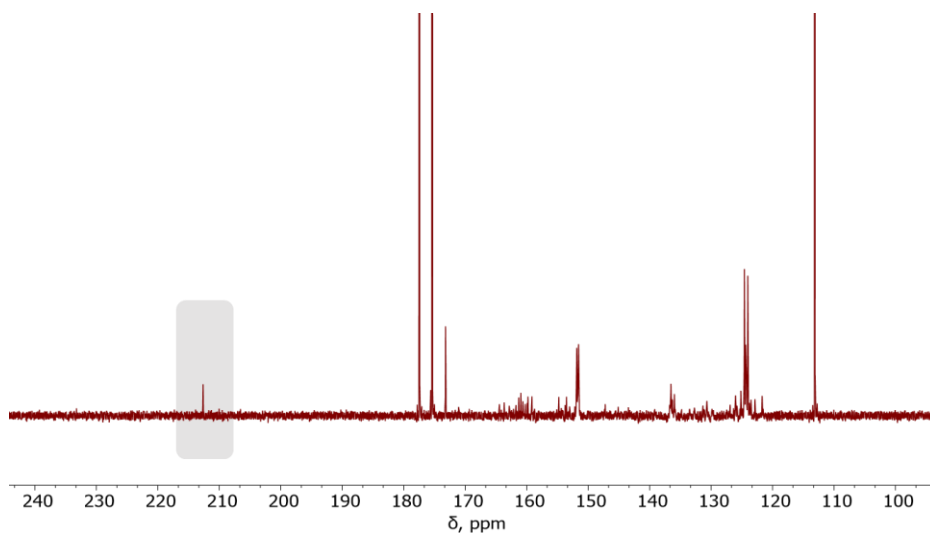


**Figure S4.**  $^{13}\text{C}$  NMR of  $4^{3-}$  in  $\text{D}_2\text{O}$  in the presence of sodium ascorbate at RT.



IV

**Figure S5.**  $^{13}\text{C}$  NMR (downfield) of  $4^{3-}$  in  $\text{D}_2\text{O}$  in the presence of sodium ascorbate at RT

#### 4.5.3.3 NMR characterization of related N-containing compounds

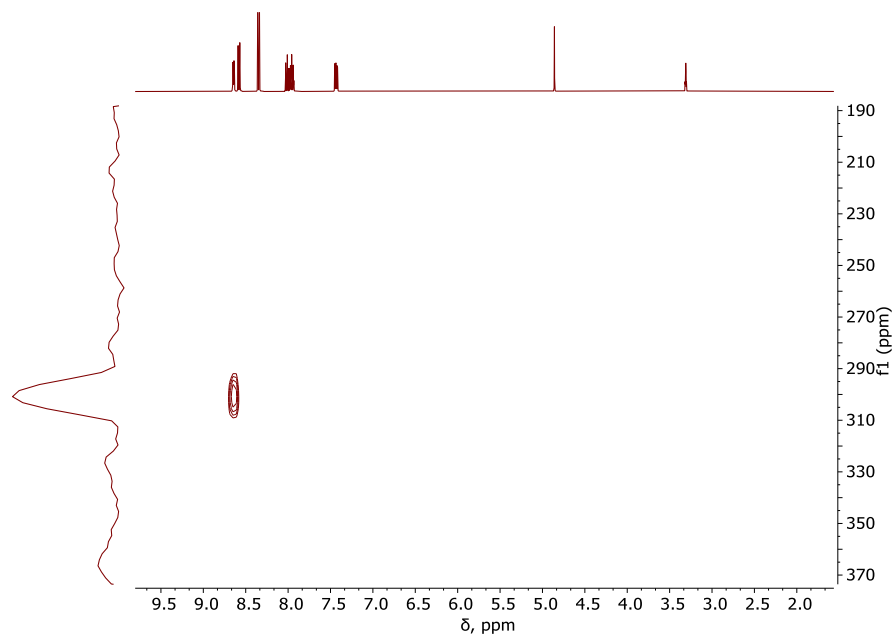


**Figure S6.**  $^1\text{H}$ - $^{15}\text{N}$  HMBC NMR of *trpy* in  $[\text{d}_4]$ -methanol at RT



## CHAPTER 4.

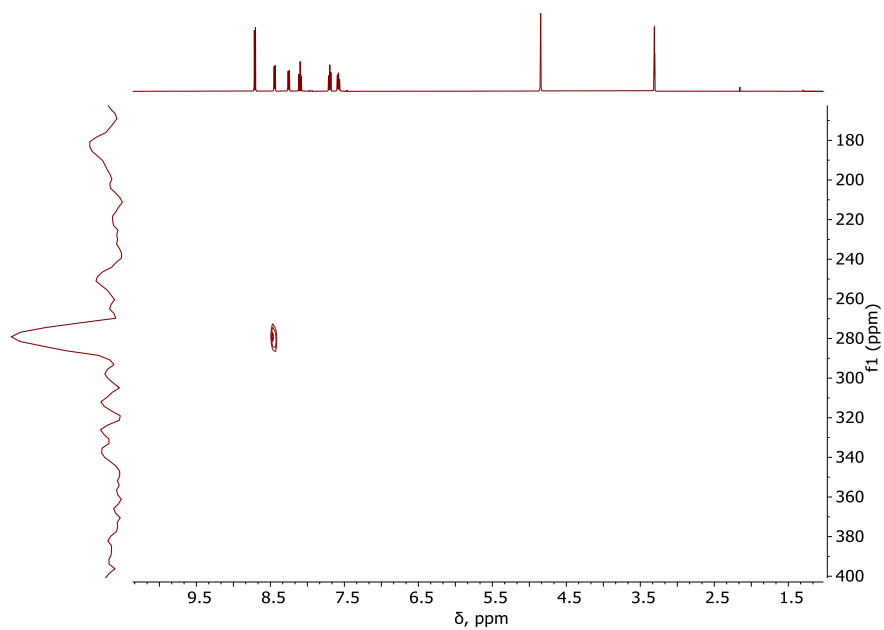


**Figure S7.**  $^1\text{H}$ - $^{15}\text{N}$  HMBC NMR of **trpy-NO,NO** in  $[\text{d}_4]$ -methanol at RT

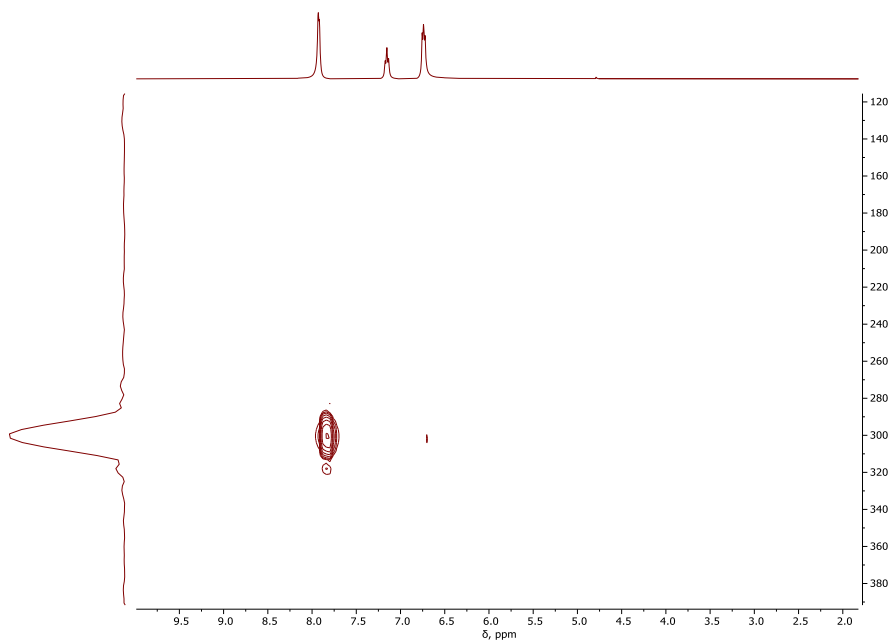


**Figure S8.**  $^1\text{H}$ - $^{15}\text{N}$  HMBC NMR of **py** in  $[\text{d}_2]$ -water at RT

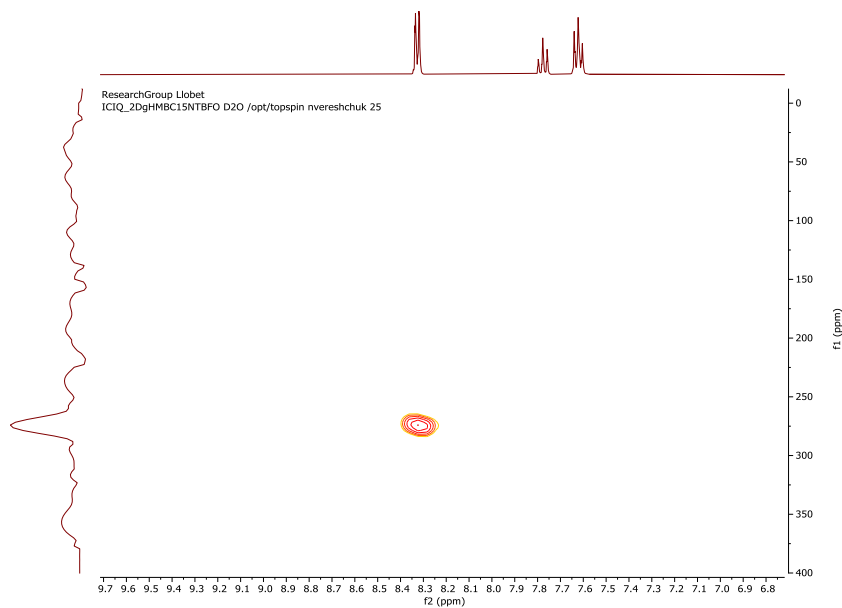


Figure S9.  $^1\text{H}$ - $^{15}\text{N}$  HMBC NMR of **py-NO** in  $[\text{d}_2]$ -water at RT

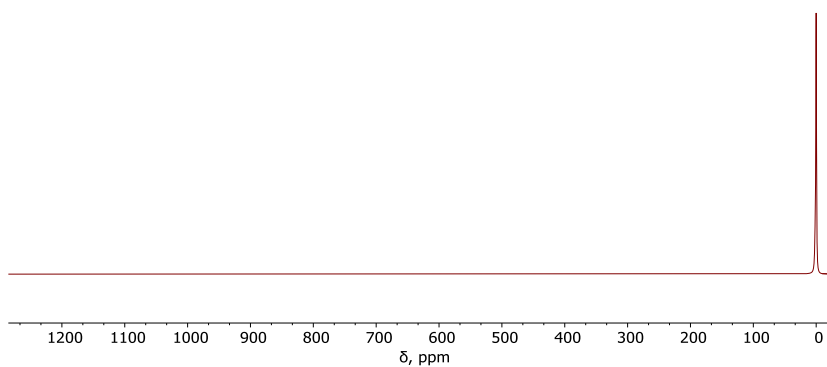
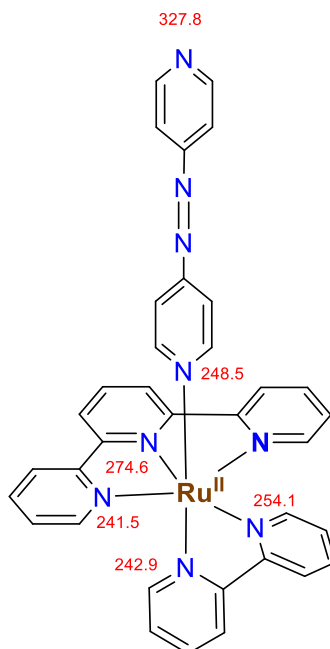


Figure S8.  $^{17}\text{O}$  NMR of **1** in 1 : 1 : 1 =  $\text{H}_2\text{O}^{17}$ :  $\text{D}_2\text{O}^{16}$  mixture at RT

## CHAPTER 4.

# IV



**Figure S9.** Chemical structure and chemical shift assignment for polypyridyl Ru complexes containing 4,4'-azobis(pyridine) ligand.<sup>4</sup>

**Scheme S1.** Proposed Strategy for the <sup>31</sup>P NMR with the labeling of a precursor.

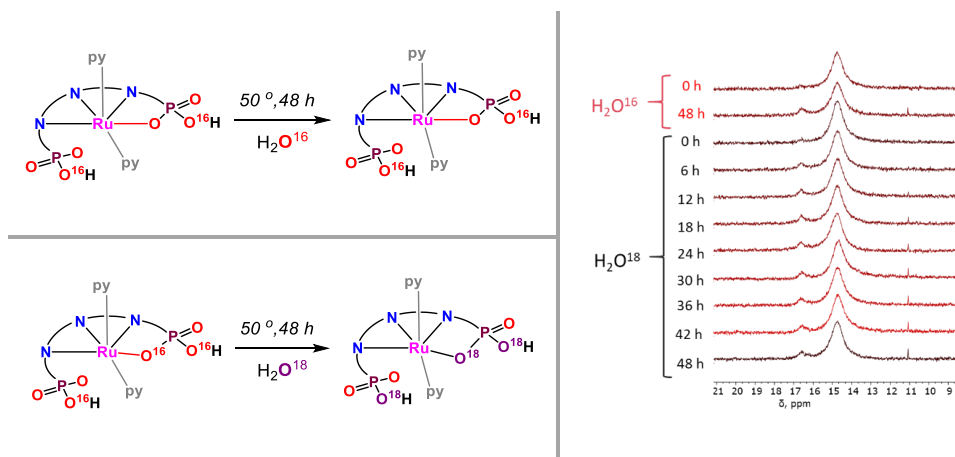
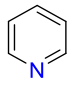
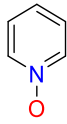
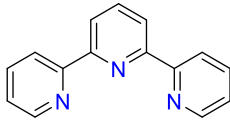
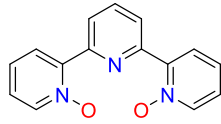
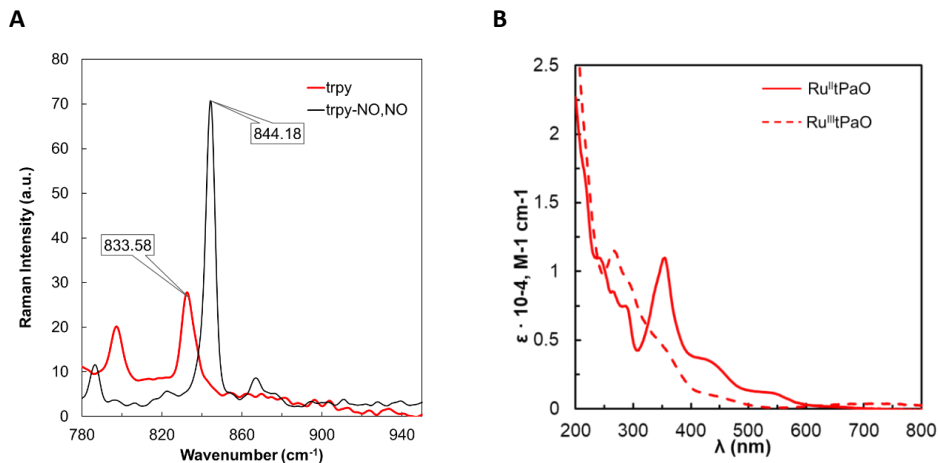


Table S1.  $^{15}\text{N}$  Chemical shift of the ligands discussed in this work.

$^{15}\text{N}$ shift					
	DMSO- $\text{d}_6$	<b>317</b>	<b>293</b>		
	$\text{D}_2\text{O}$	<b>300</b>	<b>274</b>		
	methanol- $\text{d}_4$			<b>300</b>	<b>280</b>

## CHAPTER 4.

### 4.5.3.4 Vibrational Spectroscopy



**Figure S10.** (A) The selected frequency range of FTIR-Raman of trpy and trpy-NO,NO. (B) UV-vis spectra of  $5^{II}$  (red solid) and  $5^{III}$  (red dashed) in a pH of 7.0 pbhf.

**Table S2.** Calculated shifts for the different Ru-O-R derivatives expected for a quantum-mechanical harmonic oscillator.

Experimental shift, $\text{cm}^{-1}$	Calculated shifts, $\text{cm}^{-1}$	
<b>24</b>	$\text{Ru}-\text{O}-\text{P}-\text{L}$ 	<b>29</b>
	$\text{Ru}-\text{O}-\text{N}-\text{L}$ 	<b>21</b>
	$\text{Ru}-\text{O}-\text{O}-\text{L}$ 	<b>22</b>
	$\text{Ru}-\text{O}-\text{C}-\text{L}$ 	<b>19</b>

4.5.3.5 Redox properties

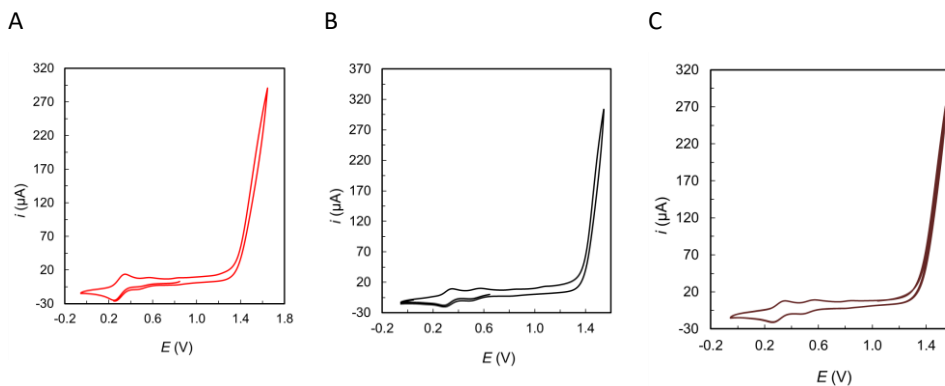


**Figure S11.** **A**, CV of the  $5^{\text{III}}$  after CPE at pH 7 in  $\text{H}_2\text{O}^{16}$  for rR measurements. **B**, CV of the  $5^{\text{III}}$  after CPE at pH 7 in  $\text{H}_2\text{O}^{18}$  for rR measurements. **C**, CV of the  $5^{\text{III}}$  after CPE at pH 7 in  $\text{H}_2\text{O}^{17}$  for  $^{17}\text{O}$  NMR measurements.

## CHAPTER 4.

### 4.5.4 References

- (1) Elgrishi, N.; Rountree, K. J.; McCarthy, B. D.; Rountree, E. S.; Eisenhart, T. T.; Dempsey, J. L. A Practical Beginner's Guide to Cyclic Voltammetry. *J. Chem. Educ.* **2018**, *95* (2), 197–206.
- (2) Thummel, R. P.; Jahng, Y. N-Oxides of 2,2':6',2''-Terpyridine. *J. Org. Chem.* **1985**, *50* (19), 3635–3636.
- (3) Belton, P. S. J. B. Lambert and F. G. Riddell (Editors). The Multinuclear Approach to NMR Spectroscopy. D. Reidel, Dordrecht, 1983, Xvi + 548 Pp. Cloth: Dfl. 165.00, US \$72.00. *Org. Magn. Reson.* **1984**, *22* (5), 354.
- (4) Pérez-Trujillo, M.; Nolis, P.; Parella, T. CN-HMBC: A Powerful NMR Technique for the Simultaneous Detection of Long-Range  $^1\text{H}$ ,  $^{13}\text{C}$  and  $^1\text{H}$ ,  $^{15}\text{N}$  Connectivities. *Org. Lett.* **2007**, *9* (1), 29–32.

## 5 CHAPTER 5

### **The Fate of Molecular Ru-phosphonate Water Oxidation Catalyst under Turnover Conditions**

---

*In the present work, we clarify the oxidative decay of a Ru-based WOC that was discussed in the previous two chapters. The work shows how pH and applied potential can affect the structural transformation of the catalyst as well as significant changes in the catalytic performance. Electrochemical methods, together with surface characterization techniques, have shown the complex mechanistic scenario, which consists of the coexistence of two catalytic mechanisms depending on the pH: a homogeneous pathway driven by the molecular complex and a heterogeneous pathway based on  $\text{RuO}_x$ .*

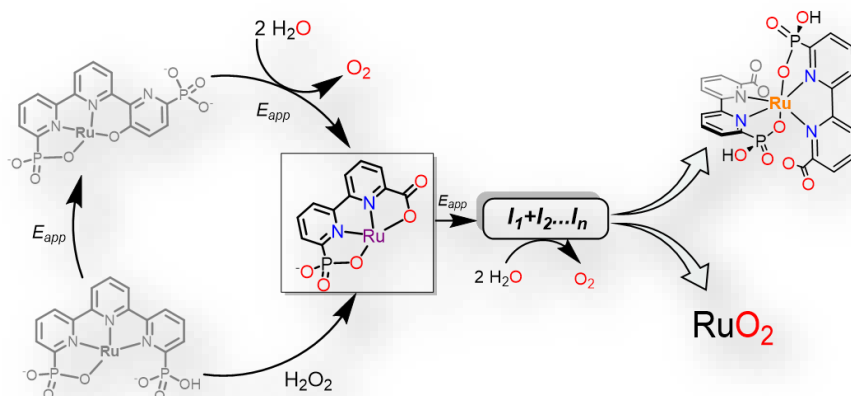
---



**The research results presented in this chapter were included in the following scientific publication:**

Vereshchuk, N.; Holub, J.; Gil-Sepulcre M.; Benet-Buchholz, J.; Llobet, A. **The Fate of Molecular Ru-phosphonate Water Oxidation Catalyst under Turnover Conditions** (*submitted*).

## The Fate of Molecular Ru-phosphonate Water Oxidation Catalyst under Turnover Conditions



### Abstract

The present chapter uncovers the oxidative transformations of a recently reported polypyridyl phosphonate-phenoxo Ru water oxidation catalyst  $[\text{Ru}^{\text{III}}(\text{tPaO}-\kappa\text{-N}^2\text{OPc})(\text{py})_2]^{2-}$  where  $\text{tPaO}^{5-}$  is the 3-(hydroxo-[2,2':6',2''-terpyridine]-6,6''-diyl)bis(phosphonate) ligand. Herein we describe how the catalyst  $[\text{Ru}^{\text{III}}(\text{tPaO}-\kappa\text{-N}^2\text{OPc})(\text{py})_2]^{2-}$  suffers oxidative degradation during water oxidation catalysis and generate the phosphonate-carboxylate Ru complex  $[\text{Ru}^{\text{II}}(\text{Hbpc})(\text{py})_2]$ , where  $\text{bpc}^{3-}$  is 6'-phosphono-[2,2'-bipyridine]-6-carboxylic. Complex  $[\text{Ru}^{\text{II}}(\text{Hbpc})(\text{py})_2]$  has been prepared by three different methods and its oxidative transformations were studied in detail. Through the electrochemical analysis of  $[\text{Ru}^{\text{II}}(\text{Hbpc})(\text{py})_2]$ , we discovered several transformations, that  $[\text{Ru}^{\text{II}}(\text{Hbpc})(\text{py})_2]$  is undergoing during catalysis and, consequently, forming the non-catalytic species  $[\text{Ru}^{\text{II}}(\text{bpc}-\kappa\text{-N}^2\text{OP})_2]$  and  $\text{RuO}_2$ . Herein presented electrochemical data provide strong evidence of the  $[\text{Ru}^{\text{III}}(\text{tPaO}-\kappa\text{-N}^2\text{OPc})(\text{py})_2]^{2-}$  oxidative transformations and support the proposed mechanistic scenario. Furthermore, the data also suggest the co-occurrence of two WOC paths: a homogeneous pathway driven by the molecular complex/generated intermediates and a heterogeneous pathway, based on  $\text{RuO}_2$ .

## CHAPTER 5.

### 5.1 Introduction

Water oxidation to molecular dioxygen is an essential reaction in biological systems that occurs in the Photosystem II (PSII) of green plants and cyanobacteria.<sup>1,2</sup> On the other hand is also one of the key reactions in artificial photosynthetic devices based on water splitting with sunlight, that can provide the clean and sustainable energy needed by our society.<sup>3-5</sup> In this context, molecular complexes are attractive as water oxidation catalysts (WOCs) since they can potentially provide working overpotentials that can be fine-tuned by ligand design and long term stability.<sup>6-10</sup> Indeed, one of the appealing features of molecular WOCs is the synthetic versatility provided by the ligand backbone, which allows tuning the electronic, steric, and supramolecular properties of the catalyst.<sup>11-14</sup> Besides, there is a wide range of spectroscopic and electrochemical techniques that can provide a thorough characterization of the reaction intermediates involved in the catalytic cycle, especially in the homogeneous phase.<sup>12,15-17</sup>

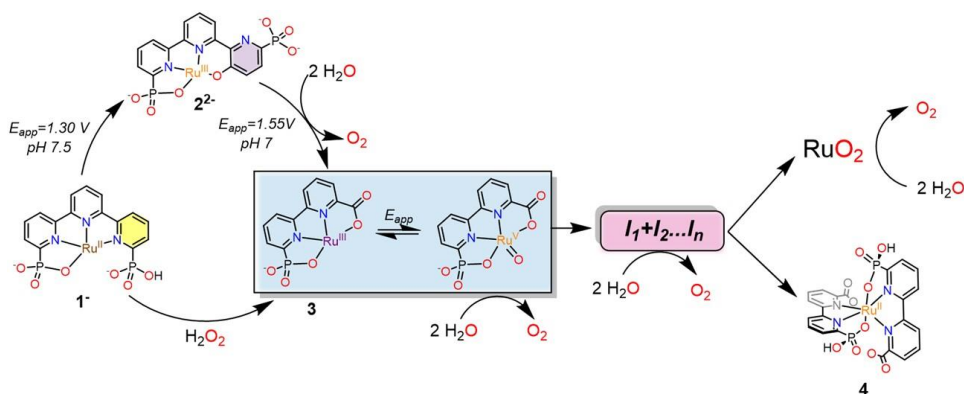
This, together with the accumulated knowledge in the field provides an ideal platform for the design of new molecular WOCs as well as the understanding of the reaction mechanisms they undergo. Further, it is also of paramount importance to identify and understand the factors that govern the activity and robustness of the catalyst,<sup>18,19</sup> which are indispensable to avoid deactivation pathways.<sup>20-28</sup> This is particularly important in order to incorporate these catalysts into complete photoelectrochemical cells (PEC) for the production of solar fuels based on water splitting.<sup>25,29-33</sup>

The best catalysts described up to now are based on the family of Ru complexes containing *fame* (Flexible Adaptive Multidentate Equatorial) ligands<sup>6,7,18</sup> and in particular the ones based on Ru-tda and Ru-bda.<sup>8,34</sup> Recently, we reported the complex  $[\text{Ru}^{\text{II}}(\text{HtPa-}\kappa\text{-N}^3\text{O})(\text{py})_2]^-$ , **1**<sup>-</sup>, which acts as a precursor of the water oxidation catalyst,  $[\text{Ru}^{\text{III}}(\text{tPaO-}\kappa\text{-N}^2\text{O}_p\text{Oc})(\text{py})_2]^{2-}$ , **2**<sup>2-</sup>.<sup>6</sup> We now report the behavior of the **2**<sup>2-</sup> under turnover conditions operating at different pHs and applied potentials.

## 5.2 Results and discussion

### 5.2.1 Synthesis of **3H**

We have previously shown that complex  $[\text{Ru}^{\text{II}}(\text{HtPa}-\kappa\text{-N}^3\text{O})(\text{py})_2]^-$ , **1<sup>-</sup>**, acts as a precursor for the generation of complex  $[\text{Ru}^{\text{III}}(\text{tPaO}-\kappa\text{-N}^2\text{O}_p\text{OC})(\text{py})_2]^{2-}$ , **2<sup>2-</sup>** under catalytic conditions at an applied potential of 1.30 V at pH 7.5, as indicated in the left-hand side of Scheme 1.



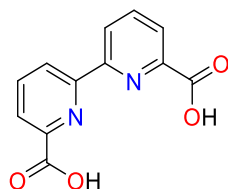
**Scheme 1.** Reactions and intermediates associated with the water oxidation catalyst precursor **1<sup>-</sup>**, under different conditions. Axial pyridine ligands for **1<sup>-</sup>**, **2<sup>2-</sup>** and **3** are not shown for simplicity reasons.

During this transformation, one of the pyridyl phosphonate arms of the  $\text{tPa}^{4-}$  ligand decoordinates, rotates, and finally undergoes an oxo-transfer forming the phenoxo group that coordinates to the metal center. This transformation can be easily monitored *via* Cyclic Voltammetry (CV) since the redox features of the initial and final compounds are radically different. At pH 7.0, two waves associated with the III/II and IV/III redox couples appear at  $E_{1/2} = 0.83$  and  $E_{1/2} = 0.92$  V respectively for **1<sup>-</sup>** (Figure 1, black trace) whereas for **2<sup>2-</sup>**, one wave appears at  $E_{1/2} = 0.31$  V, associated with the III/II couple, and an electrocatalytic wave in the range of 1.35 -1.60 V is observed. (Figure 1, blue trace). Under turnover conditions, **2<sup>2-</sup>** further evolves to another water oxidation catalyst  $[\text{Ru}^{\text{II}}(\text{Hbpc})(\text{py})_2]$ , **3H**, that contains a phosphonate and a carboxylate group bonded to the Ru metal center (see Scheme 1 and red trace in Figure 1) that has been previously reported as WOC at pH 1.0.<sup>7</sup> This step involves a ligand reorganization, the loss of a pyridyl phosphonate arm of  $\text{tPaO}^{5-}$  initial ligand and with the further oxidation of phenoxo moiety generating a carboxylate group. Complex **3H**

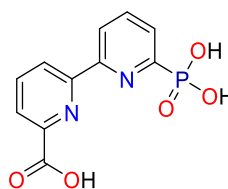
## CHAPTER 5.

is characterized by III/II redox couple at  $E_{1/2} = 0.59$  V and a water oxidation catalytic wave in the range of 1.30 - 1.60 V (Figure 1, red trace). The green trace in Figure 1 is associated with the partial transformation of  $2^{2-}$  into  $3^{-}$ , when a pH 7.0 solution of  $2^{2-}$  is exposed to an applied potential of  $E_{app} = 1.55$  V for 1 hour.

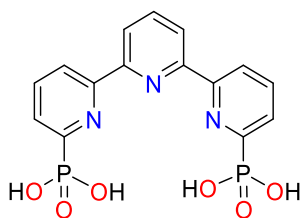
**Chart 1.** Drawing and labeling of ligands, which are discussed in this work.



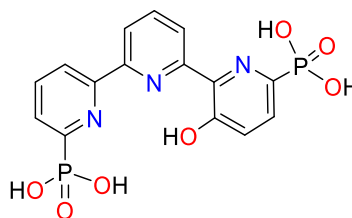
H<sub>2</sub>bda



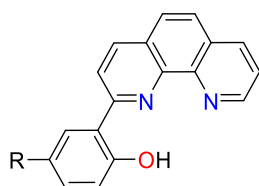
H<sub>3</sub>bpc



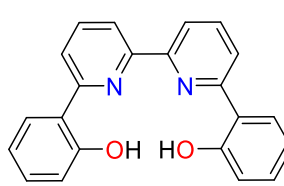
H<sub>4</sub>tPa



H<sub>5</sub>tPaO



HppO



H<sub>2</sub>L

It is interesting to realize the large degree of reorganization that occurs in the ligand framework when the tPaO<sup>5-</sup> ligand in  $2^{2-}$  is transformed into the bpc<sup>3-</sup> ligand in  $3^{-}$ . First, bimolecular oxidation of the phenolate group in  $2^{2-}$  by a Ru=O group of another  $2^{2-}$  molecule is needed to form a 3-pyridone group. Then, the latter must be a further attack by another Ru=O group, which after successive reactions lead to a formation of a carboxylate group. A similar pathway has been proposed for the Ru complex [Ru(L)(pic)<sub>2</sub>], **5**, (L = 6,6'-bis(2-hydroxyphenolate)-2,2'-bipyridine),<sup>35,36</sup> containing phenolates as coordinating groups.

Upon oxidation, this complex further evolves to the corresponding bis-carboxylate complex  $[\text{Ru}(\text{bda})(\text{pic})_2]$ , **6**, where both phenolates are transformed into carboxylates. A similar transformation from phenolate to carboxylate was also recently described by Thummel *et al.*<sup>37</sup> for a related Ru complex  $[\text{Ru}(\text{trpy})(\text{ppO})]^+$  (see Chart 1 for the drawings of the ligands).

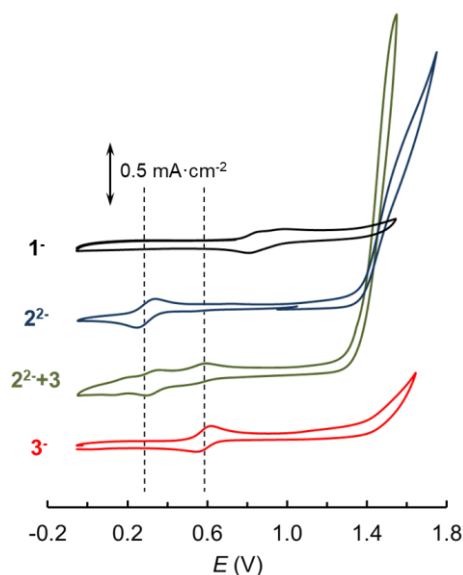


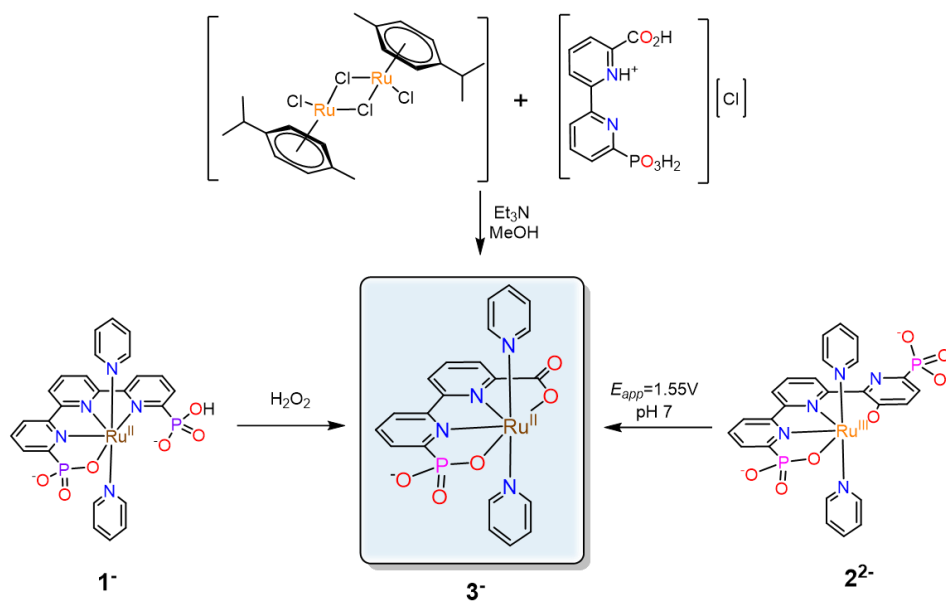
**Figure 1.** Cyclic voltammetry at pH 7.0 in a 0.1 M phosphate buffer (phbf) aqueous solution of:  $[\text{Ru}^{\text{II}}(\text{HtPa}-\kappa\text{-N}^3\text{O})(\text{py})_2]$ , **1**<sup>-</sup> (black trace);  $[\text{Ru}^{\text{III}}(\text{tPaO}-\kappa\text{-N}^2\text{O}_p\text{Oc})(\text{py})_2]^{2-}$ , **2**<sup>2-</sup> (blue trace);  $[\text{Ru}^{\text{II}}(\text{Hbpc})(\text{py})_2]$ , **3**<sup>-</sup> (red trace); and a mixture of **2**<sup>2-</sup> and **3**<sup>-</sup> (green trace) obtained from the CPE electrolysis of **2**<sup>2-</sup> at 1.55 V (see text for details).

As indicated in Scheme 2, complex  $[\text{Ru}^{\text{III}}(\text{bpc})(\text{py})_2]$ , **3**, can be prepared directly from the H<sub>3</sub>bpc ligand and a Ru precursor such as  $\{[\text{Ru}(\text{Cl})(p\text{-cymene})]_2(\mu\text{-Cl})_2\}$  (Figures S1-7),<sup>7</sup> by adding an excess of H<sub>2</sub>O<sub>2</sub> to **1** (see Figures S8 and S14) and electrochemically as indicated in the previous paragraph. The electrochemical synthesis can be carried out by multiple CV cycling or *via* Controlled Potential Electrolysis (CPE). The degree of transformation from **2**<sup>2-</sup> to **3** using the electrochemical methods depends on the pH and the applied potential. The higher the pH and  $E_{\text{app}}$  the faster the transformation as can be seen in Figure S9 in the Supporting Information. This degree of transformation can be easily monitored by cyclic



## CHAPTER 5.

voltammetry, see Figure 1, following the III/II redox couples of **2<sup>2-</sup>** and **3** at pH 7.0 that appear at 0.31 V and 0.59 V, respectively.



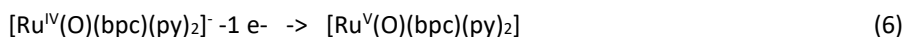
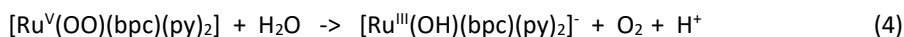
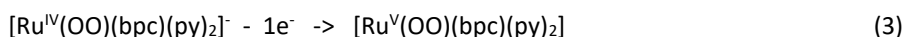
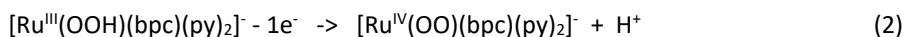
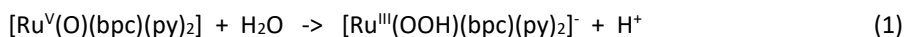
**Scheme 2.** Synthetic routes for the preparation of [Ru<sup>II</sup>(bpc)(py)<sub>2</sub>]<sup>-</sup>, **3<sup>-</sup>** complex.

### 5.2.2 Evolution of 3H under turnover conditions

The catalytic performance of [Ru<sup>II</sup>(bpc)(py)<sub>2</sub>]<sup>-</sup>, **3<sup>-</sup>**, as a water oxidation catalyst was studied by electrochemical techniques including multiple cyclic voltammetry and CPE at pH 1.0 and pH 7.0 and by UV-Vis spectroscopy. The results are reported in Figures 2-4.

#### a) pH 7

In Figure 2A-2D, are shown multiple consecutive CVs at pH 7.0 of **3<sup>-</sup>** in the potential range of 0.35 V and 1.55 V. The first reversible wave at 0.59 V is associated with III/II redox couple whereas the one in the range of 1.30-1.59 V is responsible for electrocatalytic water oxidation activity. The latter includes presumably a slow IV/III wave and a second wave involving the V/IV species. The Ru(V) species are in general highly reactive for this type of complexes<sup>7,26,38-42</sup> and is generally associated with the O-O bond formation step as well as for setting off the catalytic process.<sup>43-45</sup> The following step indicated in the equations below are proposed to occur in this catalytic cycle,



base on previously reported mechanistic analysis for this<sup>7</sup> and related complexes.<sup>10,46,47</sup> The suggested IV/III wave is proposed since the Ru(IV)=O species of this type of complexes are either not capable of oxidizing water to dioxygen or they do very slowly *via* disproportionation.<sup>48</sup> Additional oxidation to Ru(V)=O is generally needed to achieve fast water oxidation kinetics.

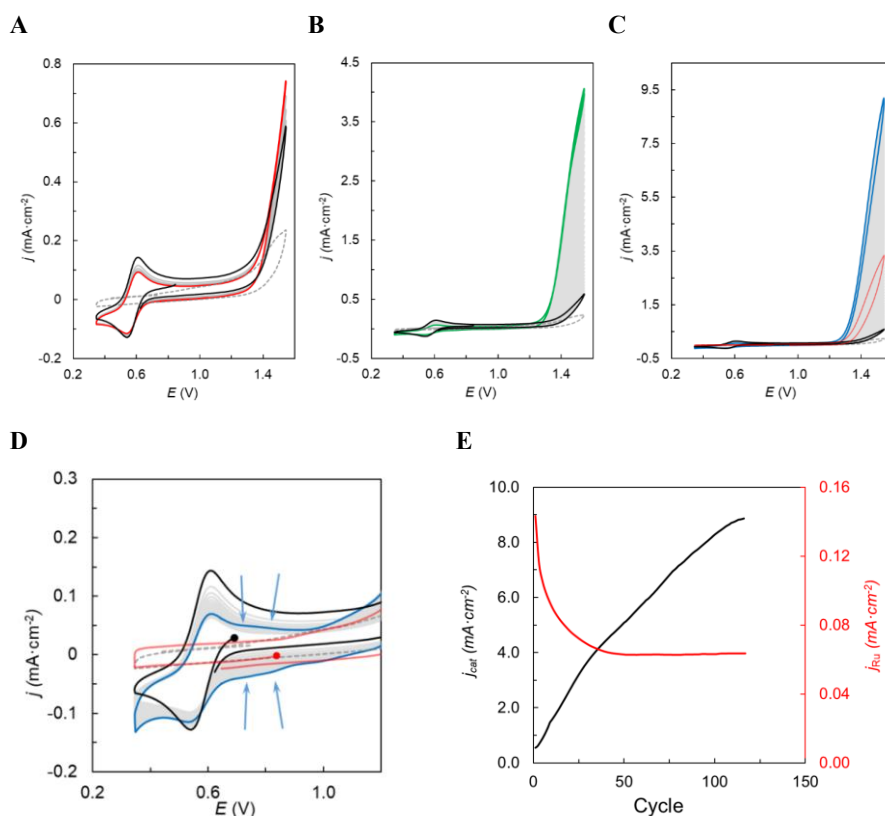


**Figure 2.** Consecutive CVs in an aqueous solution containing 0.1 mM of **3**<sup>-</sup> at pH 7.0 pbhf ( $V_i = 0.85$  V,  $V_{c1} = 0.35$  V;  $V_{c2} = 1.55$  V). **A**, 1<sup>st</sup> cycle (black solid) - 5<sup>th</sup> cycle (red solid line). **B**, 1<sup>st</sup> (black line) - 40<sup>th</sup> (green solid line). **C**, 1<sup>st</sup> (black solid line) - 125<sup>th</sup> (blue solid line). The red



## CHAPTER 5.

line corresponds to the CV of the working electrode after 125 cycles, immersed in a catalyst-free electrolyte solution. **D**, enlargement of the 0.3-1.1 V range from Figure 2C. **E**, a plot of current intensity at 0.60 (solid red) and 1.55 V (solid black) vs. the number of cycles. Intermediate cycles and blank experiments for A, B, C, and D are displayed in solid and dashed grey, respectively.

Figure 2A also shows the result of five consecutive CV cycles. At this stage, it can be clearly observed that the Ru(III/II) couple loses intensity whereas the catalytic current increases. This is an indication that the initial  $\mathbf{3}^-$  species are slowly consumed and transformed into unknown species that are more catalytically active than the initial species. Indeed, Figure 2B shows 40 consecutive cycles where this phenomenon is strongly manifested, as is also the case in Figure 2C with 125 consecutive scans. Figure 2C (red trace) also shows the electrochemical response of the glassy carbon electrode under the same conditions after the 125 consecutive cycles but in a catalyst-free electrolyte solution and after rinsing with water. In this CV, the III/II wave of  $\mathbf{3}^-$  is completely gone and only a large catalytic wave is observed at 1.40 V, which is the typical response of  $\text{RuO}_2$  absorbed at the surface of an electrode (Figure 2D). It thus points out that under applied turnover conditions the initial  $\mathbf{3}^-$  complex completely degrades all the way to  $\text{RuO}_2$ . Interestingly, Figure 2C shows that the intensity of the catalytic wave at 1.55 V is about a third of the intensity after 125 cycles and thus indicates that the rest of the activity comes from molecular species still present at the double layer. An interesting feature of this system is uncovered by observing how the III/II redox couple and the current density at 1.55 V changes at each CV cycle, as depicted in Figure 2E. Up to the first 50 cycles, the current intensity in both cases increases as the number of cycles increases. Then after further cycling, the III/II wave intensity remains constant while the catalytic current continues to increase. This combined with the fact that  $\text{RuO}_2$  is only responsible for about 30% of current density suggests, that there is a progressive transformation of the initial  $\mathbf{3}^-$  species into other species that are more active than the initial  $\mathbf{3}^-$ . This is graphically depicted in Scheme 1, where these active species are labeled as  $\text{I}_1$ ,  $\text{I}_2$ ,  $\text{I}_n$ . The nature of these species is unknown, but they should be halfway between  $\mathbf{3}^-$  and  $\text{RuO}_2$ , and thus point out to potential partly oxidized ligand with the different number of Ru-O type of groups,  $[(\text{L}')_2\text{Ru}-(\text{O}_x\text{H}_y)_n]^{m+}$ . The existence of these

molecular species can be further confirmed by carefully observing the CV in the range of the non-catalytic wave. Indeed, a zoom-in of this region (Figure 2D, blue trace; 125 consecutive cycles) shows the presence of additional electroactive species indicated by the blue arrows.

Further, we have also found evidence of the generation of inactive species such as  $[\text{Ru}^{\text{II}}(\text{bpc}-\kappa\text{-N}^2\text{O}_p)_2]$ , **4**, (see crystal structure in Figure 5) that precipitates out of a solution after CPE experiments that will be described in the next section. Curiously, the potential for the III/II redox couple of **4**, occurs at 0.70 V, which is very similar to that of the initial **3H** complex.

#### *b) pH 1*

The performance of **3H** was also studied at pH 1.0 and the main results are presented in Figures 3 and 4. At pH 1.0 the III/II couple for **3H** appears at  $E_{1/2} = 0.71$  V, a weak wave associated with the IV/III wave appears at 1.43 V and a catalytic wave in the range of 1.50 - 1.65 V. As was the case at pH 7.0, multiple cycling in the range of 0.15 to 1.65 V reveals an increase of the catalytic current as the cycling increases indicating the formation of new more active species. The latter can be clearly observed after 150 consecutive CV cycles as shown in the green trace of Figure 3B. As opposed to the previous case, the CV of the glassy carbon electrode after these 150 cycles in a clean electrolyte solution shows no active species attached to the electrode. The latter does not discard the potential formation of  $\text{RuO}_2$  since at pH 1.0 the latter is soluble and thus might be forming, but not adsorbing at the surface of the electrode. In contrast to the multiple cycling at pH 7.0, here the III/II couple remains constant over the consecutive cycling (see Figure 3C) while the catalytic wave at 1.64 V progressively increases as the number of CV cycles increases.

CHAPTER 5.

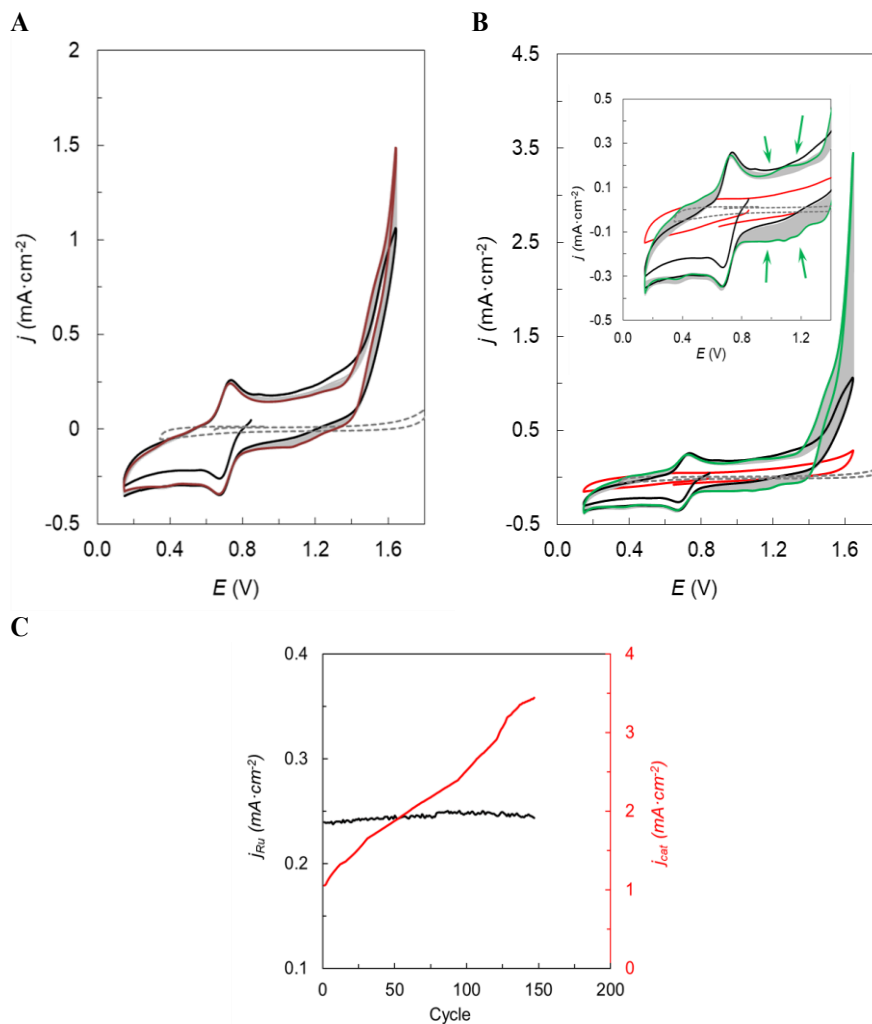


**Figure 3.** Consecutive CVs in an aqueous solution containing 0.1 mM of  $\mathbf{3}^-$  at pH 1.0 in a 0.1 M HTfO aqueous solution ( $V_i = 0.85$  V,  $V_{c1} = 0.15$  V;  $V_{c2} = 1.65$  V). **A**, 1<sup>st</sup> cycle (black solid) - 25<sup>th</sup> cycle (red solid line). **B**, 1<sup>st</sup> (black solid line) - 150<sup>th</sup> (green solid line). The red line corresponds to the CV of the working electrode after 150 cycles, immersed in a catalyst-free electrolyte solution. Inset, enlargement of the 0.3-1.2 V range. **C**, a plot of current intensity at 0.72 (solid red) and 1.64 V (solid black) vs. a number of cycles. Intermediate cycles and blank experiments for A and B are displayed in solid and dashed grey, respectively.

This is again consistent with the fact that new species generated at the double layer, present electrocatalytic activity in a potential region similar to that of the original complex. Besides, the formation of the non-catalytic species  $[\text{Ru}^{\text{II}}(\text{bpc-}\kappa\text{-N}^2\text{O}_\text{P})_2]$ , **4**, that is obtained in a CPE at the same pH, presents a redox wave for the III/II couple at nearly the same potential as for **3H** at this pH, as can be observed in Figure 4A (See also Figure S10).

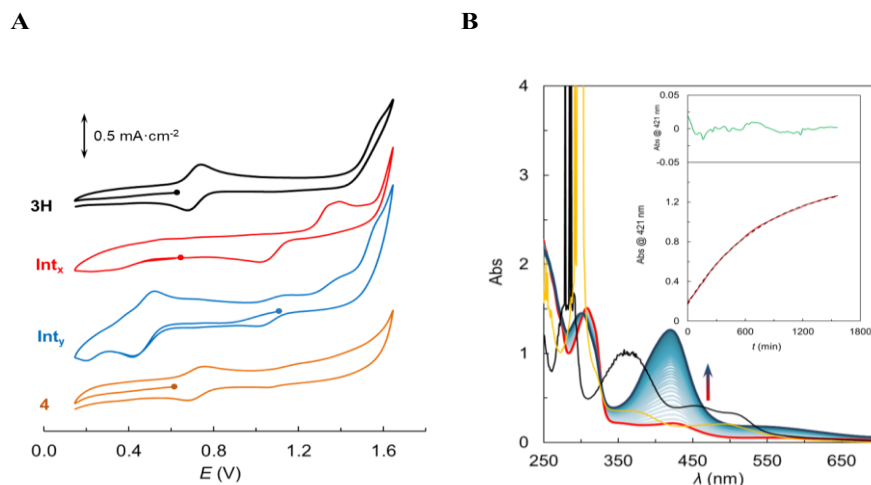


**Figure 4.** All experiments carried out in a pH = 1.0, 0.1 M HTFO aqueous solution. **A**, CV of 0.2 mM **3H** (black solid line). CV of **3H** after CPE at 1.55 V (red line) and CV of its evolution under air after 12 h (blue line). CV of **4** (yellow line). **B**, UV-vis spectrum of **3H** (black solid line). UV-Vis of 0.2 mM **3H** after CPE at 1.55 V (red line). UV-Vis spectra of the evolution of the latter under air over 12 h (initial, red line; final, deep blue line; intermediate every 20 minutes, blue lines). The inset shows the absorption changes of this evolution at  $\lambda = 421$  nm vs. time for 25 hours (solid red line) and its mathematical fit (dashed black line; top green line, residuals) assuming pseudo first-order kinetics equation,  $A \rightarrow B$  ( $\text{Ru(IV)} + \text{H}_2\text{O} \rightarrow \text{Ru(II)} + \text{O}_2$ ). UV-Vis of **4** (yellow line).

To further characterize the complex reactions that involve the generation of high oxidation state species from **3H** under catalytic conditions, a CPE experiment was carried out at pH 1.0 at an  $E_{\text{app}} = 1.55$  V (See Figure S11). Figure 4A shows the CV before (black trace) and immediately after (red trace) the CPE experiment as well as their UV-Vis spectra in Figure 4B, using the same color code. The red trace in Figure 4A clearly shows that after CPE, the

## CHAPTER 5.

original species completely disappeared, and a new set of molecular species is generated as indicated by new waves in the 0.9 - 1.5 V range. Further evolution of the latter over long periods of time follows pseudo first-order kinetics, with very a clearly defined isobestic point at 328 nm, giving a  $k$  value of  $1.3 \times 10^{-3} \pm 0.0078 \text{ min}^{-1}$ , ( $t_{1/2} = 533 \text{ min}$ ; see Figure 4B and S13). The new species present electroactivity in the 0.2 - 0.6 V range and their UV-Vis spectroscopic features are illustrated in Figure 4B. The evolution of the species generated was also monitored *via* their open circuit potential (OCP) that changes from 1.19 V just after the CPE, to 0.90 V after 24h (see Figure S12). Based on these OCP values we assign this transformation as the slow oxidation of water by a Ru(V)=O type of species that is overall being reduced to Ru(III). A related phenomenon was also observed for [Ru(trpy)(bpp)(OH<sub>2</sub>)] complex.<sup>48</sup> These experiments show that at pH 1.0 when high oxidation state species are reached (as well as during turnover), the initial **3H** complex completely disappears but the catalytic activity increases. This suggests the formation of new intermediate species that are even more catalytically active than **3H**, as was also the case at pH 7.0, and that is graphically summarized in Scheme 1. Finally, leaving the solution standing for a few days generates the formation of a few crystals of **4**. Both UV-Vis and CV show that either this new species do not exist after the CPE or its concentration is extremely small. However, it indicates that at low oxidation states the newly formed species can deactivate *via* the generation of **4**. This is interesting because the formation of the latter uncovers the presence of an equilibrium between the catalytically active species and **4**. This necessarily involves a full decoordination of the bpc<sup>3-</sup> ligand, in order to be able to generate [Ru<sup>II</sup>(bpc- $\kappa$ -N<sup>2</sup>O<sup>P</sup>)<sub>2</sub>], **4**, as well as the formation of new Ru species that do not contain the initially coordinated ligand.

V

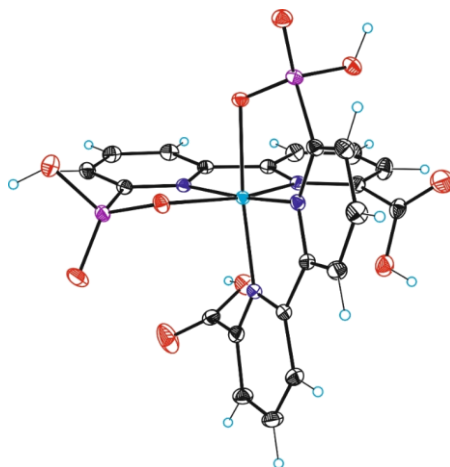


**Figure 5.** X-ray structure ORTEP view (ellipsoid at 50%probability) of **4**. Color code: Ru, cyan; N, blue; O, red; C, black; P, purple; H, empty blue circle.

Complex **4**, possess a pseudo-octahedral type of coordination, as expected for a low spin high field Ru(II) with the  $bpc^{3-}$  ligand coordinated in a  $\kappa^3$  fashion with the two pyridyls and the phosphonate bonded to Ru while the carboxylates are dangling and non-bonded to the Ru center (See Figure 5).

### 5.3 Conclusions

In the present work, we have shown how the polypyridyl phosphonate-phenoxo Ru water oxidation catalyst  $[Ru^{III}(tPaO-\kappa-N^2O_POC)(py)_2]^{2-}$ , **2<sup>2-</sup>**, undergoes oxidative degradation in the course of catalysis generating the phosphonate-carboxylate Ru complex  $[Ru^{II}(Hbpc)(py)_2]$ , **3H**. This transformation occurs due to the relative facile oxidation of the phenoxo group to pyridone, which in turn experience several further transformations all the way to **3H**. The latter is also a WOC, undergoing further transformations during electrocatalytic activity all the way to  $RuO_2$ , *via* a number of highly active WOC molecular intermediates. This transformation uncovers a large degree of reorganization from the original catalyst that involves complete ligand loss, but also the generation of stable and highly performing species as WOCs denoted generically as  $I_n$  (see Scheme 1), and whose molecular nature is under investigation in our laboratories. Overall, these results manifest the importance of the ligand selection in order to come up with rugged and performing WOCs.

## CHAPTER 5.

The present work clearly indicates that the pyridyl carboxylate type of ligands turns out to be much more stable than the corresponding phosphonate derivate. It is difficult to further extend this comparison to other groups since, in most of the reported literature related to molecular WOCs, a similar study under heavy-duty conditions is not generally performed. Finally, this work highlights the need to carry out this type of detailed analysis on the performance of a molecular WOC under turnover conditions not only to decipher the nature of the active species but also for its successful implementation into a technologically useful photoelectrochemical cell for the generation of solar fuels.

## 5.4 References

- (1) Mirkovic, T.; Ostroumov, E. E.; Anna, J. M.; van Grondelle, R.; Govindjee; Scholes, G. D. Light Absorption and Energy Transfer in the Antenna Complexes of Photosynthetic Organisms. *Chem. Rev.* **2017**, *117* (2), 249–293.
- (2) Eaton-Rye, J. J.; Tripathy, B. C.; Sharkey, T. D., E. *Photosynthesis: Plastid Biology, Energy Conversion and Carbon Assimilation; Advances in Photosynthesis and Respiration*, Vol.34.; Springer: Dordrecht, The Netherlands: The Netherlands, 2012.
- (3) McEvoy, J. P.; Brudvig, G. W. Water-Splitting Chemistry of Photosystem II. *Chem. Rev.* **2006**, *106* (11), 4455–4483.
- (4) Melis, A. Photosynthesis-to-Fuels: From Sunlight to Hydrogen, Isoprene, and Botryococcene Production. *Energy Environ. Sci.* **2012**, *5* (2), 5531–5539.
- (5) Berardi, S.; Drouet, S.; Francàs, L.; Gimbert-Suriñach, C.; Guttentag, M.; Richmond, C.; Stoll, T.; Llobet, A. Molecular Artificial Photosynthesis. *Chem. Soc. Rev.* **2014**, *43* (22), 7501–7519.
- (6) Vereshchuk, N.; Matheu, R.; Benet-Buchholz, J.; Pipelier, M.; Lebreton, J.; Dubreuil, D.; Tessier, A.; Gimbert-Suriñach, C.; Z. Ertem, M.; Llobet, A. Second Coordination Sphere Effects in an Evolved Ru Complex Based on Highly Adaptable Ligand Results in Rapid Water Oxidation Catalysis. *J. Am. Chem. Soc.* **2020**, *142* (11), 5068–5077.
- (7) Shaffer, D. W.; Xie, Y.; Szalda, D. J.; Concepcion, J. J. Lability and Basicity of Bipyridine-Carboxylate-Phosphonate Ligand Accelerate Single-Site Water Oxidation by Ruthenium-Based Molecular Catalysts. *J. Am. Chem. Soc.* **2017**, *139* (43), 15347–15355.
- (8) Matheu, R.; Ertem, M. Z.; Benet-Buchholz, J.; Coronado, E.; Batista, V. S.; Sala, X.; Llobet, A. Intramolecular Proton Transfer Boosts Water Oxidation Catalyzed by a Ru Complex. *J. Am. Chem. Soc.* **2015**, *137* (33), 10786–10795.
- (9) Matheu, R.; Garrido-Barros, P.; Gil-Sepulcre, M.; Ertem, M. Z.; Sala, X.; Gimbert-Suriñach, C.; Llobet, A. The Development of Molecular Water Oxidation Catalysts. *Nat. Rev. Chem.* **2019**, *3* (5), 331–341.
- (10) Shatskiy, A.; Bardin, A. A.; Oschmann, M.; Matheu, R.; Benet-Buchholz, J.; Eriksson, L.; Kärkäs, M. D.; Johnston, E. V.; Gimbert-Suriñach, C.; Llobet, A.; Åkermark, B. Electrochemically Driven Water Oxidation by a Highly Active Ruthenium-Based Catalyst. *ChemSusChem* **2019**, *12* (10), 2251–2262.
- (11) Ghaderian, A.; Holub, J.; Benet-Buchholz, J.; Llobet, A.; Gimbert-Suriñach, C. A Ru-Bda Complex with a Dangling Carboxylate Group: Synthesis and Electrochemical Properties. *Inorg. Chem.* **2020**, *59* (7), 4443–4452.
- (12) Gil-Sepulcre, M.; Böhrer, M.; Schilling, M.; Bozoglian, F.; Bachmann, C.; Scherrer, D.; Fox, T.; Spingler, B.; Gimbert-Suriñach, C.; Alberto, R.; Bofill, R.; Sala, X.; Luber, S.; Richmond, C. J.; Llobet, A. Ruthenium Water Oxidation Catalysts Based on Pentapyridyl Ligands. *ChemSusChem* **2017**, *10* (22), 4517–4525.
- (13) Shaffer, D. W.; Xie, Y.; Szalda, D. J.; Concepcion, J. J. Manipulating the Rate-Limiting Step in Water Oxidation Catalysis by Ruthenium Bipyridine–Dicarboxylate Complexes. *Inorg. Chem.* **2016**, *55* (22), 12024–12035.
- (14) Yang, J.; An, J.; Tong, L.; Long, B.; Fan, T.; Duan, L. Sulfur Coordination Effects on the Stability and Activity of a Ruthenium-Based Water Oxidation Catalyst. *Inorg. Chem.* **2019**, *58* (5), 3137–3144.
- (15) Ghaderian, A.; Franke, A.; Gil-Sepulcre, M.; Benet-Buchholz, J.; Llobet, A.; Ivanović-Burmazović, I.; Gimbert-Suriñach, C. A Broad View on the Complexity Involved in Water Oxidation Catalysis Based on Ru–Bpn Complexes. *Dalt. Trans.* **2020**.
- (16) Li, J.; Güttinger, R.; Moré, R.; Song, F.; Wan, W.; Patzke, G. R. Frontiers of Water Oxidation: The Quest for True Catalysts. *Chem. Soc. Rev.* **2017**, *46* (20), 6124–6147.



## CHAPTER 5.

- (17) Sandford, C.; Edwards, M. A.; Klunder, K. J.; Hickey, D. P.; Li, M.; Barman, K.; Sigman, M. S.; White, H. S.; Minter, S. D. A Synthetic Chemist's Guide to Electroanalytical Tools for Studying Reaction Mechanisms. *Chem. Sci.* **2019**, *10* (26), 6404–6422.
- (18) Garrido-Barros, P.; Gimbert-Suriñach, C.; Matheu, R.; Sala, X.; Llobet, A. How to Make an Efficient and Robust Molecular Catalyst for Water Oxidation. *Chem. Soc. Rev.* **2017**, *46* (20), 6088–6098.
- (19) Matheu, R.; Ertem, M. Z.; Gimbert-Suriñach, C.; Sala, X.; Llobet, A. Seven Coordinated Molecular Ruthenium–Water Oxidation Catalysts: A Coordination Chemistry Journey. *Chem. Rev.* **2019**, *119* (6), 3453–3471.
- (20) Kagalwala, H. N.; Tong, L.; Zong, R.; Kohler, L.; Ahlquist, M. S. G.; Fan, T.; Gagnon, K. J.; Thummel, R. P. Evidence for Oxidative Decay of a Ru-Bound Ligand during Catalyzed Water Oxidation. *ACS Catal.* **2017**, *7* (4), 2607–2615.
- (21) Moore, C. M.; Bark, B.; Szymczak, N. K. Simple Ligand Modifications with Pendent OH Groups Dramatically Impact the Activity and Selectivity of Ruthenium Catalysts for Transfer Hydrogenation: The Importance of Alkali Metals. *ACS Catal.* **2016**, *6* (3), 1981–1990.
- (22) Li, X.; Cui, Y.; Feng, Y.; Xie, Z.; Gu, J.-D. Reaction Pathways and Mechanisms of the Electrochemical Degradation of Phenol on Different Electrodes. *Water Res.* **2005**, *39* (10), 1972–1981.
- (23) Francàs, L.; Sala, X.; Benet-Buchholz, J.; Escriche, L.; Llobet, A. A Ru-Hbpp-Based Water-Oxidation Catalyst Anchored on Rutile TiO<sub>2</sub>. *ChemSusChem* **2009**, *2* (4), 321–329.
- (24) Matheu, R.; Francàs, L.; Chernev, P.; Ertem, M. Z.; Batista, V.; Haumann, M.; Sala, X.; Llobet, A. Behavior of the Ru-Bda Water Oxidation Catalyst Covalently Anchored on Glassy Carbon Electrodes. *ACS Catal.* **2015**, *5* (6), 3422–3429.
- (25) Radaram, B.; Ivie, J. A.; Singh, W. M.; Grudzien, R. M.; Reibenspies, J. H.; Webster, C. E.; Zhao, X. Water Oxidation by Mononuclear Ruthenium Complexes with TPA-Based Ligands. *Inorg. Chem.* **2011**, *50* (21), 10564–10571.
- (26) Xie, Y.; Shaffer, D. W.; Lewandowska-Andralojc, A.; Szalda, D. J.; Concepcion, J. J. Water Oxidation by Ruthenium Complexes Incorporating Multifunctional Bipyridyl Diphosphonate Ligands. *Angew. Chemie - Int. Ed.* **2016**, *55* (28), 8067–8071.
- (27) Duan, L.; Wang, L.; Li, F.; Li, F.; Sun, L. Highly Efficient Bioinspired Molecular Ru Water Oxidation Catalysts with Negatively Charged Backbone Ligands. *Acc. Chem. Res.* **2015**, *48* (7), 2084–2096.
- (28) Kärkäs, M. D.; Åkermark, B. Catalytic Water Oxidation by Ruthenium Complexes Containing Negatively Charged Ligand Frameworks. *Chem. Rec.* **2016**, *16* (2), 940–963.
- (29) Wang, J.-W.; Sahoo, P.; Lu, T.-B. Reinvestigation of Water Oxidation Catalyzed by a Dinuclear Cobalt Polypyridine Complex: Identification of CoOx as a Real Heterogeneous Catalyst. *ACS Catal.* **2016**, *6* (8), 5062–5068.
- (30) Pelosin, P.; Gil-Sepulcre, M.; Garrido-Barros, P.; Moonshiram, D.; Benet-Buchholz, J.; Gimbert-Suriñach, C.; Llobet, A. Analysis of the Active Species Responsible for Water Oxidation Using a Pentanuclear Fe Complex. *iScience* **2020**, *23* (8), 101378.
- (31) Kaeffer, N.; Morozan, A.; Fize, J.; Martinez, E.; Guetaz, L.; Artero, V. The Dark Side of Molecular Catalysis: Diimine–Dioxime Cobalt Complexes Are Not the Actual Hydrogen Evolution Electrocatalyst in Acidic Aqueous Solutions. *ACS Catal.* **2016**, *6* (6), 3727–3737.
- (32) Folkman, S. J.; Soriano-Lopez, J.; Galán-Mascarós, J. R.; Finke, R. G. Electrochemically Driven Water-Oxidation Catalysis Beginning with Six Exemplary Cobalt Polyoxometalates: Is It Molecular, Homogeneous Catalysis or Electrode-Bound, Heterogeneous CoOx Catalysis? *J. Am. Chem. Soc.* **2018**, *140* (38), 12040–12055.
- (33) Garrido-Barros, P.; Grau, S.; Drouet, S.; Benet-Buchholz, J.; Gimbert-Suriñach, C.; Llobet, A. Can Ni Complexes Behave as Molecular Water Oxidation Catalysts? *ACS Catal.* **2019**, *9* (5), 3936–3945.

- (34) Duan, L.; Bozoglian, F.; Mandal, S.; Stewart, B.; Privalov, T.; Llobet, A.; Sun, L. A Molecular Ruthenium Catalyst with Water-Oxidation Activity Comparable to That of Photosystem II. *Nat. Chem.* **2012**, *4* (5), 418–423.
- (35) Liu, Y.; Chen, G.; Yiu, S.-M.; Wong, C.-Y.; Lau, T.-C. Intermediates in the Oxidative Degradation of a Ruthenium-Bound 2,2'-Bipyridyl-Phenoxy Ligand during Catalytic Water Oxidation. *ChemCatChem* **2018**, *10* (3), 501–504.
- (36) Wang, Y.; Duan, L.; Wang, L.; Chen, H.; Sun, J.; Sun, L.; Ahlquist, M. S. G. Alkene Epoxidation Catalysts [Ru(Pdc)(Tpy)] and [Ru(Pdc)(Pybox)] Revisited: Revealing a Unique RuIV=O Structure from a Dimethyl Sulfoxide Coordinating Complex. *ACS Catal.* **2015**, *5* (7), 3966–3972.
- (37) Kagalwala, H. N.; Tong, L.; Zong, R.; Kohler, L.; Ahlquist, M. S. G.; Fan, T.; Gagnon, K. J.; Thummel, R. P. Evidence for Oxidative Decay of a Ru-Bound Ligand during Catalyzed Water Oxidation. *ACS Catal.* **2017**, *7* (4), 2607–2615.
- (38) Wang, L.; Duan, L.; Wang, Y.; Ahlquist, M. S. G.; Sun, L. Highly Efficient and Robust Molecular Water Oxidation Catalysts Based on Ruthenium Complexes. *Chem. Commun.* **2014**, *50* (85), 12947–12950.
- (39) Matheu, R.; Ertem, M. Z.; Gimbert-Suriñach, C.; Sala, X.; Llobet, A. Seven Coordinated Molecular Ruthenium-Water Oxidation Catalysts: A Coordination Chemistry Journey. *Chem. Rev.* **2019**, *119* (6), 3453–3471.
- (40) Polyansky, D. E.; Muckerman, J. T.; Rochford, J.; Zong, R.; Thummel, R. P.; Fujita, E. Water Oxidation by a Mononuclear Ruthenium Catalyst: Characterization of the Intermediates. *J. Am. Chem. Soc.* **2011**, *133* (37), 14649–14665.
- (41) Lebedev, D.; Pineda-Galvan, Y.; Tokimaru, Y.; Fedorov, A.; Kaeffer, N.; Copéret, C.; Pushkar, Y. The Key RuV=O Intermediate of Site-Isolated Mononuclear Water Oxidation Catalyst Detected by in Situ X-Ray Absorption Spectroscopy. *J. Am. Chem. Soc.* **2018**, *140* (1), 451–458.
- (42) Kärkäs, M. D.; Verho, O.; Johnston, E. V.; Åkermark, B. Artificial Photosynthesis: Molecular Systems for Catalytic Water Oxidation. *Chemical Reviews.* 2014, pp 11863–12001.
- (43) Shaffer, D. W.; Xie, Y.; Concepcion, J. J. O-O Bond Formation in Ruthenium-Catalyzed Water Oxidation: Single-Site Nucleophilic Attack: Vs. O-O Radical Coupling. *Chem. Soc. Rev.* **2017**, *46* (20), 6170–6193.
- (44) Clark, A. E.; Hurst, J. K. Mechanisms of Water Oxidation Catalyzed by Ruthenium Coordination Complexes. *Progress in Inorganic Chemistry.* November 16, 2011, pp 1–54.
- (45) Luque-Urrutia, J. A.; Solà, M.; Poater, A. The Influence of the PH on the Reaction Mechanism of Water Oxidation by a Ru(Bda) Catalyst. *Catal. Today* **2020**, *358*, 278–283.
- (46) Matheu, R.; Ghaderian, A.; Francàs, L.; Chernev, P.; Ertem, M. Z.; Benet-Buchholz, J.; Batista, V. S.; Haumann, M.; Gimbert-Suriñach, C.; Sala, X.; Llobet, A. Behavior of Ru–Bda Water-Oxidation Catalysts in Low Oxidation States. *Chem. – A Eur. J.* **2018**, *24* (49), 12838–12847.
- (47) Hoque, M. A.; Benet-Buchholz, J.; Llobet, A.; Gimbert-Suriñach, C. Catalytic Oxidation of Water to Dioxygen by Mononuclear Ru Complexes Bearing a 2,6-Pyridinedicarboxylato Ligand. *ChemSusChem* **2019**, *12* (9), 1949–1957.
- (48) Roeser, S.; Farràs, P.; Bozoglian, F.; Martínez-Belmonte, M.; Benet-Buchholz, J.; Llobet, A. Chemical, Electrochemical, and Photochemical Catalytic Oxidation of Water to Dioxygen with Mononuclear Ruthenium Complexes. *ChemSusChem* **2011**, *4* (2), 197–207.

## CHAPTER 5.

### 5.5 Supporting Information

#### 5.5.1 Materials and methods

All materials were provided by Sigma-Aldrich unless indicated otherwise. High-purity deionized water was obtained by passing distilled water through a Nanopure Milli-Q water purification system. Unless specifically written, reactions were carried out under rigorously anhydrous conditions and with a positive pressure of argon. Automated flash chromatography was performed on the Teledyne Isco CombiFlash Rf flash chromatography purification system using SiliCycle silica gel columns (24 or 40 g, 230–400 mesh 40–63  $\mu\text{m}$ ).

##### 5.5.1.1 General instrumentation

Electrospray ionization mass spectrometry (ESI-MS) experiments were performed on a Waters Micromass LCT Premier equipment. UV–Vis spectroscopy was performed on a Cary 50 Bio (Varian) UV–Vis spectrophotometer with 1 cm quartz cells unless indicated otherwise. A 400 MHz Bruker Avance II spectrometer and a Bruker Avance 500 MHz were used to carry out NMR spectroscopy. The pH of the solutions was determined by a pH meter (CRISON, Basic 20\*) calibrated before measurements through standard solutions at pH= 4.01, 7.00, and 9.21.

##### 5.5.1.2 Preparation of 0.1 M ionic strength phosphate solutions.

- **pH = 1.0** solution was prepared as a 0.1 M  $\text{CF}_3\text{SO}_3\text{H}$  (HTfO) solution in the deionized water.
- **pH = 2.0** buffered solution: solids of  $\text{H}_3\text{PO}_4$  (10.5 g, 0.1073 M) and  $\text{NaH}_2\text{PO}_4$  (11.83 g, 0.0986 M) were dissolved in 1 L of deionized water.
- **pH = 7.0** buffered solution: solids of  $\text{NaH}_2\text{PO}_4$  (2.31 g, 0.0193 M) and  $\text{Na}_2\text{HPO}_4$  (3.77g, 0.0266 M) were dissolved in 1 L of deionized water.

### 5.5.1.3 Single Crystal X-Ray Methods

**Crystal preparation:** Crystals of  $[\text{Ru}^{\text{II}}(\text{H}_2\text{bpc-}\kappa\text{-N}^2\text{O}^{\text{P}})_2]$  and  $[\text{Ru}^{\text{II}}(\text{Hbpc})(\text{py})_2]$  were grown by slow diffusion of diethyl ether into 2,2,2-trifluoroethanol solution (with the addition of 10% HTfO in TFE). The crystal used for structure determination was selected using a Zeiss stereomicroscope using polarized light and prepared under inert conditions immersed in perfluoropolyether as protecting oil for manipulation.

**Data collection:** Crystal structure determination for sample  $[\text{Ru}^{\text{II}}(\text{H}_2\text{bpc-}\kappa\text{-N}^2\text{O}^{\text{P}})_2]$  and  $[\text{Ru}^{\text{II}}(\text{Hbpc})(\text{py})_2]$  were carried out using an Apex DUO Kappa 4-axis goniometer equipped with an APPEX 2 4K CCD area detector, a Microfocus Source E025 luS using  $\text{MoK}\alpha$  radiation, Quazar MX multilayer Optics as monochromator and an Oxford Cryosystems low-temperature device Cryostream 700 plus ( $T = -173$  °C). Full-sphere data collection was used with  $\omega$  and  $\varphi$  scans. *Programs used:* Data collection APEX-2<sup>1</sup>, data reduction Bruker Saint<sup>2</sup> V/.60A and absorption correction SADABS<sup>3</sup>.

**Structure Solution and Refinement:** Crystal structure solution was achieved using the computer program SHELXT<sup>4</sup>. Visualization was performed with the program SHELXle.<sup>5</sup> Missing atoms were subsequently located from difference Fourier synthesis and added to the atom list. Least-squares refinement on  $F^2$  using all measured intensities was carried out using the program SHELXL 2015.<sup>6</sup> All non-hydrogen atoms were refined including anisotropic displacement parameters.

**Comments to structure  $[\text{Ru}^{\text{II}}(\text{H}_2\text{bpc-}\kappa\text{-N}^2\text{O}^{\text{P}})_2]$ , 4:** The asymmetric unit contains one molecule of the metal complex. Hydrogen atoms on Oxygen atoms were localized experimentally. The asymmetric unit contains one molecule of the metal complex. Hydrogen atoms on Oxygen atoms were localized experimentally. **Structure  $[\text{Ru}^{\text{II}}(\text{Hbpc})(\text{py})_2]$ :** The asymmetric unit contains one molecule of the metal complex, one methanol, and one diethyl ether molecule. The solvent molecules are disordered in two orientations (ratio: methanol 60:40 and diethyl ether 70:30).

CIF files for complexes  $[\text{Ru}^{\text{II}}(\text{H}_2\text{bpc-}\kappa\text{-N}^2\text{O}^{\text{P}})_2]$  and  $[\text{Ru}^{\text{II}}(\text{Hbpc})(\text{py})_2]$  with CCDC numbers 2044298 and 2045432 respectively are available at <https://www.ccdc.cam.ac.uk/>.

## CHAPTER 5.

### 5.5.1.4 Electrochemical methods

#### *General considerations*

All electrochemical experiments were performed in an IJ-Cambria HI-730 bipotentiostat and IJ-Cambria CHI-660 potentiostat, using a three-electrode cell.  $E_{1/2}$  values reported in this work were estimated from Cyclic Voltammetry (CV) experiments as the average of the oxidative and reductive peak potentials  $(E_{p,o}+E_{p,c})/2$ . Glassy carbon disk (GC) ( $\phi = 0.3$  cm,  $S = 0.07$  cm<sup>2</sup>) was used as working electrode (WE), Mercury/Mercurous sulfate ( $K_2SO_4$  sat.) (MSE) as reference electrode (RE) (unless explicitly mentioned) and Pt disk as counter electrode (CE). Working electrode pretreatment before each measurement consisted of polishing with 0.05  $\mu$ m alumina paste, rinsing after with water and acetone, and blow-dried finally. CVs and DPVs were  $iR$  compensated (85%) by the potentiostat in all the measurements unless indicated. CV was recorded at a 100 mV·s<sup>-1</sup> scan rate unless explicitly expressed. All redox potentials in the present work are reported versus NHE by adding 0.65 V to the measured potential.<sup>7</sup>

#### *Electrochemical cells*

A 15 mL vial was used as an electrochemical cell for CV measurements. A Teflon-made holder equipped for the three electrodes was used as a lid to ensure a reproducible distance between the electrodes. A two compartments cell (25 mL per compartment or 7 mL per compartment) with a separation grid was used for (Controlled Potential Electrolysis) CPE experiments.

#### *Controlled potential electrolysis (CPE)*

A Pt grid was used as a WE, Pt grid as a CE, and a Mercury/Mercurous sulfate ( $K_2SO_4$  saturated) as a RE.  $iR$  compensation by the potentiostat was not applied in this technique.

### 5.5.1.5 UV-Vis spectroscopy and kinetics

Studies were performed at various concentrations of complexes **3** and **4**. In a typical experiment, a solution of Ru complex (0.2 mM) in 0.1 M triflic acid solution and monitored during the time. The absorption spectra were recorded at 25 °C in a 1.0 cm path length quartz cell. The spectral changes accompanying the formation and decay of the reaction intermediates as well as kinetic traces at a fixed wavelength were analyzed using the SPECFIT/32 global analysis program (Version 2.10, 1993–1996, Spectrum Software

## CHAPTER 5.

Associates, P.O. Box 4494, Chapel Hill, NC 27515-4494, USA). The reported  $k_{\text{obs}}$  value was obtained from the fit of experimental data to the exponential function using the kinetic model  $A \rightarrow B$ .

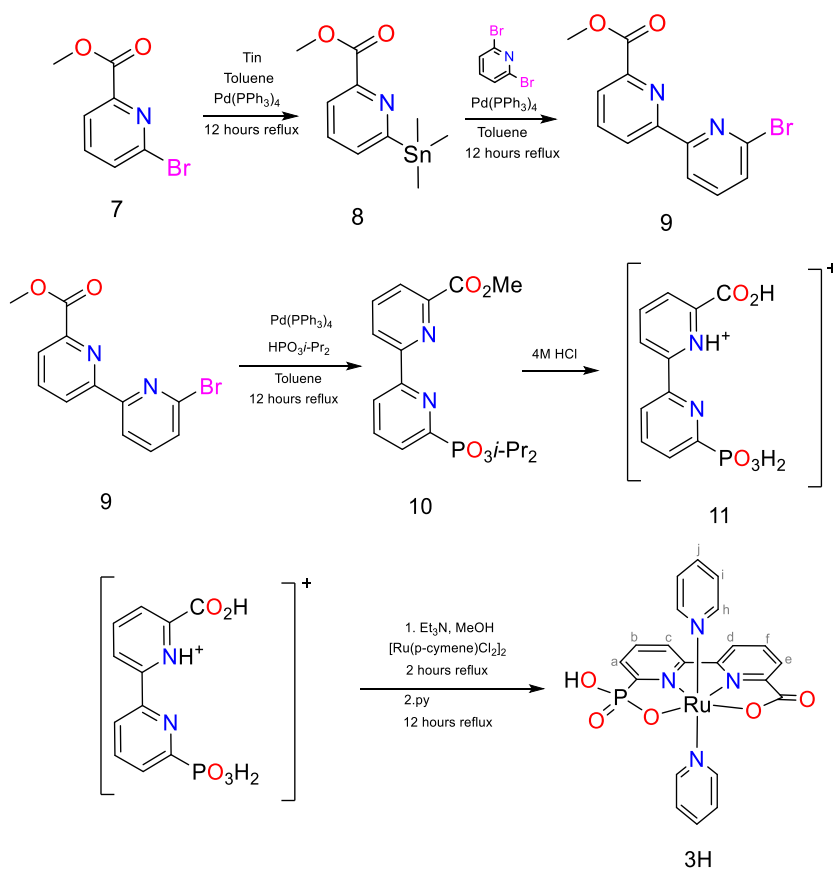
V

## CHAPTER 5.

### 5.5.2 Synthetic Procedures and Analytical Data

#### 5.5.2.1 Synthesis and Structure of H<sub>3</sub>bcp ligand

To confirm the transformation pathway of complex **2<sup>2-</sup>**, we independently synthesized and characterized complex **3H** and studied its electrochemical properties. The synthesis of the H<sub>3</sub>bcp ligand was originally performed according to the synthetic strategy reported in the literature<sup>8</sup>. However, due to the irreproducibility of the original procedure within CrO<sub>3</sub> oxidation, the synthetic strategy was changed to the following (Scheme S1).



**Scheme S1:** Synthetic route for the preparation of H<sub>3</sub>bcp ligand and [Ru<sup>II</sup>(Hbcp)(py)<sub>2</sub>], **3H** complex

**Synthesis of methyl 6-(trimethylstannyl)picolinate, 8.**<sup>9</sup> A solution of methyl 6-bromopicolinate (1.48 g, 6.87 mmol, 1eq), Me<sub>3</sub>Sn<sub>2</sub> (2.7 g, 8.24 mmol, 1eq) and Pd(PPh<sub>3</sub>)<sub>4</sub> (0.4 g, 0.35 mmol, 0.05eq) in degassed toluene (30 mL) was heated at 80 °C for 12 h under argon atmosphere. The mixture was cooled to RT (room temperature) and filtered through a pad of celite. The filtrate was concentrated, and the residue was directly used for the next step.

**Synthesis of methyl 6'-bromo-[2,2'-bipyridine]-6-carboxylate, 9.**<sup>9</sup> Under an argon atmosphere, in the previous step obtained 8, 2,6-dibromopyridine (1.90 g, 8.0 mmol) and Pd(PPh<sub>3</sub>)<sub>4</sub> (0.4 g, 0.35 mmol, 0.05eq) were dissolved in the degassed toluene (30 mL). The reaction was refluxed and stirred at 120 °C for 12 h, and the toluene evaporated on a water-bath under reduced pressure. The residue was then purified by column chromatography on silica gel and eluted with ethyl acetate to afford pale yellow powder 0.32 g (16%). The NMR analysis of the obtained compound is in the agreement with the reported in the literature.<sup>8</sup>

**Synthesis of Methyl 6'-(diisopropoxyphosphoryl)-[2,2'-bipyridine]-6-carboxylate (10) and 6'-phosphono-[2,2'-bipyridine]-6-carboxylic acid (11).** They were synthesized according to the reported procedure.<sup>8</sup>

**Synthesis of [Ru<sup>II</sup>(Hbpc)(py)<sub>2</sub>], 3H.** [RuCl<sub>2</sub>(p-cymene)]<sub>2</sub> (54.6 mg, 90 μmol, 0.50 eq) and **11** (50.0 mg, 178.5 μmol, 1 eq) were suspended in 5 mL anhydrous methanol. The mixture was degassed by bubbling with argon for 15 min and then heated to reflux for 2 h. The dark purple reaction mixture was removed from heat and treated with triethylamine (0.20 mL) and pyridine (5 mL). After an additional 12 h reflux, the dark red reaction mixture was cooled to RT and filtered. The filtrate was evaporated to dryness. The residue was then purified by column chromatography on silica gel and eluted with methanol to afford **3H** as a brown powder 0.045 g (48 %).



## CHAPTER 5.

### 5.5.2.2 Spectroscopy characterization of the 3<sup>-</sup>

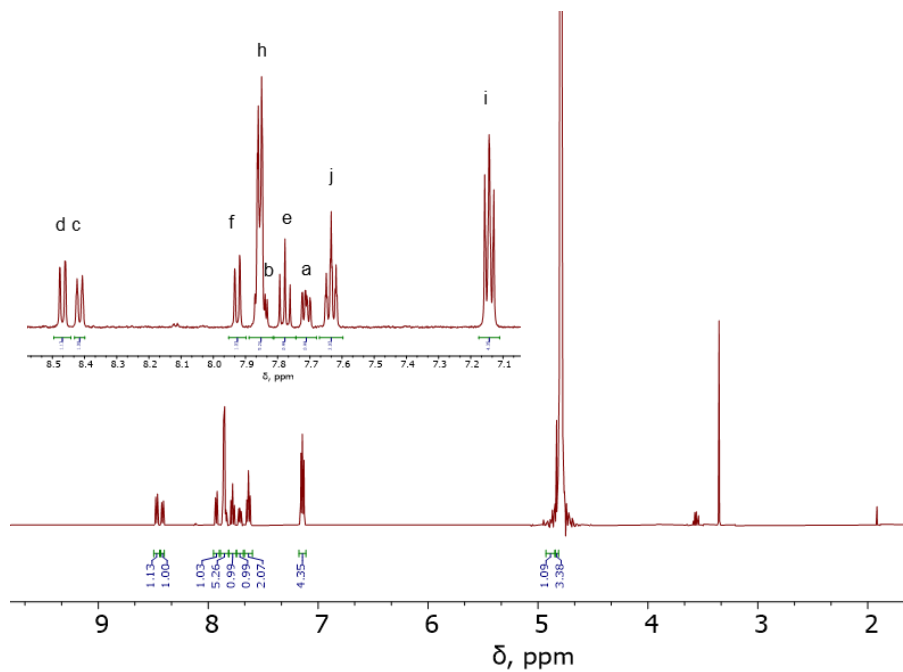


**Figure S1.** <sup>1</sup>H NMR of 3<sup>-</sup> in D<sub>2</sub>O at RT with the addition of 0.1 mL of 0.1M NaOD.

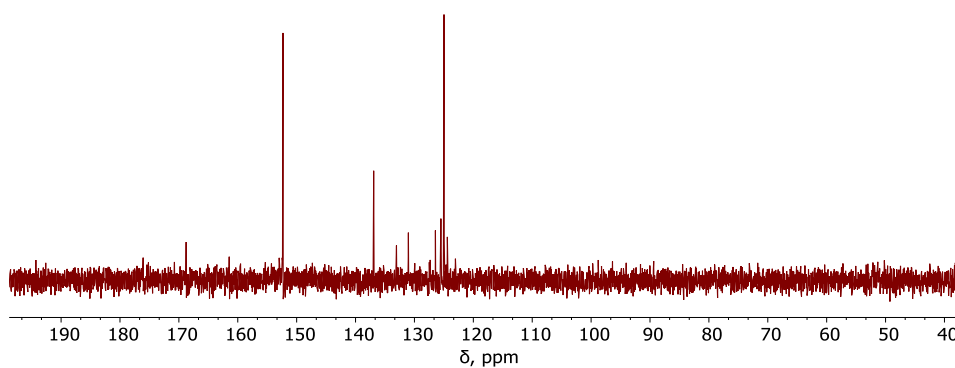


**Figure S2:** <sup>13</sup>C NMR of 3<sup>-</sup> in D<sub>2</sub>O at RT with the addition of 0.1 mL of 0.1M NaOD

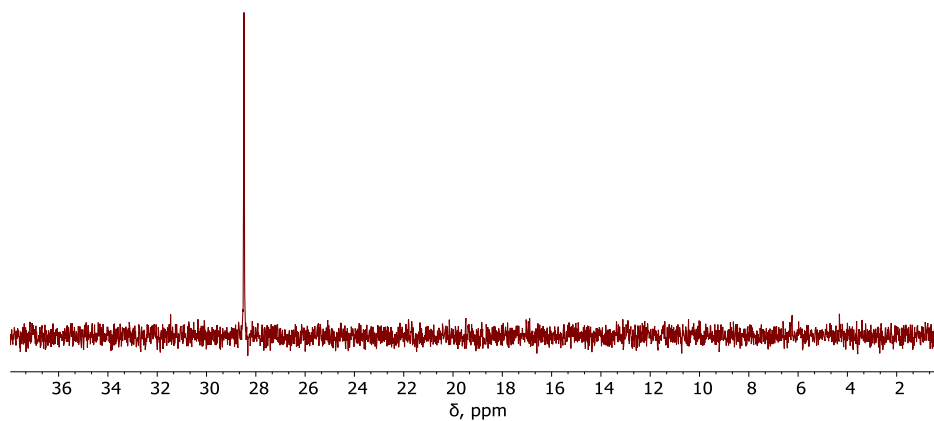


**Figure S3:**  $^{31}\text{P}$  NMR of  $\mathbf{3}^-$  in  $\text{D}_2\text{O}$  at RT with the addition of 0.1 mL of 0.1M NaOD.

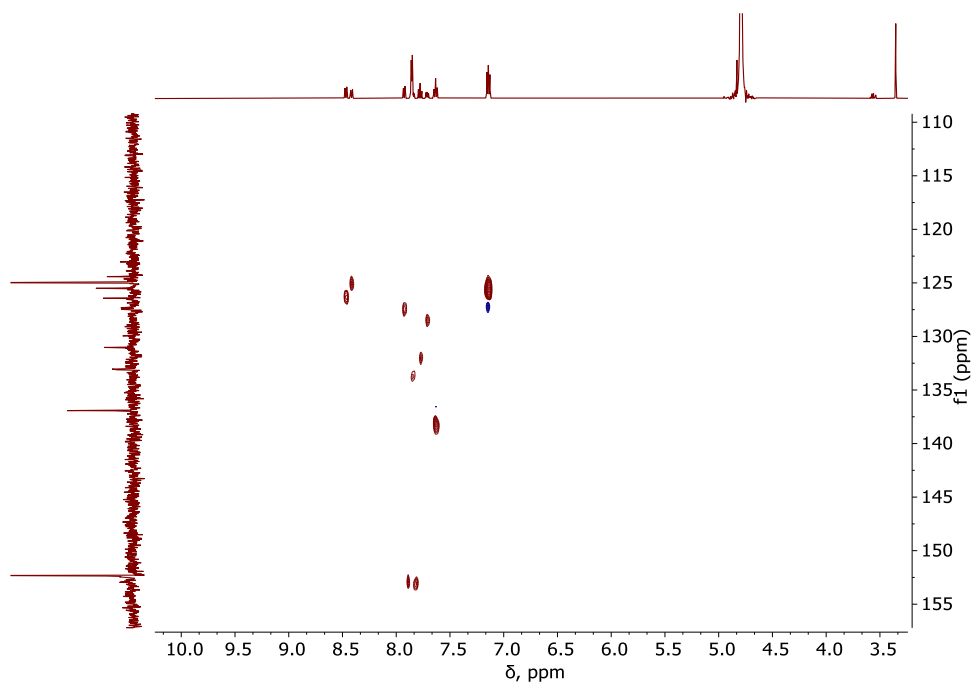


**Figure S4:**  $^1\text{H}$  -  $^{13}\text{C}$  HSQC NMR of  $\mathbf{3}^-$  in  $\text{D}_2\text{O}$  at RT with the addition of 0.1 mL of 0.1M NaOD.

V

## CHAPTER 5.

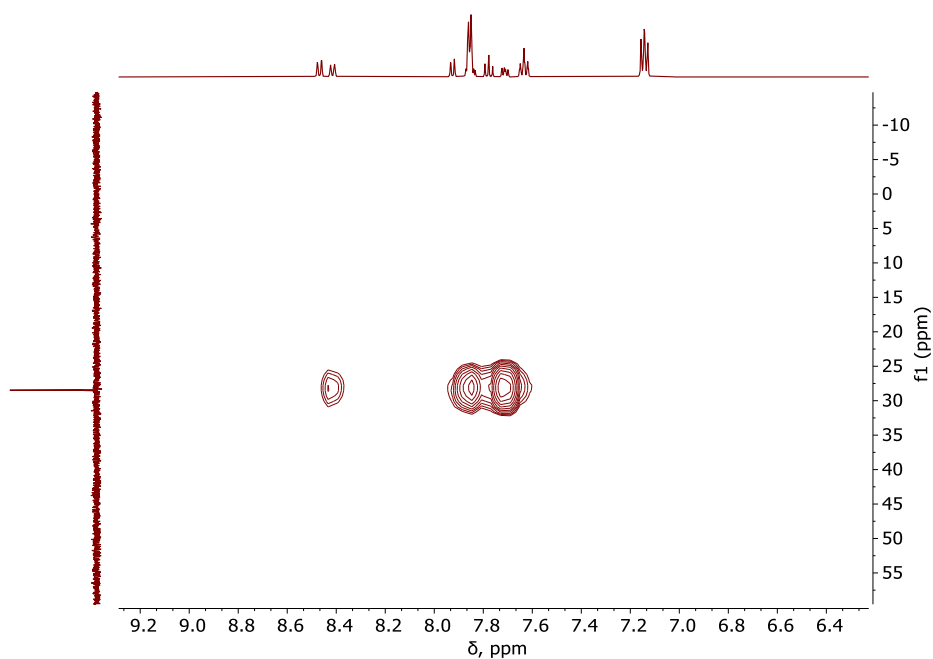


**Figure S5:**  $^1\text{H}$ - $^{31}\text{P}$  HMBC NMR of  $3^-$  in  $\text{D}_2\text{O}$  at RT with the addition of 0.1 mL of 0.1M NaOD.

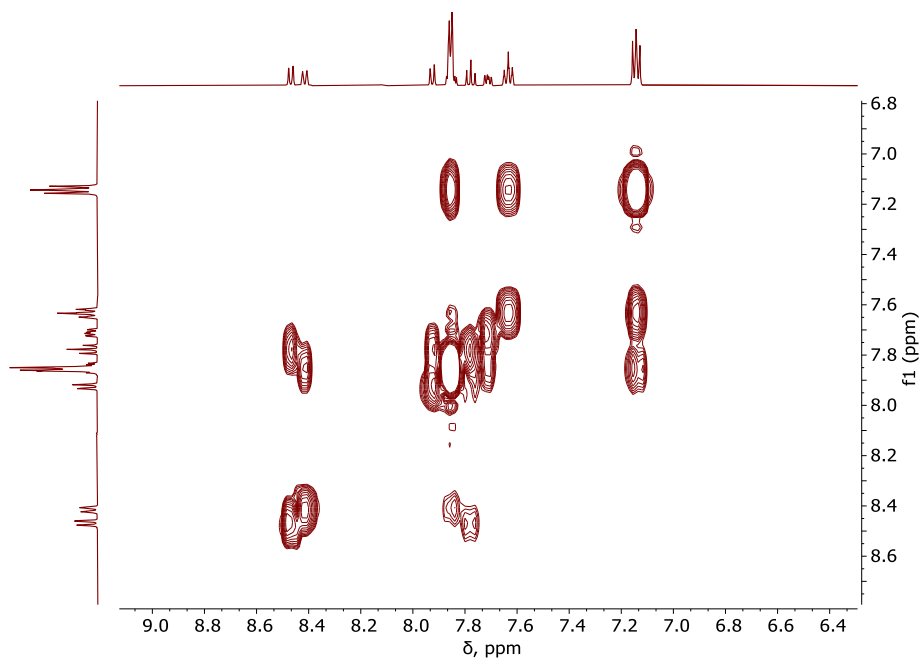


**Figure S6:**  $^1\text{H}$ - $^1\text{H}$  COSY NMR of  $3^-$  in  $\text{D}_2\text{O}$  at RT with the addition of 0.1 mL of 0.1 M NaOD.

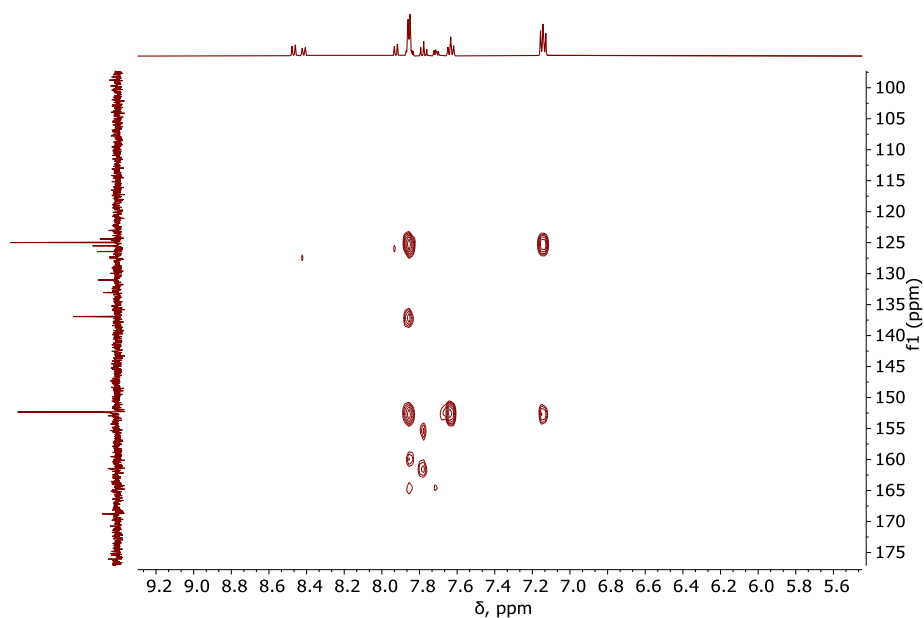


**Figure S7:**  $^1\text{H}$ - $^{13}\text{C}$  HMBC NMR of **3** in  $\text{D}_2\text{O}$  at RT with the addition of 0.1 mL of 0.1 M NaOD.

V

## CHAPTER 5.

### 5.5.3 Electrochemical analysis of molecular catalysts

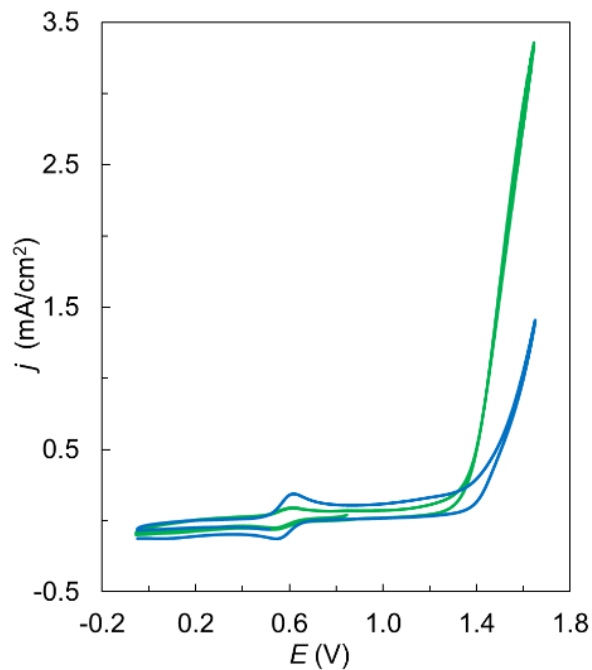


**Figure S8.** Cyclic voltammetry at pH 7.0 in a 0.1 M phosphate buffer aqueous solution of:  $[\text{Ru}^{\text{II}}(\text{H}_2\text{tPa}-\kappa\text{-N}^3\text{O})(\text{py})_2], \mathbf{1}^-$  after addition of excess  $\text{H}_2\text{O}_2$  (green trace) and synthesized  $[\text{Ru}^{\text{II}}(\text{bpc})(\text{py})_2]^-, \mathbf{3}^-$  (blue trace).<sup>8</sup>

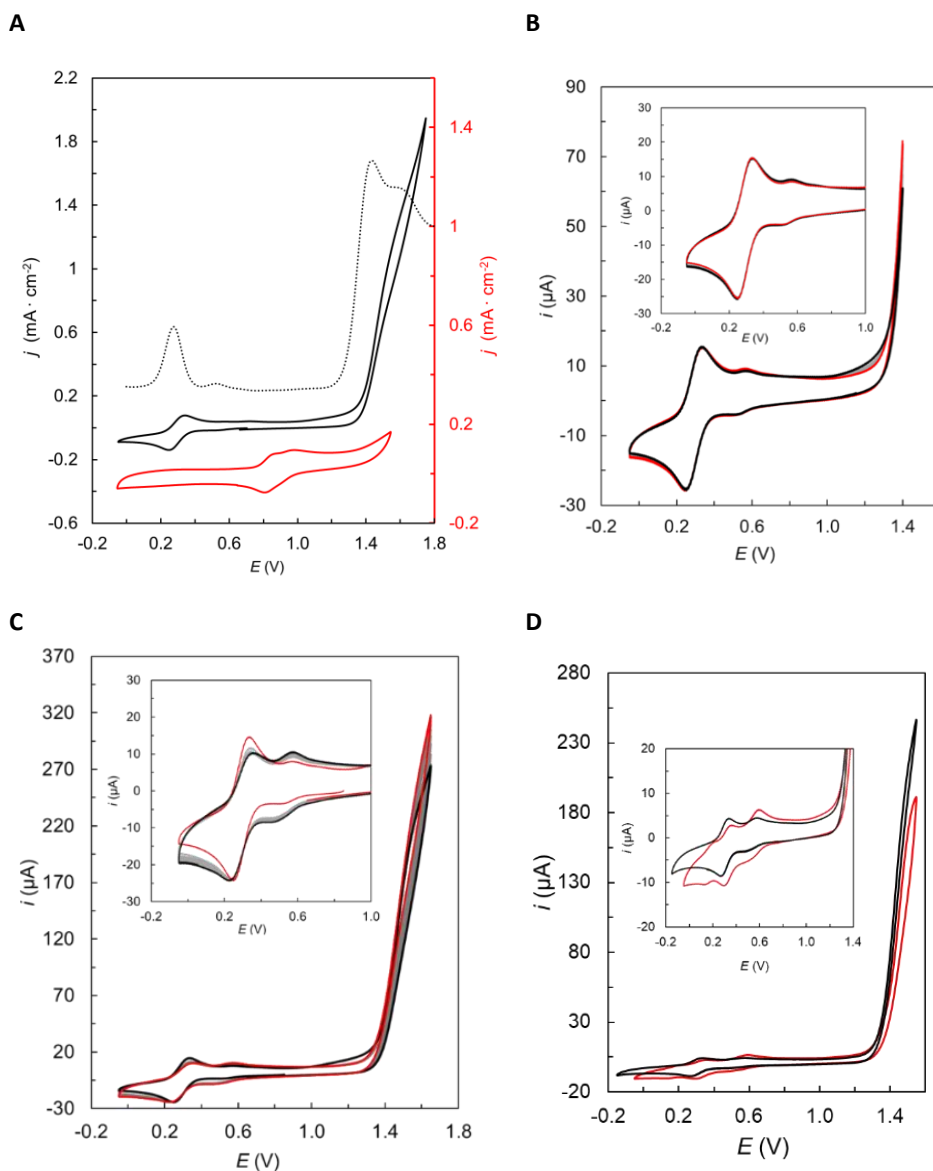


**Figure S9.** **A**, Cyclic voltammetry of a 0.6 mM solution of  $1^-$ , at pH 7.0 in a 0.1 M phosphate buffer aqueous solution (red trace). Solid black line, cyclic voltammetry of 0.6 mM  $2^{2-}$ , at pH 7.0 in a 0.1 M phosphate buffer aqueous solution, generated from the precursor, by a 3 hours CPE at 1.30 V. Dotted line correspond to the DPV of the same solution. **B**, Transformation of  $1^-$  into  $2^{2-}$  at pH 7.3 by cycling up to 1.45 V (1<sup>st</sup> cycle (black solid line) and 10<sup>th</sup> cycle (red solid line)). **C**, Transformation  $1^-$  into  $2^{2-}$  at pH 7.3 by cycling

## CHAPTER 5.

up to 1.65 V (1<sup>st</sup> cycle (black solid line) and 10<sup>th</sup> cycle (red solid line)). **D**, Transformation of **1**<sup>2-</sup> into **2**<sup>2-</sup> at pH 8.5 by CPE at 1.55 V, black solid line corresponds to the CV before CPE and red solid line – to the CV after CPE.

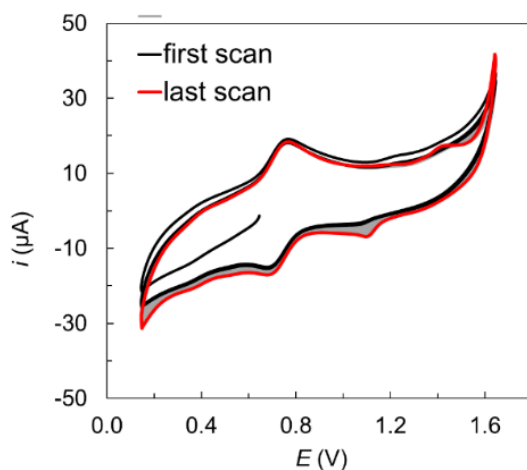


**Figure S10.** CVs of an aqueous solution containing crystalline of **4** at pH 1.0 before (black trace) and after (red trace) 125 cycles. CVs cycles evolution are displayed in solid grey.

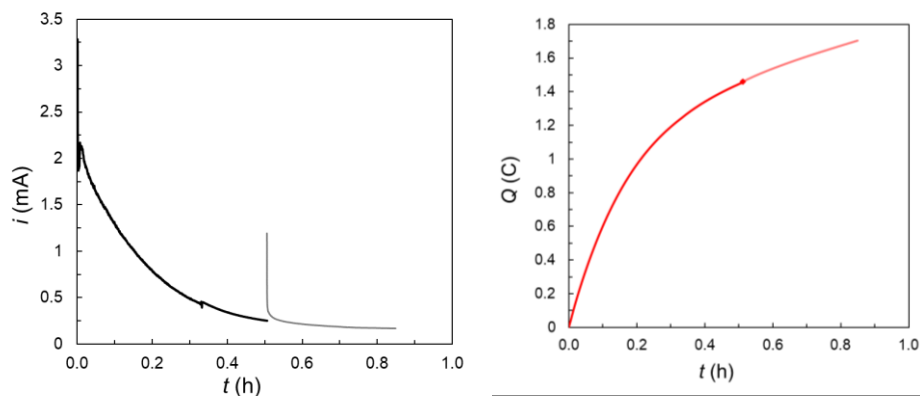


**Figure S11.** CPE at  $E_{app} = 1.55$  V vs. NHE of a solution of **3H** (2.3 mM, 5 mL pH 1.0) using a Pt mesh as a working electrode  $Hg/Hg_2SO_4$  as reference electrode and a Pt mesh as the auxiliary electrode. The charge passed was integrated to be 1.7 C (17.6  $\mu$ mol of  $e^-$ )

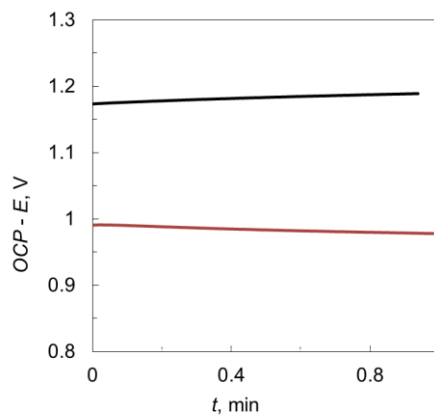


**Figure S12.** OCP evolution before (black line) and 16 h after (red line) the CPE experiment in Figure S11.



## CHAPTER 5.

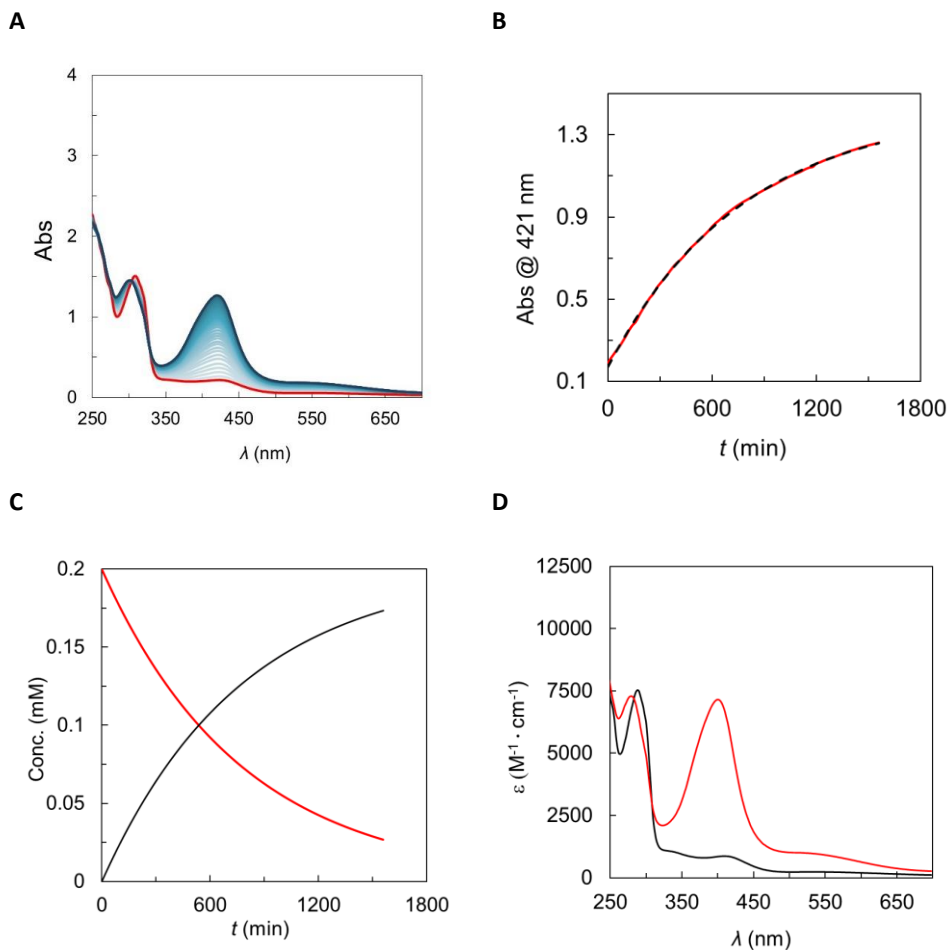


**Figure S13.** **A**, Evolution of UV-Vis absorption spectra of a 0.2 mM solution of **3H** after CPE at 1.55 V at pH 1.0 at 25 °C for 25 hours, in red – just after CPE and in dark blue after 25 hours staying at the open-air (spectra in blue color shows an evolution in spectra each 60 min). **B**, Changes in the absorbance at 421 nm vs. time for 25 hours (black line) and its mathematical fit (red line). **C**, Calculated concentration distribution diagram vs. time for the different species. **D**, Calculated spectra for the proposed species in solution.

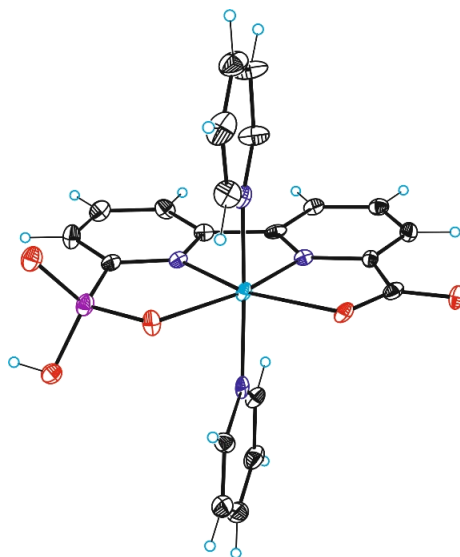


**Figure S14.** X-ray structure ORTEP view (ellipsoid at 50% probability) of **3H**. Color code: Ru, cyan; N, blue; O, red; P, purple; C, black; H, empty blue circle. Solvent molecules have been omitted for the sake of clarity

V

## CHAPTER 5.

### 5.5.4 Reference

- (1) Data Collection with APEX II Version V2013.4-1. Bruker (2007). Bruker AXS Inc., Madison, Wisconsin, USA.
- (2) Data Reduction with Bruker SAINT Version V8.30c. Bruker (2007). Bruker AXS Inc., Madison, Wisconsin, USA.
- (3) SADABS: V2012/1 Bruker (2001). Bruker AXS Inc., Madison, Wisconsin, USA. Blessing, *Acta Cryst.* 1995, A51, 33-38.
- (4) SHELXT; V2014/4 (Sheldrick 2014). Sheldrick, G.M. *Acta Cryst.* 2015, A71, 3-8.
- (5) SHELXL; C.B. Huebschle, G.M. Sheldrick & B. Dittrich; *J. Appl. Cryst.* 2011, 44, 1281-1284.
- (6) SHELXL; SHELXL-2014/7 (Sheldrick 2014). Sheldrick, G.M. *Acta Cryst.* 2015, C71, 3-8.
- (7) Elgrishi, N.; Rountree, K. J.; McCarthy, B. D.; Rountree, E. S.; Eisenhart, T. T.; Dempsey, J. L. A Practical Beginner's Guide to Cyclic Voltammetry. *J. Chem. Educ.* **2018**, 95 (2), 197–206.
- (8) Shaffer, D. W.; Xie, Y.; Szalda, D. J.; Concepcion, J. J. Lability and Basicity of Bipyridine-Carboxylate-Phosphonate Ligand Accelerate Single-Site Water Oxidation by Ruthenium-Based Molecular Catalysts. *J. Am. Chem. Soc.* **2017**, 139 (43), 15347–15355.
- (9) McDonald, A. Therapeutic Inhibitory Compounds WO 2015/103317 A1. EP3089746, 2015.

## 6 CHAPTER 6

### Efficient Ru-based Molecular 2D Catalyst on the Heterogeneous Phase

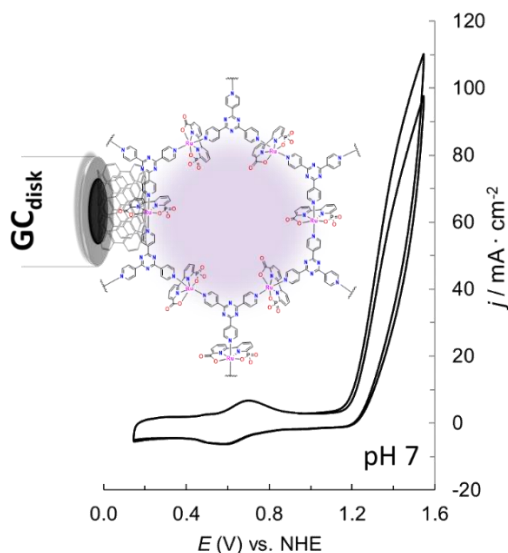
---

*The present chapter uncovers the borderline between homogeneous and heterogeneous water oxidation catalysis using a Ru-based WOC containing  $bpc^{3-}$  as an equatorial ligand, whose spectroscopic and catalytic properties were described in detail in Chapter 5. Here we presented a functional 2-dimensional coordination polymer based on  $[Ru(bpc)(DMSO)Cl]$  monomer, which has been prepared and evaluated as a water oxidation catalyst at neutral and acidic pHs. Different anchoring strategies were applied for anode preparation and their redox and spectroscopic features have been analyzed over various conditions.*

---

## CHAPTER 6

## Efficient Ru-based Molecular 2D Catalyst on the Heterogeneous Phase



### Abstract

We report a coordination polymer based on molecular Ruthenium complex within a 2-dimensional (2D) framework with the general formula  $[\text{Ru}(\text{Hbpc})(\text{tpt})_{2/3}]_n$ , where H<sub>3</sub>bpc is the tetradentate equatorial ligand 6'-phosphono-[2,2'-bipyridine]-6-carboxylic acid and tpt is the bridging ligand 2,4,6-tris(4-pyridyl)-1,3,5-triazine. This polymer shows the existence of solid-state interactions among 2D sheets within the packing structure upon changing from a solution to the solid-state. 2D polymer strongly anchored on carbon nanotube (CNT) surfaces through supramolecular interactions. This new hybrid material is an active and robust water oxidation anode that shows impressive catalytic current densities in the range of 0.1-0.2 A/cm $^2$ .

### Contributions:

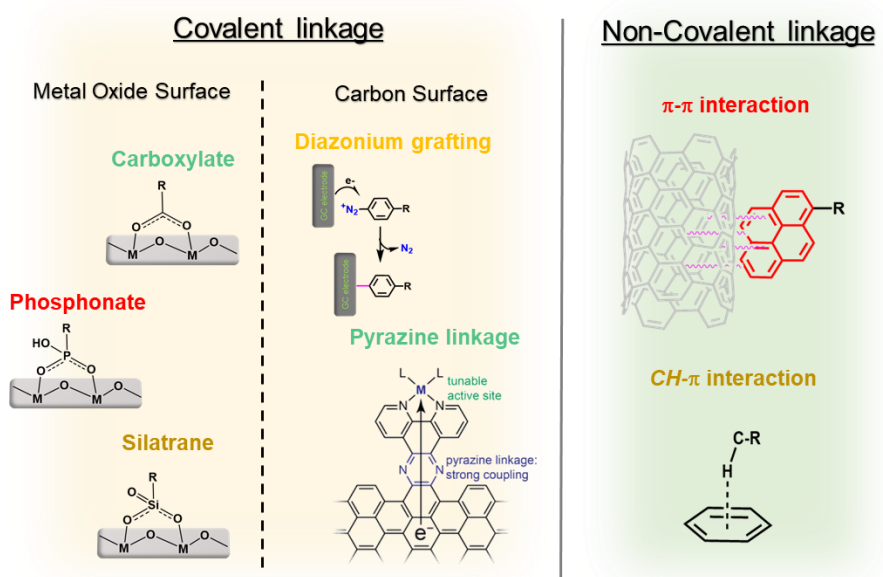
Nataliia Vereshchuk synthesized and characterized all the compounds, carried out all the electrochemical, as well as spectroscopic experiments.

## CHAPTER 6.

### 6.1 Introduction

Considerable progress has been made over the last decades in the development of molecular WOCs and valuable mechanistic understanding of catalytic water oxidation has been acquired.<sup>1-4</sup> In particular, the class of molecular Ru(bda) and Ru(tda) has shown high catalytic efficiencies about two orders of magnitude higher than nature's oxygen-evolving complex.<sup>4-6</sup> However, for the implementation of such WOCs in water splitting devices their immobilization on proper surfaces, is required.<sup>7,8</sup> For the immobilization of homogeneous WOCs onto electrodes, mainly two strategies have been employed (see Scheme 1).

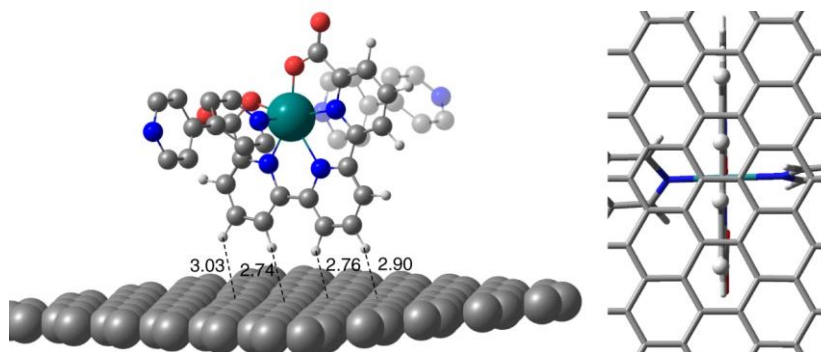
VI



**Scheme 1.** Schematic representation of the strategies for the immobilization of molecular catalysts on metal oxide and carbon surfaces

The first approach is based on the covalent attachment of molecular catalysts to electrode surfaces by silatrane, carboxylate-, or phosphonate-functionalized ligands.<sup>9-14</sup> Whereas an alternative approach is the supramolecular one, comprising the introduction of aromatic groups to the WOCs to facilitate non-covalent  $\pi$ - $\pi$  interactions between the catalyst and supporting material like carbon nanotubes (CNTs).<sup>8,15</sup> Due to their large surface area, which will allow high loading of the catalyst, as well as high conductivity and stability,<sup>16</sup> CNTs are

properly suited for the immobilization of catalysts on electrodes. One of the promising strategies for robust functional anchoring is to develop polymeric catalyst structures, which will be capable of being strongly anchored onto graphitic surfaces due to the “multiple anchoring points”. A successful example of such anchoring was recently reported, where new functional molecular coordination oligomers can be strongly adsorbed onto graphitic surfaces such as CNTs, *via* aromatic catalyst-surface CH- $\pi$  interactions (Scheme 1).<sup>17</sup>



**Scheme 2.** Ball and stick representation of the interaction of one of the Ru fragments of Ru(tda)-based polymer, with the graphene surface showing the CH- $\pi$  bonding distances. The interacting Ru-tda hydrogen atoms with the graphene surface are depicted as white balls. Colour code: Ru, green; O, red; N, blue; C, grey; H, white.

The resulting hybrid molecular material behaves as a rugged and powerful electroanode for the water oxidation reaction achieving unprecedented current densities for immobilized molecular catalysts in the range of 0.2-0.3 mA/cm<sup>2</sup>. The difficulties within using Ru(tda)-based<sup>5</sup> WOCs is a needed activation step, which includes controlling potential electrolysis in basic pH, which might significantly decrease the loading of the catalyst. Taking this into account, it would be appropriate to build a polymer with the WOC catalyst, which does not require an activation step. Moreover, using a variety of bridging ligands allows an increase in the number of Ru-centers in the polymer and overall improves stability. Thus, we envisioned the latter anchoring strategy with [Ru(bpc)(DMSO)Cl], and tpt (2,4,6-tris(4-pyridyl)-1,3,5-triazine) bridging ligand, which could be a promising way to increase the stability of the electroanode.



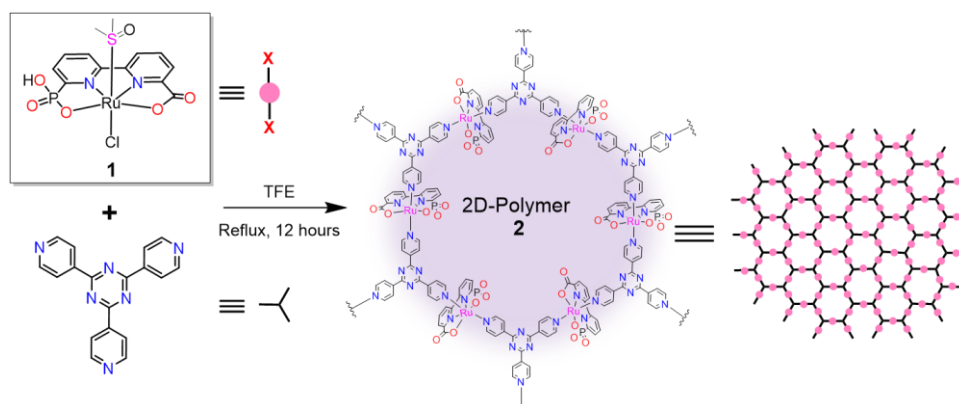
## CHAPTER 6.

Here on we synthesized and characterized a functional coordination 2D polymer based on [Ru(bpc)(DMSO)Cl] catalyst within a 2-dimensional framework. The resulting hybrid material is a powerful molecular electroanode for water oxidation to dioxygen with impressive current densities above  $0.1 \text{ A/cm}^2$  and remarkable stability at neutral pH.

## 6.2 Results and Discussion

### 6.2.1 Synthesis and Characterization of Coordination Polymer

The reaction of 1.5 eq. of  $[\text{Ru}(\text{bpc})(\text{DMSO})\text{Cl}]$ , **1** with 1.0 eq. of bridging ligand 2,4,6-tris(4-pyridyl)-1,3,5-triazine in trifluoroethanol (TFE) at  $78^\circ\text{C}$  after 12 hours of reflux results in the deep violet color solution of the 2D polymer **2** with the general formula  $[\text{Ru}(\text{Hbpc})(\text{tpt})_{2/3}]_n$  (see Scheme 3). The 2D polymer was further characterized directly from the reaction solution without precipitation or washing due to complete insolubility after precipitation, which indicates the existence of solid-state interactions among 2D sheets within the packing structure.



**Scheme 3:** Synthetic route for the preparation of the coordination polymer **2**.

Due to the limited solubility, this 2D polymer was characterized mostly electrochemically and anchored on different surfaces. Additional characterization also included elemental analysis, resonance Raman spectroscopy, and EPR spectroscopy.

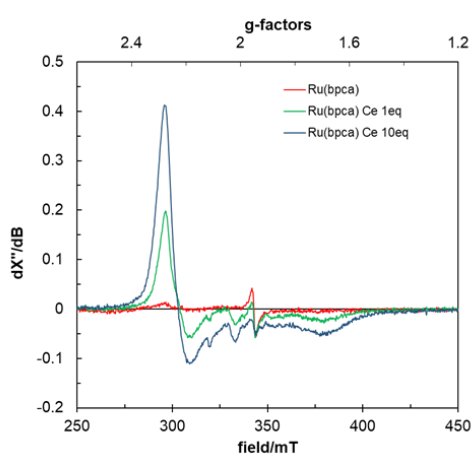
### 6.2.2 EPR Spectroscopy characterization of **2**

In order to characterize different oxidation states of the polymer, we performed an EPR study.<sup>19,20</sup> Figure 1A shows the EPR titration of the crude reaction solution of **2** in TFE (spectra in red), which shows the absence of almost any EPR response and indices, as expected for  $\text{Ru}^{\text{II}}$ , diamagnetic nature of the polymer. Further, a small addition of the CAN in water shows the increase of the signal due to the generation of  $\text{Ru}^{\text{III}}$  (spectra in green a blue). During chemical oxidation, we observed precipitation appearance, which might be

## CHAPTER 6.

the result of the limited solubility of the Ru<sup>III</sup> in the analyzed mixture. Due to the low solubility, the 2D polymer **2** can be properly characterized in the solid-state or anchored. This motivates us to develop a methodology for *in situ* / *operando* studies that allow EPR characterization of catalyst **2**.

**A**



**B**

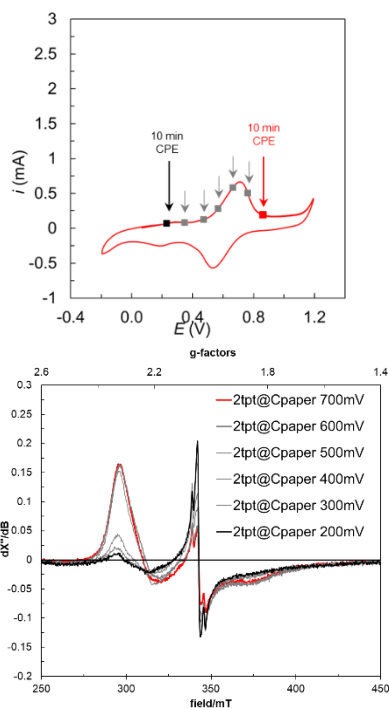


**Figure 1.** (A) Oxidation titration of the **2** with the Ce<sup>4+</sup> in TFE. Spectra in red correspond to **2**, and spectra in green and blue correspond to the addition of 1 eq and 10 eq of Ce respectively to **2**. (B) EPR spectra of **2@C<sub>paper</sub>** after each CPE (down) and CV of the **2@C<sub>paper</sub>** at pH 7 with the highlighted points for the CPE for EPR (up).

For performing *in situ* oxidation/reduction of **2** and simultaneous EPR measurement, a special spectroelectrochemical EPR cell was designed (see Figure S1). Due to designed cell features, it was decided to anchor the polymer on the carbon paper surface without CNT. To anchor the **2** to the carbon paper (C<sub>paper</sub>) electrode we used the strategy of the direct soaking of the electrode inside the solution of the polymer. A clean new carbon paper

electrode (1 cm × 0.3 cm) was dipped into a solution that contains 1 mg of the oligomer **2** in 1 mL of TFE solvent for 10 seconds. The functionalized electrode **2**@C<sub>paper</sub> was then rinsed with TFE and water. It was then dried by airflow and was ready for the electrochemical experiment.

Figure 1B shows EPR spectra after stepwise oxidation of the **2**@C<sub>paper</sub> from Ru<sup>II</sup> to Ru<sup>III</sup>. The CPE was applied for 10 min at each point, which indicated in the CV in Figure 1B up and the corresponding EPR spectra after each CPE indicated with the color below. The EPR spectra of the species at Ru<sup>II</sup> (spectra in black) show no signal appearing which supports the diamagnetic nature of the species. The signal at 340 mT corresponds to the carbon material from the C<sub>paper</sub> (see Figure S1). Further electrochemical oxidation shows an increase in the EPR spectra and reaches its maximum after complete transformation into Ru<sup>III</sup> (spectra in red). The shift of the signal of the anchored polymer is identical to the one measured in a homogeneous phase with its chemical oxidation. The described experiment gives us important information about the molecular nature of the system and the consistency of the oxidation state of the Ru center in a homogeneous and heterogeneous environment.

### 6.2.3 Anchoring of **2** on Graphitic Surfaces and redox properties

As has been recently published by our group, Ru(tda)-based linear oligomers have an extraordinary ability to be strongly anchored on graphitic surfaces such as CNT, GC disk, and graphene nanosheets.<sup>17</sup> This novel anchoring strategy is possible thanks to the perpendicular disposition of the H groups from the tda<sup>2-</sup> equatorial ligand, which can interact with the π electronic network of the graphitic surfaces resulting in high stability on the surface and a high catalytic performance towards water oxidation.<sup>17</sup> In this context, [Ru(bpc)(py)<sub>2</sub>] is a good candidate due to the capability of bpc<sup>3-</sup> ligand to form mentioned CH-π interactions. In this work, we describe different anchoring strategies tested for the polymer anchoring, which include: 1) anchoring to a flat GC electrode 2) anchoring on the CNT with the followed up anchoring of the GC electrode, and 3) anchoring to a metal-oxide surface.

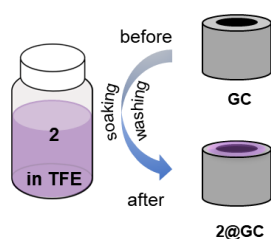
#### 6.2.3.1 Direct anchoring of **2** into a GC electrode

The first applied anchoring strategy was chosen a direct immobilization of **2** into the GC electrode. A clean glassy carbon electrode was dipped into a solution that contains 1 mg of

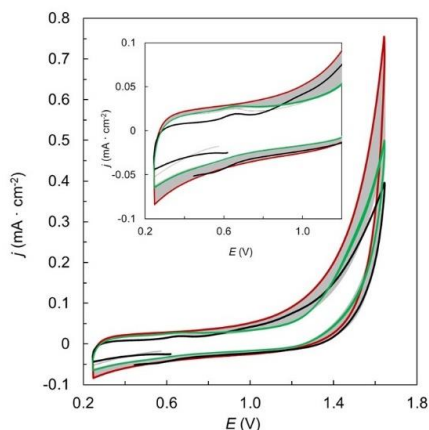
## CHAPTER 6.

the oligomer **2** in 1 mL of TFE solvent for 12 hours Figure 2A. The functionalized electrode **2@GC** was then rinsed with TFE and water. Afterward, it was dried by airflow and it was ready for electrochemical experiments. The electrochemical properties of **2@GC** were first analyzed by cyclic voltammetry (CV) experiments by immersion of prepared molecular anode in a three-electrode set-up cell containing a pH 7 1M phosphate buffer solution (phbf). Platinum mesh and Hg/HgSO<sub>4</sub> (K<sub>2</sub>SO<sub>4</sub> sat.) electrodes were used as a counter (CE) and reference electrodes (RE), respectively. All potentials reported hereinafter are converted and to NHE by adding 0.65 V to the measured potential.

**A**



**B**



**C**

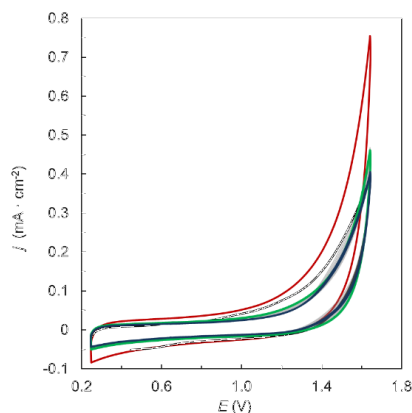


**Figure 2.** (A) Schematic representation of the **2@GC** electrode preparation. (B) 200 consecutive CVs of **2@GC** electrode in a pH 7 1 M phbf solution, the first cycle in black, the second cycle in green, and the last cycle in red. (C) 200 consecutive CVs of **GC** electrode in a pH 7 1 M phbf solution, the first cycle in blue, the last cycle in green, the CV in black and red correspond to the cycling of **2@GC** electrode, first cycle in black, and the last cycle in red.

Figure 2A shows the redox process at  $E_{1/2} = 0.64$  V due to the  $\text{Ru}^{\text{III/II}}$  oxidation, which is consistent with its monomeric analog, but already in the second CV cycle, the redox wave started disappearing, and after 200 repetitive CV cycles were completely gone. Those results might occur due to low anchoring strength and therefore rapid detachment of the polymer from the electrode surface during oxidation. On the other hand, the oxidative catalytic current keeps increasing during the cycling and might be an effect of two phenomena: 1) catalyst degradation and formation of  $\text{RuO}_2$ , which would be absorbed on the surface being catalytically active; 2) oxidation of the bare electrode surface over repetitive cycling; or 3) oxidation of the surface of the electrode by the polymer. To confirm the bare electrode response over cycling, we performed an experiment in identical conditions with the clean glassy carbon (Figure 2C). Comparing both CVs, we observed, that only a very small amount of current coming from the electrode surface oxidation. This allowed us to assume that the catalytic current over the cycling is coming from the oxidation of the polymer on the GC surface.

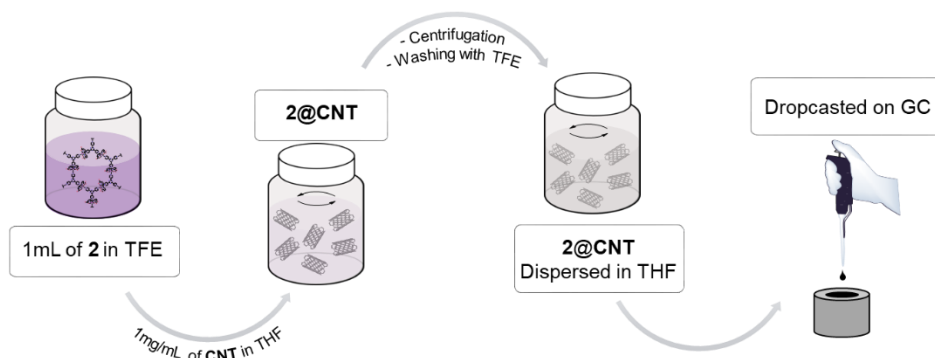
To improve the stability of the material was decided to test the anchoring on the GC with the CNT with absorbed polymer on it. CNT was chosen as solid conductive support due to their high surface area, high thermal and chemical stability, excellent electrical conductivity, and insolubility in most solvents.

### 6.2.3.2 Anchoring of **2** adsorbed on the CNTs

The present polymer **2** thanks to the water nucleophilic attack mechanism and the high activity in homogeneous media are expected to generate unprecedented powerful electroanodes due to both, the enhancement of surface coverages and the enormously improved stability provided by the nature of the new anchoring interactions.<sup>17</sup> The 2D polymer shows a strong affinity for graphitic surfaces. This behavior is similar to the parent 2D polymer described in the doctoral dissertation of Dr. Asmaul Hoque<sup>18</sup> and in sharp contrast to the mononuclear  $[\text{Ru}(\text{bpc})(\text{py})_2]$  complex that does not adsorb. The addition of 0.1 mL of a saturated solution of 2D in TFE to a suspension of 1mg/ml of CNT dispersed in THF, which results in the immediate decoloration of the final mixture, indicating the complete adsorption of the **2** onto the CNT (see Scheme 4). This new hybrid material is represented as **2@CNT**. For the further studies suspension **2@CNT** was dropcasted ( $4 \times 10$

## CHAPTER 6.

$\mu\text{L}$ ) onto GC (Glassy carbon disc,  $S = 0.07 \text{ cm}^2$ ) electrodes. Each drop was placed after the previous drop was completely dried. An electrode was then ready for electrochemical measurements as **2@CNT@GC**.



**Scheme 4.** Methodology for the **2@CNT@GC** electrode preparation.

### 6.2.4 Redox properties of the **2@CNT@GC** electrode

The electrochemical properties of **2@CNT@GC** were first analyzed by CV in a 1 M pH 7 pbhf using a three-electrode cell set up. Figure 3 shows a CV of the **2@CNT** deposited at the surface of a glassy carbon electrode *via* drop-casting that is labeled as **2@CNT@GC**. As can be seen in Figure 3A one single electron redox process is observed at  $E_{1/2} = 0.64 \text{ V}$  due to the  $\text{Ru}^{\text{III/II}}$  oxidation are not influenced by the immobilization of the catalyst. The redox potential obtained here is very similar to the monomer precursor ( $[\text{Ru}(\text{bpc})(\text{py})_2]$  in **Chapter 5**) in homogenous solution at the same pH, and thus suggests that each Ru center of the polymer acts similarly as in the discrete mononuclear complex. This is a consequence of the anchoring nature of the polymer at CNT, where each metal center has the same access to the surface and thus facilitates a synchronized transfer process to the electrode. Analogous to the monomer precursor  $[\text{Ru}(\text{bpc})(\text{py})_2]$ , the  $\text{Ru}^{\text{IV/III}}$  and  $\text{Ru}^{\text{V/IV}}$  oxidation are difficult to distinguish as both waves are in the potential where the catalysis already occurring. The increase in the oxidation current was initiated at an onset potential of 1.15 V and current densities of about  $40 \text{ mA/cm}^2$  at  $E = 1.45 \text{ V}$  were observed in the first CV cycle (CV in black). As the number of cycles increase, higher catalytic current densities were observed (see Figure 3A). Control CV experiment (CV in green) confirmed that CNT without the catalyst (**CNT@GC**, Figure 3A) does not produce any significant oxidative current under identical

experimental conditions. Figure 3B shows another interesting feature of polymer **2**, which is a significant increase in the oxidative current after Controlled potential electrolysis (CPE). The increase of the oxidative current can result from several phenomena occurring: 1) activation/aquo coordination of the catalyst, which according to the catalytic properties of its monomeric analog, should not appear; 2) partial decomposition of **2** and transformation into more active species; 3) Polymeric rearrangements of the anchored material.

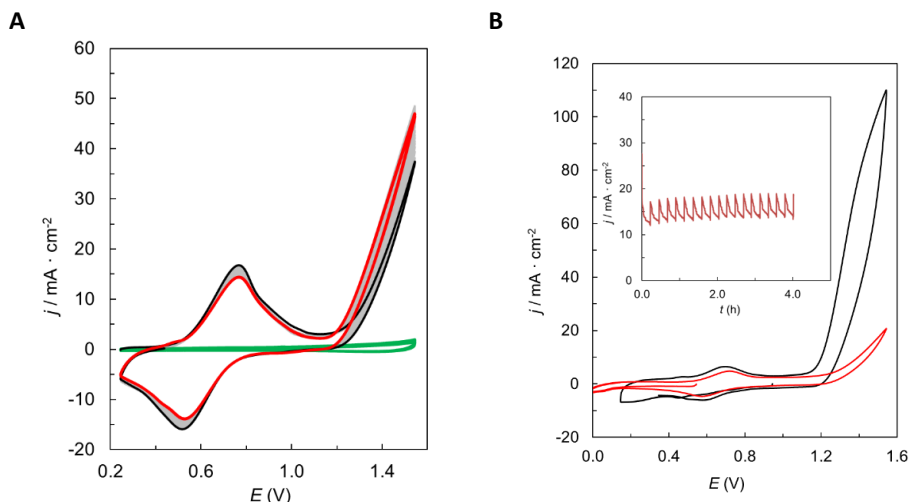


**Figure 3.** (A) Repetitive 50 CV cycles of **2@CNT@GC**, first scan in black, last scan in red, and repetitive 50 CVs of **CNT@GC** in green (pH 7 1 M phbf solution, 100 mV/s). (B) CV of **2@CNT** before (red graph) and after (black graph) CPE at 1.35V over 4 hours (pH 7 1 M phbf solution, 100 mV/s). The inset figure shows a CPE at 1.35V.

As can be seen from Figure 3B, the intensity of the Ru<sup>III/II</sup> oxidation wave appears higher after CPE, which allowed us to exclude the decomposition pathway. This increase in the oxidation wave current, as well as the catalytic one, can indicate the packing reorganization that happening over a few minutes during CPE (Figure 3B inset).

An important asset of any WOC is its capacity to work under a broad pH range. For this purpose, we also explore the behavior of **2** under acidic conditions. A CV analysis of **2@CNT@GC** electrode at pH 1 revealed that the first oxidation wave of immobilized **2** corresponds to the Ru<sup>III/II</sup> redox couples at  $E = 0.82$  V (CV in red) and are not influenced by the immobilization of the catalyst (see Figure 4). Interestingly, already with the second



## CHAPTER 6.

cycle, we can detect the appearance of the new oxidation wave at 1.11 V (CV in black), and after 10 repetitive CV cycles, we did not detect further evolution. However, the catalytic current remains stable (see Figure 4).

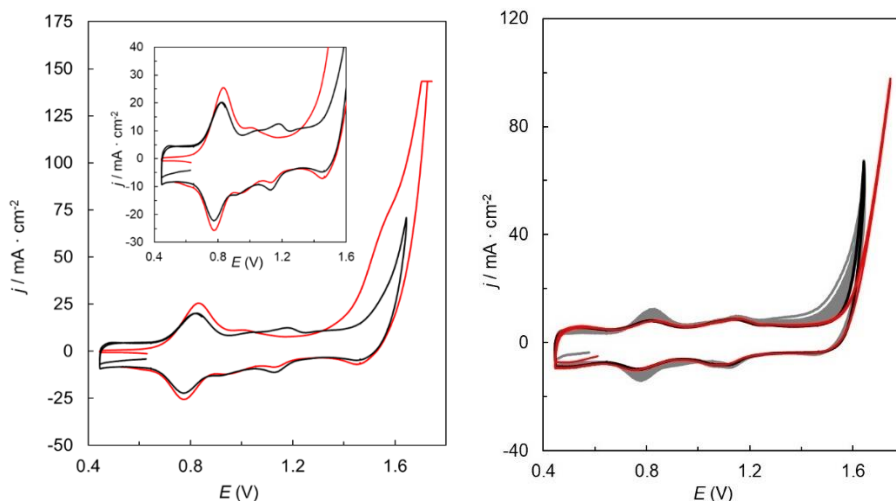


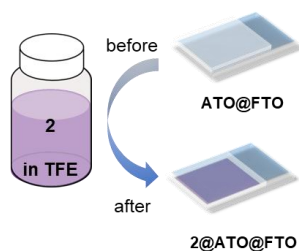
**Figure 4.** (left) CV of **2@CNT@GC** (40 $\mu$ L dropcasted) in pH 1 (0.1M HTfO, 100 mV/s) from 0.25 V to 1.55 V. The CV in red represent the first scan, the CV in black represents the second scan. Inset shows the zoom of the redox waves. (right) CV of **2@CNT@GC** (40 $\mu$ L dropcasted) in pH 1 (0.1M HTfO, 100 mV/s) from 0.25 V to 1.55 V. The CV in red represent the first scan, the CV in black represents the second scan and all the following cycles. Inset shows a zoom of the redox waves

The observed behavior is expected due to the similar events happening in the monomeric analog of  $[\text{Ru}(\text{Hbpc})(\text{tpt})_{2/3}]_n$ , **2**, wherein acidic conditions the starting complex facing the series of transformations and generate several intermediates. However, the transformation of system **2** should be studied in-depth due to the high complexity of the structure and possible transformation occurrences.

### 6.2.5 Anchoring of **2** on Metal Oxide Surfaces and redox properties

Most of the examples of the molecular anodes reported in the literature are based on the immobilization of the molecular catalyst on a variety of conductive and semiconductive metal oxide surfaces<sup>21</sup> such as fluorine-doped tin oxide (FTO), tin-doped indium oxide (ITO),

TiO<sub>2</sub>, BiVO<sub>4</sub>, etc.<sup>22,23</sup> To study redox properties of **2** on the metal-oxide surface we used flat fluorine tin oxide (FTO) glass plate (previously washed) coated with antimony tin oxide nanoparticles (**ATO@FTO**). To anchor the **2** to the **ATO@FTO** electrode we used the strategy of the direct soaking of the electrode inside the solution of the polymer (see Scheme 5).



**Scheme 5.** Schematic representation of the **2@ATO@FTO** electrode preparation.

The **ATO@FTO** electrode was soaked in the solutions of **2** in TFE, allowing the polymer to be adsorbed onto the **ATO@FTO** surface. After 12h, the coloration of the **ATO@FTO** from white-transparent to light purple indicates the adsorption of **2** onto **ATO@FTO**, which is labeled here as **2@ATO@FTO**. Figures 5A and 5B show repetitive CVs cycling and redox wave appearing at  $E_{1/2} = 0.61$  in pH 7.0 and at  $E_{1/2} = 0.71$  pH 1.0 solutions. During the repetitive cycling, no changes appeared, and no catalytic activity was observed, as opposed to previous results in homogeneous and heterogeneous phases on graphitic surfaces.

## CHAPTER 6.

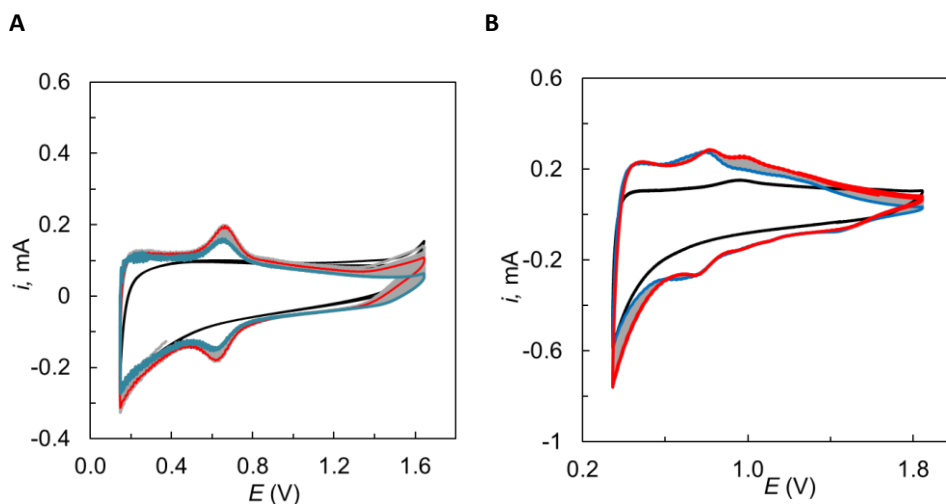


**Figure 5.** (A) 250 consecutive CVs of **2@ATO@FTO** electrode in pH 7. (B) 250 consecutive CVs of **2@ATO@FTO** electrode pH 1. The CVs in red correspond to the first cycles, the spectra in blue corresponds to the last ones after 250 cycles, the spectra in black correspond to the blank experiments of the **ATO@FTO** electrode without polymer attached.

# VI

The absence of catalytic current could be a consequence of the deactivation of the catalyst due to the coordination of the dangling carboxylate/phosphonate groups to the metal oxide surface.<sup>18</sup>

### 6.2.6 Surface characterization after the catalysis

Resonance Raman (RR) spectroscopy<sup>24,25</sup> was used to explore the nature of the hybrid material and to explore the nature of the interaction between the polymer and the graphitic surfaces. To prepare the electrode for the measurements we used the same strategy as for **2@CNT@GC**, but instead, we used glassy carbon plate electrodes (**GC<sub>p</sub>**). To dismiss RuO<sub>2</sub> formation during CPE, we perform electrolysis of the **2@CNT@GC<sub>p</sub>** and compared the obtained result with the rR spectra of RuO<sub>2</sub>. The CPE at  $E_{app} = 1.35$  V in a pH 7 1 M phbf solution was performed for 3 hours and the rR using 514 nm excitation was measured (Figures S3 and S4). The spectra were compared with the rR spectra of RuO<sub>2</sub> and no characteristic peaks of RuO<sub>2</sub> were found on the spectra of the **2@CNT@GC<sub>p</sub>** after CPE. This experiment confirms the stability of the anchored compound over harsh oxidation

conditions. The observed decrease in the catalytic current during CPE occurred can then be ascribed to the mechanical detachment of the **2@CNT** from the electrode surface, which can be also be visually observed during the CPE experiment.

To characterize these hybrid materials further, X-ray absorption near edge structure (XANES) and extended X-ray absorption fine structure (EXAFS) spectra will be performed for the powder and anchored polymer.

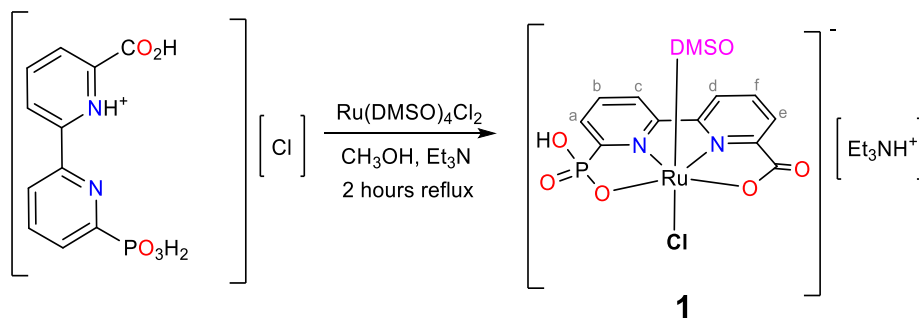
### 6.3 Conclusion

We have synthesized new coordination 2D polymer material, which is based on a monomeric efficient WOC, and had successfully immobilized it onto a carbon-based surface as well as the metal-oxide surface. The molecular nature and redox properties were investigated by electrochemical and spectroscopic techniques. Taking advantage of the intrinsic properties of CNTs, we have employed it to anchor catalyst **2** on glassy carbon electrodes. A current density as high as  $110 \text{ mA}\cdot\text{cm}^{-2}$  was observed, which is among the highest values for molecular Ru catalysts anchored on solid-state anodes.<sup>26</sup> The Resonance Raman spectroscopy confirms that the activated species do not undergo any unproductive side reactions during the catalytic process and neither leads to the formation of  $\text{RuO}_2$ . With high stability and catalytic activity, **2@CNT@GC** electrodes are efficient devices for electrochemically driven heterogeneous water oxidation.

## CHAPTER 6.

### 6.4 Experimental section

All chemicals and solvents were purchased from Sigma-Aldrich, Fluka, Acros Organics, Alfa Aesar, VWR, and were used without further purification unless otherwise specified. Instrumentation details are provided in the Supporting Information.



**Scheme 6:** Synthetic route for the preparation of the **1**.

#### Synthesis of [Ru<sup>II</sup>(bpc)(DMSO)Cl][HNEt<sub>3</sub>], **1**.

Under nitrogen atmosphere a mixture of [Ru(DMSO)<sub>4</sub>Cl<sub>2</sub>] (54.5 mg, 112.4 μmol, 1.0 eq) and H<sub>3</sub>bpc (30.0 mg, 107.1 μmol, 1 eq) were suspended in 2.5 mL anhydrous methanol, followed by Et<sub>3</sub>N (0.1 mL). The mixture was degassed by bubbling with argon for 15 min and then heated to reflux for 2 h until precipitate appeared. The reaction mixture was cool down to rt and the solid was washed with methanol (2.5 mL) and diethyl ether (5 mL). The obtained yellow-brown solid was dried under vacuum in the amount of 25 mg (44%).

**Anal. Calc. for 1** (C<sub>19</sub>H<sub>29</sub>ClN<sub>3</sub>O<sub>6</sub>PRuS), C, 37.88 %; H, 4.69 %; N, 6.84 %, S, 5.52 %. Found C, 37.79 %; H, 4.74 %; N, 6.94 %, S, 5.48 %. **HR-MS m/z:** Calculated for C<sub>13</sub>H<sub>12</sub>N<sub>2</sub>Na<sub>2</sub>O<sub>6</sub>PRuS [M]<sup>+</sup>: m/z 502.89928, found: m/z 502.8982. **<sup>1</sup>H NMR (500 MHz, D<sub>2</sub>O)** δ 8.30 (dd, *J* = 8.1, 1.1 Hz, 1H), 8.25 (dt, *J* = 8.1, 1.4 Hz, 1H), 8.07 (dd, *J* = 7.8, 1.0 Hz, 1H), 7.98 (tt, *J* = 7.9, 1.6 Hz, 2H), 7.82 (ddd, *J* = 7.7, 4.7, 1.1 Hz, 1H), 3.14 (s, 3H), 2.72 (s, 3H), 2.59 (q, *J* = 7.2 Hz, 6H), 1.04 (t, *J* = 7.2 Hz, 9H). **<sup>31</sup>P NMR (162 MHz, D<sub>2</sub>O)** δ 29.48, 9.72. **<sup>31</sup>P NMR (162 MHz, D<sub>2</sub>O)** δ 29.48.

#### Synthesis of [Ru(bpc)<sub>2</sub>(tpt)<sub>3</sub>]<sub>n</sub>, **2**.

Under a nitrogen atmosphere, a mixture of 1 eq. of [Ru(bpc)(DMSO)Cl] (25 mg) with 2/3 eq. of the bridging ligand tri(4-pyridyl)triazine (9.74 mg) was dissolved in 3 mL of 2,2,2-trifluoroethanol and refluxed overnight. The obtained purple solution was cooled to rt. The

obtained 2D polymer, **2** with the general formula  $[\text{Ru}(\text{Hbpc})(\text{tpt})]_n$ , was directly used for further characterization.

**Anal. Calc. for 2:** Found C, 42.24 %; H, 3.91 %; N, 10.94 %, S, 0.42%.

## CHAPTER 6.

### 6.5 References

- (1) Ye, S.; Ding, C.; Liu, M.; Wang, A.; Huang, Q.; Li, C. Water Oxidation Catalysts for Artificial Photosynthesis. *Advanced Materials*. 2019.
- (2) Moonshiram, D.; Alperovich, I.; Concepcion, J. J.; Meyer, T. J.; Pushkar, Y. Experimental Demonstration of Radicaloid Character in a RuV=O Intermediate in Catalytic Water Oxidation. *Proc. Natl. Acad. Sci.* **2013**, *110* (10), 3765 LP – 3770.
- (3) Hoque, M. A.; Benet-Buchholz, J.; Llobet, A.; Gimbert-Suriñach, C. Catalytic Oxidation of Water to Dioxygen by Mononuclear Ru Complexes Bearing a 2,6-Pyridinedicarboxylato Ligand. *ChemSusChem* **2019**, *12* (9), 1949–1957.
- (4) Duan, L.; Bozoglian, F.; Mandal, S.; Stewart, B.; Privalov, T.; Llobet, A.; Sun, L. A Molecular Ruthenium Catalyst with Water-Oxidation Activity Comparable to That of Photosystem II. *Nat. Chem.* **2012**, *4* (5), 418–423.
- (5) Matheu, R.; Ertem, M. Z.; Benet-Buchholz, J.; Coronado, E.; Batista, V. S.; Sala, X.; Llobet, A. Intramolecular Proton Transfer Boosts Water Oxidation Catalyzed by a Ru Complex. *J. Am. Chem. Soc.* **2015**, *137* (33), 10786–10795.
- (6) Matheu, R.; Ertem, M. Z.; Gimbert-Suriñach, C.; Benet-Buchholz, J.; Sala, X.; Llobet, A. Hydrogen Bonding Rescues Overpotential in Seven-Coordinated Ru Water Oxidation Catalysts. *ACS Catal.* **2017**, *7* (10), 6525–6532.
- (7) Xie, L.; Li, X.; Wang, B.; Meng, J.; Lei, H.; Zhang, W.; Cao, R. Molecular Engineering of a 3D Self-Supported Electrode for Oxygen Electrocatalysis in Neutral Media. *Angew. Chemie Int. Ed.* **2019**, *58* (52), 18883–18887.
- (8) Niu, F.; Wang, D.; Li, F.; Liu, Y.; Shen, S.; Meyer, T. J. Hybrid Photoelectrochemical Water Splitting Systems: From Interface Design to System Assembly. *Adv. Energy Mater.* **2020**, *10* (11), 1900399.
- (9) Gao, Y.; Ding, X.; Liu, J.; Wang, L.; Lu, Z.; Li, L.; Sun, L. Visible Light Driven Water Splitting in a Molecular Device with Unprecedentedly High Photocurrent Density. *J. Am. Chem. Soc.* **2013**, *135* (11), 4219–4222.
- (10) Yamamoto, M.; Nishizawa, Y.; Chábera, P.; Li, F.; Pascher, T.; Sundström, V.; Sun, L.; Imahori, H. Visible Light-Driven Water Oxidation with a Subporphyrin Sensitizer and a Water Oxidation Catalyst. *Chem. Commun.* **2016**, *52* (94), 13702–13705.
- (11) Zhang, B.; Sun, L. Artificial Photosynthesis: Opportunities and Challenges of Molecular Catalysts. *Chem. Soc. Rev.* **2019**, *48* (7), 2216–2264.
- (12) Odrobina, J.; Scholz, J.; Pannwitz, A.; Francàs, L.; Dechert, S.; Llobet, A.; Jooss, C.; Meyer, F. Backbone Immobilization of the Bis(Bipyridyl)Pyrazolate Diruthenium Catalyst for Electrochemical Water Oxidation. *ACS Catal.* **2017**, *7* (3), 2116–2125.
- (13) Jackson, M. N.; Surendranath, Y. Molecular Control of Heterogeneous Electrocatalysis through Graphite Conjugation. *Acc. Chem. Res.* **2019**, *52* (12), 3432–3441.
- (14) Materna, K. L.; Crabtree, R. H.; Brudvig, G. W. Anchoring Groups for Photocatalytic Water Oxidation on Metal Oxide Surfaces. *Chem. Soc. Rev.* **2017**, *46* (20), 6099–6110.
- (15) Creus, J.; Matheu, R.; Peñafiel, I.; Moonshiram, D.; Blondeau, P.; Benet-Buchholz, J.; García-Antón, J.; Sala, X.; Godard, C.; Llobet, A. A Million Turnover Molecular Anode for Catalytic Water Oxidation. *Angew. Chemie Int. Ed.* **2016**, *55* (49), 15382–15386.
- (16) Karousis, N.; Tagmatarchis, N.; Tasis, D. Current Progress on the Chemical Modification of Carbon Nanotubes. *Chem. Rev.* **2010**, *110* (9), 5366–5397.
- (17) Hoque, M. A.; Gil-Sepulcre, M.; de Aguirre, A.; Elemans, J. A. A. W.; Moonshiram, D.; Matheu, R.; Shi, Y.; Benet-Buchholz, J.; Sala, X.; Malfois, M.; Solano, E.; Lim, J.; Garzón-Manjón, A.; Scheu, C.; Lanza, M.; Maseras, F.; Gimbert-Suriñach, C.; Llobet, A. Water Oxidation Electrocatalysis Using Ruthenium Coordination Oligomers Adsorbed on Multiwalled Carbon Nanotubes. *Nat. Chem.* **2020**.
- (18) Md Asmaul Hoque. A Journey towards Efficient Molecular WOCs: From Mononuclear to

- Polynuclear Complexes, Institute of Chemical Research of Catalonia, 2019.
- (19) Bonke, S.; Chhabra, S. Schematic of an in situ electrochemical cell integrated in an EPR spectrometer. o Title.
- (20) Pineda-Galvan, Y.; Ravari, A. K.; Shmakov, S.; Lifshits, L.; Kaveevivitchai, N.; Thummel, R.; Pushkar, Y. Detection of the Site Protected 7-Coordinate RuV = O Species and Its Chemical Reactivity to Enable Catalytic Water Oxidation. *J. Catal.* **2019**, *375*, 1–7.
- (21) Bullock, R. M.; Das, A. K.; Appel, A. M. Surface Immobilization of Molecular Electrocatalysts for Energy Conversion. *Chem. – A Eur. J.* **2017**, *23* (32), 7626–7641.
- (22) Sheehan, S. W.; Thomsen, J. M.; Hintermair, U.; Crabtree, R. H.; Brudvig, G. W.; Schmuttenmaer, C. A. A Molecular Catalyst for Water Oxidation That Binds to Metal Oxide Surfaces. *Nat. Commun.* **2015**, *6* (1), 6469.
- (23) Meyer, T. J.; Sheridan, M. V.; Sherman, B. D. Mechanisms of Molecular Water Oxidation in Solution and on Oxide Surfaces. *Chem. Soc. Rev.* **2017**, *46* (20), 6148–6169.
- (24) Gimbert-Surifñach, C.; Moonshiram, D.; Francàs, L.; Planas, N.; Bernales, V.; Bozoglian, F.; Guda, A.; Mognon, L.; López, I.; Hoque, M. A.; Gagliardi, L.; Cramer, C. J.; Llobet, A. Structural and Spectroscopic Characterization of Reaction Intermediates Involved in a Dinuclear Co-Hbpp Water Oxidation Catalyst. *J. Am. Chem. Soc.* **2016**, *138* (47), 15291–15294.
- (25) Nakamoto, K. Infrared and Raman Spectra of Inorganic and Coordination Compounds. *Handbook of Vibrational Spectroscopy*. December 20, 2001.
- (26) Schindler, D.; Gil-Sepulcre, M.; Lindner, J. O.; Stepanenko, V.; Moonshiram, D.; Llobet, A.; Würthner, F. Efficient Electrochemical Water Oxidation by a Trinuclear Ru(Bda) Macrocycle Immobilized on Multi-Walled Carbon Nanotube Electrodes. *Adv. Energy Mater.* **2020**, *n/a* (n/a), 2002329.
- (27) Hyun, Y.; Choi, J.-Y.; Park, H.-K.; Lee, C.-S. Synthesis and Electrochemical Performance of Ruthenium Oxide-Coated Carbon Nanofibers as Anode Materials for Lithium Secondary Batteries. *Appl. Surf. Sci.* **2016**, *388*, 274–280.



## CHAPTER 6.

### 6.6 Supporting information

#### 6.6.1 Materials and methods

All chemicals and reagents were purchased from commercial suppliers and used without any further purification unless noted otherwise. Multi-walled carbon nanotubes (CNTs) in bulk with a purity of > 95 %, OD > 50 nm, length ~ 50  $\mu\text{m}$  were obtained from HeJi, Inc., China. Glassy carbon plates ( $\text{GC}_p$ , 20 x 10 x 0.18 mm) were purchased from HTW, Germany. For electrochemical experiments, highly pure water was obtained by filtration of distilled water through a nanopure Milli-Q water purification system. All solvents used in electrochemical studies were of a purity of 99.8 % and higher.

##### 6.6.1.1 Preparation of electrodes **2@CNT@GC**

A dispersion of CNTs (5 mg) in THF (5 mL) was prepared by sonicating the mixture for 40 min. 0.1 mL of the purple catalyst solution was added to 1 mL of a freshly prepared dispersion of CNTs in THF. Immediately, solution decolorization occurred, indicating the anchoring of the catalyst on the CNTs. The dispersion of **2@CNT** was used for the preparation of electrodes.

*Electrodes for cyclic voltammetry (CV) experiments* were prepared by drop-casting the **2@CNT** suspension in THF/TFE (1:0.1) onto the surface of the glassy carbon disk (4 x 10  $\mu\text{L}$ ). Only after the solvent of the first 10  $\mu\text{L}$  was completely evaporated, the next 10  $\mu\text{L}$  were placed onto the electrode.

##### 6.6.1.2 Preparation of phosphate buffer for electrochemical experiments

Phosphate buffers used in the electrochemical experiments were prepared by dissolving different amounts of phosphate salts in highly pure Mili-Q water: pH 7, 1 M ionic strength:  $\text{NaH}_2\text{PO}_4$  (23.1 g, 193 mmol) and  $\text{Na}_2\text{HPO}_4$  (37.7 g, 266 mmol) in water (1000 mL).

pH = 1.0 solution was prepared as a 0.1M TfOH solution in the deionized water.

##### 6.6.1.3 Electrochemistry

All electrochemical experiments were carried out on an IJ-Cambria CHI-730 potentiostat. As working electrodes (WE), glassy carbon disks (GC,  $\varphi = 0.3 \text{ cm}$ ,  $S = 0.07 \text{ cm}^2$ ) or a glassy carbon plate ( $\text{GC}_p$ , 20 mm x 10 mm x 0.18 mm) were used. Pt mesh was used as a counter electrode (CE).  $\text{Hg}/\text{Hg}_2\text{SO}_4$  ( $\text{K}_2\text{SO}_4$  sat.) was used as a reference electrode (RE) in CV. All

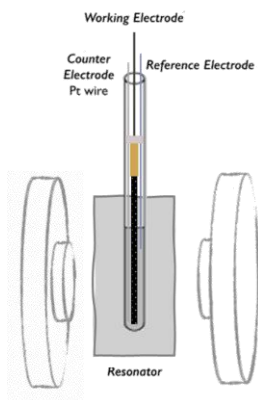
potentials were converted to a normal hydrogen electrode (NHE) by adding 0.65 V to the measured potential. Electrochemical cells For CV a 20 mL glass vial was used. A self-made Teflon cap with three holes was applied to hold the electrodes at the same distance and ensure reproducibility. For CV experiments, the scan rate was 100 mV/s unless stated otherwise. iR compensation at 85 % was applied for a single CV experiment.

#### 6.6.1.4 *Controlled potential electrolysis (CPE)*

For CPE experiments, a two-compartment cell was used. The chambers were separated with a frit. The working electrode and the reference electrode were placed in one compartment, the counter electrode in the other one. Both chambers were equipped with a magnetic stirring bar.

## CHAPTER 6.

A



B

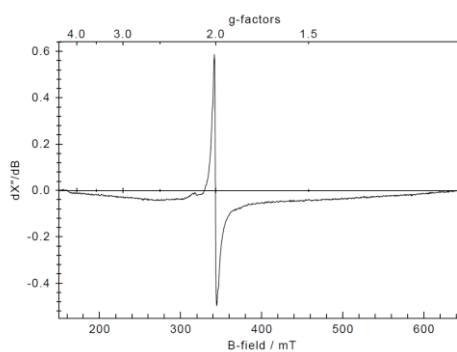
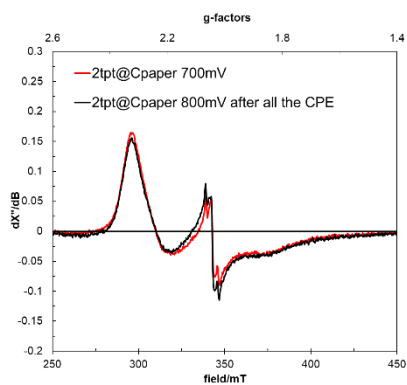


**Figure S1.** (A) Schematic of *in situ* electrochemical cells integrated into an EPR spectrometer. (B) EPR spectra of  $C_{\text{paper}}$  after CPE at 1.2 V

A



B

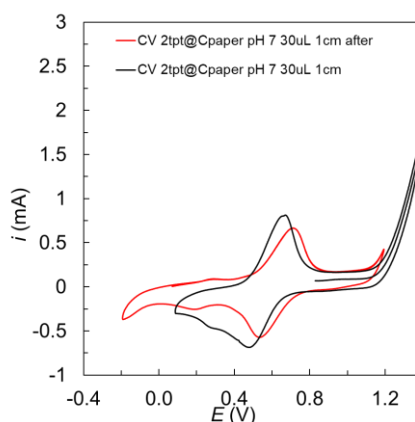


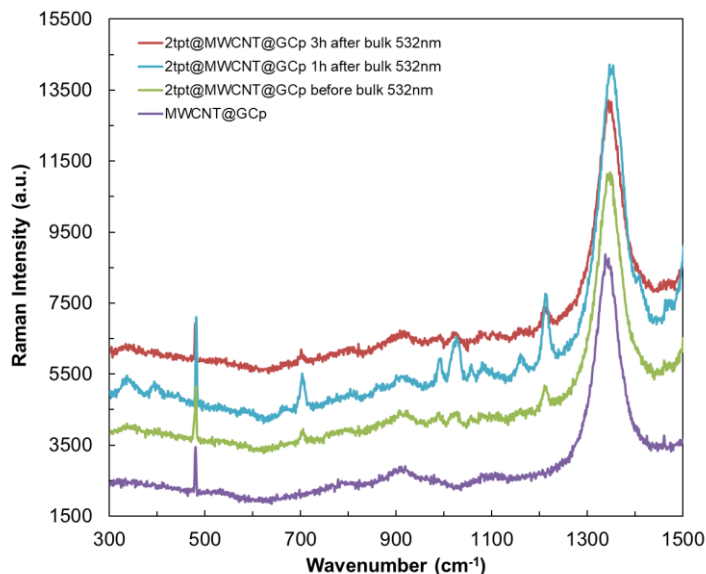
**Figure S2.** (A) EPR spectra comparison of the electrode  $2@C_{\text{paper}}$  loading and catalytic response before and after EPR measurements. (B) CV comparison of the electrode  $2@C_{\text{paper}}$  loading and catalytic response before and after EPR measurements in pH 7.

VI

### 6.6.2 Resonance Raman Spectroscopy

Raman spectroscopy was performed to analyze the presence of the ruthenium oxide after CPE of **2@CNT@GC<sub>p</sub>**. The results are shown in the Figure below.

**A**



**B**

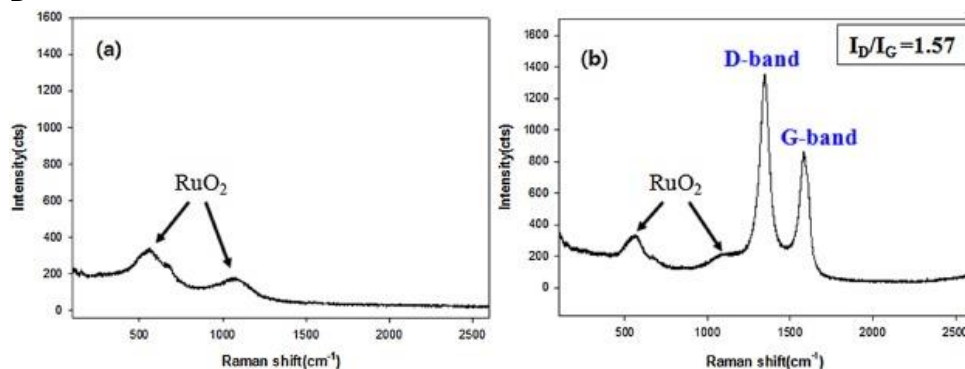


**Figure S3.** (A), Resonance Raman spectra of **CNT@GC<sub>p</sub>**, **2@CNT@GC<sub>p</sub>** before CPE, **2@CNT@GC<sub>p</sub>**, and **2@CNT@GC<sub>p</sub>** after control potential electrolysis ( $E_{app} = 1.35$  V in a pH 7 1 M phbf solution) for 1h and 3h respectively. (B), Resonance Raman spectra of RuO<sub>2</sub>/Ni foam (left) and RuO<sub>2</sub>/CNFs/Ni foam (right)<sup>27</sup>.

## CHAPTER 6.

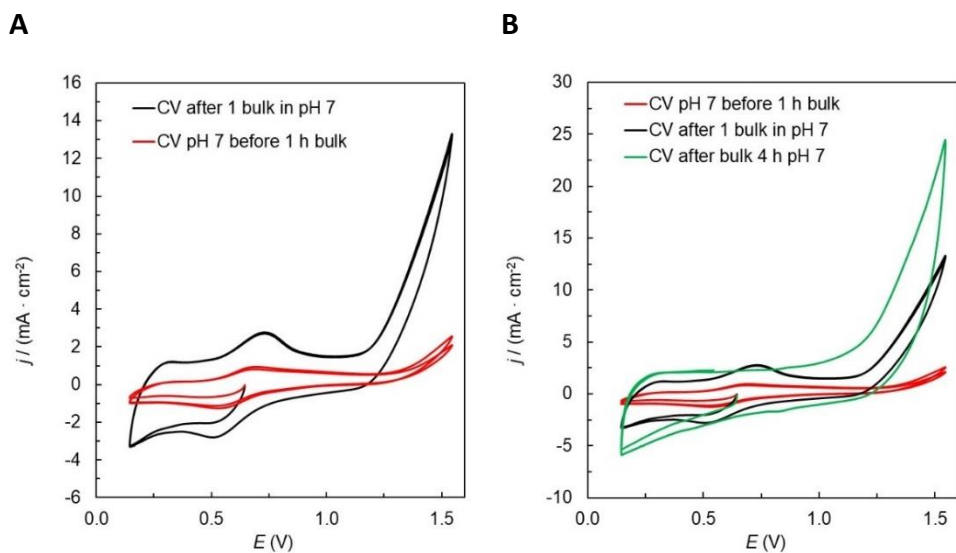


**Figure S4.** (A), CV of 2@CNT@GC<sub>p</sub> before CPE (in red) and 2@CNT@GC<sub>p</sub> after control potential electrolysis ( $E_{app} = 1.35$  V in a pH 7 1 M phbf solution) for 1h (in black). (B), CV of 2@CNT@GC<sub>p</sub> before CPE (in red), 2@CNT@GC<sub>p</sub> after control potential electrolysis ( $E_{app} = 1.35$  V in a pH 7 1 M phbf solution) for 1h (in black), and 2@CNT@GC<sub>p</sub> after control potential electrolysis ( $E_{app} = 1.35$  V in a pH 7 1 M phbf solution) for 4h (in green).

## 7 CHAPTER 7

### Ruthenium-based cyclometalated complexes: Synthesis, structure, and redox properties

---

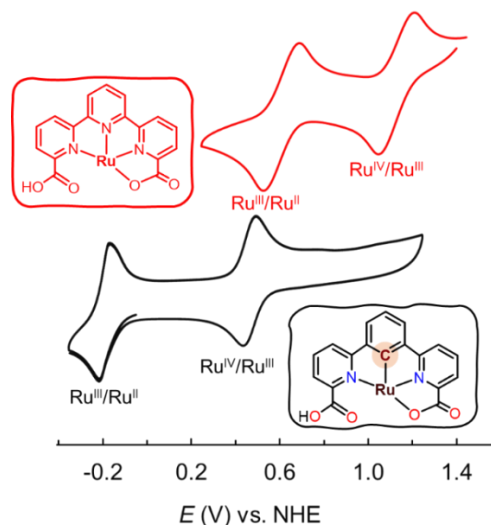
*The present chapter uncovers a series of novel cyclometalated Ru complexes featuring the pentadentate **H<sub>3</sub>pda** ligand platform (**H<sub>3</sub>pda** is 6,6'-(1,3-phenylene)dipicolinic acid), in order to utilize the octahedral coordination mode around the Ru center and thus modulate its electrochemical and physical properties. The chelation mode was defined by the steric effects and C-H activation selectivity of the ligand, which directed the development of a general synthetic protocol. Furthermore, the structural and electrochemical properties of the ruthenium complexes were studied in-depth, and the results are presented below.*

---

## CHAPTER 7

VII

## Ruthenium-based cyclometalated complexes: Synthesis, structure, and redox properties



### **Abstract**

In this chapter of the thesis, we present new cyclometalated Ru complexes based on the pentadentate (pda) ligand platform ( $\text{H}_3\text{pda}$  is 6,6'-(1,3-phenylene)dipicolinic acid), that were synthesized and fully characterized. The complexes were designed in order to utilize the octahedral coordination environment around the Ru center to modulate its electrochemical properties. The chelation mode was controlled by the steric effects and C–H activation selectivity of the ligand, which prompted the development of a general synthetic protocol. The in-depth electrochemical studies show significant stability at high-applied potentials over a wide range of pHs (pH 2 until pH 12).

### **Contributions:**

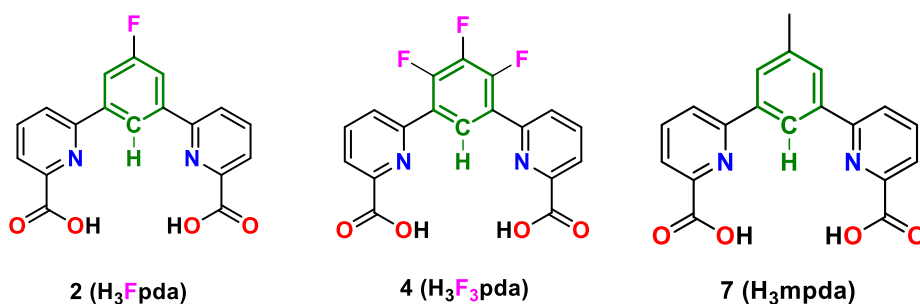
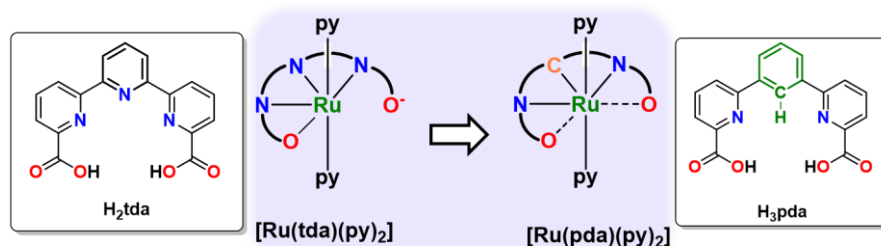
Natalia Vereshchuk synthesized and characterized complexes **5** and **6**, as well as carried out all the electrochemical and spectroscopic experiments for them.



## CHAPTER 7.

### 7.1 Introduction

As recently shown, terpyridyldicarboxylate (tda) type of ligands form highly active water oxidation catalysts (WOC) with Ruthenium<sup>1,2</sup> (see Scheme 1) which can even be used in photo-activated systems in homogeneous phase using photosensitizers of the family of [Ru(bpy)<sub>3</sub>]<sup>2+</sup> or on the surface of semiconductors such as silicon.<sup>3,4</sup> However, Ru-WOC of this type suffers from high onset potentials of 1.3–1.4 V vs NHE.



**Scheme 1.** Schematic representation of the complexes and ligands described herein.

As described in Chapter 3, the substitution of the carboxylate with phosphonates<sup>5</sup> can improve kinetic and catalytic properties, however, it does not significantly reduce the potential of Ru<sup>V</sup>=O formation, the species responsible to trigger the water oxidation reaction. The high kinetic barrier could be overcome through the introduction of higher electron densities at the equatorial ligand to lower the Ru<sup>V/IV</sup> oxidation potential, consequently lowering the applied potential needed for the WOC. These results motivate us to explore the complexes containing negatively charged ligand, which would stabilize higher oxidation states due to strong  $\sigma$  donation through the metal-carbon bond. For this purpose, cyclometallating ligands of the 1,3-bis(6-carboxypyridyl)-benzene type with the

## CHAPTER 7.

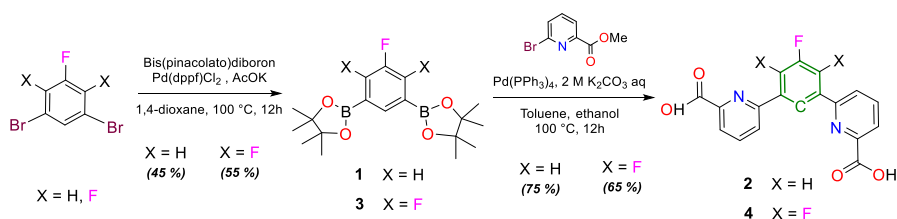
general formula  $H_3Xpda$  are particularly interesting as they are expected to lower the oxidation potentials of ruthenium complexes (see Scheme 1). This chapter presents the efforts to synthesize and characterize a small library of such ligands and their Ruthenium derivatives, featuring backbone modifications to fine-tune their electrochemical properties as well as to increase their stability under oxidative conditions.

## CHAPTER 7.

### 7.2 Results and Discussion

#### 7.2.1 Synthesis and Characterization of ligands 2 and 4.

The synthetic strategy followed for the preparation of the  $\text{pda}^{3-}$  ligands precursors  $\text{H}_3\text{Fpda}$  (6,6'-(5-fluoro-1,3-phenylene)dipicolinic acid), **2**, and  $\text{H}_3\text{F}_3\text{pda}$  (6,6'-(4,5,6-trifluoro-1,3-phenylene)dipicolinic acid), **4**, is outlined in Scheme 2. Compounds **2** and **4** were synthesized in four steps from 1,3-dibromo-5-fluorobenzene and 1,5-dibromo-2,3,4-trifluorobenzene, respectively. The latter were first converted into arylboronic esters *via* the Miyama cross-coupling reaction in moderate yields.<sup>6</sup> The desired ligand precursors were finally prepared by the Suzuki-Miyaura cross-coupling reaction,<sup>7,8</sup> followed by *in situ* hydrolyzations of the ester groups<sup>9</sup> with a yield of 75% for  $\text{H}_3\text{Fpda}$ , **2**, and 65% for  $\text{H}_3\text{F}_3\text{pda}$ , **4**. Full characterization of the new compounds, including 1D and 2D NMR, mass spectrometry, and elemental analysis was carried out and the details are collected in the experimental section and Figures S1-S28.



**Scheme 2.** Synthesis of ligands  $\text{H}_3\text{Fpda}$ , **2**, and  $\text{H}_3\text{F}_3\text{pda}$ , **4**.

This synthetic strategy combines two practical advantages from previously reported syntheses of terpyridyldicarboxylate (tda) and terpyridyldiphosphonate (tPa) ligands<sup>1,5</sup>:

- (1) No lithiation and further cross-coupling reaction steps are involved; thus, aryl-halogen substituents are tolerated and are available for subsequent cross-coupling reactions;
- (2) Utilization of the ester allows us to avoid the low-yielding methyl oxidation step by the  $\text{K}_2\text{Cr}_2\text{O}_7$  or  $\text{KMnO}_4$ .

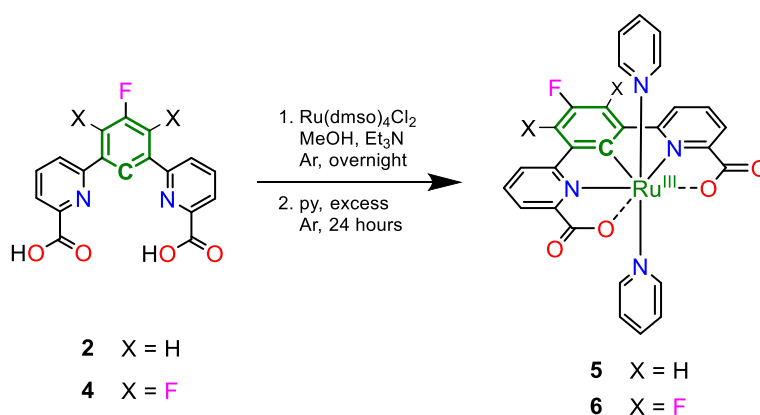
It is worth mentioning that the presence of the base ( $\text{K}_2\text{CO}_3$ ) during the second coupling reaction partially hydrolyzes the ester groups of the arylboronic ester, and promotes the precipitation of the formed acid. Consequently, it substantially lowers the purification efforts of the coupling product.

The methyl derivative ligand **7** in **Scheme 1** and related complexes were synthesized and characterized by our collaborators from KTH Royal Institute of Technology, Sweden. The detailed synthesis and characterizations of the ligands can be found in the Supporting information for comparison.

### 7.2.2 Synthesis and Characterization of complexes **5** and **6**.

The synthetic approach employed to prepare complexes **5** and **6** is a two-step coordination route procedure developed by our group for related  $[\text{Ru}(\text{tda})\text{py}_2]$  and  $[\text{Ru}(\text{tPa})\text{py}_2]$  complexes,<sup>1,5</sup> which includes: (1) coordination of the polydentate ligand to the precursor  $[\text{Ru}(\text{DMSO})_4\text{Cl}_2]$  in alcoholic solution at reflux using  $\text{Et}_3\text{N}$  as a base, and (2) addition of the axial ligands, which are usually pyridines (Scheme 3).

To our surprise, the formation of the Ruthenium complexes based on the **H<sub>3</sub>Fpda** and **H<sub>3</sub>F<sub>3</sub>pda** ligands following typical synthetic procedure was highly unselective with moderate yields of 23% and 11% for **5** and **6**, respectively.<sup>1,2,5</sup>



**Scheme 3.** Synthesis of complex  $[\text{Ru}^{\text{III}}(\text{Fpda})(\text{py})_2]$ , **5**, and  $[\text{Ru}^{\text{III}}(\text{F}_3\text{pda})(\text{py})_2]$ , **6**.

Complexes **5** and **6** were characterized electrochemically (see next section) and by mass spectrometry (see Figure S29-S30). Sufficiently good crystals for single-crystal X-ray diffraction analysis were obtained for **5** and the ORTEP plot of its cation is displayed in Figure 1. In this case, the Ru center adopts a slightly distorted octahedral geometry with the **H<sub>3</sub>Fpda** ligand occupying the equatorial positions and the pyridines occupying the axial ones.

## CHAPTER 7.

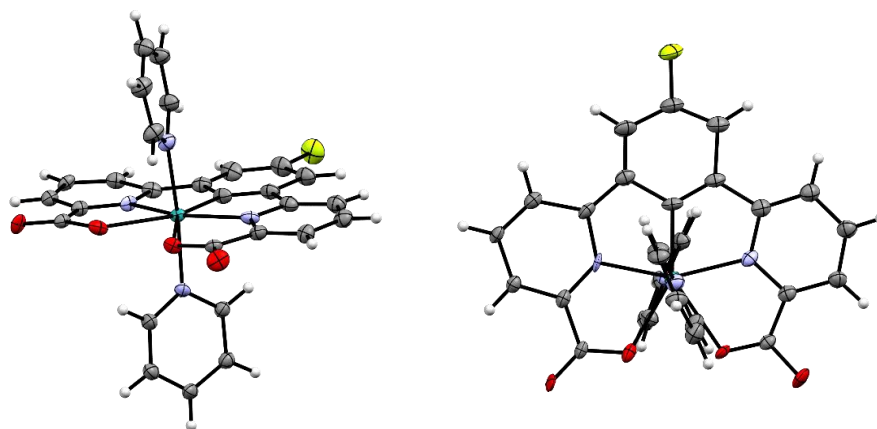


**Figure 1.** X-ray structure ORTEP views (at 50% probability) for **5** Color code: Ru, cyan; F, green; N, blue; O, red; C, black; H, white.

It is important to highlight, that complexes **5** and **6** were isolated in the Ru<sup>III</sup> oxidation state, which was confirmed by electrochemistry (open circuit potential and control potential electrolysis measurements) as well as NMR spectroscopy, where complexes showed paramagnetic behavior. The addition of an excess amount of Sodium Ascorbate as a reducing agent, typically used to reduce Ru<sup>III</sup> species to their Ru<sup>II</sup> derivatives, did not improve the NMR response, which can be explained by the relatively low reduction potential of the Sodium Ascorbate unable to reduce complexes **5** and **6**.

### 7.2.3 Redox Properties of complexes **5** and **6**.

We analyzed the redox properties of complexes **5** and **6** by Cyclic Voltammetry (CV) and Differential Pulse Voltammetry (DPV). The electrochemical experiments were carried out in a typical three-electrode configuration using glassy carbon as the working electrode, Pt as the counter electrode, and Hg/Hg<sub>2</sub>SO<sub>4</sub> (MSE) as the reference electrode. All potentials in this work were reported versus NHE ( $E_{NHE} = E_{MSE} + 0.65$  V).

At neutral conditions, the CV of complexes **5** and **6** show two chemically and electrochemically reversible waves at  $E_{1/2} = -0.18$  V and  $E_{1/2} = 0.47$  V for **5** and at  $E_{1/2} = 0.06$  V and  $E_{1/2} = 0.62$  V for **6**, which are assigned to the Ru<sup>III/II</sup> and Ru<sup>IV/III</sup> couples respectively (Figure 2 and Figure 4). The anodic shift of the redox couples of **6** as compared to those of **5** is due to the different electronic influence exerted by the three fluorine substituents in the equatorial pda ligand **F<sub>3</sub>pda<sup>3-</sup>**.

CVs for complex **5** in aqueous solutions at different pH values are shown in Figure 2A. At pH 2.0, two quasi-reversible one-electron waves appear at  $E_{1/2} = 0.0$  V and  $E_{1/2} = 0.46$  V, which are assigned to the Ru<sup>III/II</sup> and Ru<sup>IV/III</sup> couples respectively. Thus, while the potential of the Ru<sup>III/II</sup> couple displays a pH dependence, the potential of the Ru<sup>IV/III</sup> couple remains pH-independent. Such behavior can be rationalized by assuming a difference in the pK<sub>a</sub> values for complex **5** at the Ru<sup>II</sup>, Ru<sup>III</sup>, and Ru<sup>IV</sup> oxidation states, involving protonation/deprotonation of one of the carboxylate groups of the pda ligand. Indeed, simulation and fitting of the Pourbaix diagram to the experimental values reveal that at low pH complex **5** at the Ru<sup>II</sup> states is protonated with pK<sub>a</sub>=4.4 (Figure 2B, see also Supporting Information).

It is important to highlight the change in the shape of the Ru<sup>III/II</sup> oxidation wave at low pH, which becomes sharper with the pH decrease. That could be an indication of an adsorption process on the electrode surface due to the decrease in the solubility of the Ru<sup>II</sup> at low pH. Due to this phenomenon, the oxidation potentials for Ru<sup>III/II</sup> at acidic pHs were extracted from the DPV assuming a smaller error in the potential determination for the Pourbaix diagram (Figure 2B).

## CHAPTER 7.

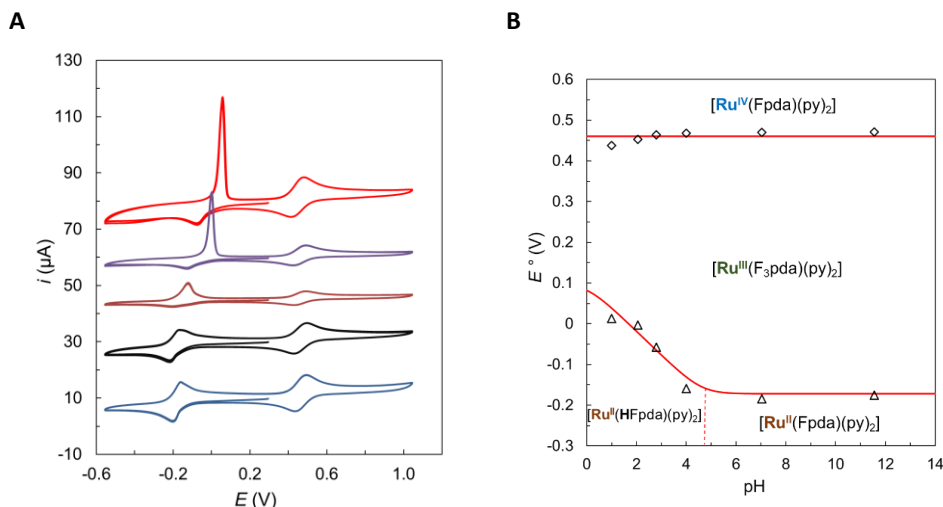


**Figure 2. (A).** Cyclic voltammetry of **5**, at pH 2.0 (red), pH 2.8 (violet), pH 4.0 (brown), pH 7.0 (black) and pH 11.6 (blue). **(B)** Pourbaix diagram for complex **5**. The red solid lines indicate the fitted redox potentials (see Supporting Information) whereas the dashed vertical lines indicate the pK<sub>a</sub>. Triangles are the experimental values obtained by CV

It is interesting to compare the potentials of the Ru<sup>IV/III</sup> and Ru<sup>III/II</sup> redox couples for **5** and **6** with those of other related Ru complexes containing polypyridylcarboxylic ligands such as [Ru<sup>II</sup>(tda)(py)<sub>2</sub>],<sup>1</sup> (see Figure 3). As expected, the redox potentials shift cathodically according to the higher electron densities at the equatorial position of the ligand. For instance, at pH 7, the Ru<sup>III/II</sup> and Ru<sup>IV/III</sup> redox couples for **5** are cathodically shifted by 730 mV and 630 mV, respectively, as compared to that of [Ru<sup>II</sup>(tda)(py)<sub>2</sub>]. Analogous comparison with complex **6** gives cathodic shifts of 490 mV and 480 mV for the Ru<sup>III/II</sup> and Ru<sup>IV/III</sup> redox couples, respectively. These significant shifts are due to the strong sigma-donation effect exerted by the carbon anion of the fluorinated pda<sup>3-</sup> ligands **Fpda<sup>3-</sup>** and **F<sub>3</sub>pda<sup>3-</sup>**.<sup>1</sup>

As described in detail in Chapters 1 and 3, in order to reach the active Ru<sup>V</sup> species, responsible to trigger the WOC reaction, it is necessary to form the derivative Ru-OH<sub>2</sub> complex, which will be involved in PCET processes. This is usually achieved by applying a high oxidation potential to quantitatively generate the Ru<sup>IV</sup> species, which successively coordinates a solvent water molecule. Thus, for all the complexes described herein different routes to generate the aqua species were attempted including multiple CV cycling through

high oxidation potentials and controlled potential electrolysis at different potentials and different pHs. Unfortunately, none of them led to the desired complex or water oxidation catalytic activity. Instead, all the complexes showed remarkable stability.

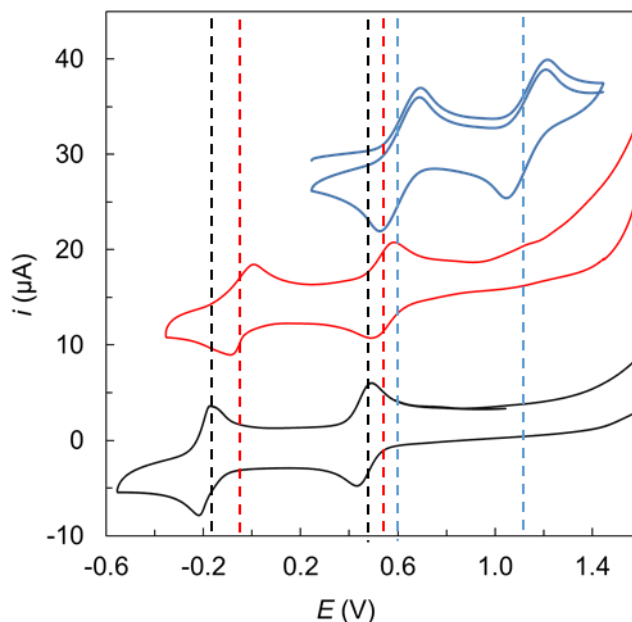


**Figure 3.** The comparison of the electrochemical properties of the complexes **5** (black), **6** (red), and  $[\text{Ru}^{\text{II}}(\text{tda})(\text{py})_2]$  (blue) was analyzed by CV at pH 7.0. The vertical dashed lines correspond to the III/II and IV/III redox couples of the Ru complexes discussed above.

An example is given in Figure 4A, which shows 25 repetitive CV cycles of **5** at pH 11.6 phosphate buffer aqueous solution. Upon cycling, the intensity of the current at 1.0-1.6 V increases more than one order of magnitude (see grey lines). Sometimes this increase in current is attributed to a catalytic process. However, in this, case the same response was reproduced by using a clean GC electrode using precisely the same condition (Figure 4B). This leads us to the conclusion that the observed increase in current comes from the oxidation of the electrode surface. At the same time, complex **5** shows significant stability over harsh oxidation potential and highly basic pH.



## CHAPTER 7.

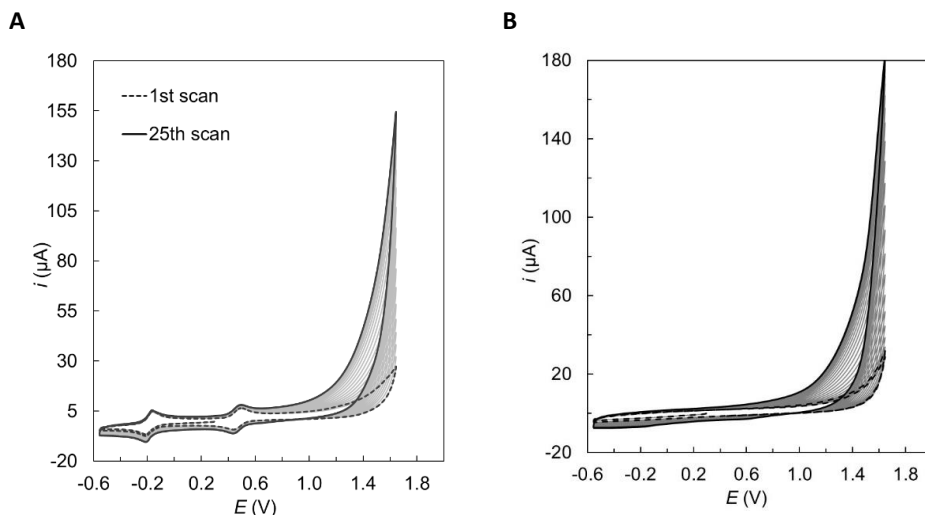


**Figure 4.** (A) Cyclic voltammetry of **5**, at pH 11.6 in a 0.1 M phosphate buffer aqueous solution (dashed black trace). Solid black line trace, cyclic voltammetry of **5** at pH 11.6 in a 0.1 M phosphate buffer aqueous solution after 25 repetitive CV cycles. The CV in grey corresponds to the evolution of the CV during cycling in pH 11.6 solution. (B) 25 repetitive CV cycles of blank pH 11.6 0.1 M phosphate buffer aqueous solution.

### 7.3 Conclusion

Here we reported the synthesis and characterization of the novel cyclometalated complexes with the general formula  $[\text{Ru}(\text{Xpda})(\text{py})_2]$  which adopt octahedral coordination of the peripheral  $\pi$ -extended carbanionic fragments based on benzene. The synthesis was optimized as well as purification protocol was simplified to a single chromatographic run using commercially available silica gel, ultimately leading to moderate yields.

The electrochemical analysis of the synthesized complexes showed a cathodic shift up to 730 V of the redox potentials upon coordination of the  $\pi$ -extended carbanionic donor sets as compared to the related  $[\text{Ru}^{\text{II}}(\text{tda})(\text{py})_2]$  and  $[\text{Ru}^{\text{II}}(\text{H}_2\text{tPa})(\text{py})_2]$  complexes. While the latter are spectacular catalysts reaching maximum TOF in the order of  $10^4 \text{ s}^{-1}$ , the replacement of one pyridine in the terpyridine by a phenyl group renders these complexes into very robust coordination compounds without any catalytic activity towards water oxidation. All the reported here complexes showed phenomenal stability and robustness over applying high potential at base pH environment.

## CHAPTER 7.

The reason for the absence of any catalytic activity can be explained by the rigid cyclometalated ring of the **H<sub>3</sub>Xpda** ligand, which does not allow hydroxo coordination and hinders the formation of the high oxidation state Ru<sup>V</sup>=O complex, required for the WOC.

Despite the activity issues, the present work enlarges the landscape of [Ru(Xpda)(py)<sub>2</sub>] complexes and uncovers additional factors influencing the water oxidation catalysis, especially regarding the presence of anionic ligands and their implication in both *pK<sub>a</sub>* and redox potentials. The complexes presented in this study suggest the possibility of utilization of the cyclometalated complexes for tuning electrochemical properties of the WOC in order to decrease the overpotential for catalysis.

## CHAPTER 7.

### 7.4 Experimental section

All chemicals and solvents were purchased from Sigma-Aldrich, Fluka, ABCR, Acros Organics, Alfa Aesar, VWR, and were used without further purification unless otherwise specified. Instrumentation details are provided in the Supporting Information.

**(1)** Into a two-necked flask, 1,3-dibromo-5-fluorobenzene (1.0 g, 3.97 mmol), bis(pinacolato)diboron (2.52 g, 9.93 mmol), potassium acetate (1.56 g, 15.88 mmol) and Pd(dppf)Cl<sub>2</sub> (0.15 g, 0.2 mmol, 5%) were successively added and dissolved in 20 mL dioxane under argon protection with stirring. The reaction was refluxed overnight under Ar, cooled down to room temperature, and filtered to remove large particles. A part of the salts was extracted with saturated brine and ethyl acetate, and the organic phase was washed with water (3×50 mL) to neutrality and dried over anhydrous magnesium sulfate. After filtration, a reddish-brown liquid was obtained, the solvent was evaporated in *vacuo* and the residue was purified by combiflash column chromatography on silica gel using an ethyl acetate/hexane gradient (ethyl acetate = 0-10%) to get the product as a white powder (0.62 g, 45 %).

<sup>1</sup>H NMR (400 MHz, CDCl<sub>3</sub>) δ 8.02 (q, J = 1.0 Hz, 1H), 7.55 (dd, J = 9.1, 1.0 Hz, 2H), 1.34 (s, 24H). <sup>13</sup>C NMR (101 MHz, CDCl<sub>3</sub>) δ 163.61, 136.81 (d, J = 2.8 Hz), 123.99 (d, J = 19.4 Hz), 84.20, 25.01. <sup>19</sup>F NMR (376 MHz, CDCl<sub>3</sub>) δ -115.64, (See Figures S1-S6). HRMS m/z: Calculated for C<sub>18</sub>H<sub>28</sub>B<sub>2</sub>FO<sub>4</sub>Na [M + H]<sup>+</sup>: m/z 349.2158, found: m/z 349.2169 (See Figures S25).

**(2)** To a mixture of **1** (1 eq, 1.67 mmol, 0.58 g), 6-bromo-2-methylpyridine (2 eq., 3.33 mmol, 0.72 g) and [Pd(PPh<sub>3</sub>)<sub>4</sub>] (0.12 mmol, 134 mg, 7%) under Ar atmosphere were added 2M K<sub>2</sub>CO<sub>3</sub> aqueous solution (5 ml), ethanol (5 ml) and toluene (20 mL). The reaction mixture was heated under reflux at 85 °C until white precipitate appeared (12 hours). After the reaction mixture was cooled down to room temperature and the precipitate was isolated and washed with ethanol. The precipitate was mixed with 50 mL of MeOH and sonicated for 15 min to form a white suspension. Then the aqueous solution of KOH (87.6% purity, 1.41 g, 22.0 mmol) in 20 mL was added to the suspension and the strongly basic mixture was stirred at 80 °C for 20 min. The reaction mixture was let to cool down to room temperature and neutralized with 1M HCl, upon which a light-pink precipitate has formed.

The precipitate was then centrifuged off, washed with water (3×90 mL) and ethanol (90 mL), and evacuated overnight, resulting in the title compound as a white solid (0.42 g, 75 %).

**<sup>1</sup>H NMR (400 MHz, DMSO-*d*<sub>6</sub>)** δ 8.75 (t, *J* = 1.5 Hz, 1H), 8.43 (dd, *J* = 7.9, 1.1 Hz, 2H), 8.21 – 8.12 (m, 4H), 8.08 (dd, *J* = 7.7, 1.0 Hz, 2H). **<sup>13</sup>C NMR (101 MHz, DMSO-*d*<sub>6</sub>)** δ 165.94, 154.39, 154.37, 148.26, 140.83, 140.75, 138.94, 124.11, 124.00, 121.18, 114.81, 114.58. **<sup>19</sup>F NMR (376 MHz, DMSO-*d*<sub>6</sub>)** δ -112.56, (See Figures S7-S13). **HRMS *m/z***: Calculated for C<sub>18</sub>H<sub>10</sub>N<sub>2</sub>O<sub>4</sub>F [M - H]<sup>-</sup>: *m/z* 337.0625, found: *m/z* 337.0628 (See Figures S26).

**(3)** Into a two-necked flask, 1,3-dibromo-3,4,5-trifluorobenzene (1 eq., 1.0 g, 3.45 mmol), bis(pinacolato)diboron (2.2 eq., 1.9 g, 7.59 mmol), potassium acetate (1.35 g, 13.80 mmol) and Pd(dppf)Cl<sub>2</sub> (0.18 g, 0.24 mmol, 7%) were added successively and dissolved in 20 mL dioxane under argon protection with stirring. The reaction was refluxed overnight under Ar, cooled down to room temperature, and filter to remove large particles. Part of the salt was extracted with saturated brine and ethyl acetate, and the organic phase was washed with water (3×50 mL) to neutrality and dried over anhydrous magnesium sulfate. After filtration, a reddish-brown liquid was obtained, the solvent was evaporated in vacuo and the residue was purified by combiflash column chromatography on silica gel using a hexane/ethyl acetate, gradient (ethyl acetate 0-10%) to get the product as a white powder (0.72 g, 55 %). **<sup>1</sup>H NMR (400 MHz, CDCl<sub>3</sub>)** δ 7.82 (td, *J* = 6.5, 2.4 Hz, 1H), 1.35 (s, 24H). **<sup>13</sup>C NMR (101 MHz, CDCl<sub>3</sub>)** δ 159.03, 156.50, 138.48, 137.65, 84.38, 83.64, 24.94. **<sup>19</sup>F NMR (376 MHz, CDCl<sub>3</sub>)** δ -120.37, -163.15, (See Figures S14-S19). **HRMS *m/z***: Calculated for C<sub>18</sub>H<sub>25</sub>B<sub>2</sub>F<sub>3</sub>O<sub>4</sub>Na [M + Na]<sup>+</sup>: *m/z* 407.1789, found: *m/z* 407.1788 (See Figures S27).

**(4)** To a mixture of **3** (1 eq., 1.82 mmol, 0.70 g), 6-bromo-2-methylpyridine (2.2 eq., 4.01 mmol, 0.86 g) and [Pd(PPh<sub>3</sub>)<sub>4</sub>] (0.18 mmol, 210 mg, 10%) under Ar atmosphere were added 2M K<sub>2</sub>CO<sub>3</sub> aqueous solution (5 ml), ethanol (5 ml) and toluene (20 mL). The reaction mixture was heated under reflux at 85 °C until white precipitate appeared (12 hours). After the reaction mixture was cooled down to room temperature, the precipitate was isolated and washed with ethanol. The precipitate was mixed with 50 mL of MeOH and sonicated for 15 min to form a white suspension. Then the aqueous solution of KOH (87.6% purity, 1.41 g, 22.0 mmol) in 20 mL was added to the suspension and the mixture was stirred at 80 °C for

## CHAPTER 7.

20 min. The reaction mixture was let cool to room temperature and neutralized with 1M HCl, upon which a light-pink precipitate has formed. The precipitate was then centrifuged off, washed with water (3×30 mL) and ethanol (30 mL), and evacuated overnight, resulting in the title compound as a white solid (0.44 g, 65 %).

**<sup>1</sup>H NMR (400 MHz, CD<sub>3</sub>OD)** δ 8.47 (td, *J* = 8.3, 2.4 Hz, 1H), 8.07 (dd, *J* = 7.7, 1.1 Hz, 2H), 7.97 (t, *J* = 7.7 Hz, 2H), 7.91 – 7.83 (m, 2H). **<sup>13</sup>C NMR (126 MHz, CD<sub>3</sub>OD)** δ 172.56, 157.32, 151.71, 151.64, 149.71, 142.69, 140.72, 138.61, 133.72, 130.04, 129.94, 127.81, 126.68, 126.45, 124.54, **<sup>19</sup>F NMR (376 MHz, CD<sub>3</sub>OD)** δ -139.77, -162.53, (See Figures S20-S24). **HRMS m/z:** Calculated for C<sub>18</sub>H<sub>8</sub>N<sub>2</sub>O<sub>4</sub>F<sub>3</sub> [M - H]<sup>-</sup>: m/z 373.0436, found: m/z 373.0432 (See Figures S28).

**(5), [Ru<sup>III</sup>(Fpda)(py)<sub>2</sub>]:** Ligand **2** (0.100 g, 0.29 mmol), [Ru(DMSO)<sub>4</sub>Cl<sub>2</sub>] (0.143g, 0.29 mmol, 1 equiv.) were mixed with 10 mL of anhydrous MeOH and 10eq. of Et<sub>3</sub>N, purged with Ar for 20 min, resulting in a homogeneous yellow solution. The solution was then heated to 70 °C, upon which the color changed to dark brown. After 16 hours, the volume of the reaction mixture was reduced, and 10 mL of dry pyridine was added. The formed brown solution was purged with Ar for 20 min and heated to 130 °C under Ar for 24 h, upon which the initial brown suspension dissolved into a homogeneous dark-brown solution. After the reaction mixture was cooled down, the solvent was evaporated and the compound purified by combiflash column chromatography on silica gel using DCM /methanol (1% Et<sub>3</sub>N) gradient (methanol 0 - 30%) to get the product as a yellow powder (0.04 g, 23 %).

**HRMS m/z:** Calculated for C<sub>28</sub>H<sub>19</sub>FN<sub>4</sub>O<sub>4</sub>Ru [M+H]<sup>+</sup>: m/z 595.0356, found: m/z 595.0378, (See Figures S29).

**6, [Ru<sup>III</sup>(F<sub>3</sub>pda)(py)<sub>2</sub>]:** Ligand **4** (0.100 g, 0.27 mmol), [Ru(DMSO)<sub>4</sub>Cl<sub>2</sub>] (0.129 g, 0.297 mmol, 1 equiv.) were mixed with 10 mL of anhydrous MeOH and 10eq. of Et<sub>3</sub>N, purged with Ar for 20 min, resulting in a homogeneous yellow solution. The solution was then heated to 70 °C, upon which the color changed to dark brown. After 12 hours, the volume of the reaction mixture reduced and 10 mL of dry pyridine was added. The brown reaction mixture was purged with Ar for 20 min and heated to 130 °C under Ar for 18 h, upon which the initial brown suspension formed a homogeneous dark-brown solution. After the reaction mixture cooled down, the solvent was evaporated and the compound was purified by combiflash

## CHAPTER 7.

column chromatography on silica gel using DCM /methanol (1% Et<sub>3</sub>N) gradient (methanol 0 - 30%) to get the product as a yellow powder (0.02 g, 11 %).

**HRMS m/z:** Calculated C<sub>28</sub>H<sub>16</sub>F<sub>3</sub>N<sub>4</sub>NaO<sub>4</sub>Ru [M+Na]<sup>+</sup>: m/z 654.0059, found: m/z 654.0069,  
(See Figures S30).

## CHAPTER 7.

## 7.5 References

- (1) Matheu, R.; Ertem, M. Z.; Benet-Buchholz, J.; Coronado, E.; Batista, V. S.; Sala, X.; Llobet, A. Intramolecular Proton Transfer Boosts Water Oxidation Catalyzed by a Ru Complex. *J. Am. Chem. Soc.* **2015**, *137* (33), 10786–10795.
- (2) Matheu, R.; Ertem, M. Z.; Gimbert-Suriñach, C.; Sala, X.; Llobet, A. Seven Coordinated Molecular Ruthenium-Water Oxidation Catalysts: A Coordination Chemistry Journey. *Chem. Rev.* **2019**, *119* (6), 3453–3471.
- (3) Francàs, L.; Matheu, R.; Pastor, E.; Reynal, A.; Berardi, S.; Sala, X.; Llobet, A.; Durrant, J. R. Kinetic Analysis of an Efficient Molecular Light-Driven Water Oxidation System. *ACS Catal.* **2017**, *7* (8), 5142–5150.
- (4) Matheu, R.; Moreno-Hernandez, I. A.; Sala, X.; Gray, H. B.; Brunschwig, B. S.; Llobet, A.; Lewis, N. S. Photoelectrochemical Behavior of a Molecular Ru-Based Water-Oxidation Catalyst Bound to TiO<sub>2</sub>-Protected Si Photoanodes. *J. Am. Chem. Soc.* **2017**, *139* (33), 11345–11348.
- (5) Vereshchuk, N.; Matheu, R.; Benet-Buchholz, J.; Pipelier, M.; Lebreton, J.; Dubreuil, D.; Tessier, A.; Gimbert-Suriñach, C.; Z. Ertem, M.; Llobet, A. Second Coordination Sphere Effects in an Evolved Ru Complex Based on Highly Adaptable Ligand Results in Rapid Water Oxidation Catalysis. *J. Am. Chem. Soc.* **2020**, *142* (11), 5068–5077.
- (6) Miller, T. M.; Neenan, T. X.; Zayas, R.; Bair, H. E. Synthesis and Characterization of a Series of Monodisperse, 1,3,5-Phenylene-Based Hydrocarbon Dendrimers Including C<sub>276</sub>H<sub>186</sub> and Their Fluorinated Analogs. *J. Am. Chem. Soc.* **1992**, *114* (3), 1018–1025.
- (7) Ishiyama, T.; Murata, M.; Miyaura, N. Palladium(0)-Catalyzed Cross-Coupling Reaction of Alkoxydiboron with Haloarenes: A Direct Procedure for Arylboronic Esters. *J. Org. Chem.* **1995**, *60* (23), 7508–7510.
- (8) Miyaura, N.; Suzuki, A. Palladium-Catalyzed Cross-Coupling Reactions of Organoboron Compounds. *Chem. Rev.* **1995**, *95* (7), 2457–2483.
- (9) Shatskiy, A.; Bardin, A. A.; Oschmann, M.; Matheu, R.; Benet-Buchholz, J.; Eriksson, L.; Kärkäs, M. D.; Johnston, E. V.; Gimbert-Suriñach, C.; Llobet, A.; Åkermark, B. Electrochemically Driven Water Oxidation by a Highly Active Ruthenium-Based Catalyst. *ChemSusChem* **2019**, *12* (10), 2251–2262.
- (10) Maji, S.; López, I.; Bozoglian, F.; Benet-Buchholz, J.; Llobet, A. Mononuclear Ruthenium-Water Oxidation Catalysts: Discerning between Electronic and Hydrogen-Bonding Effects. *Inorg. Chem.* **2013**, *52* (7), 3591–3593.
- (11) Schlotthauer, T.; Parada, G. A.; Görls, H.; Ott, S.; Jäger, M.; Schubert, U. S. Asymmetric Cyclometalated Ru(II) Polypyridyl-Type Complexes with  $\pi$ -Extended Carbanionic Donor Sets. *Inorg. Chem.* **2017**, *56* (14), 7720–7730.
- (12) Evans, I. P.; Spencer, A.; Wilkinson, G. Dichlorotetrakis(Dimethyl Sulphoxide)Ruthenium(II) and Its Use as a Source Material for Some New Ruthenium(II) Complexes. *J. Chem. Soc. Dalton Trans.* **1973**, No. 2, 204–209.
- (13) Elgrishi, N.; Rountree, K. J.; McCarthy, B. D.; Rountree, E. S.; Eisenhart, T. T.; Dempsey, J. L. A Practical Beginner's Guide to Cyclic Voltammetry. *J. Chem. Educ.* **2018**, *95* (2), 197–206.

## 7.6 Supporting Information

### 7.6.1 Materials and methods

All materials were provided by Sigma-Aldrich unless indicated otherwise.  $[\text{RuCl}_2(\text{DMSO})_4]$  was synthesized and purified according to the literature.<sup>12</sup> High-purity deionized water was obtained by passing distilled water through a nanopure Milli-Q water purification system.

#### 7.6.1.1 Preparation of 0.1 M ionic strength phosphate solutions.

a) pH = 2.0 buffered solution: Powders of  $\text{H}_3\text{PO}_4$  (10.5 g, 0.1073 M) and  $\text{NaH}_2\text{PO}_4$  (11.83 g, 0.0986 M) were dissolved in 1L of the deionized water.

b) pH = 7.0 buffered solution: Powders of  $\text{NaH}_2\text{PO}_4$  (2.31 g, 0.0193 M) and  $\text{Na}_2\text{HPO}_4$  (3.77g, 0.0266 M) were dissolved in 1L of the deionized water.

c) pH = 11.6 buffered solution: Powders of  $\text{Na}_2\text{HPO}_4$  (10.293g, 0.0073 M) and  $\text{Na}_3\text{PO}_4$  (2.06g, 0.0126 M) were dissolved in 1L of the deionized water.

Solutions at pH's between 2.0 and 12.0 were prepared by mixing the above-prepared solutions. The pH of all solutions was measured by a pH meter. All solutions used herein contained an ionic strength equal to 0.1 M.

#### 7.6.1.2 Electrochemical methods

##### General considerations

All electrochemical experiments were performed on an IJ-Cambria HI-730 bipotentiostat and IJ-Cambria CHI-660 potentiostat, using a three-electrode cell.  $E_{1/2}$  values reported in this work were estimated from Cyclic Voltammetric (CV) experiments as the average of the oxidative and reductive peak potentials  $(E_{p,a}+E_{p,c})/2$  or from DPV. Glassy carbon disk (GC) ( $\phi = 0.3$  cm,  $S = 0.07$  cm<sup>2</sup>) was used as working electrodes (WE), Mercury/Mercurous sulfate ( $\text{K}_2\text{SO}_4$  sat) (MSE) as reference electrode (RE) (unless explicitly mentioned) and Pt disk as counter electrode (CE). Working electrode pretreatment before each measurement consisted of polishing with 0.05  $\mu\text{m}$  alumina paste, rinsing after with water and acetone, and blow-dried finally. CVs and DPVs were  $iR$  compensated by the potentiostat in all the measurements unless indicated. CV was recorded at a 100  $\text{mV}\cdot\text{s}^{-1}$  scan rate unless explicitly expressed. The DPV parameters were  $\Delta E = 4$  mV, Amplitude = 0.05mV, Pulse width = 5 s, Sampling width = 0.0167 s, Pulse period = 5 s unless explicated. All redox potentials in the present work are reported versus NHE by adding 0.65 V to the measured potential.<sup>13</sup>



## CHAPTER 7.

### Cells

A 15 mL vial was used as an electrochemical cell for CV measurements. A Teflon-made with holes for the three electrodes was used as a lid to ensure a reproducible distance between the electrodes. A two compartments cell (25 mL per compartment or 7 mL per compartment) with a separation grid was used for Bulk Electrolysis Experiments.

### Bulk electrolysis

A glassy carbon rod ( $S = 13.35 \text{ cm}^2$  or  $9.35 \text{ cm}^2$ ) was used as a WE, Pt grid as a CE, and a Hg/Hg<sub>2</sub>SO<sub>4</sub> (K<sub>2</sub>SO<sub>4</sub> saturated) as a RE. iR compensation by the potentiostat was not applied in this technique.

#### 7.6.1.3 *General instrumentation*

Electrospray ionization (ESI) mass spectrometry (MS) experiments were performed on a Waters Micromass LCT Premier equipment. UV-Vis spectroscopy was performed on a Cary 50 Bio (Varian) UV-Vis spectrophotometer with 1 cm quartz cells unless indicated. A 400 MHz Bruker Avance II spectrometer and a Bruker Avance 500 MHz were used to carry out NMR spectroscopy. The pH of the solutions was determined by a pH meter (CRISON, Basic 20<sup>+</sup>) calibrated before measurements through standard solutions at pH= 4.01, 7.00, and 9.21. Oxygen evolution was analyzed with a gas phase Clark type oxygen electrode (Unisense Ox-N needle microsensor) and calibrated by the addition of small quantities of air (21%).

7.6.1.4 Simulation of the Pourbaix diagrams

The Pourbaix diagram of complex **5** was simulated and fitted to the experimental redox potential values for a more accurate estimation of the pKa values of the complex at Ru<sup>II</sup> (pKa<sup>II</sup>), Ru<sup>III</sup> (pKa<sup>III</sup>), and Ru<sup>IV</sup> (pKa<sup>IV</sup>) states using Eq. S1 and S2.

$$E(\text{III/II}) = [E(\text{III/II})_{\text{pH}=0}] + \left( 0.05916 * \log \left( \frac{[\text{H}^+] + K_{\text{a1}}^{\text{II}}}{[\text{H}^+] + K_{\text{a1}}^{\text{III}}} \right) \right) \quad \text{S1}$$

$$E(\text{IV/III}) = [E(\text{IV/III})_{\text{pH}=0}] + \left( 0.05916 * \log \left( \frac{[\text{H}^+] + K_{\text{a1}}^{\text{III}}}{[\text{H}^+] + K_{\text{a1}}^{\text{IV}}} \right) \right) \quad \text{S2}$$

This allows for obtaining the following pKa values:

$E^\circ(\text{Ru}^{\text{III}}/\text{Ru}^{\text{II}}) = 0.1 \text{ V}$	pKa <sup>1</sup>	pKa <sup>2</sup>
	-1	4.6
$E^\circ(\text{Ru}^{\text{IV}}/\text{Ru}^{\text{III}}) = 0.46 \text{ V}$	pKa <sup>1</sup>	pKa <sup>2</sup>
	-3	0

## CHAPTER 7.

### 7.6.2 Characterization of ligands

#### 7.6.2.1 Spectroscopic characterization of the 1

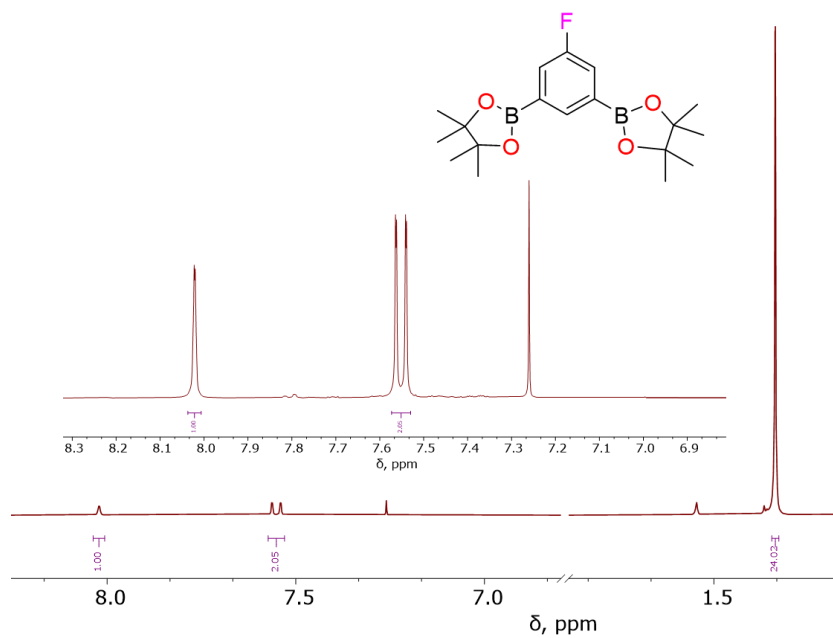


**Figure S1.**  $^1\text{H}$  NMR spectra of **1** in  $\text{CDCl}_3$  at RT. (inset) Zoom of the aromatic region.

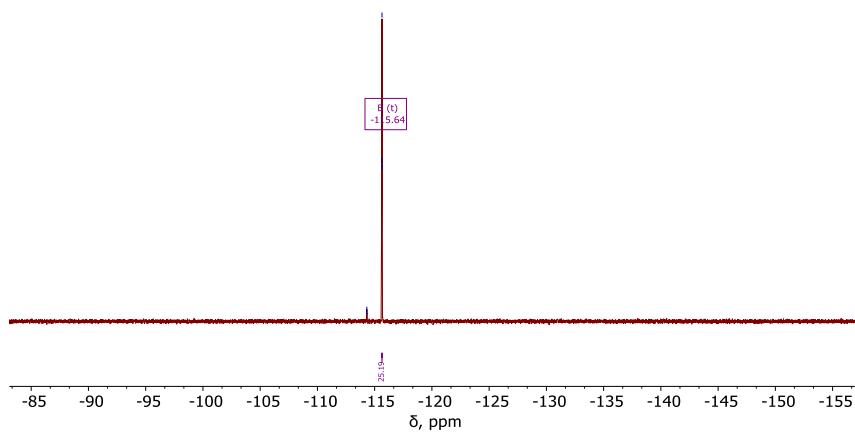


**Figure S2.**  $^{19}\text{F}$  NMR of **1** in  $\text{CDCl}_3$  at RT.

VII

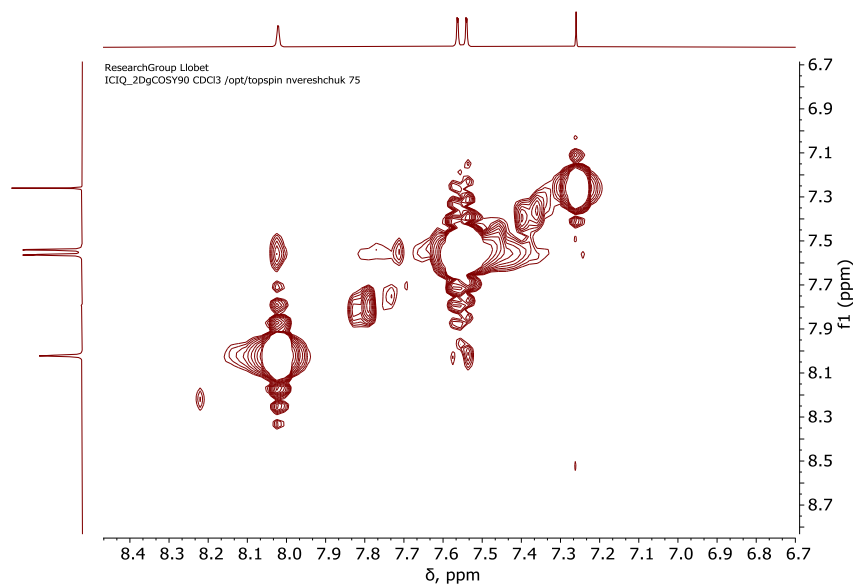


Figure S3.  $^1\text{H}$ - $^1\text{H}$  COSY NMR of **1** in  $\text{CDCl}_3$  at RT.

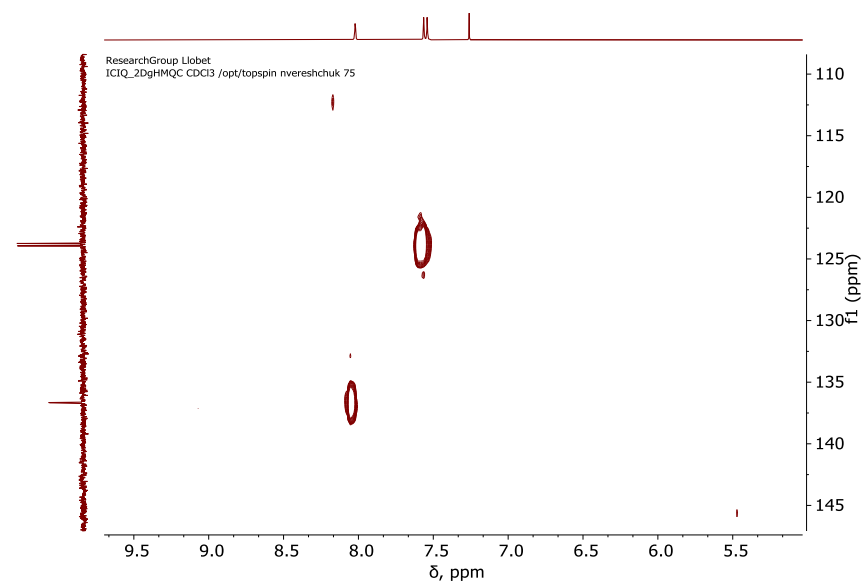


Figure S4:  $^1\text{H}$ - $^{13}\text{C}$  HMQC NMR of **1** in  $\text{CDCl}_3$  at RT.

## CHAPTER 7.

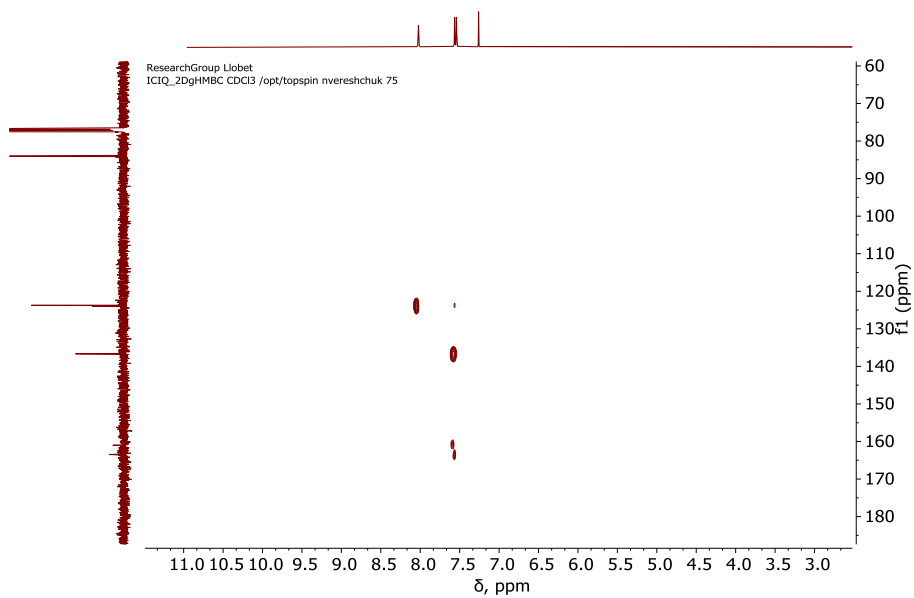


Figure S5: <sup>1</sup>H-<sup>13</sup>C HMBC NMR of **1** in CDCl<sub>3</sub> at RT.

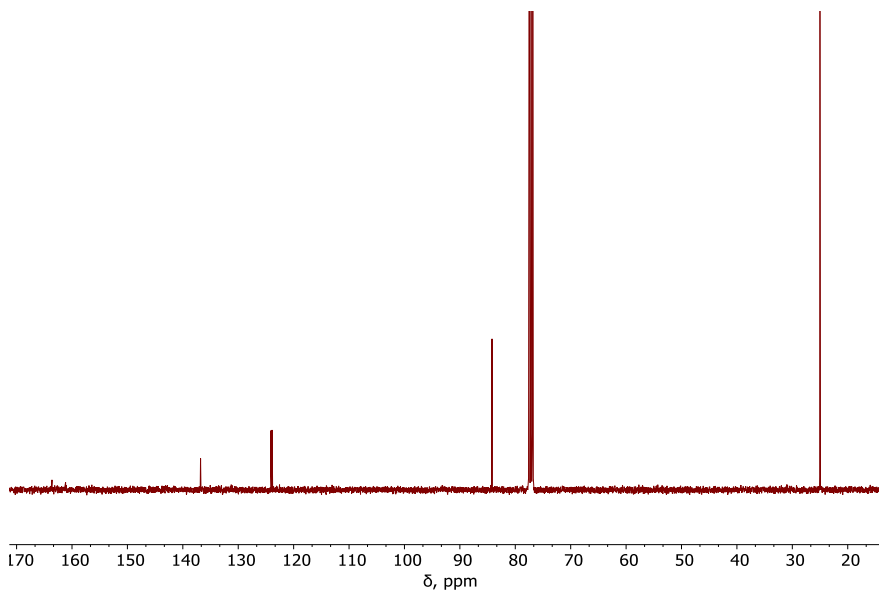


Figure S6: <sup>13</sup>C NMR of **1** in CDCl<sub>3</sub> at RT.

VII

1.1.1.1 Spectroscopic characterization of the 2

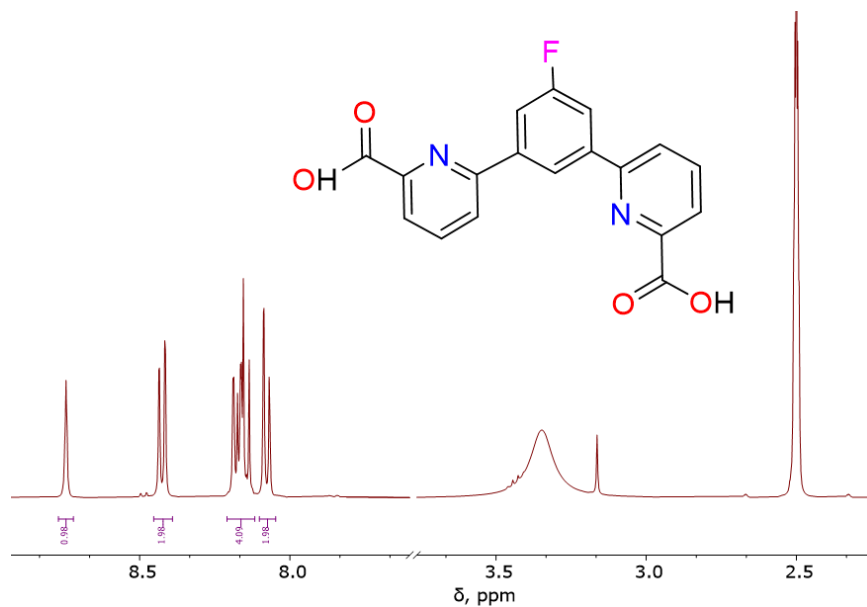


Figure S7.  $^1\text{H}$  NMR spectra of **2** in  $\text{DMSO-d}_6$  at RT.

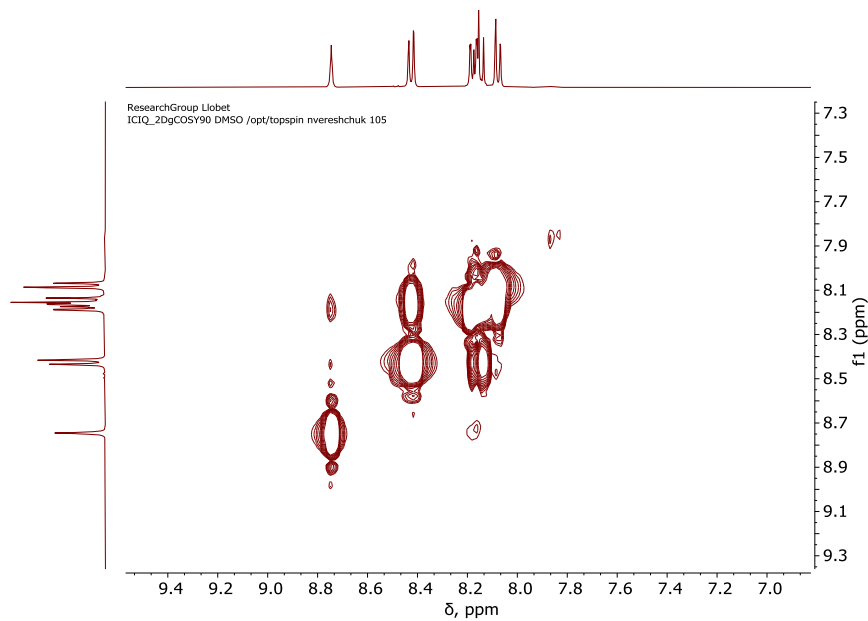
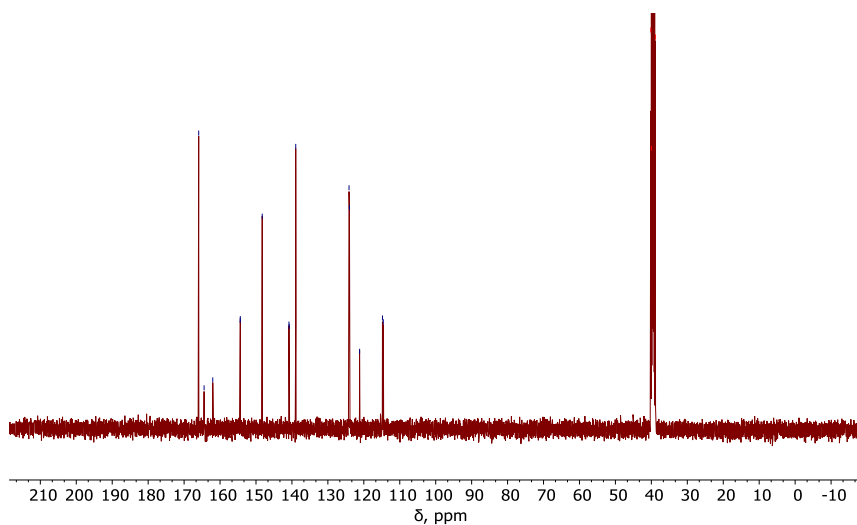
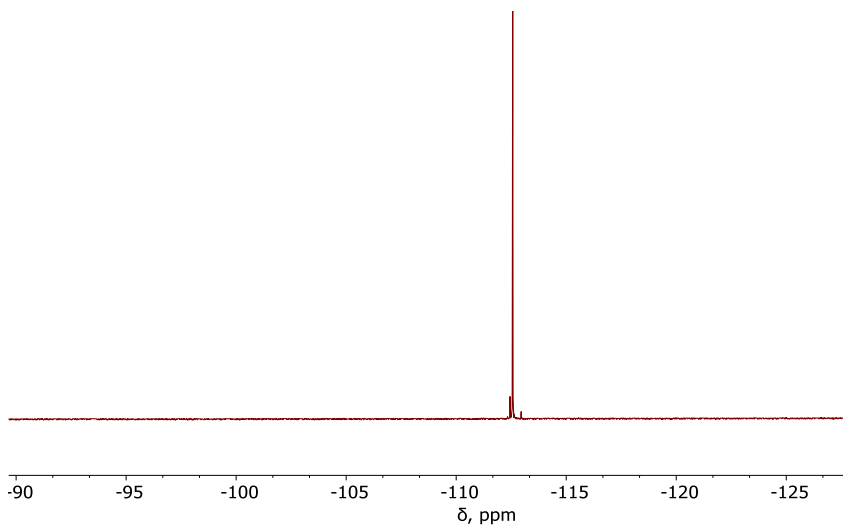


Figure S8.  $^1\text{H}$ - $^1\text{H}$  COSY NMR of **2** in  $\text{DMSO-d}_6$  at RT.

## CHAPTER 7.



**Figure S9:**  $^{13}\text{C}$  NMR of **2** in  $\text{DMSO-d}_6$  at RT.



**Figure S10:**  $^{19}\text{F}$  NMR of **2** in  $\text{DMSO-d}_6$  at RT.

VII

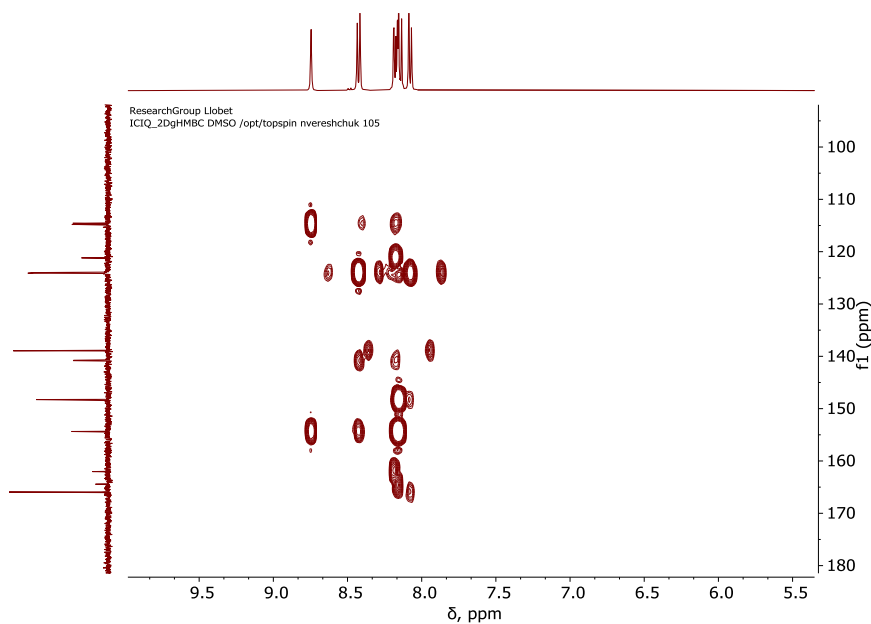


Figure S11:  $^1\text{H}$ - $^{13}\text{C}$  HMBC NMR of **2** in DMSO- $d_6$  at RT.

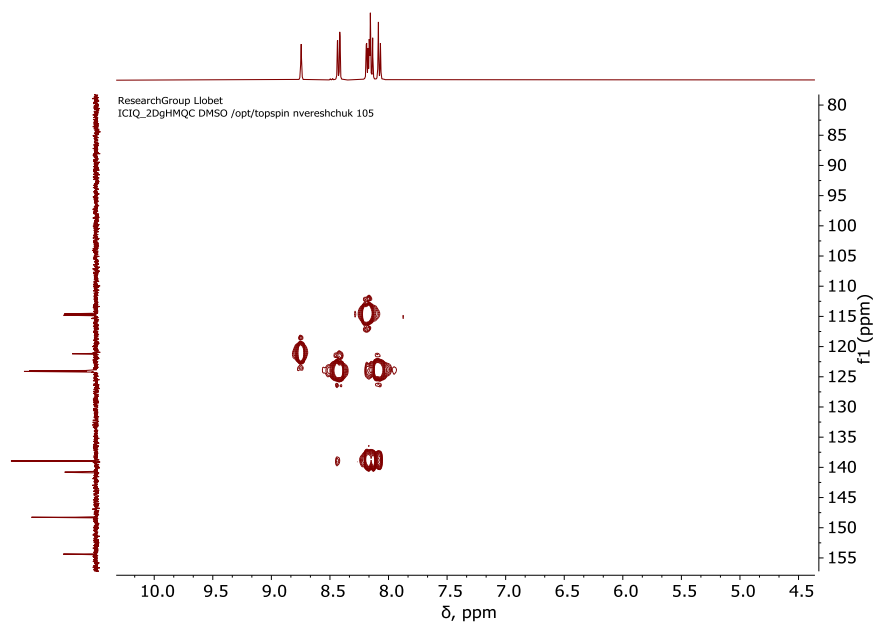
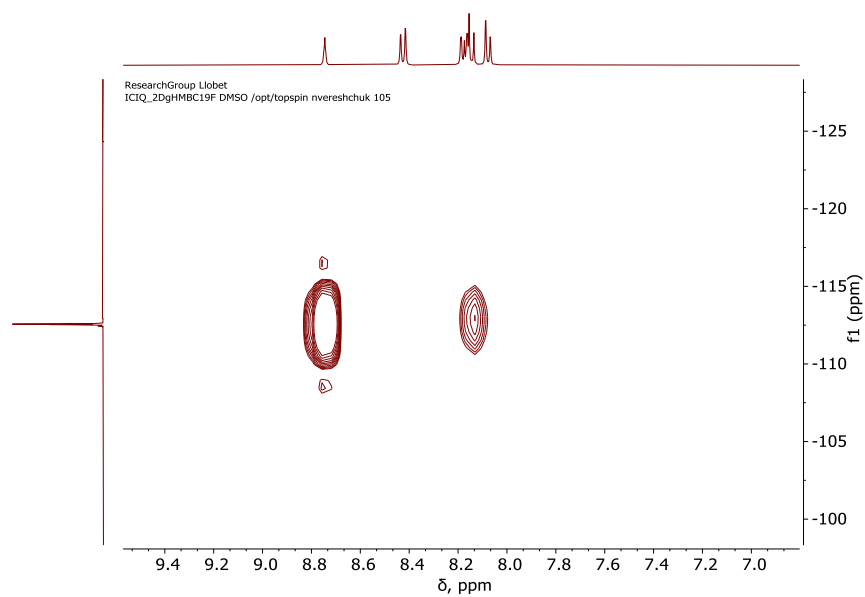


Figure S12:  $^1\text{H}$ - $^{13}\text{C}$  HMQC NMR of **2** in DMSO- $d_6$  at RT.



## CHAPTER 7.



**Figure S13:**  $^1\text{H}$ - $^{19}\text{F}$  HMBC NMR of **2** in  $\text{DMSO-d}_6$  at RT.

1.1.1.2 Spectroscopic characterization of the 3

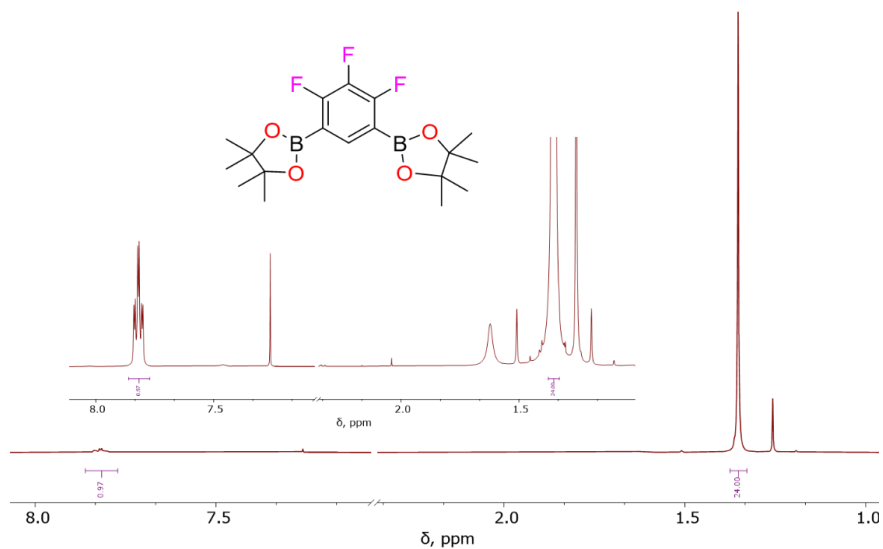


Figure S14.  $^1\text{H}$  NMR spectra of **3** in  $\text{CDCl}_3$  at RT. (inset) Zoom of the aromatic region

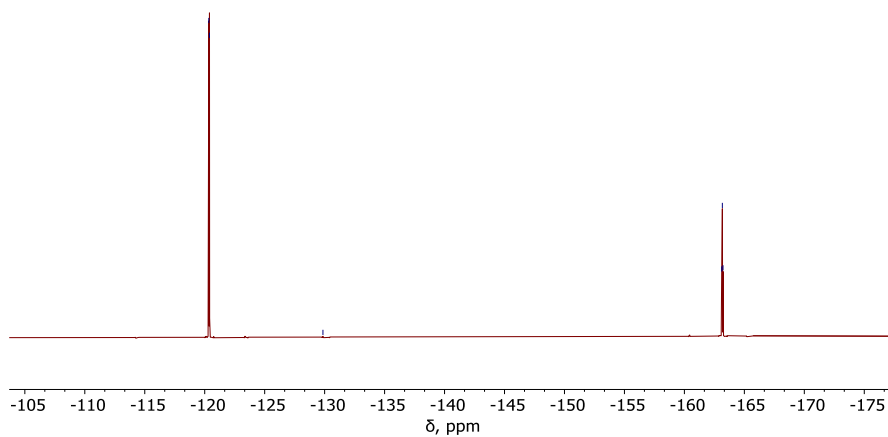


Figure S15.  $^{19}\text{F}$  NMR of **3** in  $\text{CDCl}_3$  at RT.

## CHAPTER 7.

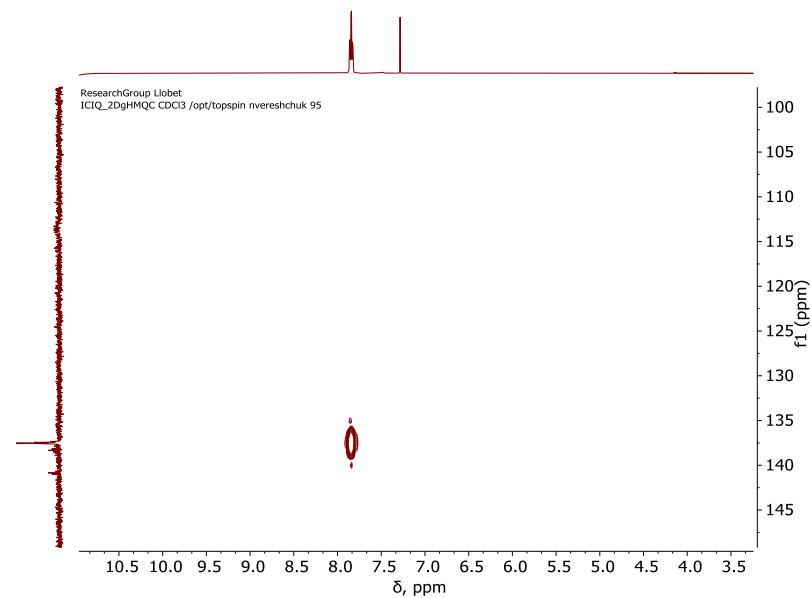


Figure S16: <sup>1</sup>H-<sup>13</sup>C HMQC NMR of **3** in CDCl<sub>3</sub> at RT.

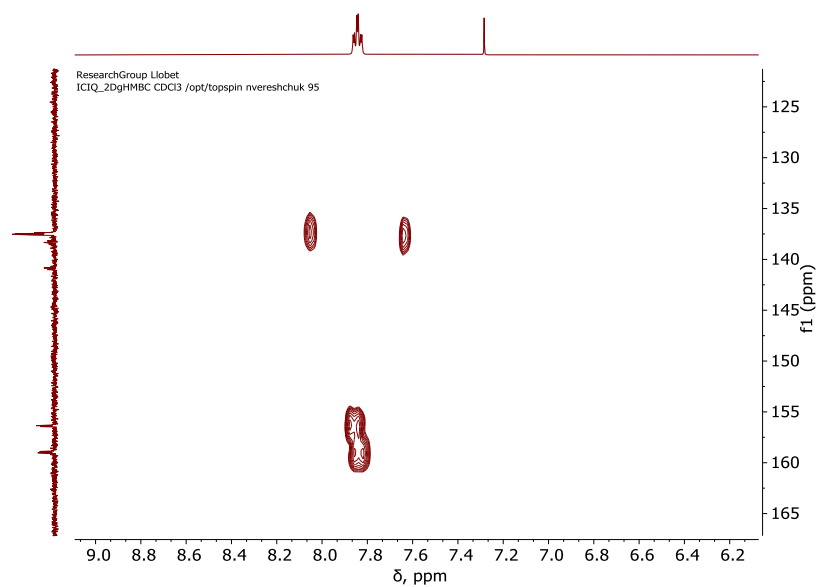


Figure S17: <sup>1</sup>H-<sup>13</sup>C HMBC NMR of **3** in CDCl<sub>3</sub> at RT

VII

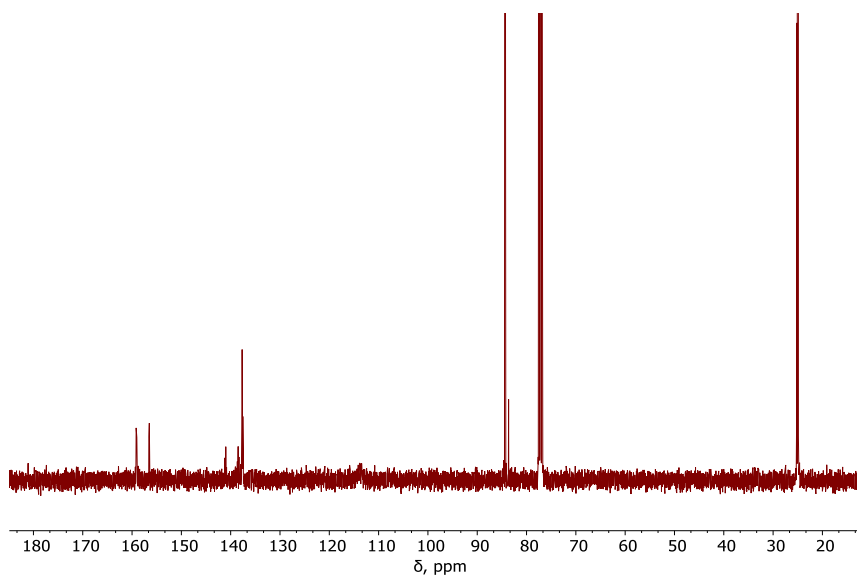


Figure S18:  $^{13}\text{C}$  NMR of **3** in  $\text{CDCl}_3$  at RT.

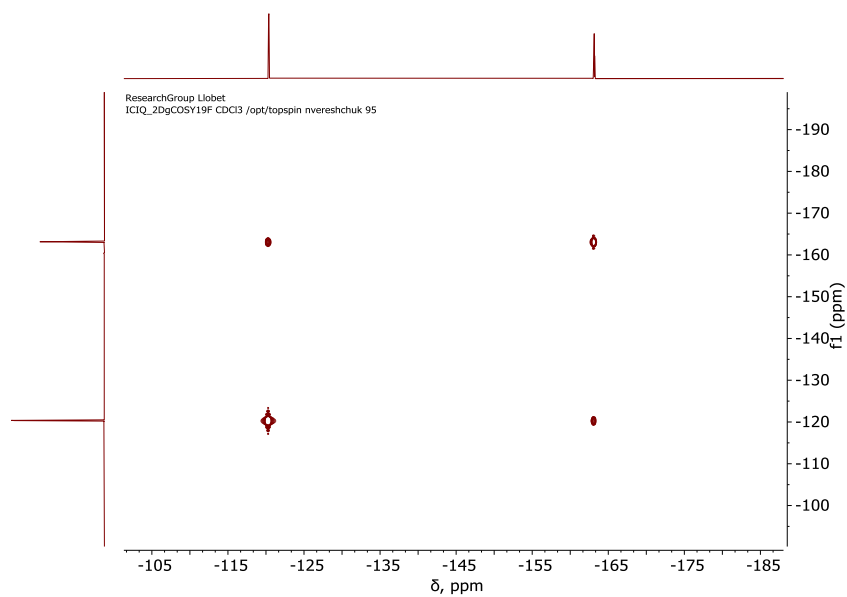


Figure S19:  $^{19}\text{F}$ - $^{19}\text{F}$  COSY NMR of **3** in  $\text{CDCl}_3$  at RT.

## CHAPTER 7.

### 1.1.1.3 Spectroscopic characterization of the 4

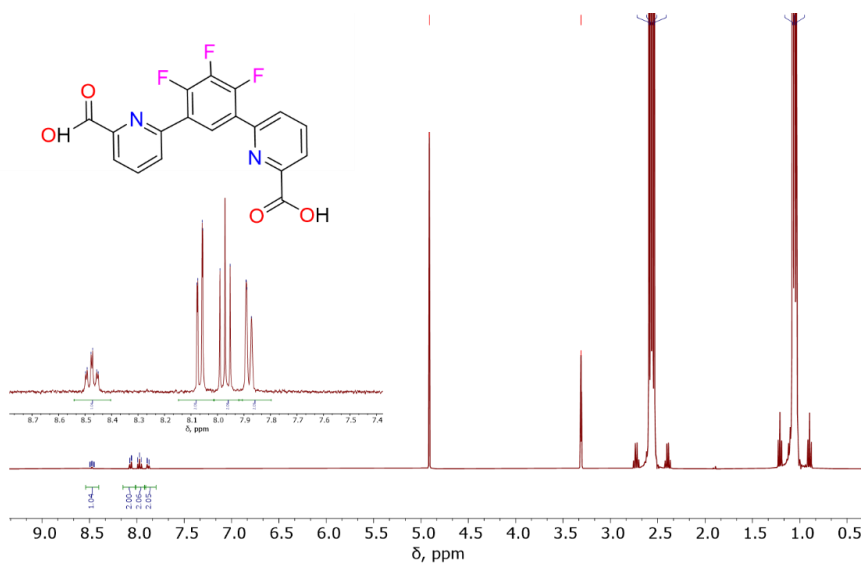


Figure S20.  $^1\text{H}$  NMR of **4** in  $\text{CD}_3\text{OD}$  at RT

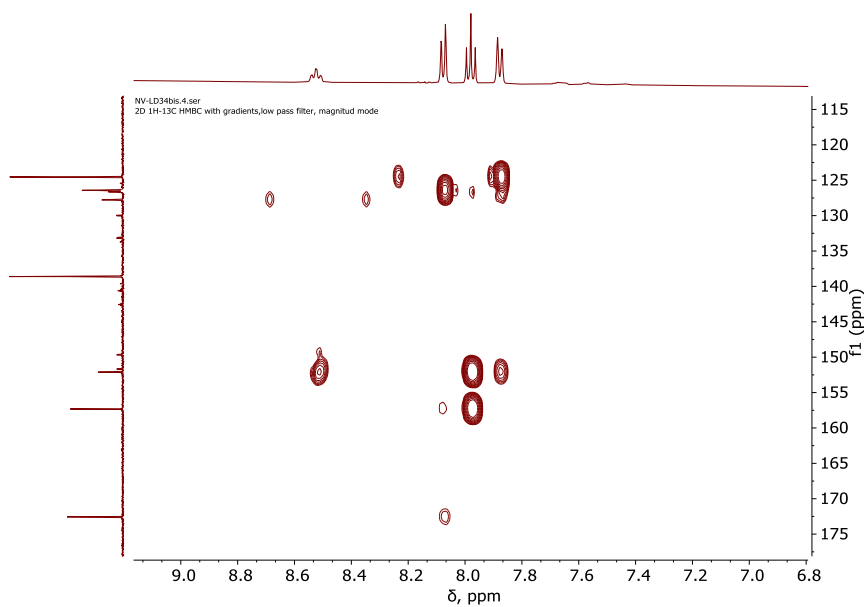
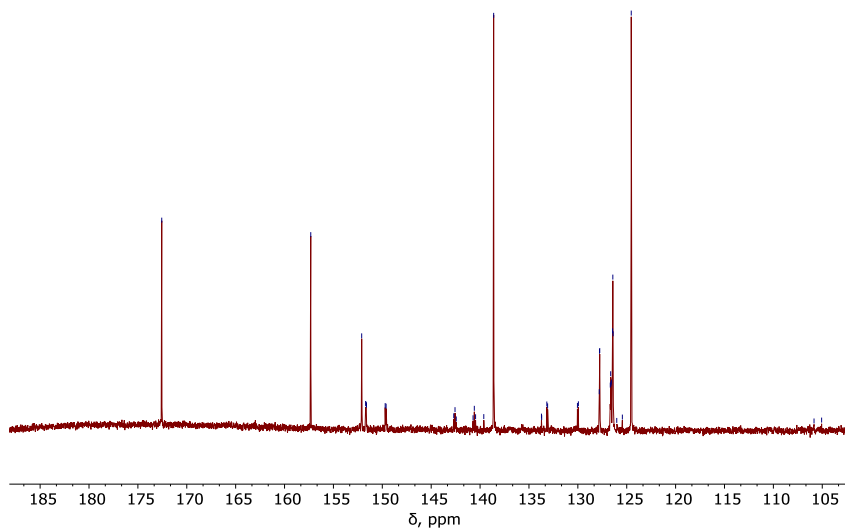
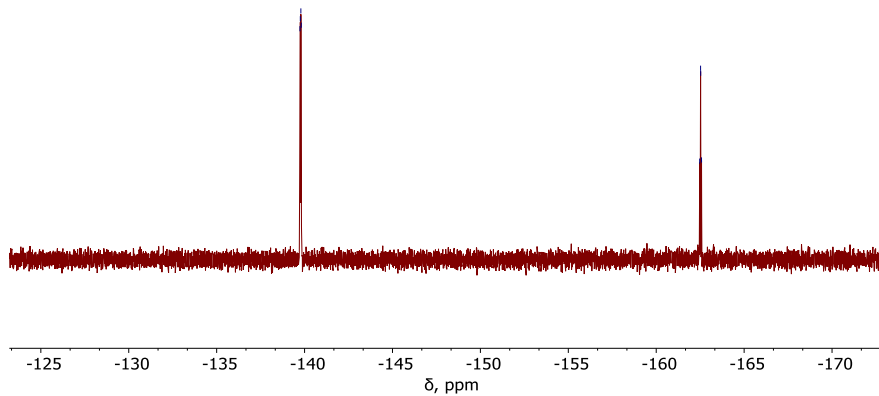


Figure S21:  $^1\text{H}$ - $^{13}\text{C}$  HMBC NMR of **4** in  $\text{CD}_3\text{OD}$  at RT.

VII



**Figure S22:**  $^{13}\text{C}$  NMR of **4** in  $\text{CD}_3\text{OD}$  at RT



**Figure S23:**  $^{19}\text{F}$  NMR of **4** in  $\text{CD}_3\text{OD}$  at RT

## CHAPTER 7.

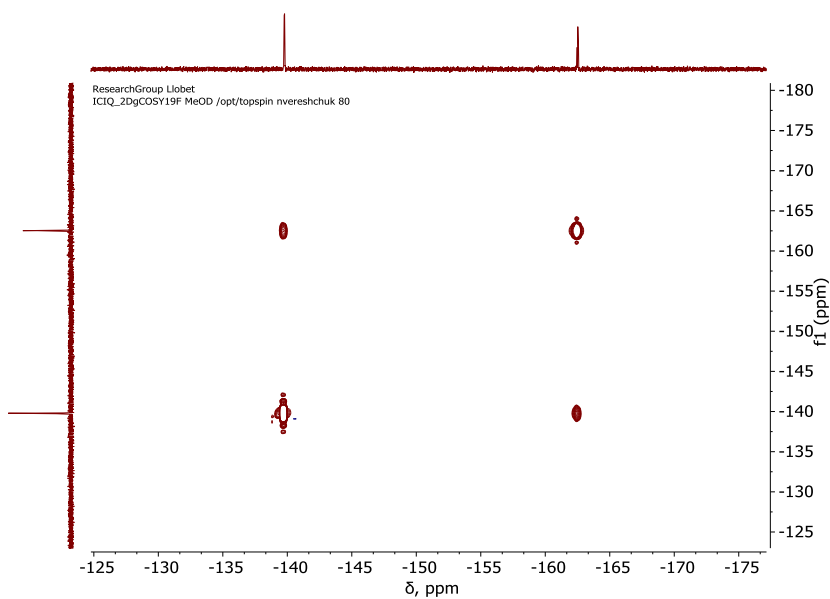


**Figure S24:**  $^{19}\text{F}$ - $^{19}\text{F}$  COSY NMR of **4** in  $\text{CD}_3\text{OD}$  at RT

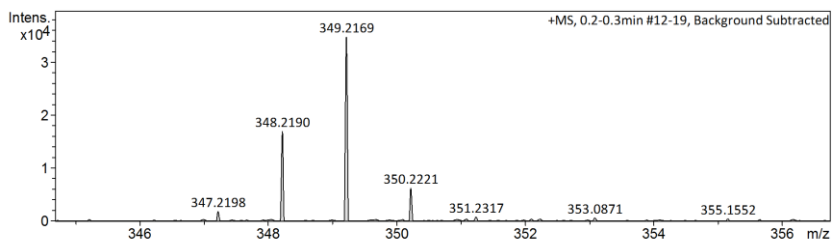


Figure S25. HR-MS for 1.

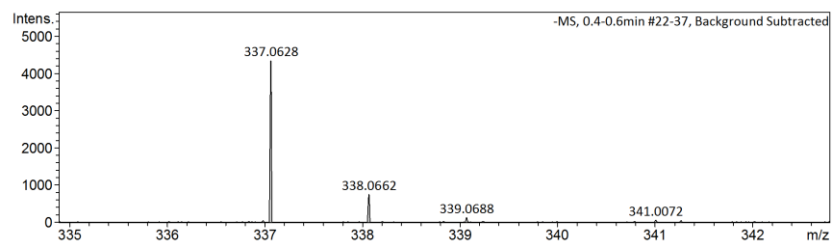


Figure S26. HR-MS for 2.

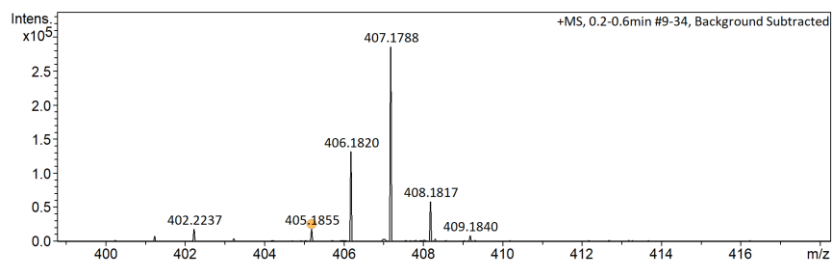


Figure S27. HR-MS for 3.

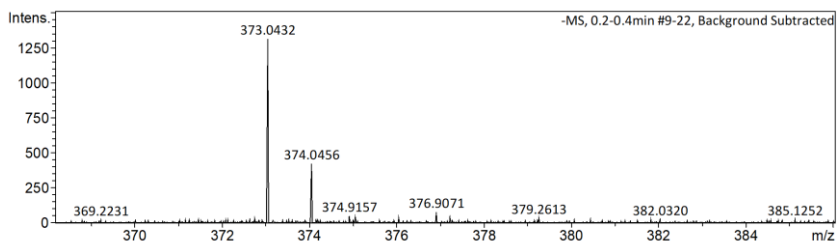


Figure S28. HR-MS for 4.



## CHAPTER 7.

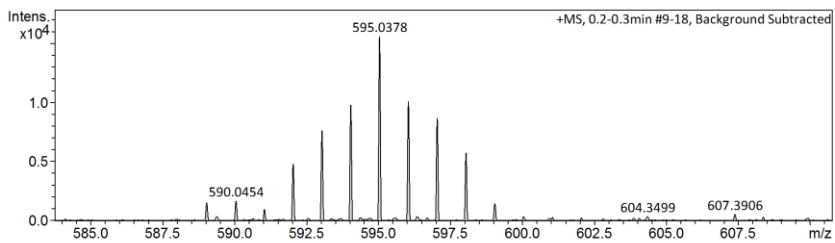


Figure S29. HR-MS for 5.

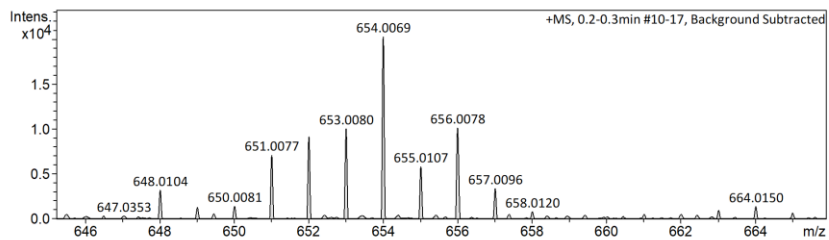
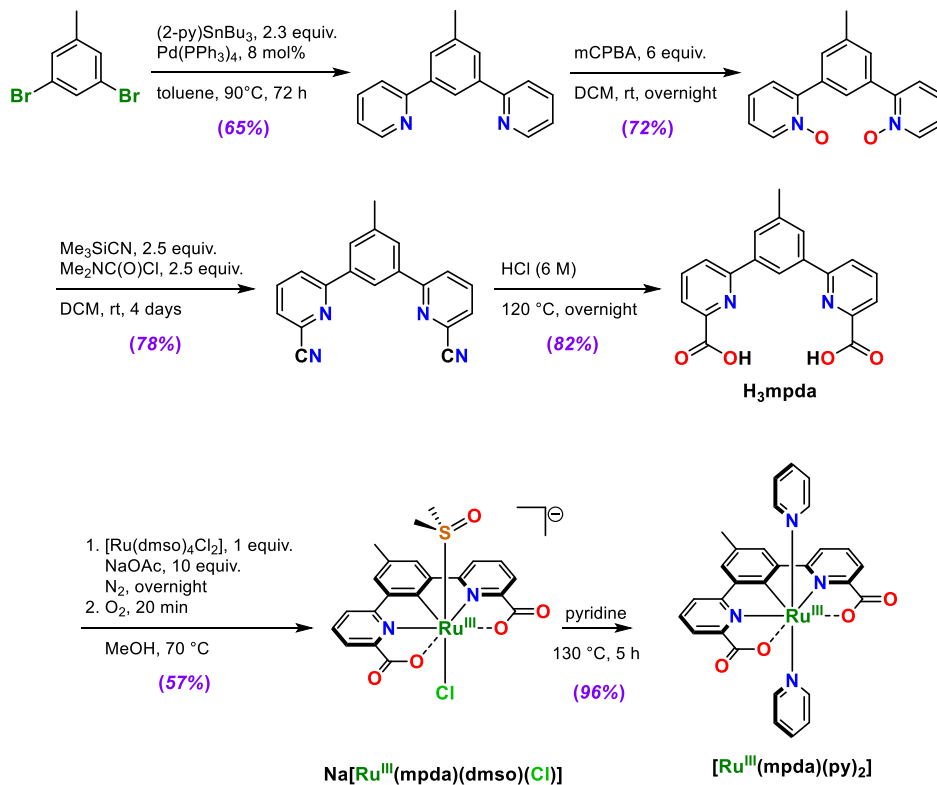


Figure S30. HR-MS for 6

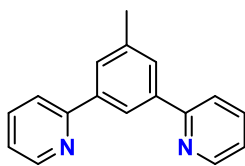
### 7.6.3 Synthetic Procedures and Analytical Data for the synthesis of ligand 7

The experiments described in this section were performed by Dr. Andrey Shatskiy (KTH Royal Institute of Technology), added here for comparison purposes.



Scheme S1. Synthesis of H<sub>3</sub>mpda ligand and complex [Ru(mpda)(py)<sub>2</sub>]

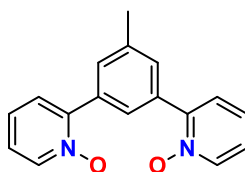
## CHAPTER 7.



**2,2'-(5-methyl-1,3-phenylene)dipyridine (8):** 3,5-dibromotoluene (3.00 g, 12.0 mmol) and tetrakis(triphenylphosphine)palladium (1.11 g, 27.6 mmol, 8 mol%) were placed in a dry Schlenk tube, evacuated and filled

with nitrogen three times. Dry toluene (150 mL) was transferred to the Schlenk tube via cannula and 2-(tributylstannyl)pyridine (85–95%, 10.2 g, 27.6 mmol, 2.3 equiv.) was added and the reaction mixture was carefully evacuated and filled with nitrogen three times. The reaction mixture was stirred in a closed Schlenk tube at 90 °C for 77 h. The reaction mixture was let cool down to room temperature and concentrated under reduced pressure resulting in a brown oil residue. The oil was dissolved in 225 mL of chloroform and washed with water (3 × 50 mL), after which the combined aqueous phases were again extracted with 100 mL of chloroform, followed by washing with water (2 × 25 mL). All the organic phases were combined, dried over MgSO<sub>4</sub>, and concentrated under reduced pressure providing the crude product as a brown oil. The crude product was purified by automated flash chromatography on a silica column (*n*-hexane/Et<sub>2</sub>O, 5% to 100% gradient of Et<sub>2</sub>O). The fractions containing the desired product were combined, concentrated under reduced pressure, and evacuated overnight, resulting in the title compound as a yellow oil (**1.93 g, 65%**).

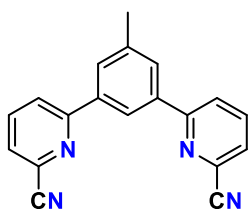
**<sup>1</sup>H NMR (400 MHz, CDCl<sub>3</sub>):** δ 8.71 (ddd, *J* = 4.8, 1.8, 1.0 Hz, 2H), 8.37 (t, *J* = 1.8 Hz, 1H), 7.91 (dd, *J* = 1.7, 0.8 Hz, 2H), 7.83 (dt, *J* = 7.9, 1.1 Hz, 2H), 7.76 (td, *J* = 7.7, 1.8 Hz, 2H), 7.24 (ddd, *J* = 7.4, 4.8, 1.2 Hz, 2H), 2.52 (s, 3H). **<sup>13</sup>C NMR (101 MHz, CDCl<sub>3</sub>):** δ 157.56, 149.76, 140.02, 139.14, 136.85, 128.42, 122.91, 122.31, 120.93, 21.74. **ESI-HRMS:** Calculated for C<sub>17</sub>H<sub>15</sub>N<sub>2</sub> [M + H]<sup>+</sup>: *m/z* 247.1230, found: *m/z* 247.1238.



**2,2'-(5-methyl-1,3-phenylene)dipyridine-*N*-oxide (9):** Compound **8** (2.23 g, 9.1 mmol) was dissolved in 100 mL of dichloromethane and mixed with a solution of *m*-chloroperbenzoic acid (75%, 13.0 g, 54.3 mmol, 6 equiv.). The mixture was stirred at room temperature for 46 h, then diluted with dichloromethane (650 mL), washed with 5 wt.% aqueous Na<sub>2</sub>CO<sub>3</sub> (3 × 150 mL). The combined aqueous phases were extracted with dichloromethane (2 × 100 mL). All organic phases were combined, dried over Na<sub>2</sub>SO<sub>4</sub>, and concentrated under reduced pressure, resulting in the crude product as a

yellow solid. The crude product was purified by automated flash chromatography on a silica column (dichloromethane/MeOH, 0% to 10% gradient of MeOH). Fractions containing the desired product were combined, concentrated under reduced pressure, and evacuated overnight, resulting in the title compound as a white solid (**1.81 g, 72%**).

**<sup>1</sup>H NMR (400 MHz, CDCl<sub>3</sub>):**  $\delta$  8.33 (ddd,  $J = 6.4, 1.3, 0.5$  Hz, 2H), 7.99 (td,  $J = 1.7, 0.6$  Hz, 1H), 7.50 (ddd,  $J = 7.8, 2.2, 0.6$  Hz, 2H), 7.31 (td,  $J = 7.7, 1.3$  Hz, 2H), 7.29–7.19 (m, 4H), 2.48 (d,  $J = 0.7$  Hz, 3H). **<sup>13</sup>C NMR (101 MHz, CDCl<sub>3</sub>):**  $\delta$  149.11, 140.57, 138.23, 132.78, 131.27, 127.83, 127.67, 125.91, 124.83, 21.68. **ESI-HRMS:** Calculated for C<sub>17</sub>H<sub>15</sub>N<sub>2</sub>O<sub>2</sub> [M + H]<sup>+</sup>:  $m/z$  279.1128, found:  $m/z$  279.1124.

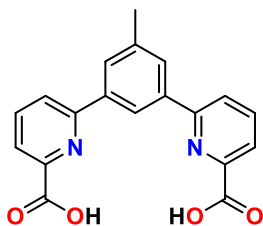


**6,6'-(5-methyl-1,3-phenylene)dipicolinonitrile (10):** *N*-oxide 9

(1.43 g, 5.1 mmol) was placed in the reaction flask, evacuated, and filled with nitrogen three times. Then 3 mL of dry dichloromethane, trimethylsilyl cyanide (1.60 mL, 12.8 mmol, 2.5 equiv.), dimethylcarbonyl chloride (1.18 mL, 12.8 mmol, 2.5 equiv.) were added, and the reaction mixture stirred at room temperature for 120 h. After that, 3.8 mL of 10 wt.% aqueous K<sub>2</sub>CO<sub>3</sub> was added and the mixture was stirred for an additional 10 min. Then the reaction mixture was extracted with dichloromethane (4 × 20 mL) and the combined organic phases were dried over K<sub>2</sub>CO<sub>3</sub> and concentrated under reduced pressure giving the crude product as a light-brown solid. The crude product was purified by automated flash chromatography (pentane-dichloromethane(1:1)/MeOH, 0% to 3% gradient of MeOH). The fraction containing the desired product were combined, concentrated under reduced pressure, and evacuated overnight, resulting in the title compound as an off-white solid (**1.18 g, 78%**).

**<sup>1</sup>H NMR (400 MHz, CDCl<sub>3</sub>):**  $\delta$  8.47 (td,  $J = 1.7, 0.6$  Hz, 1H), 8.07 (dd,  $J = 8.1, 1.0$  Hz, 2H), 7.98 (dd,  $J = 1.7, 0.8$  Hz, 2H), 7.94 (dd,  $J = 8.2, 7.6$  Hz, 2H), 7.67 (dd,  $J = 7.6, 1.0$  Hz, 2H), 2.55 (d,  $J = 0.7$  Hz, 3H). **<sup>13</sup>C NMR (101 MHz, CDCl<sub>3</sub>):**  $\delta$  158.63, 139.84, 138.09, 138.02, 133.99, 129.61, 127.03, 123.92, 123.17, 117.52, 21.77. **ESI-HRMS:** Calculated for C<sub>19</sub>H<sub>12</sub>N<sub>4</sub>Na [M + Na]<sup>+</sup>:  $m/z$  319.0954, found:  $m/z$  319.0950.

## CHAPTER 7.



### 6,6'-(5-methyl-1,3-phenylene)dipicolinic acid ( $H_3mpda$ ):

Nitrile **10** (1.18 g, 4.0 mmol) was suspended in 40 mL of 6 M HCl and refluxed under nitrogen at 123 °C. After 24 h the reflux condenser was substituted with the distillation apparatus and all the solvent was distilled off under reduced pressure. The resulting solid residue was suspended in 1000 mL of MeCN, heated to the boiling point, and let cool to room temperature, after which it was filtered through a glass frit to remove  $NH_4Cl$  formed during the reaction. The filtrate was concentrated under reduced pressure and evacuated overnight, resulting in the title compound as an off-white solid (**1.33 g, 82%**).

$^1H$  NMR (400 MHz,  $CDCl_3$ ):  $\delta$  8.32 (d,  $J = 1.7$  Hz, 1H), 8.24 (q,  $J = 4.3$  Hz, 2H), 8.09 (d,  $J = 4.4$  Hz, 4H), 7.93 (s, 2H), 2.60 (s, 3H).  $^{13}C$  NMR (101 MHz,  $CDCl_3$ ):  $\delta$  164.08, 156.27, 146.19, 140.04, 139.68, 138.29, 129.55, 125.34, 123.13, 122.53, 21.83. ESI-HRMS: Calculated for  $C_{19}H_{14}N_2O_4Na$  [ $M + Na$ ] $^+$ :  $m/z$  357.0846, found:  $m/z$  357.0841.

**Na[Ru<sup>III</sup>(mpda)(DMSO)Cl]Cl<sup>-</sup>**: Ligand  $H_3mpda$  (0.150 g, 0.45 mmol),  $[Ru(DMSO)_4Cl_2]$  (0.217 g, 0.45 mmol, 1 equiv.) and anhydrous NaOAc (0.368 g, 4.49 mmol, 10 equiv.) were mixed with 10 mL of anhydrous MeOH and purged with  $N_2$  for 10 min, resulting in a homogeneous yellow solution. The solution was then heated to 70 °C, upon which the color changed to dark red. After 17 h the reaction mixture was allowed to cool to room temperature, purged with  $O_2$ , and heated to 70 °C under  $O_2$ . After 20 min a light-brown precipitate formed, after 1 h the reaction mixture was allowed to cool down to room temperature and the precipitate was centrifuged off. The filter was then washed with MeOH (2 × 2 mL) and evacuated overnight, resulting in the title compound as dark-yellow solid (**0.100 g, 37%**).

**Elemental analysis**: Calculated for  $Na[Ru^{III}(mpda)(dmsO)Cl] \cdot NaCl \cdot MeOH$ : C, 40.07; H, 3.21; N, 4.25; S, 4.86. Found: C, 39.83; H, 3.50; N, 4.24; S, 4.95. ESI-HRMS: Calculated for  $C_{21}H_{17}ClN_2NaO_5RuS$   $[Ru^{IV}(mpda)(DMSO)Cl + Na^+]$ :  $m/z$  568.9488, found:  $m/z$  568.9466. ATR-FTIR ( $\nu_{max}$ ,  $cm^{-1}$ ): 3403, 3073, 3013, 2918, 1623, 1592, 1562, 1545, 1479, 1443, 1391, 1372, 1280, 1261, 1111, 1099, 1018, 835, 776, 722.

**[Ru<sup>III</sup>(mpda)(DMSO)(H<sub>2</sub>O)] (7(DMSO)(H<sub>2</sub>O))**: Complex **7(DMSO)Cl<sup>-</sup>** (0.0091 g, 0.0155 mmol) was mixed with 0.8 mL of water and heated to 95 °C in a closed vial, resulting in a homogeneous orange solution. After 15 min the reaction mixture was left to cool down to

room temperature, upon which a light-brown precipitate has formed. The reaction mixture was diluted with water (0.2 mL), the precipitate was centrifuged off, washed with water (2 × 0.1 mL), and dried in vacuo, resulting in the desired product as a yellow solid (**0.0069 g, 84%**).

**Elemental analysis:** Calculated for  $[\text{Ru}^{\text{III}}(\text{mpda})(\text{dmsO})(\text{H}_2\text{O})]\cdot 3\text{H}_2\text{O}$ : C, 43.30; H, 4.33; N, 4.81; S, 5.50. Found: C, 42.94; H, 3.82; N, 4.61; S, 5.42. **ATR-FTIR ( $\nu_{\text{max}}$ ,  $\text{cm}^{-1}$ ):** 3387, 3213, 3063, 3012, 2924, 1634, 1589, 1563, 1549, 1480, 1446, 1392, 1366, 1351, 1289, 1263, 1122, 1007, 841, 777, 728.

**$[\text{Ru}^{\text{III}}(\text{mpda})(\text{py})_2]$ :** Complex  $[\text{Ru}^{\text{III}}(\text{mpda})(\text{DMSO})\text{Cl}]^-$  (0.0214 g, 0.0364 mmol) was placed into a dry 5 mL vial, suspended in 2 mL of dry pyridine, and purged with Ar for 10 min. After that, the reaction mixture was heated to 130 °C under Ar, upon which the initial orange suspension formed a homogeneous dark-brown solution. After 5 h the reaction mixture was cooled down to room temperature and placed in the fridge for 30 min. The formed precipitate was centrifuged off, washed with ether (2 × 2 mL), and dried in vacuo, resulting in the desired product as brown solid (**0.0207 g, 96%**).

**ESI-HRMS:** Calculated for  $\text{C}_{29}\text{H}_{21}\text{N}_4\text{NaO}_4\text{Ru}$   $[\text{Ru}^{\text{III}}(\text{mpda})(\text{py})_2 + \text{Na}^+]^+$ : m/z 614.0504, found: m/z 614.0509. **Elemental analysis:** Calculated for  $[7(\text{py})_2]\cdot 3\text{CF}_3\text{CH}_2\text{OH}$ : C, 47.20; H, 3.40; N, 6.29. Found: C, 46.85; H, 3.35; N, 7.36. **ATR-FTIR ( $\nu_{\text{max}}$ ,  $\text{cm}^{-1}$ ):** 3402, 3110, 3074, 1642, 1597, 1560, 1541, 1482, 1445, 1387, 1374, 1349, 1281, 1260, 1217, 1154, 1068, 947, 840, 778, 767, 721, 695, 575.

## CHAPTER 7.

VII

## 8 CHAPTER 8

### Oxidation Properties of Asymmetric Cyclometalated Ru Complexes with Carbanionic Donor Sets

---

*New non-symmetric mononuclear ruthenium complexes containing an anionic tetradentate **Phpp**<sup>-</sup> type of ligand (Phpp is 2-(3-(pyridin-2-yl)phenyl)-1,10-phenanthroline) have been synthesized to utilize the octahedral coordination mode around the **Ru** center to modulate the catalytic properties. These complexes and their synthetic intermediates have been characterized using spectroscopic and electrochemical techniques. Their redox properties were investigated by electrochemical techniques under different conditions.*

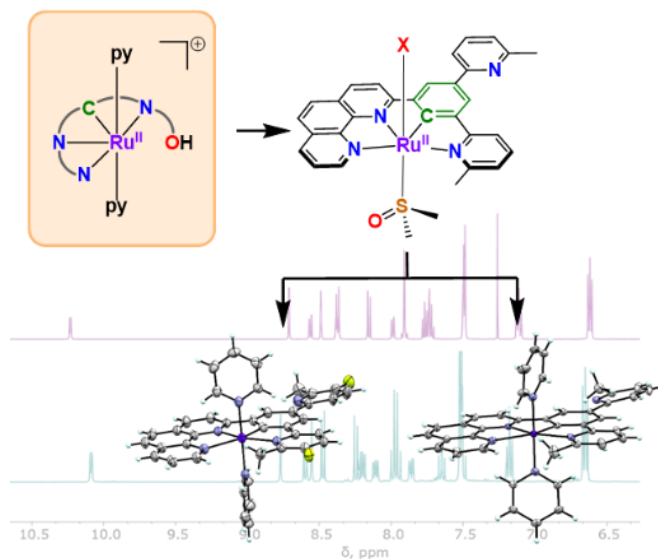
---



## CHAPTER 8.

VIII

## Oxidation Properties of Asymmetric Cyclometalated Ru Complexes with the Carbanionic Donor Sets



### Abstract

New non-symmetric mononuclear ruthenium complexes containing an anionic tetradentate **Phpp** type of ligand (Phpp is 2-(3-(pyridin-2-yl)phenyl)-1,10-phenanthroline with the general formula  $[\text{Ru}(\text{Phpp}^{\text{R}})(\text{X})(\text{Y})]$  ( $\text{R} = \text{H}$  or  $\text{F}$ ;  $\text{X} = \text{DMSO}, \text{OH}_2, \text{py}$ ;  $\text{Y} = \text{DMSO}, \text{py}$ ) have been synthesized to utilize the octahedral coordination mode around the Ru center to modulate its catalytic properties. The final complexes and their synthetic intermediates have been characterized using various structural and electrochemical techniques. Their redox properties were investigated in various conditions.

### Contributions:

Natalia Vereshchuk synthesized and characterized compound **9** and carried out electrochemical and spectroscopic experiments for all the compounds described here.

## CHAPTER 8.

### 8.1 Introduction

As was defined in the previous chapters, terpyridyldicarboxylate (tda) as well as terpyridyldiphosphonate (tPa) ligands<sup>1,2</sup> form highly active water oxidation catalysts (WOC) with Ru.<sup>1,3</sup> However, Ru-WOC of this type suffer from high onset potentials, which could be overcome by the introduction of higher electron densities at the equatorial ligand to lower the Ru<sup>V/IV</sup> oxidation potential (see Chapter 7).

We showed in the previous chapter how negatively charged ligands (**Xpda**<sup>3-</sup>, Scheme 1 in Chapter 7 and Figure 1) can have a significant effect on the oxidation/reduction potentials of the metal, with cathodic shifts up to 730 mV when compared to the related tda<sup>2-</sup> ligand. However, we found that such complexes are so stable that does not react with water to form the desired Ru-OH<sub>2</sub> complexes, required to reach Ru<sup>V</sup> species, which would trigger the water oxidation catalysis. These results motivated us to explore the further modification of the cyclometallating ligands in order to improve their putative catalytic properties. In the new family of ligands, one of the carboxylate groups has been substituted by N-donating neutral ligand of a phenanthroline derivative, while the cyclometallated group is kept to ensure low oxidation potentials (Figure 1).

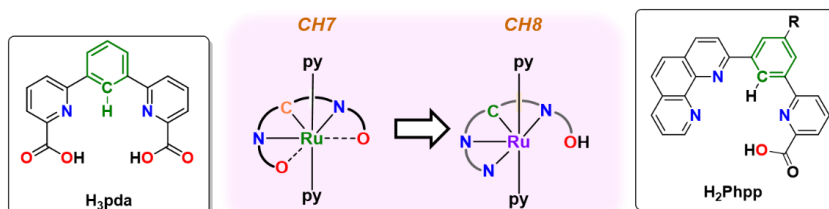
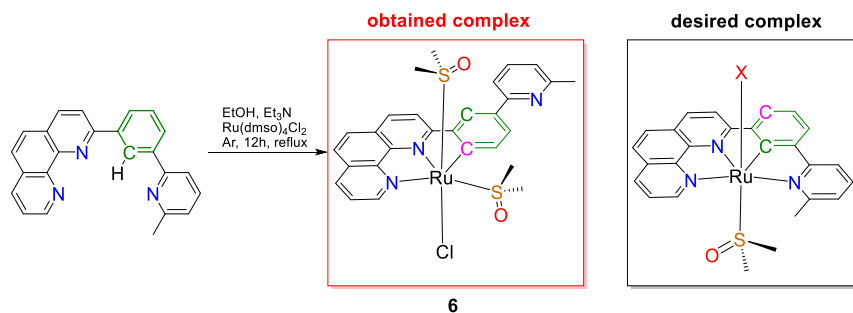


**Figure 1.** (Left) Comparison of Ru-WOC design for Chapter 7 and Chapter 8. (Right) General formula of the ligands targeted in Chapter 8.

VIII

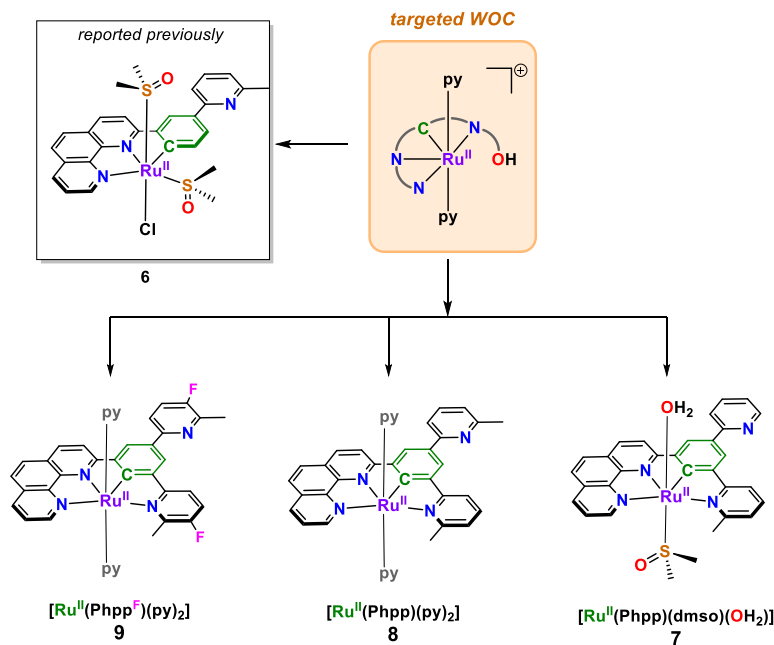
The first cyclometallating ligand of this type was studied in collaboration with Prof. Fabio Marchetti,<sup>4</sup> where the anionic tetradentate 2-(3-(pyridine-2-yl)phenyl)-1,10-phenanthroline ligand was used (see Scheme 1). To our surprise, during the complexation reaction, the ligand behaved in a different coordination manner than was expected. Single-crystal X-Ray diffraction analysis of complex **6** showed that pyridine moiety was far from the metal center, hindering its coordination, presumably due to steric effects (see Figure S33).



**Scheme 1.** Schematic representation of the complex **6** syntheses.

Different synthetic attempts changing solvent, temperature, and reaction times for promoting the desired coordination were used without success.

The results described above inspired us to design new ligands that should favor the desired complexation of the pyridine group (see complexes **7**, **8**, and **9**, shown in Scheme 2).



**Scheme 2.** Representation of complexes prepared in this study.

## CHAPTER 8.

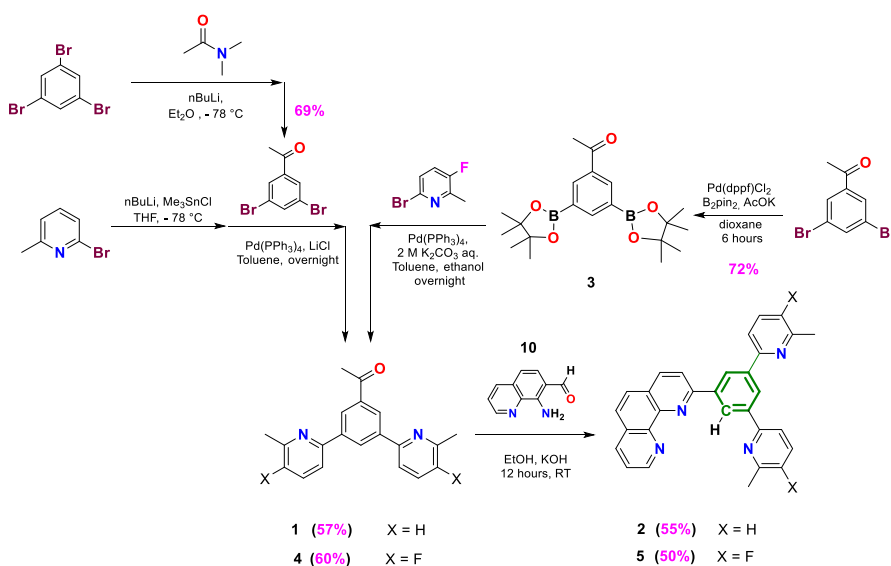
The equatorial ligand of these complexes contains an additional pyridine ring in a strategic position that ensures that one of the two pyridines is close to the metal rendering the coordination of the pyridyl nitrogen.

Herein, we report the synthesis and characterization of new mononuclear Ruthenium complexes containing anionic ligands. Their redox properties are investigated by electrochemical techniques in different pH range and different solvents. Efforts towards the oxidation of the methyl group to form the corresponding carboxylate derivative with the aim of preparing Ru-WOC are also described.

## 8.2 Results and Discussion

### 8.2.1 Synthesis and characterization of the ligands **2** and **5**

Scheme 3 shows the synthetic strategy to prepare Phpp type of ligands **2** and **5**. In the case of ligand **2**, the appropriate aromatic ketone to carry out the Friedländer condensation for the synthesis of phenanthroline core is 3,5-bis-(3-methylpyridyl)-acetophenone (**1**). This compound can be prepared by the Hiyama cross-coupling reaction, using 3,5-dibromoacetophenone. The latter can be prepared from 1,3,5-tribromobenzene using the literature procedure.<sup>5</sup> This synthesis involves an initial lithiation of 1,3,5-tribromobenzene (with *n*-butyllithium), followed by a nucleophilic attack of the lithiated derivative to *N,N*-dimethylacetamide.



**Scheme 3.** Schematic representation of the ligand **2** and **5** syntheses.

Once 3,5-bis-(3-methylpyridyl)-acetophenone (**1**) is prepared, ligand **2** can be obtained *via* condensation reaction with 8-amino-7-quinolinecarbaldehyde (**10**). Through this synthetic route, **2** was isolated in good yield after chromatography purification on silica gel and was fully characterized by NMR spectroscopy and mass spectrometry (Figure S1).

Fluoro- substituted ligand **5** was also prepared following the same condensation reaction with 8-amino-7-quinolinecarbaldehyde (**6**) with a yield of 50%. In this case, the appropriate

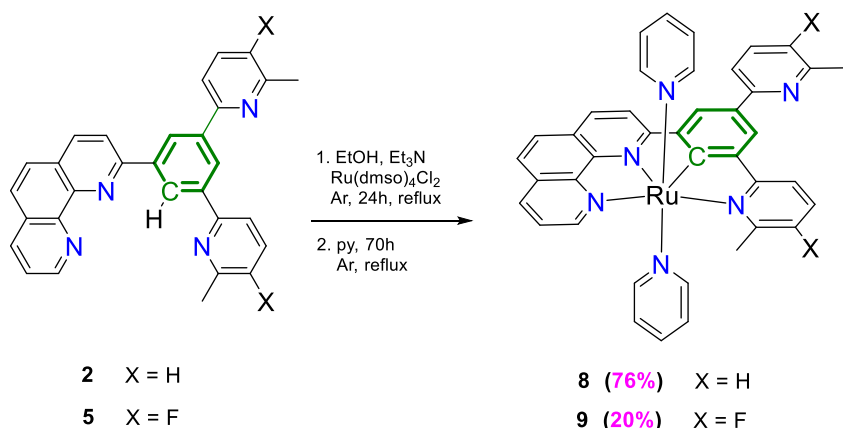
## CHAPTER 8.

aromatic ketone to carry out the Friedlän condensation is 1-(3,5-bis(5-fluoro-6-methylpyridin-2-yl)phenyl)ethan-1-one (**4**). This compound can be prepared by the Suzuki-Miyaura cross-coupling reaction, analogously to the synthesis of **1** using boronic esters **3** as the starting ketone. The latter can be prepared from 1-(3,5-dibromophenyl)ethan-1-one with Bis(pinacolato)diboron using Miyaura borylation reaction.<sup>6</sup> The product **5** and intermediate compounds were confirmed by <sup>1</sup>H NMR spectroscopy and their spectra matched those already reported in the literature (Figures S5-S19).

The chemical oxidation of the methyl group of ligand precursor **5** has been attempted by using K<sub>2</sub>Cr<sub>2</sub>O<sub>7</sub> and SeO<sub>2</sub> (in pyridine and 1,4-dioxane respectively).<sup>7,8</sup> Both of these reactions turned out to be unsuccessful. In fact, in the first case, it decomposed, whereas, in the second attempt the <sup>1</sup>H NMR indicated that no oxidation reaction whatsoever occurred (see SI for more details). Thus, the oxidation of the methyl group to form the corresponding carboxylate will be pursued once the ligand is coordinated to the Ru as explained later.

### 8.2.2 Synthesis and characterization of complexes 7-9.

The synthetic approach employed to prepare the targeted complexes **8** and **9** is a two-step coordination route procedure developed by our group for related [Ru(tda)py<sub>2</sub>] and [Ru(tPa)py<sub>2</sub>] complexes (Scheme 4).<sup>1,2</sup> The two steps can be successively performed *in situ* or after isolation of the intermediate. In the case of complex **8**, when **2** was refluxed in an ethanol solution with [RuCl<sub>2</sub>(DMSO)<sub>4</sub>] and an excess of Et<sub>3</sub>N, a red-brown solid precipitated from the solution. This solid was then isolated *via* filtration and subsequently refluxed in pyridine for 3 days. Simple washing with water a solution of the dark purple product in methylene chloride, followed by slow diffusion of diethyl ether into a saturated acetone solution of the complex, allowed to purify **8** and thus obtain the dark-purple powder in high yield.



**Scheme 4.** Schematic representation of the complex **8** and **9** syntheses.

An analogous procedure was followed with ligand precursor **5**, to yield complex **9** in 20 % yield. Both complexes were fully characterized by NMR spectroscopy and mass spectrometry (see Figure 2 and Figure S20-S28). It is worth to highlight that Figure S21 shows the <sup>13</sup>C NMR spectrum, where the metal-bound carbon manifests itself with a characteristic resonance at 226.9 ppm for complex **9**.<sup>9</sup>

Crystals of **8** and **9** suitable for single-crystal X-ray diffraction analysis were obtained. A view of the structure is shown in Figures 2, S34, and S35, while relevant bonding parameters, resembling those previously reported for related complexes, are listed in SI (Table S2). The complexes present an octahedral geometry in which the ligand **2** and **5** coordinates in a chelating fashion *via* three nitrogen atoms and a carbanion of the central phenyl ring. The two axial coordination positions are occupied by pyridines. The asymmetric unit contains a molecule of the metal complex, one acetone, and one chloride anion. An interesting feature is the Ru1-N3 bond distance (2.365(5) Å) which is about 0.2 Å longer than the other Ru1-N bonds, due to *trans* influence of the σ-donating carbanion.



## CHAPTER 8.

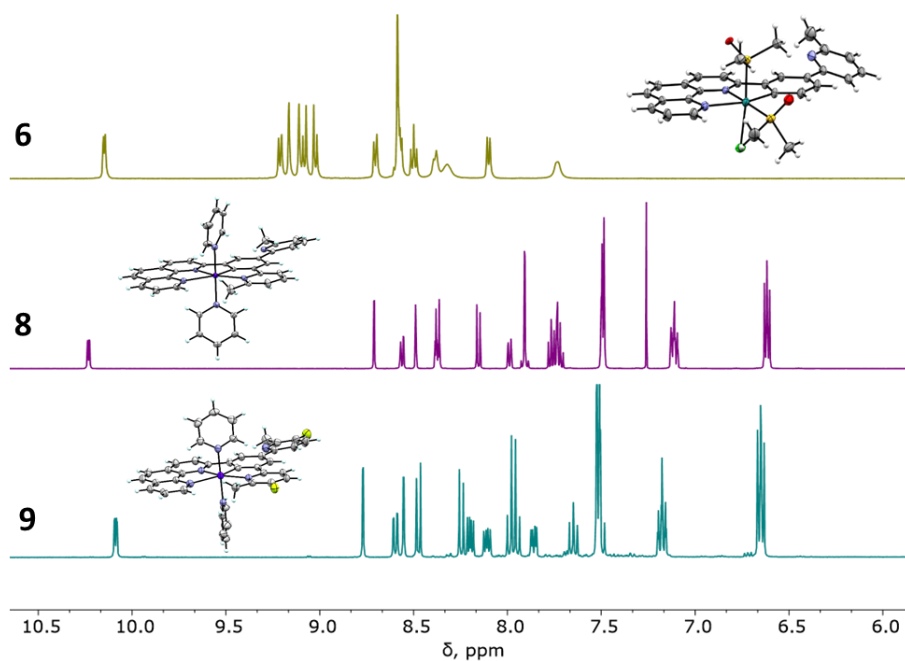
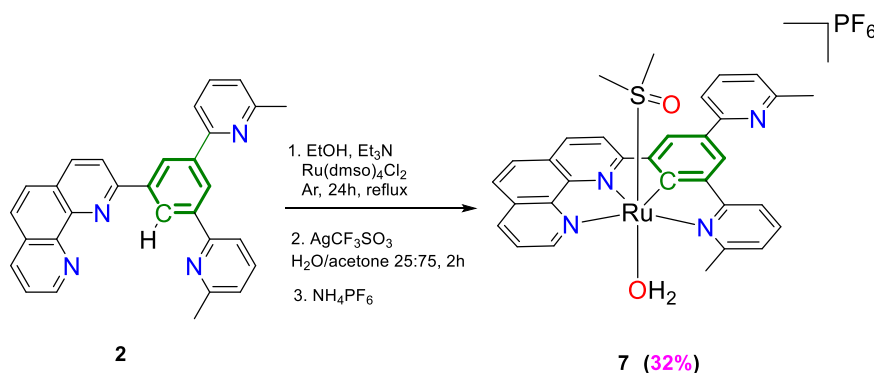


**Figure 2.** ORTEP views of the complexes **6**, **8**, and **9** and  $^1\text{H}$  NMR of complexes described in this work. The green spectrum corresponds to  $^1\text{H}$  NMR of **8** in methanol- $d_4$ , the violet spectrum to  $^1\text{H}$  NMR of **9** in chloroform- $d_1$ , and the blue spectrum to  $^1\text{H}$  NMR of **9** in dichloromethane- $d_2$ . Color code: Ru, cyan; F, green; N, blue; C, black; H, white

Scheme 5 shows the synthesis of complex **7**. The latter differs from the pyridine complex **8** in the axial ligands: a molecule of DMSO and a molecule of water replace the two pyridines.

Complex **7** can be prepared using a two-step route similar to the synthesis described for **6**, **8**, and **9**. In the first step **2** was refluxed in an ethanol solution with  $[\text{RuCl}_2(\text{DMSO})_4]$  and an excess of  $\text{Et}_3\text{N}$ , and after 24 hours the red-brown precipitate was isolated by filtration. The intermediate was subsequently refluxed for 2 hours in an acetone/water solution with silver trifluoromethanesulfonate, and the subsequent addition of a saturated aqueous solution of  $\text{NH}_4\text{PF}_6$  provided the pure product as an orange solid.<sup>10</sup>



**Scheme 5.** Schematic representation of the complex **7** synthesis

Complex **7** was fully characterized by NMR spectroscopy and mass spectrometry. The <sup>1</sup>H NMR spectrum (Figure S4) exhibits a significant shift of one methyl resonance with respect to **8**, i.e. from 3.65 to 2.42 ppm (see Figure S2 and S3). The two DMSO ligands give rise to two resonances, one at 2.42 ppm and the other one being overlaid with the non-deuterated residue of the solvent. In the infrared spectrum of **7** (Figure S28), a broad peak around 3100 cm<sup>-1</sup> can be observed, ascribable to the water molecule.

### 8.2.3 Redox properties of complexes 7-9

The redox properties of **7**, **8**, and **9** were investigated by electrochemical techniques in an aqueous solution at pH 7 with the addition of small amounts of trifluoroethanol (TFE) to increase their solubility as well as in organic solvents with the addition of NBu<sub>4</sub>PF<sub>6</sub> (TBAPF<sub>6</sub>, 0.1 M) as a supporting electrolyte. All potentials were measured using Hg/Hg<sub>2</sub>SO<sub>4</sub> as reference electrode and converted to vs NHE by adding 0.65 V to the measured value.

The cyclic voltammetry in pH 7 for all complexes are shown in Figure 3. They all display one chemically reversible and electrochemically quasireversible wave and one electrochemically irreversible redox processes. The first redox process appears at the same potential ( $E_{1/2} = 0.55$  V) and was attributed to the one-electron oxidation of Ru<sup>II</sup> forming Ru<sup>III</sup>. The second wave was attributed to the Ru<sup>IV</sup>/Ru<sup>III</sup> couple. While **8** and **9** show this oxidation at  $E_a = 1.41$  V and 1.33 V respectively, for complex **7** it appears at  $E_a = 1.11$  V.

## CHAPTER 8.

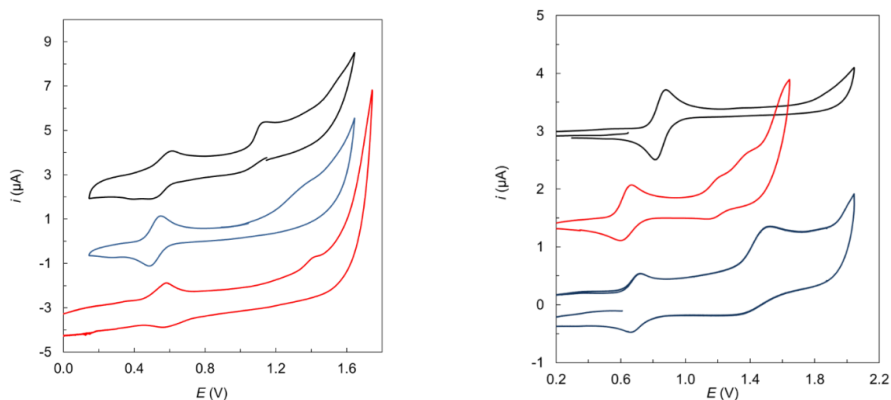


**Figure 3.** Electrochemical behavior of **7** (black), **8** (red), and **9** (blue) analyzed by CV in a mixture of TFE and pH 7 phosphate buffer (**left**) and acetonitrile (CH<sub>3</sub>CN) (**right**).

The redox data in pH 7 and different organic solvents are summarised in Table 1. For complex **7**, which contains DMSO and H<sub>2</sub>O axial ligands, although the potential of the Ru<sup>III</sup>/Ru<sup>II</sup> redox couple is not shifted compared to **8** and **9**, it presents a redox potential for the Ru<sup>III</sup>/Ru<sup>IV</sup> couple which is 250 mV lower. Both the electrochemical oxidation and the water oxidation catalysis should benefit from this.

**Table 1:** Redox Data for Ru Complexes **7-9** in different organic solvents.

	CH <sub>3</sub> CN		DCM		pH 7 + TFE	
	(Ru <sup>III/II</sup> )	(Ru <sup>IV/III</sup> )	(Ru <sup>III/II</sup> )	(Ru <sup>IV/III</sup> )	(Ru <sup>III/II</sup> )	(Ru <sup>IV/III</sup> )
<b>7</b>	0.89	>2	-	-	0.55	1.11
<b>8</b>	0.69	1.43	0.82	1.21	0.55	1.41
<b>9</b>	0.65	1.21	0.79	1.45	0.52	1.33
[Ru(tda)(py) <sub>2</sub> ]	-	-	-	-	0.55	1.10

It appears that the strong  $\sigma$ -donation effect exerted by the tda<sup>2-</sup> ligand having two carboxylates is equivalent to that of **2** and **5** bearing a carbanion moiety.

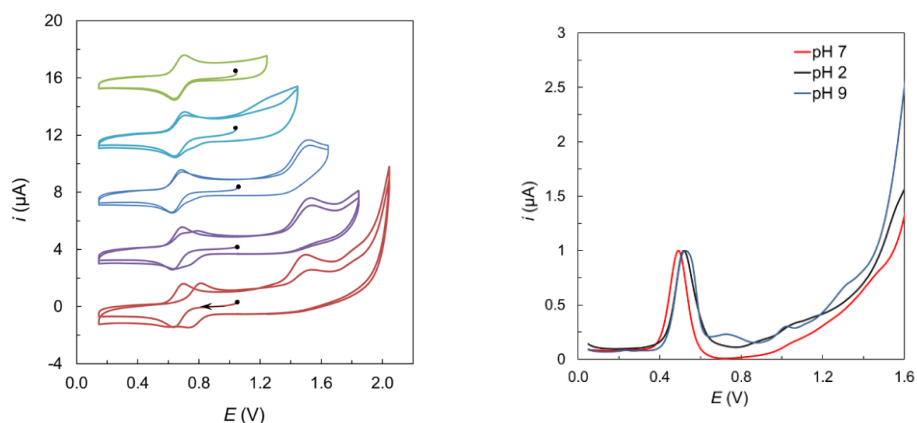


**Figure 4 (left)** Electrochemical behavior of **9** analyzed by CV and DPV in PC (propylene carbonate),  $\text{NBu}_4\text{PF}_6$ , and 10% of  $\text{H}_2\text{O}$ . All CVs were run in the cathodic direction. **(right)** Electrochemical behavior of **9** was analyzed by CV in TFE and phosphate buffer in pH range 2-9.

Additionally, for complex **9** we performed electrochemical measurements in propylene carbonate with the addition of 10%  $\text{H}_2\text{O}$  (Figure 4 left and S31). From an analysis, we can observe that applying a potential below 1.65 V, the complex shows stable and reversible waves over cycling. However, when applying potentials higher than 1.65 V, the  $\text{Ru}^{\text{III}}/\text{Ru}^{\text{II}}$  wave of the initial compound disappears and a new wave appears, 200 mV higher in the potential. This result shows that complex **9** is not stable in an aqueous condition over oxidation condition and converts into a new compound. DPV of **9** in the different pHs with the addition of TFE for better solubility showed no pH dependency of the redox wave (see Figure 4 right).

#### 8.2.4 Oxidation of the methyl group of complexes **7-9**.

Oxidation of the methyl groups of **7** was attempted by Controlled Potential Electrolysis (CPE) electrolysis in a water solution buffered at pH 11.65 by applying a potential of 1.45 V for 3 hours. The redox properties of **7** before and after bulk electrolysis were investigated by cyclic voltammetry at pH 7, as illustrated in Figure 5, observing the complete decomposition of the complex after bulk electrolysis.

## CHAPTER 8.

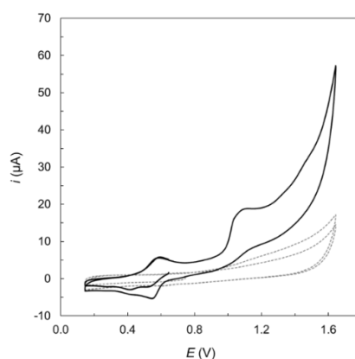


**Figure 5.** Electrochemical behavior of **7** was analyzed by CV in phosphate buffer in pH 7 before (black) and after (grey) CPE in pH 11.65,  $E_{app} = 1.45$  V.

Different routes to oxidize the methyl groups within **8** including electrochemical oxidation by CPE at different pHs as well as chemical oxidation by CAN (cerium ammonium nitrate) and  $Ag^+$  were attempted, but they all proved unsuccessful. The redox properties before and after CPE were investigated by cyclic voltammetry at pH 7 (Figure 6 left) and pH 11.65 (Figure 6 right), where can be seen no new redox couple appearance, but high catalytic current appearance, which could be due to decomposition during bulk electrolysis

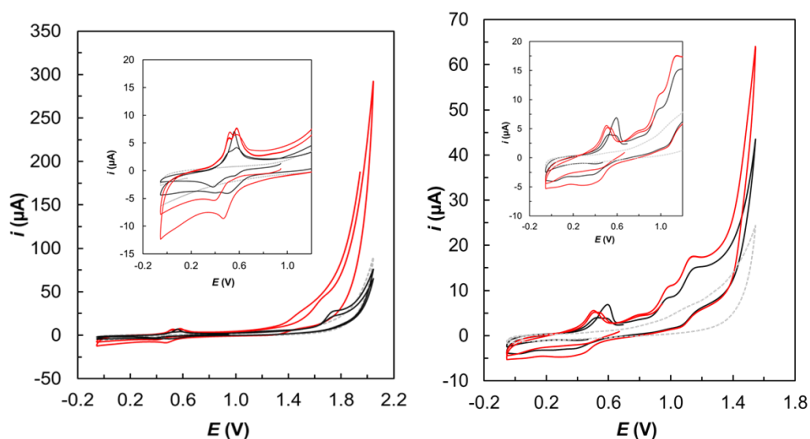
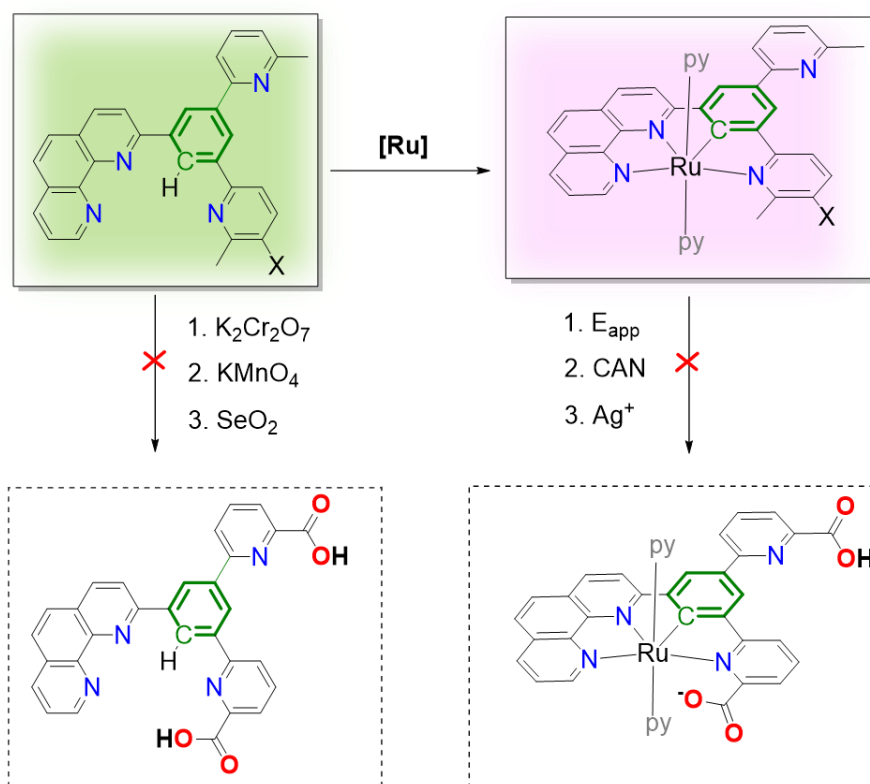


**Figure 6: (left)** Electrochemical behavior of **8** analyzed by CV in phosphate buffer in pH 7 before (black) and after (red) CPE at  $E_{app} = 1.75$  V in the pH 7 phosphate buffer. **(right)** The

electrochemical behavior of **8** was analyzed by CV in phosphate buffer in pH 11.65 before (black) and after (red) CPE at  $E_{app} = 1.55V$  in pH 11.65 phosphate buffer.

Moreover, chemical oxidation has been attempted on complex **9** using CAN and  $Ag^+$  (See Figure 29). Nevertheless, these reactions turned out to be also unsuccessful, highlighting that none of the used methods is sufficient to oxidize the complexes and form the  $Ru^{IV}-OH$  and further  $Ru^V=O$ , which would intramolecularly oxidize the methyl (see Scheme 7).



**Scheme 7.** A general overview of the oxidation pathways described in this section.

## CHAPTER 8.

### 8.3 Conclusion

A series of novel cyclometalated complexes, which adopt six-membered coordination of the peripheral  $\pi$ -extended carbanionic fragments based on benzene were synthesized. The synthesis was optimized and identified the C–H activation. The purification protocol was simplified to a single chromatographic run using commercially available silica gel, which ultimately leads to good isolated yields of up to 76%. The structures were confirmed by NMR spectroscopy and X-ray crystallography analyses.

Different routes to oxidize chemically and electronically the methyl groups that were attempted turned to be unsuccessful. Consequently, complexes **7**, **8**, and **9** did not show catalytic toward oxidation due to the inability to CH<sub>3</sub> oxidation, and lack of proton-coupled electron-transfer processes, which has a strong effect on the catalytic properties. Moreover, under harsh oxidation conditions, complexes show the formation of different species, which are reflecting on the CV from the new wave's appearance.

The complexes presented in this study suggest the possibility of further modification of the coordination environment in cyclometalated complexes.

## 8.4 Experimental section

All chemicals and solvents were purchased from Sigma-Aldrich, Fluka, ABCR, Acros Organics, Alfa Aesar, VWR, and were used without further purification unless otherwise specified. Instrumentation details are provided in the Supporting Information.

**(1)** To a stirred solution of 2-bromo-6-methylpyridine (0.49 mL, 4.327 mmol) in dry ether (20 mL) at  $-78\text{ }^{\circ}\text{C}$  was added n-butyllithium (1.73 mL, 4.327 mmol) dropwise over a period of 10 min under nitrogen. The reaction mixture was stirred at  $-78\text{ }^{\circ}\text{C}$  for 1 h, followed by dropwise addition of a solution of trimethyltin chloride (0.888 mg, 4.327 mmol) solution in dry THF (5 mL). The reaction mixture was stirred for 3 h at room temperature, filtered through a pad of celite and concentrated under vacuum to give the tin derivative 2-methyl-6-trimethylstannylpyridine as a yellow oil. The crude product was used in the next step without additional purification. To a mixture of 3,5-dibromoacetophenone (0.602 g, 1.904 mmol), LiCl (0.367 g, 8.654 mmol) and Pd(PPh<sub>3</sub>)<sub>4</sub> (0.150 g, 0.1112 mmol) was added a solution of 2-methyl-6-trimethylstannylpyridine in toluene (25 mL) under nitrogen atmosphere. The reaction mixture was heated under reflux for 20 h, the solvent was evaporated under vacuum and the residue was purified on silica gel column chromatography using diethyl ether/acetone as eluting solvent mixture, affording the product as a yellow oil. Yield: 328mg, 57%. **ESI-MS(+):**  $m/z = 439.2$  [M - H]<sup>+</sup>. **IR (solid):**  $\tilde{\nu}/\text{cm}^{-1} = 3059\text{vw}; 300\text{vw}; 2963\text{vw}; 2921\text{vw}; 1682\text{s} (\text{C}=\text{O}); 1599\text{w-m}; 1585\text{m}; 1572\text{s}; 1469\text{m-s}; 1430\text{m-s}; 1355\text{m-s}; 1246\text{m-s}; 1224\text{s}; 1160\text{w}; 1095\text{w-m}; 1027\text{w}; 989\text{w}; 967\text{w}; 887\text{w}; 788\text{vs}; 740\text{m-s}; 691\text{s}$ . **<sup>1</sup>H NMR (400 MHz, CDCl<sub>3</sub>):**  $\delta/\text{ppm} = 8.81$  (d, 1 H, <sup>4</sup>J<sub>HH</sub> = 1.6, H<sup>3</sup>); 8.61 (d, 2 H, <sup>4</sup>J<sub>HH</sub> = 1.6 Hz, H<sup>2</sup>); 7.73-7.65 (m, 4 H, H<sup>4</sup>, H<sup>5</sup>); 7.16 (dd, 2 H, <sup>4</sup>J<sub>HH</sub> = 5.9 Hz, 2.6 Hz, H<sup>6</sup>); 2.76 (s, 3 H, H<sup>1</sup>); 2.66 (s, 6 H, H<sup>7</sup>). **<sup>13</sup>C NMR (400 MHz, CDCl<sub>3</sub>):**  $\delta/\text{ppm} = 198.3; 158.6; 155.8; 140.7; 138.1; 137.1; 130.1; 127.1; 122.3; 118.0; 27.0; 24.7$ .

**(2)** To a mixture of 8-ammino-7-quinolinecarboxaldehyde (**10**) (0.331 g, 1.914 mmol) and 3,5-bis-(3-methylpyridyl)-acetophenone (**1**) (0.526 g, 1.739 mmol) in absolute EtOH (20 mL) was added saturated ethanolic KOH (0.7 mL) dropwise, and the mixture was refluxed for 15 h. After cooling to room temperature, water was added, and the mixture was extracted with CH<sub>2</sub>Cl<sub>2</sub>. The combined organic layers were washed with water and dried over MgSO<sub>4</sub>. The crude material was purified on silica gel column chromatography with diethyl ether/acetone as eluting solvent mixture, affording the product as a pink solid. Yield: 185



## CHAPTER 8.

mg, 46%. **ESI-MS(+):**  $m/z = 439.2$   $[M - H]^+$ . **IR (solid):**  $\tilde{\nu}/\text{cm}^{-1} = 2336\text{br}; 2100\text{br}; 1619\text{vw}; 1583\text{m-s}; 1571\text{s}; 1552\text{m}; 1506\text{m}; 1491\text{w-m}; 1466\text{m-s}; 1445\text{m-s}; 1429\text{s-s}; 1415\text{m}; 1378\text{m}; 1290\text{vw}; 1273\text{w}; 1256\text{w-m}; 1239\text{w-m}; 1222\text{w-m}; 1237\text{w-m}; 1224\text{m}; 1160\text{w}; 1139\text{w}; 1111\text{w-m}; 1095\text{w-m}; 1082\text{w-m}; 1035\text{w}; 987\text{w}; 908\text{w-m}; 886\text{w-m}; 847\text{s}; 829\text{w-m}; 789\text{vs}; 780\text{vs}; 742\text{s}; 720\text{s}; 695\text{m}; 671\text{s}; 654\text{m}$ .  **$^1\text{H NMR}$  (400 MHz,  $\text{CDCl}_3$ ):**  $\delta/\text{ppm} = 9.21$  (dd, 1 H,  $^4J_{\text{HH}} = 4.3$  Hz, 1.6 Hz,  $\text{H}^{12}$ ); 8.96 (d, 2 H,  $^4J_{\text{HH}} = 1.6$  Hz,  $\text{H}^5$ ,  $\text{H}^4$ ); 8.69 (t, 1 H,  $^4J_{\text{HH}} = 1.5$  Hz,  $\text{H}^{13}$ ); 8.26 (q, 2 H,  $^3J_{\text{HH}} = 8.4$  Hz,  $\text{H}^8$ ,  $\text{H}^9$ ); 8.20 (d, 1 H,  $^3J_{\text{HH}} = 8.0$  Hz,  $\text{H}^{10}$ ); 7.79 (d, 2 H,  $^3J_{\text{HH}} = 7.8$  Hz,  $\text{H}^{14}$ ,  $\text{H}^{15}$ ); 7.75, 7.70 (d, 2 H,  $^3J_{\text{HH}} = 8.7$  Hz,  $\text{H}^6$ ,  $\text{H}^7$ ); 7.66 (t, 2 H,  $^3J_{\text{HH}} = 7.6$ ,  $\text{H}^2$ ,  $\text{H}^3$ ); 7.59 (dd, 1 H,  $^3J_{\text{HH}} = 8.0$  Hz,  $^4J_{\text{HH}} = 4.3$  Hz,  $\text{H}^{11}$ ); 7.11 (d, 2 H,  $^3J_{\text{HH}} = 7.6$  Hz,  $\text{H}^1$ ); 2.68 (s, 6 H,  $\text{H}^{17}$ ).  **$^{13}\text{C NMR}$  (400 MHz,  $\text{CDCl}_3$ ):**  $\delta/\text{ppm} = 158.5; 157.5; 156.7; 150.2; 146.3; 146.0; 140.8; 140.7; 137.0; 136.9; 136.2; 132.2; 132.1; 129.1; 128.6; 128.5; 127.7; 127.0; 126.8; 126.5; 126.3; 123.0; 122.0; 121.1; 118.3; 24.8$ .

**(3)**<sup>11</sup>. Into a three-necked flask, 3,5-dibromoacetophenone (1 eq, 1.0 g, 3.60 mmol) and bis(pinacolato)diboron (2.5 eq, 2.29 g, 9.0 mmol) were successively added, potassium acetate (1.41 g, 14.39 mmol), 20 mL dioxane; under nitrogen protection, add  $\text{Pd}(\text{dppf})\text{Cl}_2$  (0.13 g, 0.18 mmol, 5%) with stirring. After that, the reaction was refluxed for 6 hours under nitrogen. After the reaction is completed, cooled down to room temperature and filter to remove large particles. Part of the salt was extracted with saturated brine and ethyl acetate, and the organic phase was washed with water to neutrality and dried over anhydrous magnesium sulfate. After filtration, a reddish-brown liquid was obtained, the solvent was evaporated in vacuo and the residue was purified by combiflash column chromatography on silica gel using a DCM/hexane gradient (DCM= 50-80%) to get the product as a yellow oil.

## VIII

After standing at a low temperature, the yellow oil became a white solid with a yield of 72%.

**$^1\text{H NMR}$  (300 MHz,  $\text{CDCl}_3$ )**  $\delta$  8.44 (dd,  $J = 6.4, 1.2$  Hz, 3H), 2.64 (s, 3H), 1.35 (s, 24H).  **$^{13}\text{C NMR}$  (101 MHz,  $\text{CDCl}_3$ )**  $\delta$  198.67, 145.77, 137.44, 136.00, 84.24, 83.63, 26.99, 25.02. **HR-MS  $m/z$ :** Calculated for  $\text{C}_{20}\text{H}_{29}\text{B}_2\text{O}_5\text{Na}^+ [M + \text{Na}]^+$ :  $m/z$  394.2208, found:  $m/z$  394.2202

**(4)** To a mixture of **3** (1 eq, 2.15 mmol, 0.80 g), 6-bromo-3-fluoro-2-methylpyridine (2 eq., 4.3 mmol, 0.817 g) and  $\text{Pd}(\text{PPh}_3)_4$  (0.151 mmol, 174 mg, 7%) was added a solution of 2M  $\text{K}_2\text{CO}_3$  in water (5 ml), ethanol (5 ml) and toluene (40 mL) under Ar atmosphere. The reaction mixture was heated under reflux at 85 °C for 2 h, the solvent was evaporated in vacuo and the residue was purified by two combiflash column chromatography on silica gel using an

Ethyl acetate/hexane gradient (Ethyl acetate = 30-40%) to get the product as a yellow/white powder with a yield of 60%. **<sup>1</sup>H NMR (400 MHz, CDCl<sub>3</sub>)** δ 8.74 (t, J = 1.7 Hz, 1H), 8.56 (d, J = 1.7 Hz, 2H), 7.73 – 7.69 (m, 2H), 7.43 (t, J = 8.7 Hz, 2H), 2.75 (s, 3H), 2.64 (d, J = 3.0 Hz, 6H). **<sup>13</sup>C NMR (101 MHz, CDCl<sub>3</sub>)** δ 198.04, 158.89, 156.34, 151.45, 151.40, 146.90, 146.73, 139.73, 138.16, 129.56, 126.74, 123.18, 122.98, 119.65, 119.61, 26.98, 18.25, 18.23. **<sup>19</sup>F NMR (376 MHz, CDCl<sub>3</sub>)** δ -126.58. **HR-MS m/z:** Calculated for C<sub>20</sub>H<sub>17</sub>F<sub>2</sub>N<sub>2</sub>O [M + H]<sup>+</sup>: m/z 339.1309, found: m/z 339.1308

**(5)**<sup>12</sup> To a mixture of 8-ammino-7-quinolinecarboxaldehyde (**10**)<sup>13</sup> (1 eq; 0.148 g, 0.86 mmol) and **4** (1 eq; 0.290 g, 0.857 mmol) in absolute EtOH (15 mL) was added saturated ethanolic KOH (0.5 mL) dropwise, and the mixture was stirring for 48 h. After stopped, water was added, and the mixture was extracted with CH<sub>2</sub>Cl<sub>2</sub>. The combined organic layers were washed with water and dried over MgSO<sub>4</sub>. Removal of the solvent gave a crude material which was purified by chromatography on silica gel, eluting with an Ethyl acetate/hexane gradient (Ethyl acetate = 0-40%) affording the product as a purple-white powder (0.3 g, 75%). **<sup>1</sup>H NMR (400 MHz, CDCl<sub>3</sub>)** δ 9.25 (dd, J = 4.3, 1.8 Hz, 1H), 8.90 (d, J = 1.7 Hz, 2H), 8.68 (t, J = 1.7 Hz, 1H), 8.37 (d, J = 8.4 Hz, 1H), 8.32 – 8.25 (m, 2H), 7.89 – 7.77 (m, 4H), 7.66 (dd, J = 8.0, 4.4 Hz, 1H), 7.43 (t, J = 8.8 Hz, 2H), 2.65 (d, J = 3.0 Hz, 6H). **<sup>13</sup>C NMR (101 MHz, CDCl<sub>3</sub>)** δ 158.74, 157.49, 156.20, 152.40, 152.35, 150.29, 146.49, 146.33, 140.76, 139.85, 136.93, 136.24, 129.13, 127.79, 126.66, 126.47, 126.41, 126.29, 122.99, 122.96, 122.76, 121.24, 119.92, 119.88, 18.29, 18.27. **<sup>19</sup>F NMR (376 MHz, CDCl<sub>3</sub>)** δ -127.49. **HR-MS m/z:** Calculated for C<sub>30</sub>H<sub>21</sub>F<sub>2</sub>N<sub>4</sub> [M + H]<sup>+</sup>: m/z 475.1734, found: m/z 475.1721

**(7)** [RuCl<sub>2</sub>(DMSO)<sub>4</sub>] (0.205 g, 0.4231 mmol), **2** (0.223 g, 0.5085 mmol) and NEt<sub>3</sub> (0.30 mL, 2.115 mmol) were refluxed in EtOH (35 mL) for 24 h. Within this time a red-brown solid precipitated in the solution. After cooling to room temperature, the suspension was filtrated and the solid was washed with EtOH and diethyl ether and dried under vacuum. (274 mg). The solid was used in the next step without additional purification. The intermediate product (0.274 g, 0.4201mmol) was heated at reflux for 2 h with AgCF<sub>3</sub>SO<sub>3</sub> (0.162 g, 0.6302 mmol) in an acetone/water 75:25 solution (120 mL). AgCl was filtered off on a celite pad, the solution volume reduced on a rotary evaporator and an excess of saturated aqueous NH<sub>4</sub>PF<sub>6</sub> was added dropwise. The resulting dark- red precipitate was separated from the solution by filtration, washed with water and diethyl ether and dried

## CHAPTER 8.

under vacuum. Yield: 106 mg, 32 %. **ESI-MS(+)**:  $m/z = 617 [M^+]$ . IR (solid):  $\tilde{\nu}/\text{cm}^{-1} = 3071\text{w}; 1618\text{vw}; 1594\text{m}; 1571\text{m}; 1538\text{w}; 1512\text{w}; 1468\text{m}; 1442\text{w-m}; 1381\text{w}; 1259\text{vs}; 1269\text{vs}; 1223\text{m-s}; 1149\text{s}; 1051\text{m-s}; 1030\text{vs}; 1005\text{s}; 957\text{w-m}; 916\text{w}; 857\text{m-s}; 792\text{s}; 748\text{m}; 719\text{w}; 683\text{w}; 662\text{m-s}$ .  **$^1\text{H NMR (400 MHz, DMSO-}d_6)$** :  $\delta/\text{ppm} = 9.66$  (d, 1 H,  $^4J_{\text{HH}} = 4.1$ ,  $\text{H}^{12}$ ); 8.84 (d, 2 H,  $^4J_{\text{HH}} = 5.7$  Hz,  $\text{H}^5$ ,  $\text{H}^{10}$ ); 8.77 (s, 1 H,  $\text{H}^4$ ); 8.69 (s, 2 H,  $\text{H}^6$ ,  $\text{H}^7$ ); 8.32 (d, 1 H,  $^3J_{\text{HH}} = 7.8$  Hz,  $\text{H}^{11}$ ); 8.24-8.15 (m, 3 H,  $\text{H}^2$ ,  $\text{H}^8$ ,  $\text{H}^9$ ); 8.08 (m, 2 H,  $\text{H}^3$ ,  $\text{H}^{15}$ ); 7.88 (br, 1 H,  $\text{H}^{16}$ ); 7.68 (d, 1 H,  $^3J_{\text{HH}} = 7.5$  Hz,  $\text{H}^{14}$ ); 7.27 (d, 1 H,  $^3J_{\text{HH}} = 6.8$  Hz,  $\text{H}^1$ ); 2.62 (s, 3 H,  $\text{H}^{17}$ ); 2.50 (s, 3 H,  $\text{H}^{\text{DMSO}}$ , overlaid with the non-deuterated solvent residue); 2.42 (s, 6 H,  $\text{H}^{\text{DMSO}}$ ,  $\text{H}^{18}$ ).  **$^{13}\text{C NMR (400 MHz, DMSO-}d_6)$** :  $\delta/\text{ppm} = 226.9$  (C-Ru); 166.8; 166.4; 164.8; 154.5; 148.2; 147.8; 146.3; 146.1; 139.1; 138.7; 136.3; 131.3; 128.6; 127.6; 127.4; 124.6; 124.3; 124.2; 120.7; 118.6; 40.4 (C- $\text{H}^{17}$ ); 39.5 (C- $\text{H}^{\text{DMSO}}$ ); 29.0 (C- $\text{H}^{18}$ ).  **$^{31}\text{P NMR (400 MHz, DMSO-}d_6)$** :  $\delta/\text{ppm} = -144.2$  (ept,  $J = 712$  Hz).  **$^{19}\text{F NMR (400 MHz, DMSO-}d_6)$** :  $\delta/\text{ppm} = -70.13$  (d,  $J = 712$  Hz).

**(8)**  $[\text{RuCl}_2(\text{DMSO})_4]$  (0.85 g, 0.175 mmol), **2** (0.88 g, 0.211 mmol) and  $\text{NEt}_3$  (0.12 mL, 0.877 mmol) were refluxed in EtOH (12 mL) for 24 h. Within this time a red-brown solid precipitated in the solution. After cooling to room temperature, the suspension was filtrated and the solid was washed with EtOH and diethyl ether and dried under vacuum. (101 mg). The solid was used in the next step without additional purification. The intermediate product was refluxed in pyridine (10 mL) for 70 hours. After cooling to room temperature, the mixture was dried under vacuum and washed with  $\text{Et}_2\text{O}$ . The solid was dissolved in  $\text{CH}_2\text{Cl}_2$  and washed with water (2x30 mL). The solvent was removed under reduced pressure affording the pure product as a dark purple solid. Yield: 99 mg, 76%. **ESI-MS(+)**:  $m/z = 696.5 [M^+]$ .  **$^1\text{H NMR (400 MHz, CDCl}_3)$** :  $\delta/\text{ppm} = 10.23$  (d, 1 H,  $^4J_{\text{HH}} = 3.8$  Hz,  $\text{H}^{12}$ ); 8.71 (s, 1 H,  $\text{H}^5$ ); 8.57 (d, 1 H,  $^3J_{\text{HH}} = 8.2$ ,  $\text{H}^{10}$ ); 8.49 (s, 1 H,  $\text{H}^4$ ); 8.38 (d, 2 H,  $^3J_{\text{HH}} = 8.5$  Hz,  $\text{H}^6$ ,  $\text{H}^7$ ); 8.16 (d, 1 H,  $^3J_{\text{HH}} = 8.5$  Hz,  $\text{H}^{11}$ ); 8.00 (d, 1 H,  $^3J_{\text{HH}} = 7.7$  Hz,  $\text{H}^2$ ); 7.91 (s, 2 H,  $\text{H}^8$ ,  $\text{H}^9$ ); 7.80- 7.70 (m, 3 H,  $\text{H}^3$ ,  $\text{H}^{15}$ ,  $\text{H}^{16}$ ); 7.50 (m, 5 H,  $^4J_{\text{HH}} = 5.3$  Hz,  $\text{H}^{14}$ ,  $\text{H}^{19}$ ); 7.12 (t, 3 H,  $^3J_{\text{HH}} = 7.7$  Hz,  $\text{H}^1$ ,  $\text{H}^{21}$ ); 6.62 (t, 4 H,  $^4J_{\text{HH}} = 6.7$  Hz,  $\text{H}^{20}$ ); 3.65 (s, 3 H,  $\text{H}^{18}$ ); 2.72 (s, 3 H,  $\text{H}^{17}$ ).  **$^{13}\text{C NMR (400 MHz, CDCl}_3)$** :  $\delta/\text{ppm} = 226.9$  (C-Ru); 167.8; 166.6; 161.7; 158.6; 158.3; 153.6; 152.4; 149.8; 148.2; 146.3; 137.7; 137.4; 136.6; 134.7; 131.8; 131.5; 130.7; 128.2; 127.8; 127.2; 126.6; 124.4 (C); 123.7; 123.3; 122.7; 121.0; 118.9; 117.3; 29.1 (C- $\text{H}^{18}$ ); 25.0 (C- $\text{H}^{17}$ ).

**(9)**: Ligand **5** (0.100 g, 0.21 mmol),  $[\text{Ru}(\text{DMSO})_4\text{Cl}_2]$  (0.102 g, 0.21 mmol, 1 equiv.) were mixed with 10 mL of anhydrous MeOH and 10 eq. of  $\text{Et}_3\text{N}$ , purged with Ar for 20 min,

## CHAPTER 8.

resulting in a homogeneous brown solution. The solution was then heated to 70 °C, upon which the color changed to dark purple. After 16 h the volume of the reaction mixture reduced, and 5 mL of dry pyridine was added. The formed brown solution was purged with Ar for 20 min and heated to 120 °C under Ar for 24 h. After the reaction mixture was cooling down, the solvent was evaporated and the compound was purified by combiflash column chromatography on silica gel using DCM /methanol (1% Et<sub>3</sub>N) gradient (methanol = 10%) to get the product as a purple powder (0.031 g, 20 %). **<sup>1</sup>H NMR (400 MHz, CD<sub>2</sub>Cl<sub>2</sub>)** δ 10.09 (dd, J = 4.8, 1.4 Hz, 1H), 8.77 (d, J = 1.4 Hz, 1H), 8.62 – 8.54 (m, 2H), 8.47 (d, J = 8.6 Hz, 1H), 8.25 (d, J = 8.6 Hz, 1H), 8.20 (dd, J = 8.2, 4.8 Hz, 1H), 8.11 (dd, J = 8.7, 5.0 Hz, 1H), 7.97 (q, J = 8.8 Hz, 2H), 7.86 (dd, J = 8.4, 3.4 Hz, 1H), 7.65 (t, J = 8.4 Hz, 1H), 7.52 (dd, J = 6.7, 1.5 Hz, 5H), 7.18 (tt, J = 7.7, 1.5 Hz, 2H), 6.65 (td, J = 6.7, 1.2 Hz, 4H), 3.61 (d, J = 3.7 Hz, 3H), 2.66 (d, J = 2.9 Hz, 3H). **<sup>13</sup>C NMR (101 MHz, CD<sub>2</sub>Cl<sub>2</sub>)** 225.26, 167.77, 163.15, 158.09, 155.56, 153.56, 153.00, 151.53, 148.31, 146.19, 146.08, 145.66, 137.72, 134.84, 131.96, 130.91, 130.77, 128.38, 127.27, 126.81, 126.24, 124.31, 123.36, 123.30, 123.10, 122.59, 119.08, 118.69, 118.63, 118.46, 118.43, 45.77, 22.49, 18.07. **<sup>19</sup>F NMR (376 MHz, CD<sub>2</sub>Cl<sub>2</sub>)** δ -120.03, -129.67. **HR-MS m/z:** Calculated for C<sub>40</sub>H<sub>29</sub>N<sub>6</sub>F<sub>2</sub>Ru [M]<sup>+</sup>: m/z 733.1465, found: m/z 733.1479

## CHAPTER 8.

## 8.5 References

- (1) Matheu, R.; Ertem, M. Z.; Benet-Buchholz, J.; Coronado, E.; Batista, V. S.; Sala, X.; Llobet, A. Intramolecular Proton Transfer Boosts Water Oxidation Catalyzed by a Ru Complex. *J. Am. Chem. Soc.* **2015**, *137* (33), 10786–10795.
- (2) Vereshchuk, N.; Matheu, R.; Benet-Buchholz, J.; Pipelier, M.; Lebreton, J.; Dubreuil, D.; Tessier, A.; Gimbert-Suriñach, C.; Z. Ertem, M.; Llobet, A. Second Coordination Sphere Effects in an Evolved Ru Complex Based on Highly Adaptable Ligand Results in Rapid Water Oxidation Catalysis. *J. Am. Chem. Soc.* **2020**, *142* (11), 5068–5077.
- (3) Matheu, R.; Ertem, M. Z.; Gimbert-Suriñach, C.; Sala, X.; Llobet, A. Seven Coordinated Molecular Ruthenium-Water Oxidation Catalysts: A Coordination Chemistry Journey. *Chem. Rev.* **2019**, *119* (6), 3453–3471.
- (4) Dr. Alice De Palo. Synthesis and Characterization of Ruthenium-Based Organometallic Complexes with Pyridine or Phenanthroline Ligands and Iridium-Based Complexes with Suitably Functionalized Cyclopentadienyl Ligands, University of Pisa, 2019.
- (5) Miller, T. M.; Neenan, T. X.; Zayas, R.; Bair, H. E. Synthesis and Characterization of a Series of Monodisperse, 1,3,5-Phenylene-Based Hydrocarbon Dendrimers Including C276H186 and Their Fluorinated Analogs. *J. Am. Chem. Soc.* **1992**, *114* (3), 1018–1025.
- (6) Miyaura, N.; Suzuki, A. Palladium-Catalyzed Cross-Coupling Reactions of Organoboron Compounds. *Chem. Rev.* **1995**, *95* (7), 2457–2483.
- (7) Bureau, I. WO 2009/040551 A1 (74). **2009**, 2009 (April).
- (8) Luo, Q.; Dai, Z.; Cong, H.; Li, R.; Peng, T.; Zhang, J. Oxidant-Free Synthesis of Benzimidazoles from Alcohols and Aromatic Diamines Catalysed by New Ru(II)-PNS(O) Pincer Complexes. *Dalt. Trans.* **2017**, *46* (43), 15012–15022.
- (9) Schlotthauer, T.; Parada, G. A.; Görls, H.; Ott, S.; Jäger, M.; Schubert, U. S. Asymmetric Cyclometalated Rull Polypyridyl-Type Complexes with  $\pi$ -Extended Carbanionic Donor Sets. *Inorg. Chem.* **2017**, *56* (14), 7720–7730.
- (10) Maji, S.; López, I.; Bozoglian, F.; Benet-Buchholz, J.; Llobet, A. Mononuclear Ruthenium–Water Oxidation Catalysts: Discerning between Electronic and Hydrogen-Bonding Effects. *Inorg. Chem.* **2013**, *52* (7), 3591–3593.
- (11) Ishiyama, T.; Murata, M.; Miyaura, N. Palladium(0)-Catalyzed Cross-Coupling Reaction of Alkoxydiboron with Haloarenes: A Direct Procedure for Arylboronic Esters. *J. Org. Chem.* **1995**, *60* (23), 7508–7510.
- (12) Riesgo, E. C.; Jin, X.; Thummel, R. P. Introduction of Benzo[*h*]Quinoline and 1,10-Phenanthroline Subunits by Friedländer Methodology. *J. Org. Chem.* **1996**, *61* (9), 3017–3022.
- (13) R, Z.; P, K.; S, M. A.; MR, A.; M, A. An Improved Synthesis of 2-(Pyrid-2'-yl)-1,10-Phenanthroline Tridentate Terpyridyl Ligand. *Int. J. Chem. Res.* **2014**, *5* (1), 153–158.
- (14) Elgrishi, N.; Rountree, K. J.; McCarthy, B. D.; Rountree, E. S.; Eisenhart, T. T.; Dempsey, J. L. A Practical Beginner's Guide to Cyclic Voltammetry. *J. Chem. Educ.* **2018**, *95* (2), 197–206.

## 8.6 Supporting Information

### 8.6.1 Materials and methods

All materials were provided by Sigma-Aldrich unless indicated.  $[\text{RuCl}_2(\text{DMSO})_4]$  was synthesized and purified according to the literature. High-purity deionized water was obtained by passing distilled water through a nanopure Milli-Q water purification system.

#### 8.6.1.1 Preparation of 0.1 M ionic strength phosphate solutions.

a) pH = 2.0 buffered solution: Powders of  $\text{H}_3\text{PO}_4$  (10.5 g, 0.1073 M) and  $\text{NaH}_2\text{PO}_4$  (11.83 g, 0.0986 M) were dissolved with deionized water up to 1 L solution.

b) pH = 7.0 buffered solution: Powders of  $\text{NaH}_2\text{PO}_4$  (2.31 g, 0.0193 M) and  $\text{Na}_2\text{HPO}_4$  (3.77g, 0.0266 M) were with deionized water up to 1 L solution.

c) pH = 12.0 buffered solution: Powders of  $\text{Na}_2\text{HPO}_4$  (10.293g, 0.0073 M) and  $\text{Na}_3\text{PO}_4$  (2.06g, 0.0126 M) were dissolved with deionized water up to 1 L solution.

Solutions at pH's between 2.0 and 12.0 were prepared by mixing the above solutions. The pH of all solutions was measured by a pH meter. All solutions contained an ionic strength equal to 0.1 M.

#### 8.6.1.2 Electrochemical methods

##### General considerations

All electrochemical experiments were performed in an IJ-Cambria HI-730 bipotentiostat and IJ-Cambria CHI-660 potentiostat, using a three-electrode cell.  $E_{1/2}$  values reported in this work were estimated from Cyclic Voltammograms (CV) experiments as the average of the oxidative and reductive peak potentials  $(E_{p,a}+E_{p,c})/2$  or from DPV. Glassy carbon disk (GC) ( $\phi = 0.3$  cm,  $S = 0.07$  cm<sup>2</sup>) was used as working electrodes (WE), Mercury/Mercurous sulfate ( $\text{K}_2\text{SO}_4$  sat) (MSE) as reference electrode (RE) (unless explicitly mentioned) and Pt disk as counter electrode (CE). Working electrode pretreatment before each measurement consisted of polishing with 0.05  $\mu\text{m}$  alumina paste, rinsing after with water and acetone, and blow-dried finally. CVs and DPVs were  $iR$  compensated by the potentiostat in all the measurements unless indicated. CV was recorded at 100  $\text{mV}\cdot\text{s}^{-1}$  scan rate unless explicitly expressed. The DPV parameters were  $\Delta E = 4$  mV, Amplitude = 0.05mV, Pulse width = 5 s, Sampling width = 0.0167 s, Pulse period = 5 s unless explicated. All redox potentials in the present work are reported versus NHE by adding 0.65 V to the measured potential.<sup>14</sup>

## CHAPTER 8.

### Cells

A 15 mL vial was used as an electrochemical cell for CV measurements. A Teflon-made with holes for the three electrodes was used as a lid to ensure a reproducible distance between the electrodes. A two compartments cell (25 mL per compartment or 7 mL per compartment) with a separation grid was used for Bulk Electrolysis Experiments.

### Bulk electrolysis

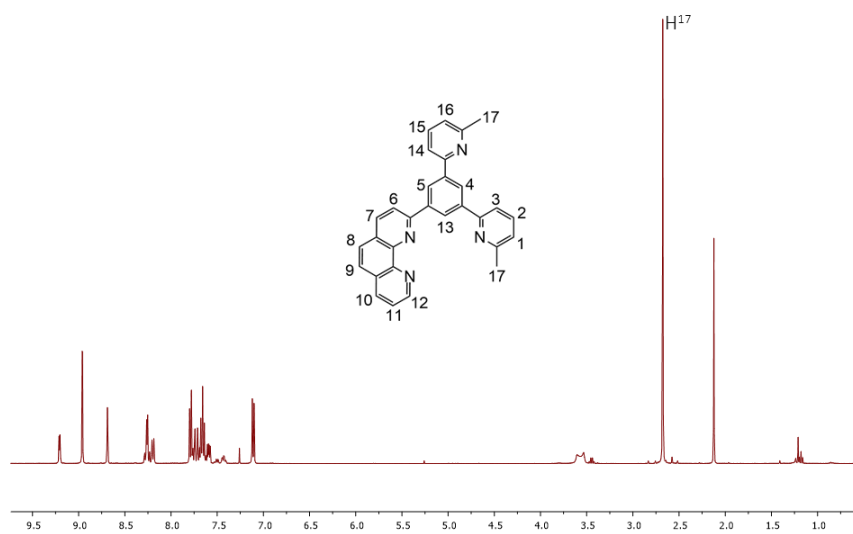
A glassy carbon rod ( $S = 13.35 \text{ cm}^2$  or  $9.35 \text{ cm}^2$ ) was used as a WE, Pt grid as a CE, and a Hg/Hg<sub>2</sub>SO<sub>4</sub> (K<sub>2</sub>SO<sub>4</sub> saturated) as a RE. iR compensation by the potentiostat was not applied in this technique.

#### *8.6.1.3 General instrumentation*

Electrospray ionization (ESI) mass spectrometry (MS) experiments were performed on a Waters Micromass LCT Premier equipment. UV-Vis spectroscopy was performed on a Cary 50 Bio (Varian) UV-Vis spectrophotometer with 1 cm quartz cells unless indicated. A 400 MHz Bruker Avance II spectrometer and a Bruker Avance 500 MHz were used to carry out NMR spectroscopy. The pH of the solutions was determined by a pH meter (CRISON, Basic 20<sup>+</sup>) calibrated before measurements through standard solutions at pH= 4.01, 7.00, and 9.21. Oxygen evolution was analyzed with a gas phase Clark type oxygen electrode (Unisense Ox-N needle microsensor) and calibrated by the addition of small quantities of air (21%).

8.6.2 Spectroscopic Characterization of ligands and complexes

A



B

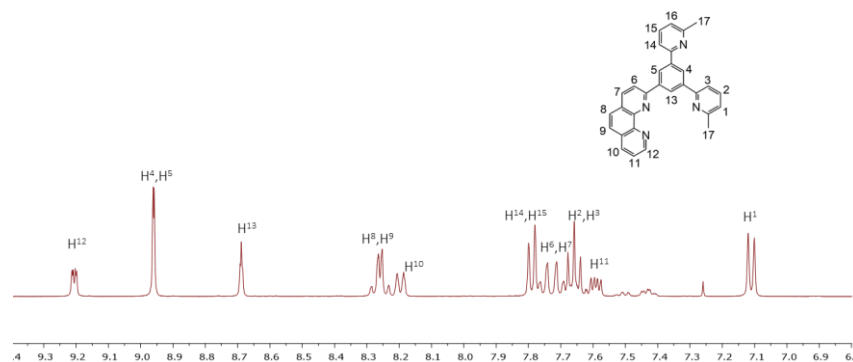


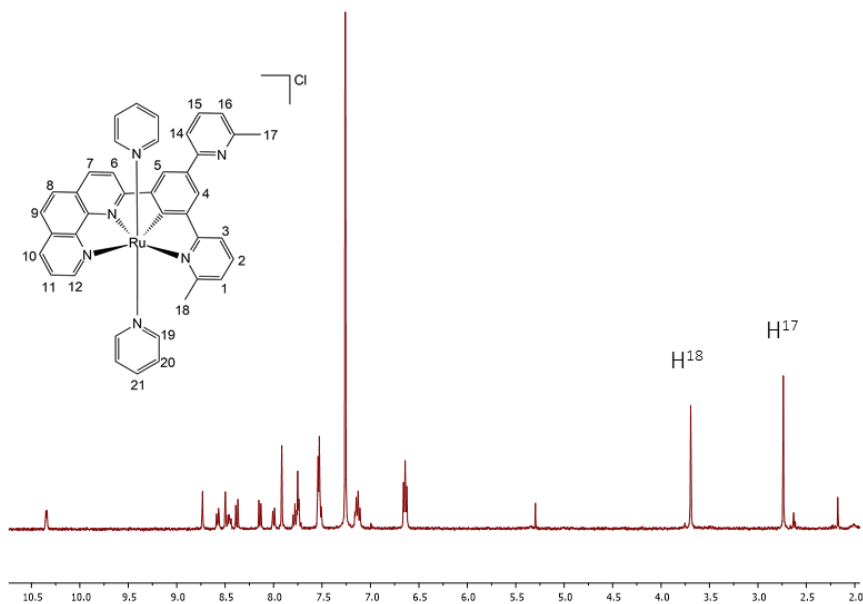
Figure S1. (A) <sup>1</sup>H NMR (400 MHz, CDCl<sub>3</sub>) spectrum of 2. (B) Zoom of the aromatic region

VIII



## CHAPTER 8.

A



B

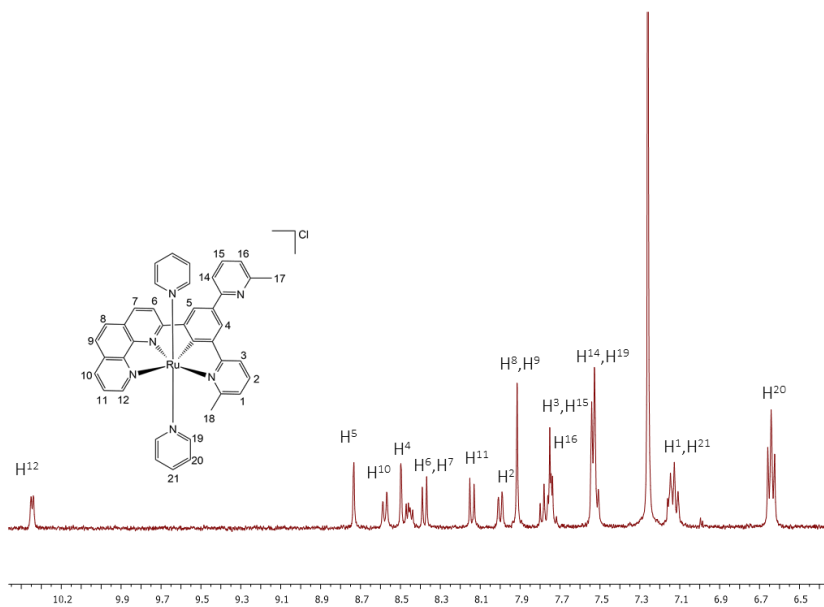


Figure S2. (A)  $^1\text{H}$  NMR (400 MHz,  $\text{CDCl}_3$ ) spectrum of **8**. (B) Zoom of the aromatic region.

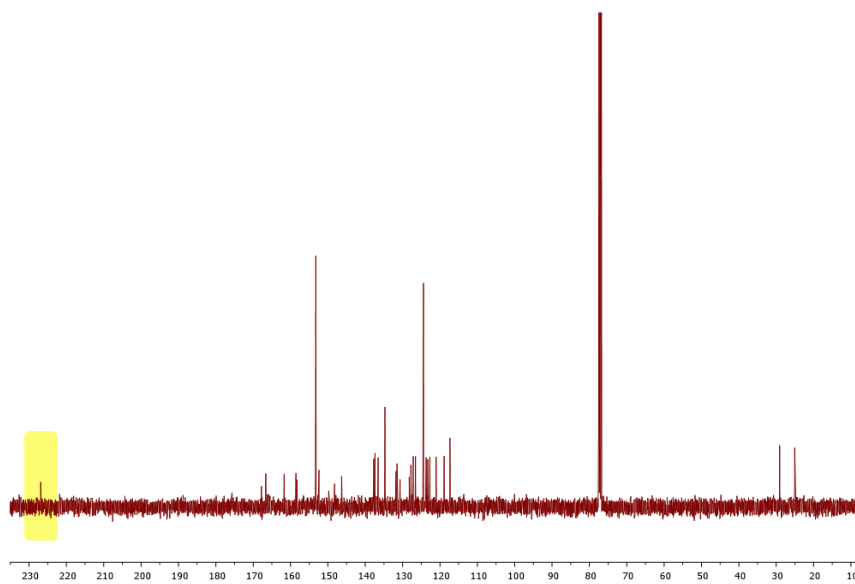
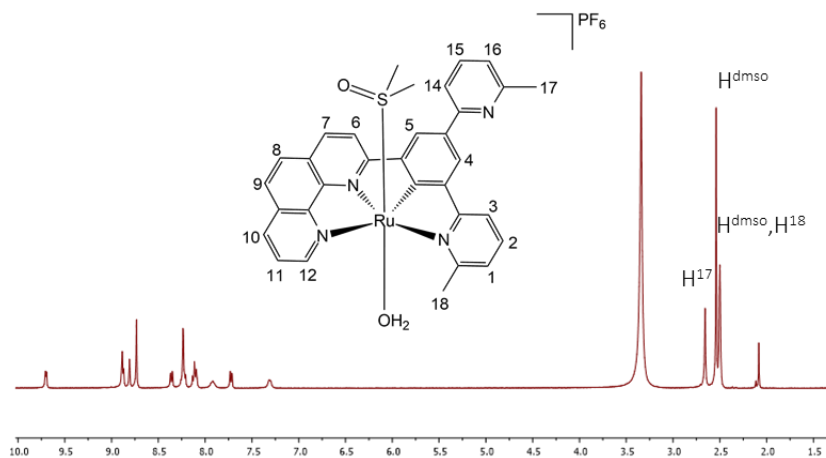


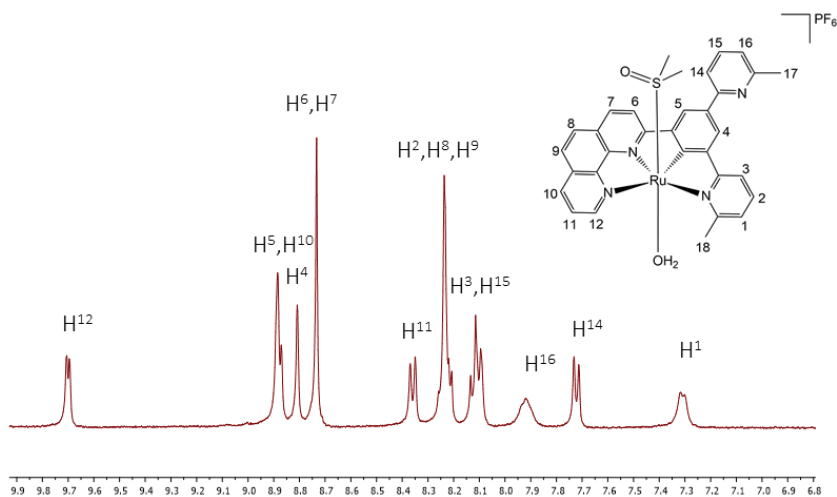
Figure S3.  $^{13}\text{C}$  NMR (400 MHz,  $\text{CDCl}_3$ ) spectrum of **8**.

## CHAPTER 8.

A



B



VIII

Figure S4. (A)  $^1\text{H}$  NMR (400 MHz,  $\text{DMSO-d}_6$ ) spectrum of **7**. (B) Zoom of the aromatic region.

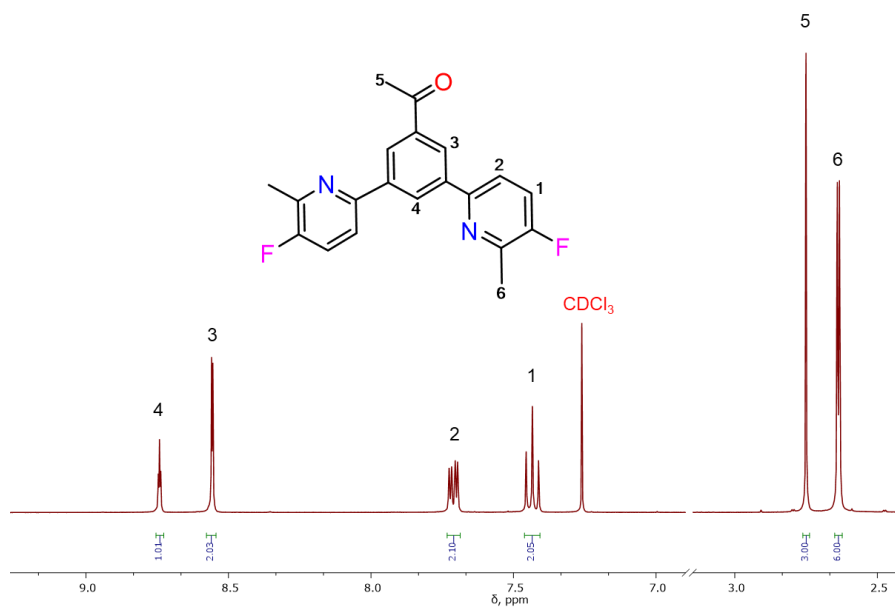


Figure S5.  $^1\text{H}$  NMR of **4** in  $\text{CDCl}_3$  at RT.

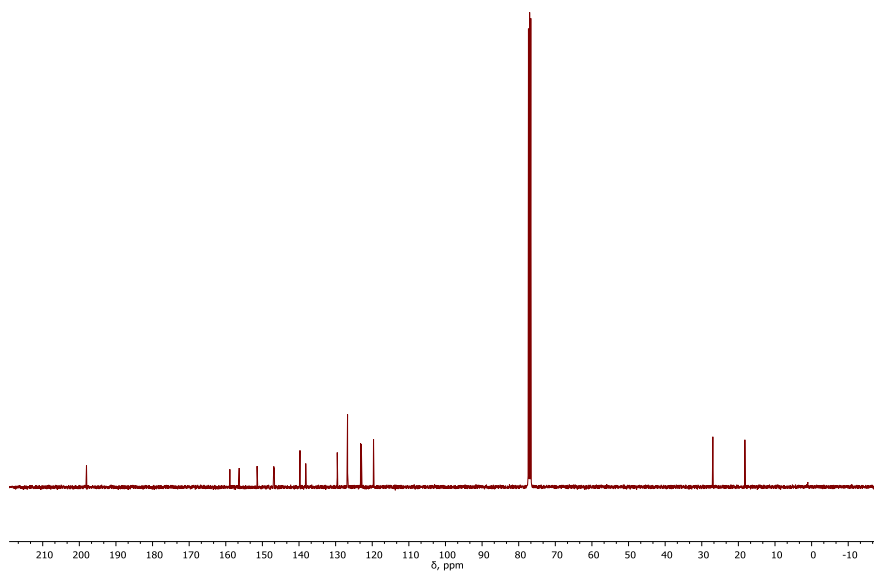


Figure S6:  $^{13}\text{C}$  NMR of **4** in  $\text{CDCl}_3$  at RT.

## CHAPTER 8.

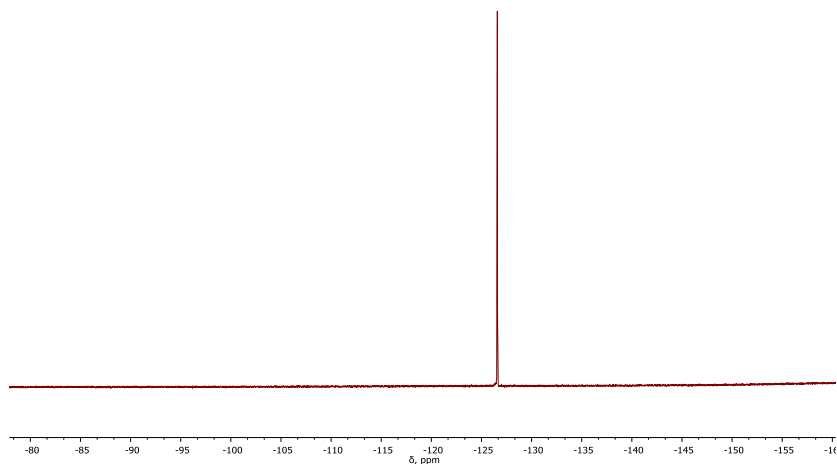


Figure S7:  $^{19}\text{F}$  NMR of **4** in  $\text{CDCl}_3$  at RT.

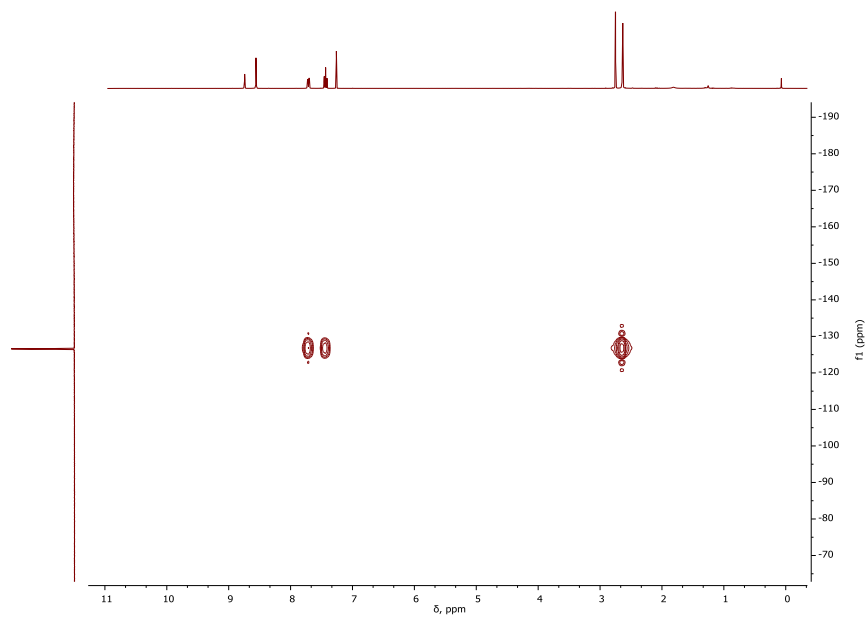


Figure S8:  $^1\text{H}$ - $^{19}\text{F}$  HMBC NMR of **4** in  $\text{CDCl}_3$  at RT.

VIII

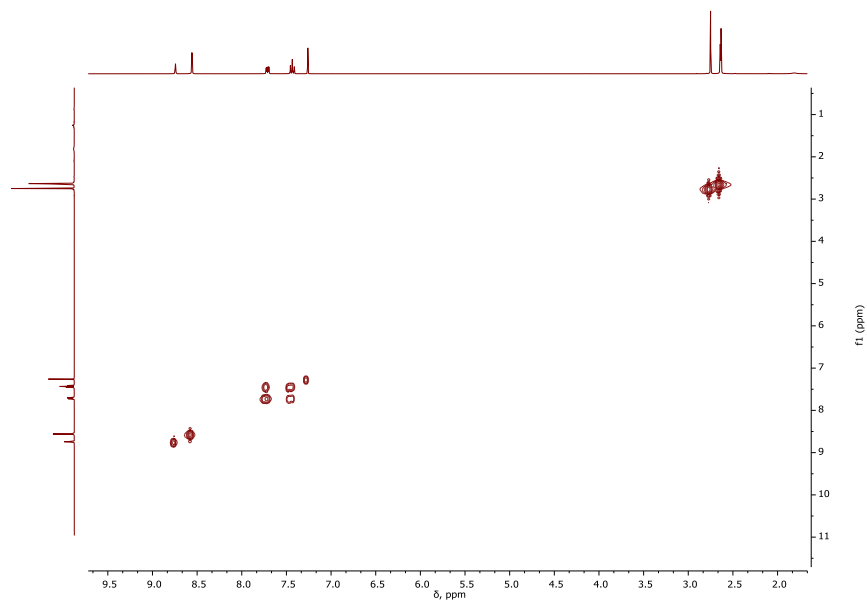


Figure S9:  $^1\text{H}$ - $^1\text{H}$  COSY NMR of **4** in  $\text{CDCl}_3$  at RT.

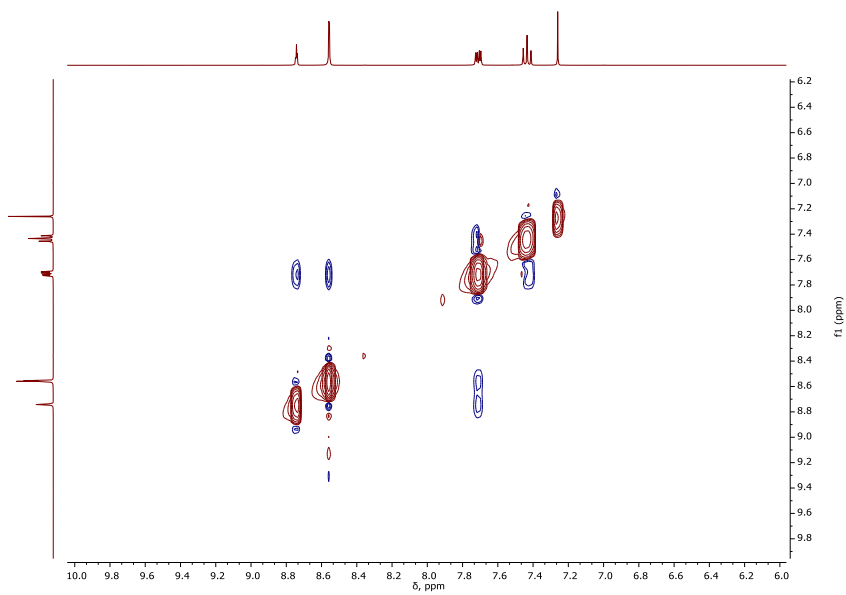
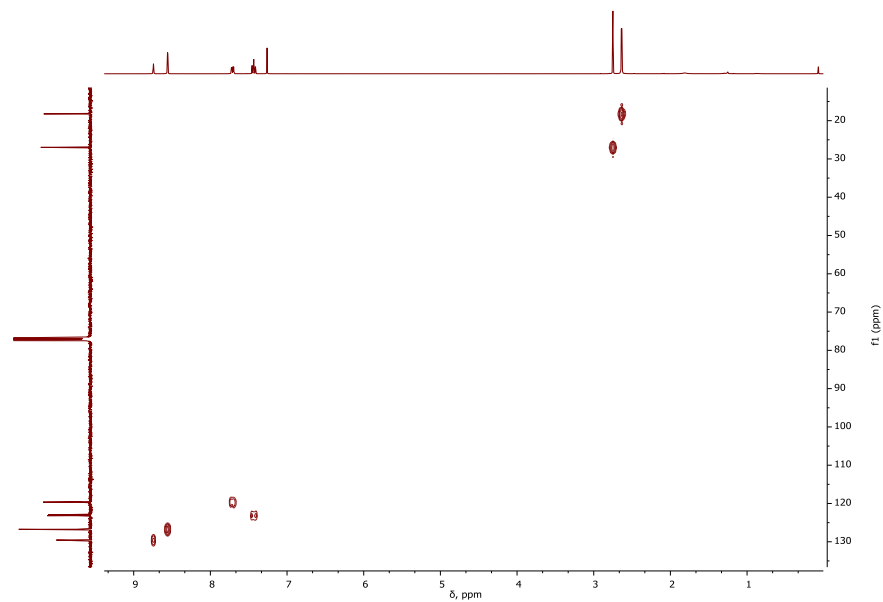
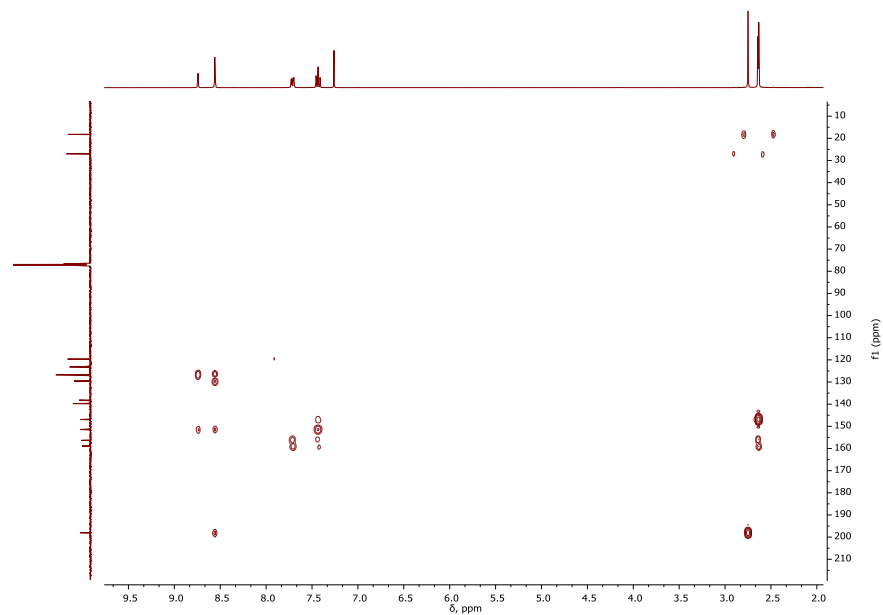


Figure S10:  $^1\text{H}$ - $^1\text{H}$  NOESY NMR of **4** in  $\text{CDCl}_3$  at RT.

## CHAPTER 8.



**Figure S11:**  $^1\text{H}$ - $^{13}\text{C}$  HMQS NMR of **4** in  $\text{CDCl}_3$  at RT.



**Figure S12:**  $^1\text{H}$ - $^{13}\text{C}$  HMBC NMR of **4** in  $\text{CDCl}_3$  at RT.

VIII

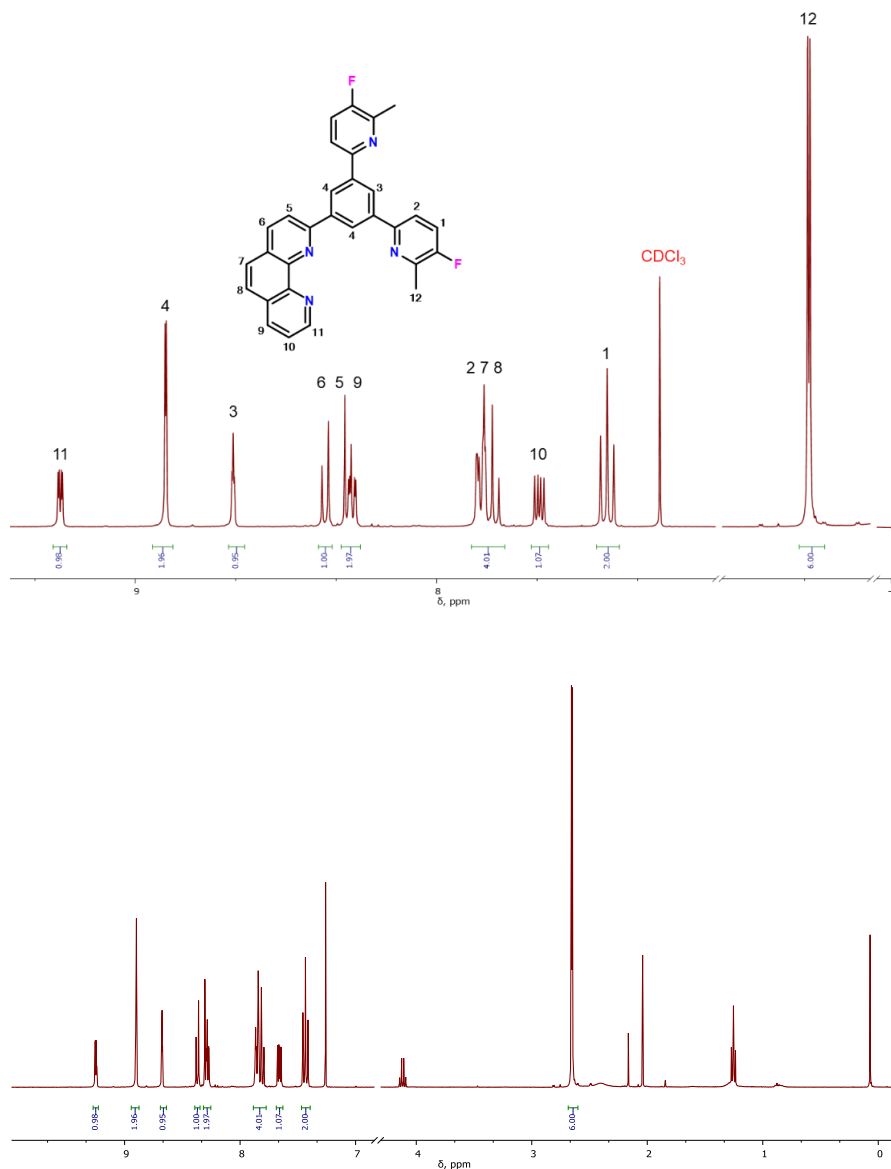
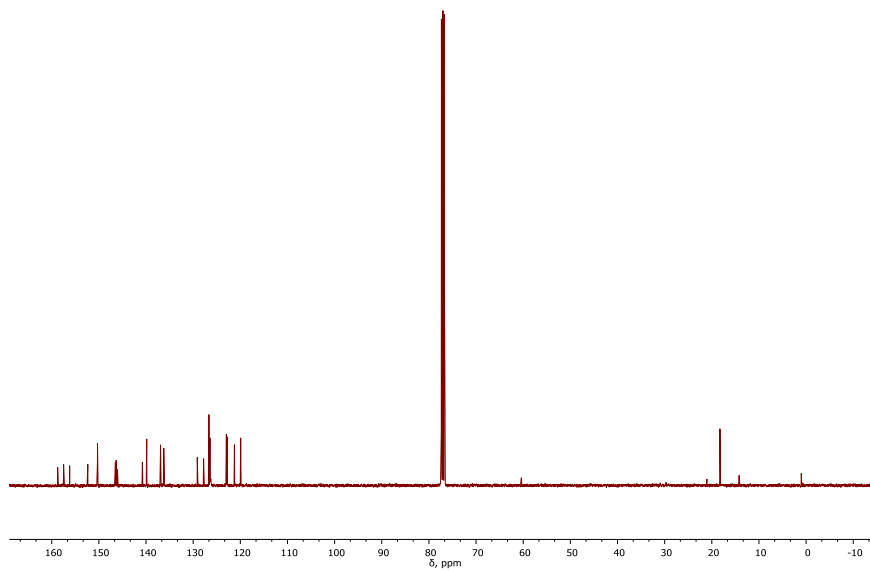


Figure S13.  $^1\text{H}$  NMR of **5** in  $\text{CDCl}_3$  at RT.

VIII



## CHAPTER 8.



**Figure S14:**  $^{13}\text{C}$  NMR of **5** in  $\text{CDCl}_3$  at RT.

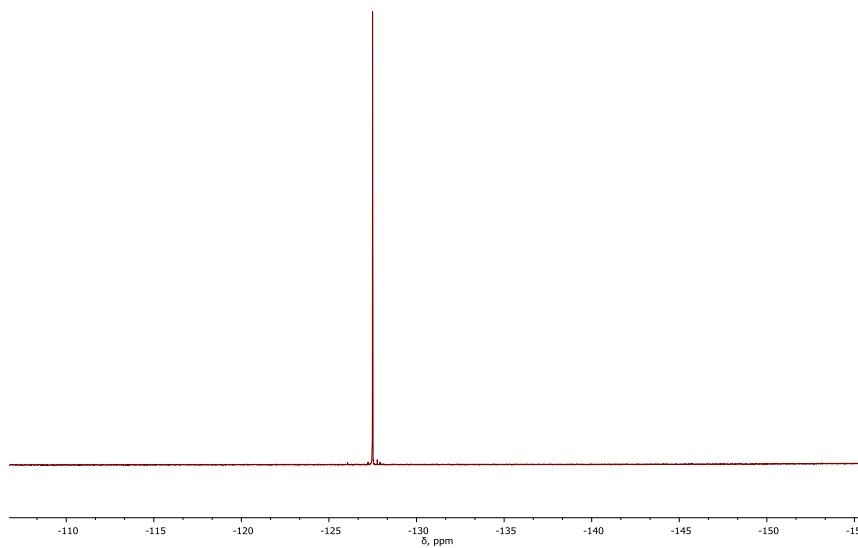


**Figure S15:**  $^{19}\text{F}$  NMR of **5** in  $\text{CDCl}_3$  at RT.

VIII

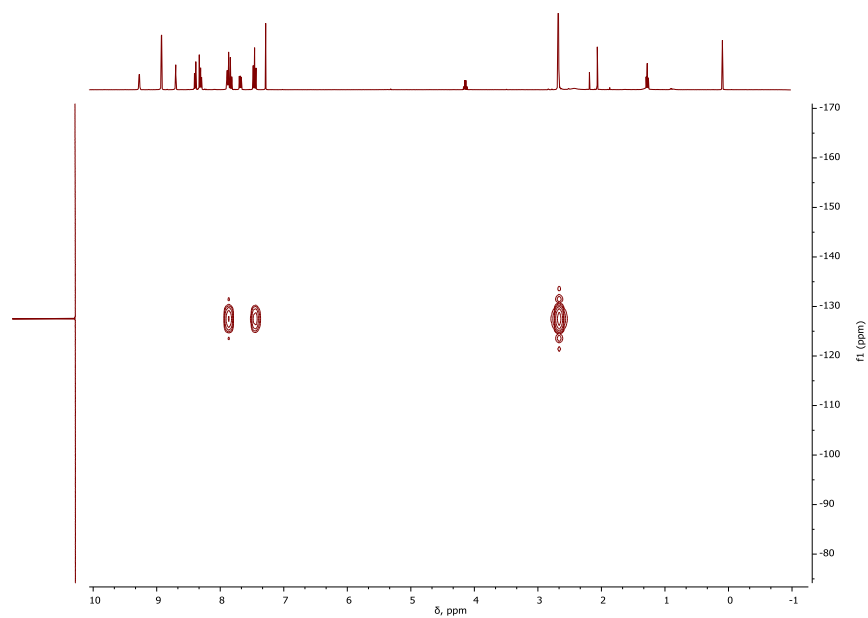


Figure S16:  $^1\text{H}$ - $^{19}\text{F}$  HMBC NMR **5** in  $\text{CDCl}_3$  at RT.

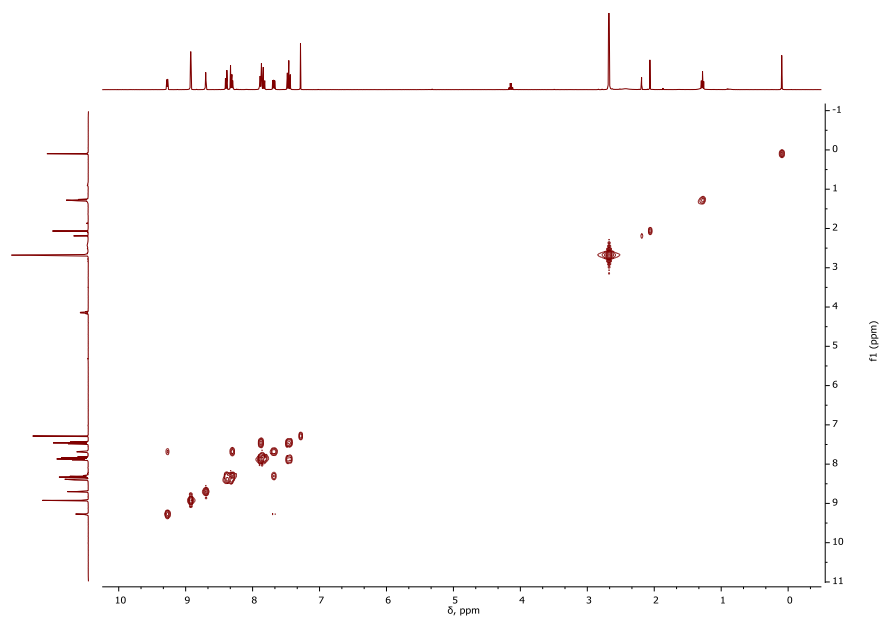
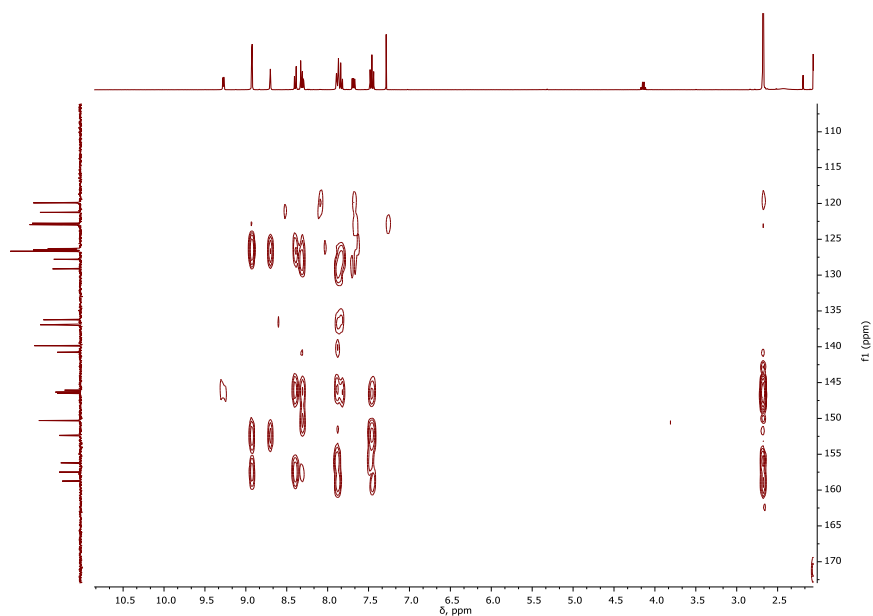
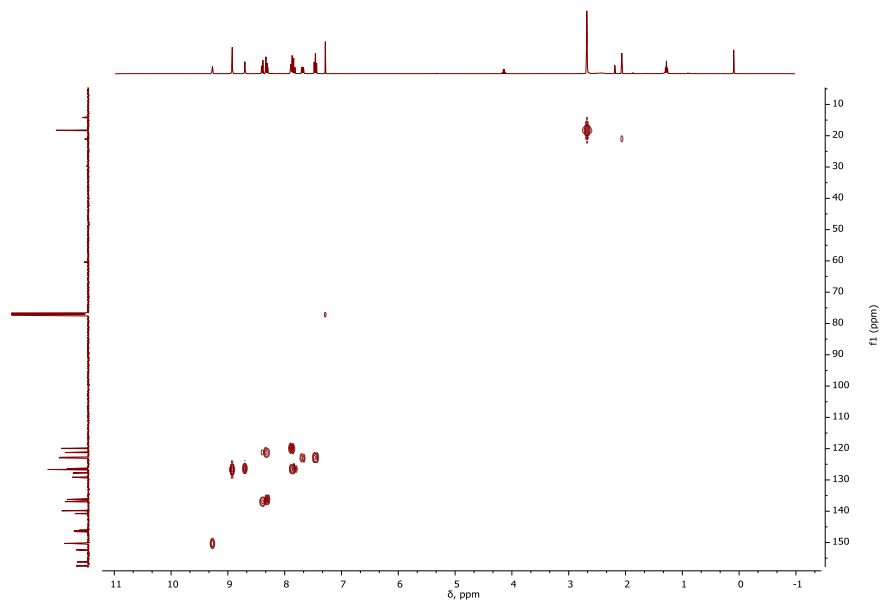


Figure S17:  $^1\text{H}$ - $^1\text{H}$  COSY NMR of **5** in  $\text{CDCl}_3$  at RT.

## CHAPTER 8.



**Figure S18:**  $^1\text{H}$ - $^{13}\text{C}$  HMBC NMR of **5** in  $\text{CDCl}_3$  at RT.



**Figure S19:**  $^1\text{H}$ - $^{13}\text{C}$  HMQS NMR **5** in  $\text{CDCl}_3$  at RT.

VIII

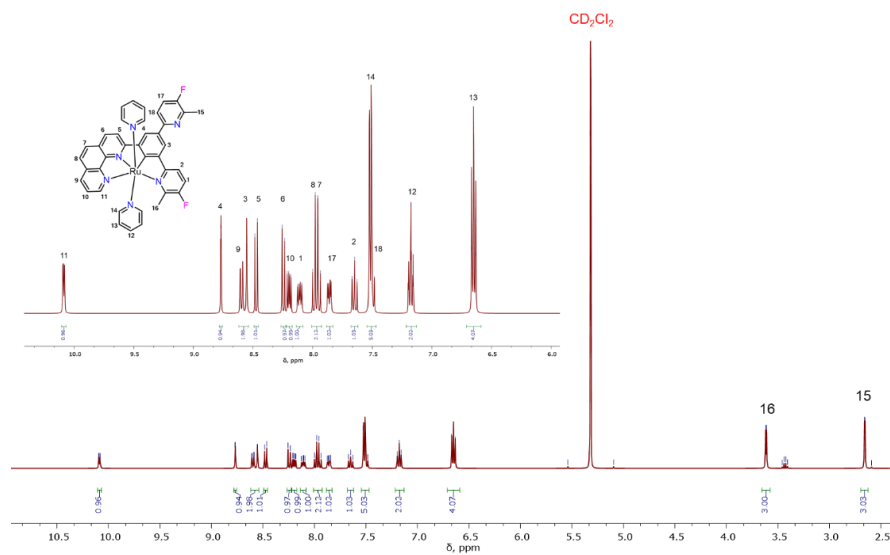


Figure S20:  $^1\text{H}$  NMR of **9** in  $\text{CD}_2\text{Cl}_2$  at RT

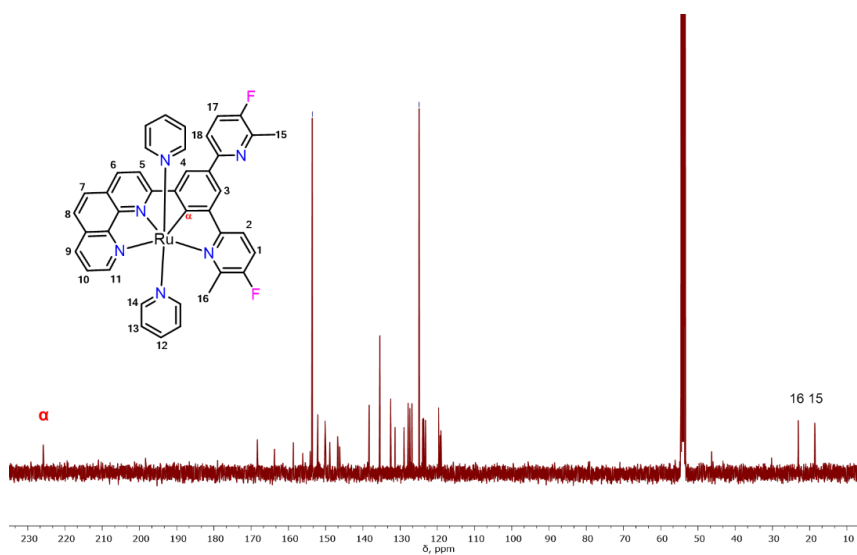
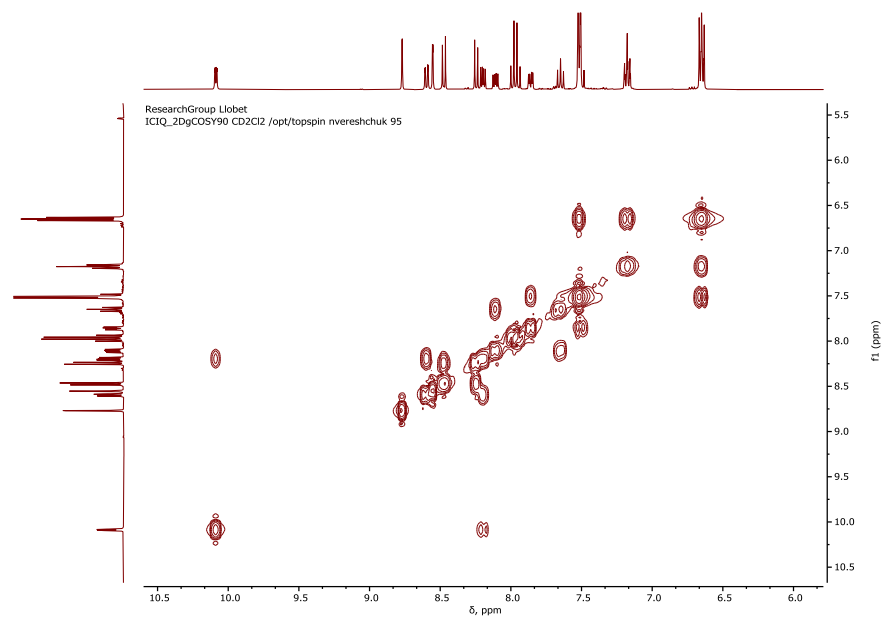
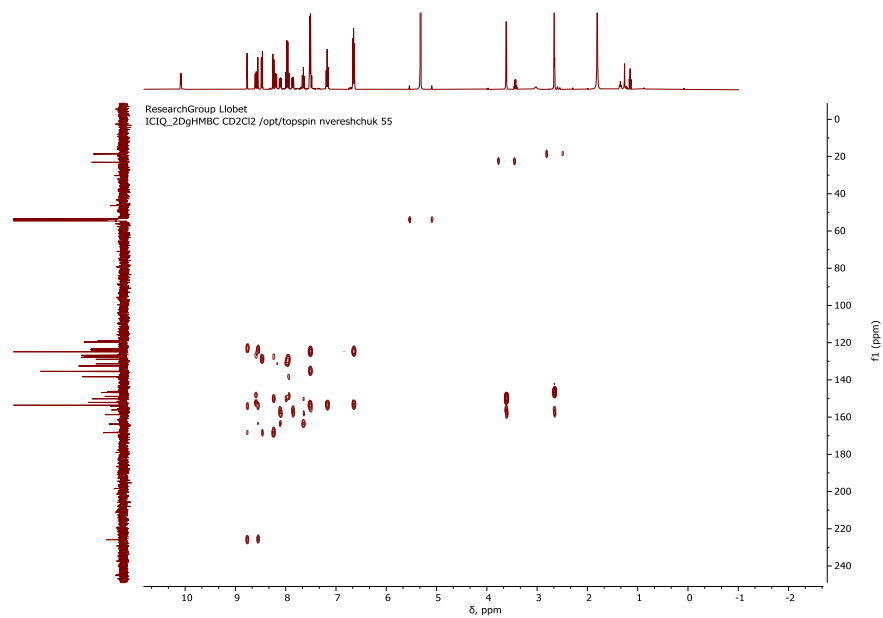


Figure S21:  $^{13}\text{C}$  NMR of **9** in  $\text{CD}_2\text{Cl}_2$  at RT

## CHAPTER 8.



**Figure S22:**  $^1\text{H}$ - $^1\text{H}$  COSY NMR of **9** in  $\text{CD}_2\text{Cl}_2$  at RT



**Figure S23:**  $^1\text{H}$ - $^{13}\text{C}$  HMBC NMR of **9** in  $\text{CD}_2\text{Cl}_2$  at RT

VIII

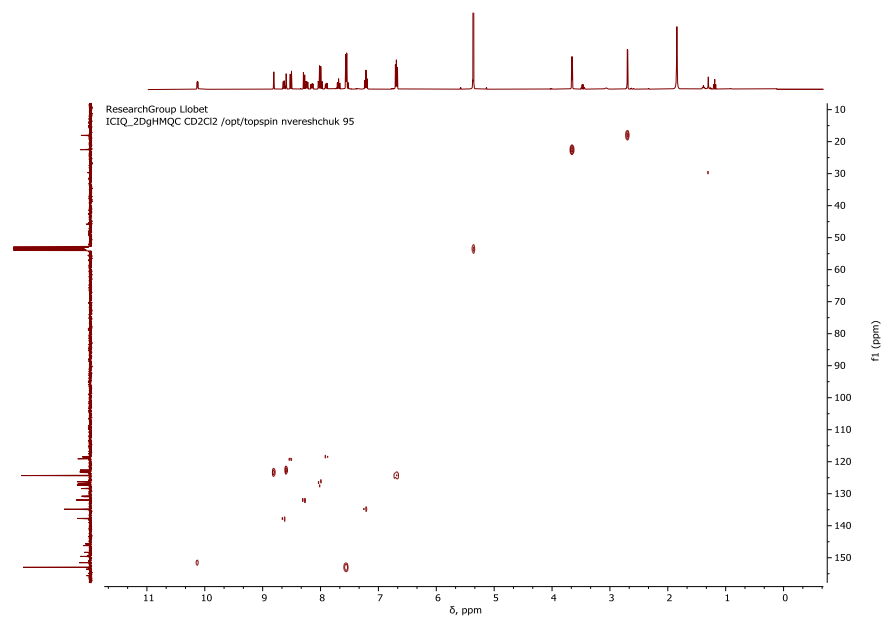


Figure S24:  $^1\text{H}$ - $^{13}\text{C}$  HMQS NMR of **9** in  $\text{CD}_2\text{Cl}_2$  at RT

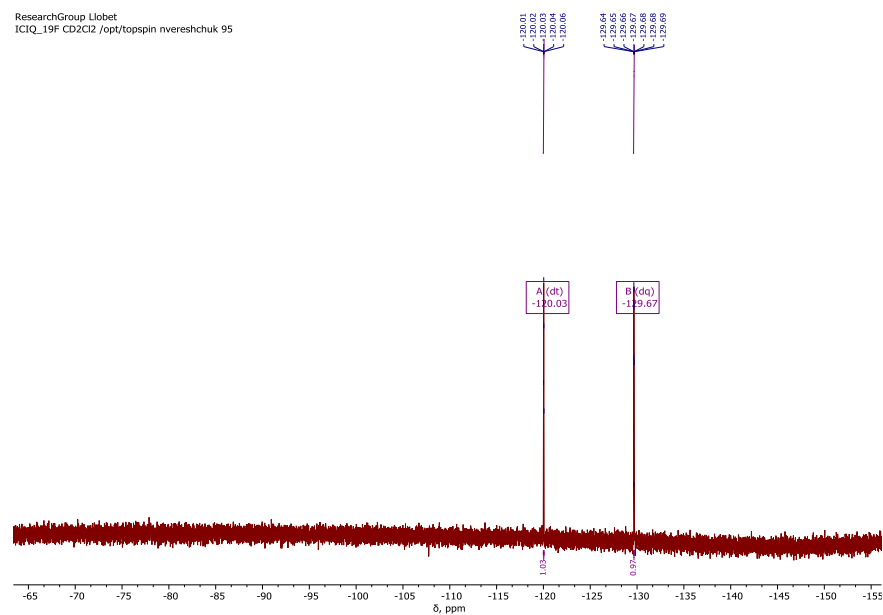


Figure S25:  $^{19}\text{F}$  NMR of **9** in  $\text{CD}_2\text{Cl}_2$  at RT.

VIII

## CHAPTER 8.

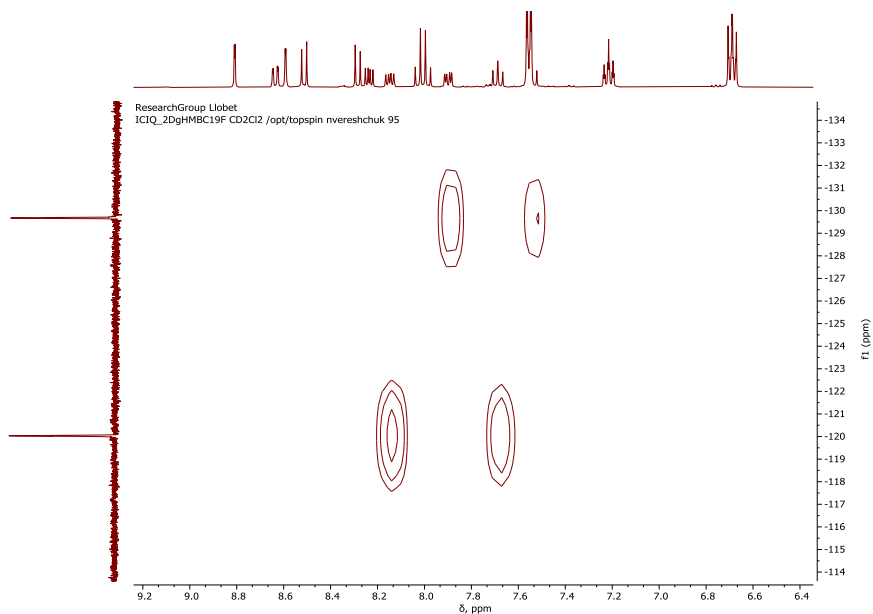


Figure S26:  $^1\text{H}$ - $^{19}\text{F}$  HMBC NMR of **9** in  $\text{CD}_2\text{Cl}_2$  at RT.

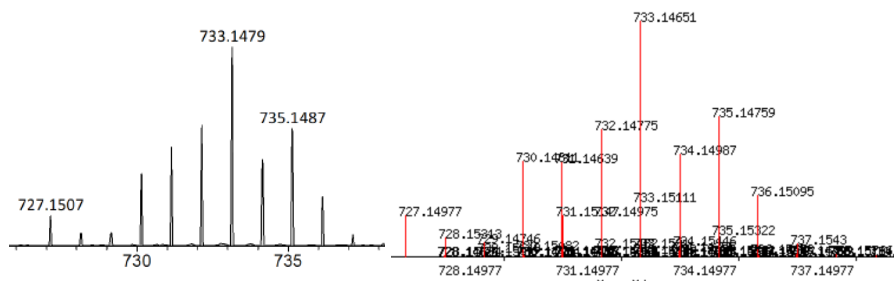


Figure S27: HR-MS for **9** (0.5 ppm error) (left) and simulated (right).

## VIII

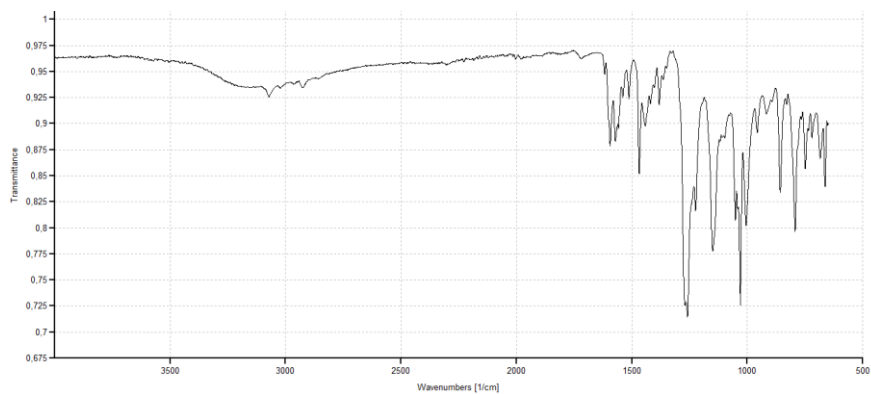
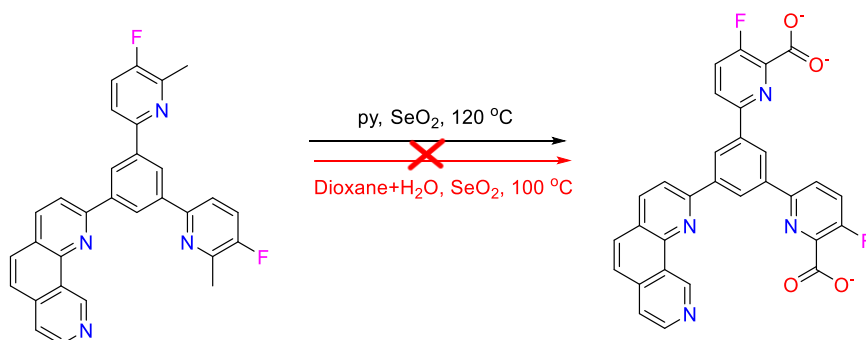


Figure S28: IR (solid-state) of **7**

### 8.6.3 Chemical oxidation of the methyl group in the ligand

#### 8.6.3.1 Chemical oxidation of the ligand by $\text{SeO}_2$ <sup>8</sup>



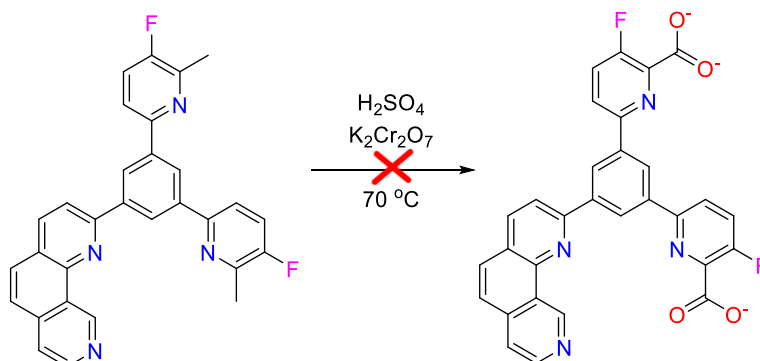
**Method 1.** To the solution of **5** (25 mg) in pyridine (2 mL) was added  $\text{SeO}_2$  (17.5 mg) and the solution was refluxed at 120°C for 12 h. After cooling to room temperature, the precipitate was filtrated off, and the solution was taken to dryness under vacuum and the residue was dispersed in water, which was adjusted to the pH ~ 12 by using KOH and then extracted with DCM. The aqueous phase was acidized by HCl (6 M) under stirring and water evaporated. All the fractions were analyzed by  $^1\text{H}$  NMR. The spectra of aqueous fraction show only pyridine signals, and spectra of the organic fraction in chloroform shows starting material.

**Method 2.** To a solution of **5** (25 mg) in 1,4-dioxane (4 mL) and water (0.5 mL) was added  $\text{SeO}_2$  (17.5 mg) and the solution was refluxed at 100°C for 3 h. The solvent was removed under reduced pressure and the dark brown residue was poured into 48% nitric acid (50 mL) and refluxed for 3 h. The reaction mixture was cooled to room temperature and poured onto crushed ice. The light-yellow precipitate was collected by filtration, washed with water until neutral, and finally washed with ice-cold acetonitrile. The product was analyzed by  $^1\text{H}$  NMR and show signals of starting material.



## CHAPTER 8.

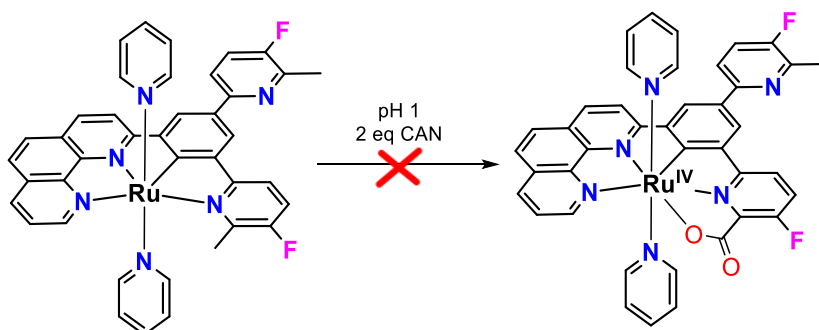
### 8.6.3.2 Chemical oxidation of the ligand by $K_2Cr_2O_7$



**Synthesis:** 50 mg of **5** was added to a solution of Sulfuric Acid (98%, 5mL). The solution was gently heated until the solution reached a temperature of  $60\text{ }^\circ\text{C}$ . Then the heating system was turned off and 130 mg of potassium dichromate was added in small portions to the resulting solution to keep the temperature between  $70\text{ }^\circ\text{C}$  and  $80\text{ }^\circ\text{C}$ . The solution should not overheat above  $85^\circ$  degrees. Once the addition was done, the solution was stirred until the temperature fell below  $40\text{ }^\circ\text{C}$ . The deep green reaction mixture was poured in 25 mL of ice and water and filtered. No precipitate appeared even after one week of staying in the fridge. The NMR of the collected precipitated shows signals with different shifts for the aromatic region than starting material, but a very clear signal of the methyl group in the aliphatic region, the most probably isolated compound is part of the ligand decomposition.

### 8.6.4 Oxidation of the methyl group in the complex

#### 8.6.4.1 Chemical oxidation of the complex **9** by CAN and Ag<sup>+</sup>



**Synthesis:** A solution of cerium ammonium nitrate (Ce<sup>4+</sup>) in pD 1 (49.52 mM, 2.0 eq, 51  $\mu$ L) was added to a solution of **9** in pD 1 (2.57 mM, 0.5 mL) and the NMR measurements were performed (**Figure S29**). From the NMR it can be seen a clear change in the aromatic region of the spectra, while in the expected aliphatic region no change in the methyl group oxidation appeared.

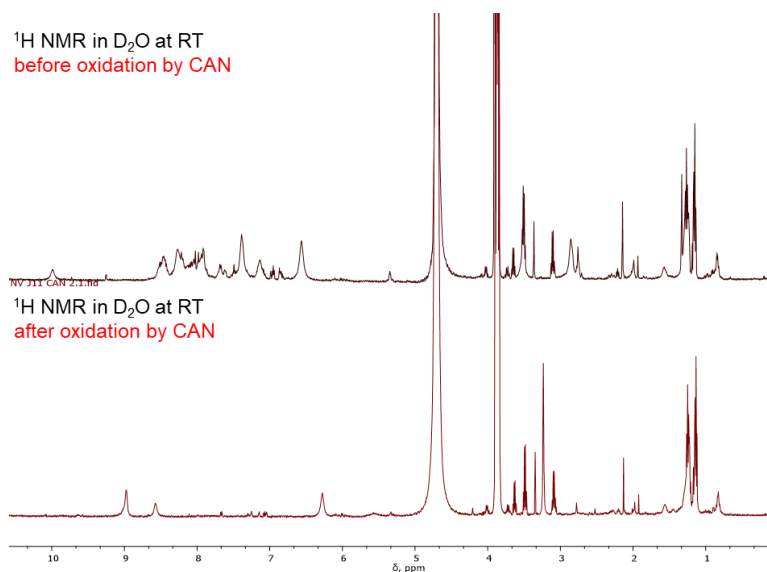


**Figure S29.** <sup>1</sup>H NMR spectra of the chemical oxidation of the complex **9** by CAN

Electrochemical properties of **9** after oxidation by CAN and Ag<sup>+</sup> were also investigated by CV in pH 7 (see Figure S24). The CV shows significant changes after oxidation and from the

## CHAPTER 8.

amounts of oxidation waves, we can conclude that oxidation by CAN and  $\text{Ag}^+$  generated few compounds, that are overlapping and has different properties. It makes it impossible to interpret oxidation processes that are happening in the system.

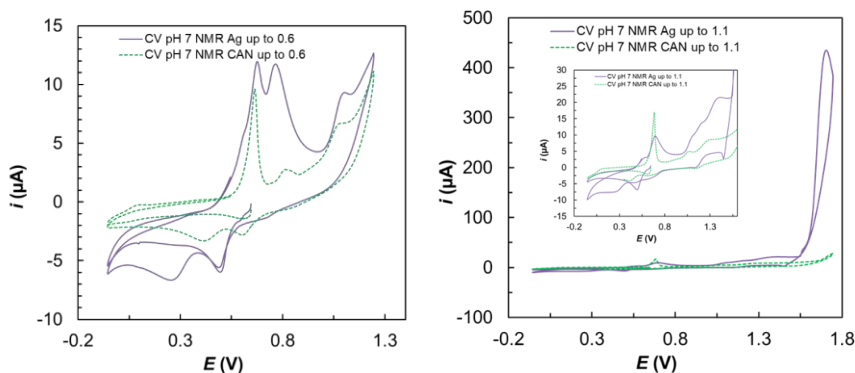


**Figure S30:** Electrochemical behavior of **9** analyzed by CV in phosphate buffer in pH 7 after oxidation by CAN and  $\text{Ag}^+$

### 8.6.5 Redox properties of the complexes

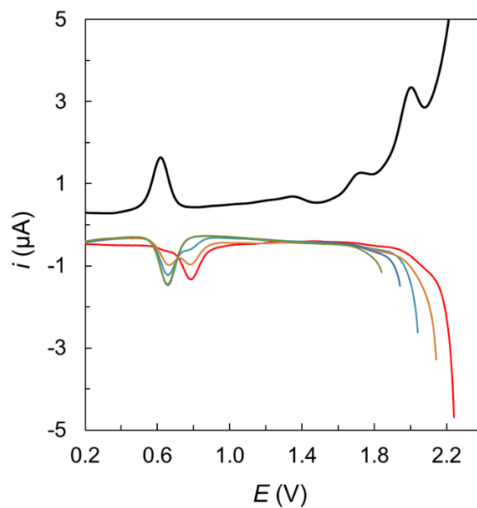


**Figure S31.** Electrochemical behavior for **8** analyzed by DPV in PC,  $\text{NBu}_4\text{PF}_6$ , and 10% of  $\text{H}_2\text{O}$

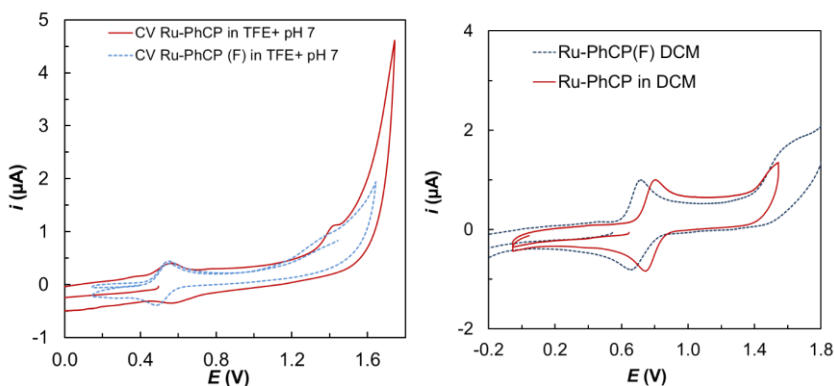


**Figure S32.** (left) Electrochemical behavior of **8** (red) and **9** (blue) was analyzed by CV in TFE and phosphate buffer in pH 7. (right) Electrochemical behavior of **8** (red) and **9** (blue) analyzed by CV in DCM with  $\text{NBu}_4\text{PF}_6$ .

## CHAPTER 8.

### 8.6.6 Single Crystal X-Ray Structure Determination

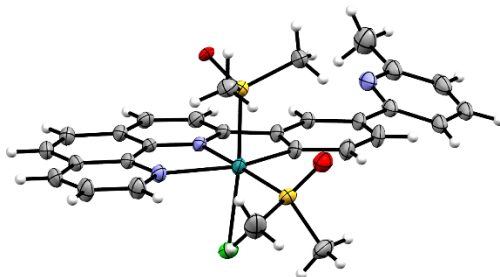


**Figure 33.** X-ray structure ORTEP views (at 50% probability) for **6** Color code: Ru, cyan; S, yellow; N, blue; O, red; C, black; H, white

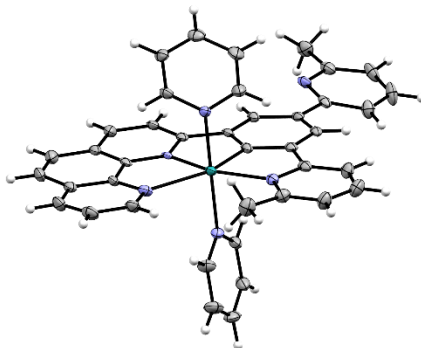


**Figure 34.** X-ray structure ORTEP views (at 50% probability) for **8** Color code: Ru, cyan; N, blue; C, black; H, white

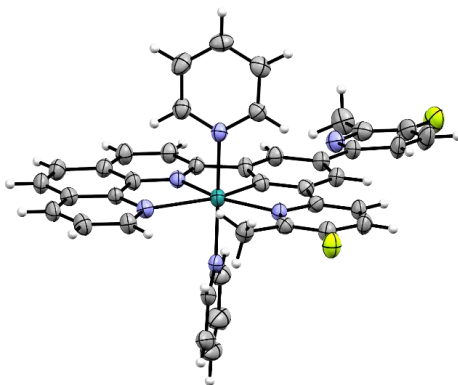


**Figure 35.** X-ray structure ORTEP views (at 50% probability) for **9** Color code: Ru, cyan; F, green; N, blue; C, black; H, white

**Table S4.2.** Selected bond lengths (Å) and angles (deg) in **9**

Distances (Å)		Angle (°)	
Ru1 N1	2.161(9)	N1 Ru1 N2	115.5(3)
Ru1 N2	2.004(6)	N1 Ru1 N6	90.3(8)
Ru1 N6	2.100(1)	N1 Ru1 N7	86.1(9)
Ru1 N7	2.103(4)	N1 Ru1 N3	125.9(0)
Ru1 N3	2.365(7)	N1 Ru1 C11	78.7(6)
Ru1 C11	1.902(1)	N2 Ru1 N6	91.9(6)
		N2 Ru1 N7	93.3(0)
		N2 Ru1 N3	75.5(0)
		N2 Ru1 C11	79.9(3)
		N6 Ru1 N7	173.5(0)
		N6 Ru1 N3	88.7(7)
		N6 Ru1 C11	91.8(0)
		N7 Ru1 N3	88.7(7)
		N7 Ru1 C11	92.9(3)
		N3 Ru1 C11	155.4(3)
		Ru1 N1 C1	129.2(2)
		Ru1 N1 C5	112.4(5)
		C1 N1 C5	118.3(3)
		Ru1 N2 C12	117.1(8)
		Ru1 N2 C16	121.8(0)
		Ru1 N3 C20	107.8(6)
		Ru1 N3 C23	135.6(0)
		C20 N3 C23	116.4(4)
		N1 C5 C6	114.8(1)
		C5 C6 C11	111.7(6)
		C11 C10 C12	112.0(6)
		Ru1 C11 C6	122.2(7)
		Ru1 C11 C10	118.4(6)
		C6 C11 C10	119.2(2)
		N2 C12 C10	112.3(4)
		N3 C20 C16	117.9(2)
		N4 C24 C8	117.0(5)

## CHAPTER 8.

## References

- (1) Matheu, R.; Ertem, M. Z.; Benet-Buchholz, J.; Coronado, E.; Batista, V. S.; Sala, X.; Llobet, A. Intramolecular Proton Transfer Boosts Water Oxidation Catalyzed by a Ru Complex. *J. Am. Chem. Soc.* **2015**, *137* (33), 10786–10795.
- (2) Vereshchuk, N.; Matheu, R.; Benet-Buchholz, J.; Pipelier, M.; Lebreton, J.; Dubreuil, D.; Tessier, A.; Gimbert-Suriñach, C.; Z. Ertem, M.; Llobet, A. Second Coordination Sphere Effects in an Evolved Ru Complex Based on Highly Adaptable Ligand Results in Rapid Water Oxidation Catalysis. *J. Am. Chem. Soc.* **2020**, *142* (11), 5068–5077.
- (3) Matheu, R.; Ertem, M. Z.; Gimbert-Suriñach, C.; Sala, X.; Llobet, A. Seven Coordinated Molecular Ruthenium-Water Oxidation Catalysts: A Coordination Chemistry Journey. *Chem. Rev.* **2019**, *119* (6), 3453–3471.
- (4) Dr. Alice De Palo. Synthesis and Characterization of Ruthenium-Based Organometallic Complexes with Pyridine or Phenanthroline Ligands and Iridium-Based Complexes with Suitably Functionalized Cyclopentadienyl Ligands, University of Pisa, 2019.
- (5) Miller, T. M.; Neenan, T. X.; Zayas, R.; Bair, H. E. Synthesis and Characterization of a Series of Monodisperse, 1,3,5-Phenylene-Based Hydrocarbon Dendrimers Including C276H186 and Their Fluorinated Analogs. *J. Am. Chem. Soc.* **1992**, *114* (3), 1018–1025.
- (6) Miyaura, N.; Suzuki, A. Palladium-Catalyzed Cross-Coupling Reactions of Organoboron Compounds. *Chem. Rev.* **1995**, *95* (7), 2457–2483.
- (7) Bureau, I. WO 2009/040551 A1 (74). **2009**, 2009 (April).
- (8) Luo, Q.; Dai, Z.; Cong, H.; Li, R.; Peng, T.; Zhang, J. Oxidant-Free Synthesis of Benzimidazoles from Alcohols and Aromatic Diamines Catalysed by New Ru(II)-PNS(O) Pincer Complexes. *Dalt. Trans.* **2017**, *46* (43), 15012–15022.
- (9) Schlotthauer, T.; Parada, G. A.; Görls, H.; Ott, S.; Jäger, M.; Schubert, U. S. Asymmetric Cyclometalated Ru(II) Polypyridyl-Type Complexes with  $\pi$ -Extended Carbanionic Donor Sets. *Inorg. Chem.* **2017**, *56* (14), 7720–7730.
- (10) Maji, S.; López, I.; Bozoglian, F.; Benet-Buchholz, J.; Llobet, A. Mononuclear Ruthenium-Water Oxidation Catalysts: Discerning between Electronic and Hydrogen-Bonding Effects. *Inorg. Chem.* **2013**, *52* (7), 3591–3593.
- (11) Ishiyama, T.; Murata, M.; Miyaura, N. Palladium(0)-Catalyzed Cross-Coupling Reaction of Alkoxydiboron with Haloarenes: A Direct Procedure for Arylboronic Esters. *J. Org. Chem.* **1995**, *60* (23), 7508–7510.
- (12) Riesgo, E. C.; Jin, X.; Thummel, R. P. Introduction of Benzo[ *h* ]Quinoline and 1,10-Phenanthroline Subunits by Friedländer Methodology. *J. Org. Chem.* **1996**, *61* (9), 3017–3022.
- (13) R, Z.; P, K.; S, M. A.; MR, A.; M, A. An Improved Synthesis of 2-(Pyrid-2'-yl)-1,10-Phenanthroline Tridentate Terpyridyl Ligand. *Int. J. Chem. Res.* **2014**, *5* (1), 153–158.
- (14) Elgrishi, N.; Rountree, K. J.; McCarthy, B. D.; Rountree, E. S.; Eisenhart, T. T.; Dempsey, J. L. A Practical Beginner's Guide to Cyclic Voltammetry. *J. Chem. Educ.* **2018**, *95* (2), 197–206.

## 9 CHAPTER 9

### CONCLUSIONS

---

*The specific and more detailed conclusions of each work are disclosed in Chapters 3-8. General conclusions are exposed in this Chapter in order to summarize the present doctoral thesis.*

---

- I. Novel Ru-based complex containing the pentadentate ligands HatPa generate the fastest molecular water oxidation catalysts described up to date ([2,2':6',2''-terpyridine-6,6''-diphosphonic acid = HatPa]). The complex has been prepared in order to study the effect of intramolecular proton transfer.
- II. It had been shown that second coordination sphere effects are responsible not only to generate the active catalyst but also to reduce energies of activation at the rate-determining step of the catalysis.
- III. We determined the possible deactivation pathways in order to design more robust catalysts targeting to utilize them into complete photoelectrochemical cells.
- IV. The new coordination 2D material was successfully immobilized onto a carbon-based surface. The molecular nature and redox properties were investigated by electrochemical and spectroscopic techniques. The presented electrode is an efficient device for electrochemically driven heterogeneous water oxidation.



## CHAPTER 9. Conclusions

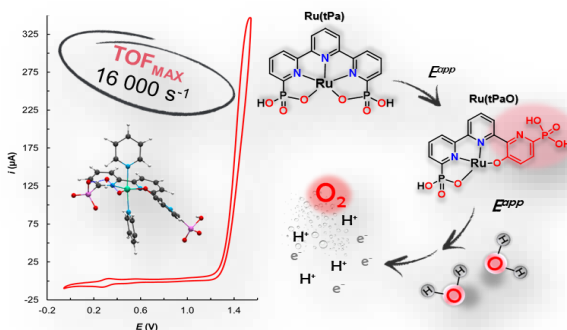
## Chapter 3 and 4:

### **Second Coordination Sphere Effects: Powerful O<sub>2</sub> Evolving Ru Catalysts Based on a FAME Ligand**

In the first part of the thesis, we designed a novel Ru-based complex consisted of a terpyridine ligand core, where we decorated terpyridines with phosphonate

moieties. Implemented changes resulted in the coordination complex **Ru(tPa)**, where tPa is [2,2':6',2''-terpyridine-6,6''-diphosphonic acid]. Together with two phosphonate groups, two extra protons were introduced into the system, promoting PCET process, which showed a substantial impact on catalyst performance. Next, we developed the synthetic chemistry for the **Ru(tPa)** complex. The initial **Ru(tPa)** complex evolves *via* intramolecular aromatic O-atom insertion into a CH bond, leading to a completely new complex **Ru(tPaO)**, that has the highest TOF<sub>max</sub> (16000 s<sup>-1</sup>) ever reported and remarkable long-term stability. The dangling phosphonate group is responsible for the low energy pathway of the two key reactions: (i) the formation of active catalyst precursor *via* oxygen insertion and (ii) the intramolecular proton transfer from the incoming water molecule for the O–O bond formation step. These two key reactions occur intramolecularly thanks to the right positioning of the Ru<sup>V</sup>=O groups *versus* the dangling phosphonate group and thus are entropically highly favored. Further, we showed how second coordination sphere effects are responsible not only to generate the active catalyst but also to reduce energies of activation at the rate-determining step of the catalysis.

This part of the thesis highlights the importance of designing catalysts with the right second coordination sphere environment and the need to evaluate the fate of the catalyst during turnover.



## CHAPTER 9. Conclusions

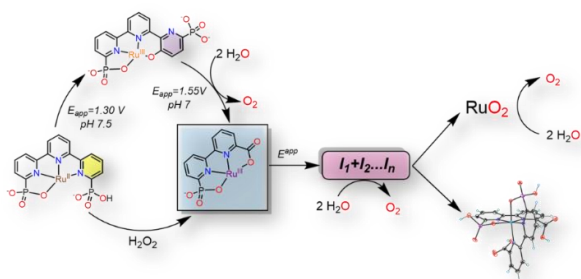
### Chapter 5:

#### *Mechanistic understanding and characterization of reaction intermediate species involved in the water oxidation catalytic cycle*

Further in the thesis, we showed the behavior of **Ru(tPaO)** under turnover conditions operating at different pHs and applied potentials. The analysis showed, that during harsh

water oxidation conditions, the **Ru(tPaO)** suffers oxidative degradation during turnover generating the phosphonate-carboxylate Ru complex **Ru(bpc)**. This transformation occurs due to the relative facile oxidation of the

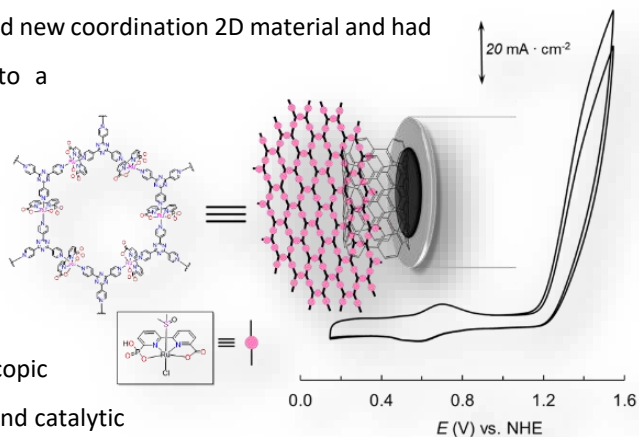
phenoxo group to quinone, which in turn suffered several further transformations to **Ru(bpc)**. The latter is also a WOC, which during electrocatalytic activity undergoes further transformations to  $\text{RuO}_2$ , *via* several molecular intermediates, that are also highly active WOCs. Overall, these results manifest the importance of the ligand selection in order to come up with rugged and performing WOCs.



## Chapter 6:

### ***Functional coordination polymers for the generation of powerful molecular electroanodes for water oxidation***

In order to generate hybrid molecular anodes, we functionalized one of the fastest and efficient Ru WOC. We synthesized new coordination 2D material and had successfully immobilized it onto a carbon-based surface as well as the metal-oxide surface. The molecular nature and redox properties were investigated by electrochemical and spectroscopic techniques. With high stability and catalytic activity, the presented electrode is an efficient device for electrochemically driven heterogeneous water oxidation with the achieving current densities in the range of 0.1-0.2 mA/cm<sup>2</sup>.

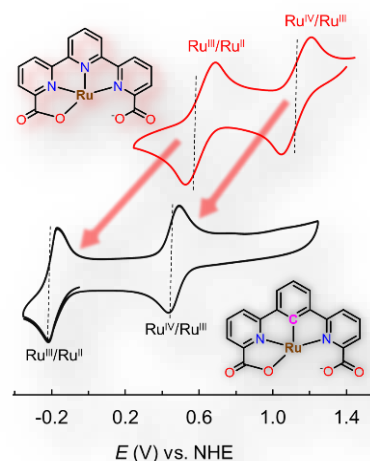


## CHAPTER 9. Conclusions

### Chapter 7 and 8:

#### *Reducing the potential: Ruthenium-based cyclometalated complexes and the effect of the carbonanion on the redox properties.*

In the next part of the thesis, inspired by the **Ru(tda)** catalyst, we designed a family of cyclometalated complexes, where we replaced one pyridine in the terpyridine with a phenyl group, in order to reduce overpotential for catalysis. The novel Ru-based complexes **Ru(pda)** and **Ru(Phpp)**, which contains negatively charged **pda**<sup>3-</sup> and **Phpp**<sup>-</sup> ligands (**pda**<sup>3-</sup> - 6,6'-(1,3-phenylene)dipicolinic acid and **Phpp**<sup>-</sup> is 2-(3-(pyridin-2-yl)phenyl)-1,10-phenanthroline) were synthesized and fully characterized. Those new ligands stabilized higher oxidation states due to strong sigma donation through the metal-carbon bond. The electrochemical analysis of the synthesized complexes showed a significant cathodic shift of the redox potentials compared to the related **Ru(tda)** and **Ru(tPa)** complexes. While the latter are spectacular catalysts, the replacement of one pyridine in the terpyridine by a phenyl group renders these complexes as very robust coordination compounds without any catalytic activity towards water oxidation. Despite the activity



issues, the present work enlarges the landscape of Ru-based complexes and uncovers additional factors influencing the water oxidation catalysis, like the presence of anionic ligands and their implication on redox potentials.

## CHAPTER 9. Conclusions



## CHAPTER 9. Conclusions





UNIVERSITAT  
ROVIRA i VIRGILI